

# **Dissertation**

submitted to the  
Combined Faculties for the Natural Sciences and for Mathematics  
of the Ruperto-Carola University of Heidelberg, Germany  
for the degree of  
Doctor of Natural Sciences

presented by  
**Dipl.-Phys. Dennis Heine**  
**born in Minden(Westfalen), Germany**

Oral examination: July 16<sup>th</sup>, 2008



# **Single Atom Detection and Non-Classical Photon Correlations**

This dissertation was carried out at the  
**Physikalisches Institut, Universität Heidelberg**  
and the  
**Atominstitut der Österreichischen Universitäten, TU Wien**

Referees

**Prof. Dr. Jörg Schmiedmayer**

**Prof. Dr. Christoph Cremer**



## Abstract

In this thesis a reliable and robust single atom detector is presented, characterised and applied to measure the fluorescence emission of single atoms.

The detector consists of a tapered single mode excitation fibre and a multi mode detection fibre, both integrated on an atom chip. Single neutral  $^{87}\text{Rb}$  atoms propagating freely in a 1D magnetic guide can be detected with an efficiency of 66% due to highly selective excitation and matched detection region.

The detector allows to identify the statistical distribution of the atoms, which, for the current experiments, was proven to be Poissonian. Non-classical correlations in the photon emission from a single atom have been measured, showing a perfect photon anti-bunching. Rabi oscillations of the correlation function have been observed and proven to be in excellent agreement with theoretical expectations.

The detector presented here is conceptionally much simpler than comparable integrated detectors employing cavity assisted detection and can be produced by using only commercially available lithographic techniques. With this detector single atom sensitivity is reached without the need for cavity assisted detection or localization of the atoms.

## Zusammenfassung

In dieser Arbeit wird ein robuster und verlasslicher Einzelatomdetektor vorgestellt, charakterisiert und benutzt, um die Fluoreszenzemission einzelner Atome zu untersuchen.

Der Detektor besteht aus auf einem Atom Chip integrierten optischen Fasern. Eine fokussierende Single Mode Faser dient zur Anregung der Atome, deren Fluoreszenzemission durch einer Multi Mode Faser zur Detektion gesammelt wird. Durch die hochselektive Anregung und ein darauf angepasstes Detektionsvolumen koennen einzelne neutrale  $^{87}\text{Rb}$  Atome mit einer Effizienz von 66% detektiert werden.

Der Detektor ermoglicht es, die statistische Verteilung atomarer Ensembles durch einfache Messungen zu bestimmen. Im Fall der vorliegenden Experimente wurde eine Poissonverteilung der Atome nachgewiesen. In einer Untersuchung der Photonenemission einzelner Atome konnte perfektes Photonen Antibunching gemessen werden, ein eindeutiges Zeichen nichtklassischer Korrelationen. Desweiteren wurden Rabioszillationen der Korrelationsfunktion in hervorragender Ubereinstimmung mit theoretischen Erwartungen beobachtet.

Durch den einfachen Aufbau sind nur konventionelle Lithographietechniken zur Fertigung des Detektors notig. Im Gegensatz zu bestehenden integrierten Einzelatomdetektoren benotigt der hier vorgestellte Detektor weder zusatzliche Fallen zur Lokalisierung der Atome, noch einen Resonator.



# Contents

<b>Abstract</b>	<b>i</b>
<b>Abbreviations &amp; Symbols</b>	<b>vi</b>
<b>1. Introduction &amp; Motivation</b>	<b>1</b>
1.1. Motivation . . . . .	1
1.2. Introduction . . . . .	3
<b>I. Physics</b>	<b>5</b>
<b>2. Basic Setup</b>	<b>7</b>
2.1. Overview . . . . .	7
2.2. The Fluorescence Detector . . . . .	10
2.3. The Absorption Detector . . . . .	14
2.4. The Fibre Cavity . . . . .	15
2.5. Photon Detection Setup . . . . .	16
<b>3. Single Atom Detection</b>	<b>21</b>
3.1. Atom Light Interaction . . . . .	21
3.2. Absorption Detection . . . . .	26
3.3. Phase Contrast Detection . . . . .	28
3.4. Fluorescence Detection . . . . .	29
3.5. Why Fluorescence Detection . . . . .	32
<b>4. Photon Detector Characterization</b>	<b>35</b>
4.1. APD Operation Principle . . . . .	35
4.2. Specifications . . . . .	37
4.3. Signal Artefacts . . . . .	39
<b>5. Signal &amp; Background</b>	<b>55</b>
5.1. Signal . . . . .	55
5.2. Background Level . . . . .	62
<b>6. Variance Analysis</b>	<b>67</b>
6.1. Atom Number . . . . .	67
6.2. Statistical Method . . . . .	72

6.3. Interaction Time . . . . .	79
6.4. Examination of Alpha . . . . .	82
6.5. Single Atom Detection Efficiency . . . . .	85
6.6. Summary . . . . .	89
<b>7. Time Interval Analysis</b>	<b>91</b>
7.1. TIA Basics . . . . .	91
7.2. Atomic Source . . . . .	94
7.3. Summary . . . . .	103
<b>8. Correlation Analysis</b>	<b>105</b>
8.1. Theoretical Introduction . . . . .	105
8.2. Measuring the Correlation Function . . . . .	112
8.3. Measurements . . . . .	120
8.4. Summary . . . . .	130
<b>II. Nuts and Bolts</b>	<b>131</b>
<b>9. Setup</b>	<b>133</b>
9.1. Overview . . . . .	134
9.2. Experiment Control . . . . .	135
9.3. Laser System . . . . .	140
9.4. Vacuum Chamber and Atom Chip . . . . .	150
9.5. External ToF Imaging . . . . .	152
9.6. Detection setup . . . . .	153
<b>10. Magnetic Traps</b>	<b>157</b>
10.1. Atoms in a Magnetic Field . . . . .	157
10.2. The Sideguide . . . . .	158
10.3. Scanning the Guide . . . . .	160
<b>11. Tapered Amplifier</b>	<b>163</b>
11.1. Standard Laser Diode Systems . . . . .	163
11.2. Tapered Amplifier Basics . . . . .	164
11.3. Tapered Amplifier Specifications . . . . .	165
11.4. Setup . . . . .	166
11.5. Transmission Grating Master . . . . .	175
11.6. Performance . . . . .	177
11.7. Cost Estimate . . . . .	182
11.8. Improvements . . . . .	183
11.9. Safety . . . . .	184



<b>III. Conclusion</b>	<b>185</b>
<b>12. Summary</b>	<b>187</b>
<b>13. Improvements</b>	<b>191</b>
13.1. Improvements of the Current Detector . . . . .	191
13.2. Improvements of Future Detectors . . . . .	192
<b>14. Outlook</b>	<b>201</b>
<b>IV. Appendices</b>	<b>203</b>
<b>A. The Rubidium-87 D2 Transition</b>	<b>205</b>
A.1. Energy Levels and Transitions . . . . .	206
A.2. Spectroscopy . . . . .	208
<b>B. Numerical Aperture</b>	<b>211</b>
B.1. Fibre Core Diameter . . . . .	212
<b>C. Poisson Distribution</b>	<b>215</b>
C.1. Derivation from the Binomial Distribution . . . . .	215
C.2. Mean and Variance . . . . .	216
C.3. Time Intervals . . . . .	217
C.4. Applicability . . . . .	217
<b>D. Analysis Programs</b>	<b>219</b>
<b>E. How to built an ECDL Laser</b>	<b>221</b>
E.1. Ingredients . . . . .	221
E.2. Building the Laser . . . . .	223
E.3. Suppliers . . . . .	226
E.4. Variants . . . . .	228
E.5. NTC . . . . .	229
E.6. Technical Drawings . . . . .	230
<b>F. Tapered Amplifier Technical Drawings</b>	<b>233</b>

## Abbreviations

<b>AOM</b>	acousto-optical modulator	<b>SE</b>	secondary emission (of an APD)
<b>AP</b>	afterpulse (of an APD)	<b>SM</b>	single mode (fibre)
<b>APD</b>	avalanche photodiode	<b>SNR</b>	signal to noise ratio
<b>BEC</b>	Bose Einstein condensate	<b>SPAD</b>	single-photon avalanche photodiode
<b>BER</b>	bit error rate (of a binary detector)	<b>SPCM</b>	single photon counting module, an APD-type single photon detector. For the presented measurements PerkinElmer SPCM-AQR-12-FC modules have been used.
<b>cps</b>	counts per second		
<b>FM</b>	frequency modulation (locking)		
<b>FO</b>	frequency offset (locking)		
<b>FWHM</b>	full width half maximum	<b>SU-8</b>	epoxy based photoresist from which our fibre-holders are fabricated
<b>HBT</b>	Hanbury Brown-Twiss		
<b>MM</b>	multi mode (fibre)	<b>TA</b>	tapered amplifier
<b>MOT</b>	magneto-optic trap	<b>TIA</b>	time interval analysis
<b>NA</b>	numerical aperture	<b>ToF</b>	time of flight (imaging)

## Symbols

### Constants

$\epsilon_0$	vacuum permittivity	$\hbar$	Planck's constant
$\mu_0$	vacuum permeability	$h$	Planck's constant $h = 2\pi\hbar$
$\mu_B$	Bohr magneton	$k_B$	Boltzman constant
$c$	speed of light in vacuum	$m_{\text{Rb}}$	mass of one $^{87}\text{Rb}$ atom

### Variables

#### Times and Parameters

$A$	area	$t_{\text{dead}}$	dead time (of an APD)
$d_c$	core diameter of a fibre	$t_{\text{int}}$	Interaction time
$\delta t$	time interval between neighbouring events	$T$	total measurement time
$t_b$	bin size	$T_C$	temperature
		$V_B$	breakdown voltage (of an APD)

## Atom Light Interaction

$\gamma$	total photon scattering rate, integrated over all directions and frequencies	$\Gamma$	natural line width (FWHM) of the atomic transition
$\delta$	detuning, $\omega - \omega_0$	$\Omega$	Rabi frequency
$\lambda_f$	wavelength of the light field	$B$	(total) magnetic field strength
$\sigma_0$	maximal photon scattering cross section (resonant, weakly pumped)	$F, m_F$	hyperfine structure (total atomic angular momentum) quantum number, magnetic quantum number
$\tau$	lifetime of the excited state	$I$	incident probe field intensity
$\phi$	phase shift	$I_{\text{sat}}$	saturation intensity
$\chi(\omega)$	electric susceptibility	$I_{\text{trans}}$	transmitted intensity
$\omega$	frequency of the light field, $c = \lambda \cdot \omega / (2\pi)$	$j$	incident photon flux
$\omega_0$	resonance frequency of the atomic transition	$\vec{P}$	total polarization
		$P_{\text{sat}}$	power at which saturation intensity is reached in the focus of the tapered fibre

## Numbers, Densities and Rates

$\alpha$	number of counts per atom	$n_{\text{ph}}^{\text{bg}}$	number of background photons collected
$\lambda$	mean count or event rate, parameter in the Poisson distribution	$n_{\text{ph}}^{\text{fluo}}$	number of fluorescence photons collected
$\rho_{\text{at}}$	atom column density	$n_{\text{ph}}^{\text{scat}}$	total number of photons absorbed/scattered
$n_{\text{at}}$	number of atoms	$m$	number of photons per atom
$\Delta n_{\text{at}}$	atom number uncertainty	$r_{\text{at}}$	rate at which atoms arrive at the detector
$n_{\text{at}}^{\text{min}}$	minimal detectable number of atoms	$r_{\text{det}}$	rate at which atoms are detected
$n_{\text{cts}}$	total number of counts		
$n_{\text{ph}}$	number of photons		

## Efficiencies and Probabilities

$\eta_{\text{at}}$	total efficiency to detect atoms in the detection region	$p_{\text{ap}}$	total afterpulse probability (of an APD)
$\eta_{\text{coll}}$	collection efficiency of the detection optics	$p_{\text{at}}(n)$	probability for $n$ atoms to be in the detection region
$\eta_{\text{gap}}$	coupling efficiency of the filter gap setup	$p_{\text{cts}}(n)$	probability to measure $n$ counts per bin
$\eta_{\text{ph}}$	total efficiency to detect photons emitted from atoms in the detection region	$p_{\text{dist}}(d)$	probability to measure two events/counts at a temporal distance $d$
$\eta_{\text{SPCM}}$	photon detection efficiency of the SPCM	$p_{\text{false}}$	probability for false positive detection (identification of a background count as atom)
$f_{\text{bg}}$	fraction of the incident probe beam photons that are collected inadvertently as background	$p_{\text{ph}}(n)$	probability to emit $n$ photons
		$p_{\text{se}}$	total probability for secondary emission generated counts

# 1. Introduction & Motivation

## 1.1. Motivation

A single two level atom is a fascinating quantum mechanical entity.

While the fluorescence of a large ensemble of atoms can be adequately described as thermal emission with classical correlations, the emission of a single atom is purely quantum. A single atom cannot emit more than a single photon at its transition frequency at a given time. Before a second photon can be emitted the atom has to be re-excited.

Therefore the emission of a single atom exhibits a peculiar phenomenon, described as anti-bunching of the photons, that can only be explained in quantum theory.

**Detecting Single Atoms** Detection of a single atom, let alone measuring correlations of its emission, is a daunting task.

The first single atom detection experiments employed photo ionization [1]. To detect a single atom by its fluorescence, its emission has to be discriminated from background noise. Even a nanowatt of background light is composed of roughly 4 billion photons per second. A  $^{87}\text{Rb}$  atom emitting at its maximum rate under ideal conditions needs more than 100 s to emit a comparable amount of photons.

It follows that background suppression is of prime importance to fluorescence detection. Very efficient detection of single particles can be realized if the background is well suppressed and if the particle remains localized, allowing to collect many fluorescence photons. For single ions strong confinement is achieved in the ion traps [2, 3], while a similar confinement and detection efficiency can be reached for neutral atoms in dipole traps [4].

Placing an optical cavity around the detection region can enhance the detection efficiency in fluorescence detection schemes and allow for efficient absorption detection, as well. Single atom sensitivity can be reached, albeit at the expense of a significant increase in complexity [5–12]. Cavity assisted observation of a beam of atoms has allowed temporal correlation functions of atom arrivals to be accurately measured [6].

**Integrated Detection** High background noise in fluorescence detection is usually caused by unspecific photon collection. The high photon collection efficiency necessary

to collect many signal photons leads to a high number of undesired background photons being collected. If external optics are employed to deliver excitation light to the detection region the problem is aggravated by the inability to selectively illuminate the atoms and stray probe light is being collected as well.

The key to low noise detection is miniaturization. If the detectors are of similar size as the atom clouds precise addressability and selective collection of light from the interaction region becomes possible.

The atom chip is a tool for efficient generation and manipulation of very small atomic ensembles [13–15], but to consistently pursue miniaturization integrated detectors are required [16, 17].

Most implementations so far have focussed on cavity assisted detection [10, 11, 18, 19], with one notable exception exploring the possibility for integrated cavity-free fluorescence detection [20].

Our approach differs in that we aim to develop a simple, but efficient, reliable and robust single atom detector that is fully integrated into an atom chip and can be produced with commercially available techniques. We believe that a detector should be as simple and maintenance-free as possible.

And while integrated cavities will be invaluable in non-destructive detection schemes and for manipulating atomic states we intend to show in this thesis, that highly efficient detection of single atoms and their statistical properties can be achieved by a passively aligned fluorescence detector.

**Applications** Apart from its interest to fundamental science the ability to detect single particles is of fundamental importance to a diverse range of sciences. This encompasses fields of science as different as life sciences, where single molecules need to be detected and localized [21, 22], and quantum information sciences [23–27], which require control over single photons and atoms, to name just two examples.

Quantum communication and cryptography [23, 28, 29] have lately increased the demand for true single photon sources.

The commonly used parametric down conversion single photon sources suffer from a broad emission spectrum and the fact that the emission of several photon pairs at a given wavelength cannot be avoided. Single atoms, on the other hand, can emit only a single photon at their transition frequency. Two photon emissions are rare and will, due to conservation laws, result in two photons of half the transition frequency being emitted, which can easily be filtered.

## 1.2. Introduction

The aim of this thesis has been to efficiently detect single neutral rubidium atoms expanding freely in a one-dimensional magnetic guide. To achieve this an atom chip with integrated detection optics was used. Fabrication details and the results of the first measurements with the detector that we performed while the experiment was still located in Heidelberg can be found in Marco Wilzbach's thesis [30].

**From Heidelberg to Vienna** With the move of the experiment from Heidelberg to Vienna a complete reconstruction of the experiment was necessary which I used to optimize the detection efficiency and improve the experiment based on what we had learned from the Heidelberg measurements.

The initial experiments had shown that, while the detector was capable of detecting small numbers of atoms, to examine the full statistics of the atom distribution typically a few thousand of consecutive measurements at identical parameters are necessary. Preferably a series of measurements should be taken without human intervention. In order to achieve this the experiment control was significantly expanded and increased in flexibility, logging of parameters was introduced and the overall stability of the experiment had to be increased greatly.

The keystone of stable and reproducible operation of a cold atom physics experiment is the laser system, supplying the initial magneto-optic trap (MOT) and probing light. The laser system was completely rebuilt to achieve locked operation for several days. The MOT-beam power was increased by integration of a self-built tapered amplifier system with pointing stable master laser to reduce MOT atom number sensitivity on power fluctuations in the beam. Overall alignment stability of the optical setup was increased by introduction of fibre coupled beams where possible, and ultra stable fixed-height mounts where not.

Additionally several loss channels in the photon detection setup were removed and the background filtering redesigned to optimize the detection efficiency.

**Non-classical Correlations** With the upgrades implemented and the time resolution of the photon detection setup increased to 1 ns, a Hanbury Brown-Twiss type photon detection setup could be realized to allow correlation measurements on the photons emitted by a single atom.

In addition to efficiently detecting single atoms and measuring the statistical distribution of the atomic ensemble, the detector is now capable of observing non-classical correlations in the photon emission of a single atom, as well.

**Structure** This thesis is separated in two major parts, corresponding to the two phases of a typical PhD work in experimental physics. The second phase, which is presented first, consists of data-collection and analysis. The first phase is dominated by the experimental work and technical developments needed to achieve these results and typically takes 80 to 90 % of the total time needed.

I consider both parts to be equally important and hence present them on an equal footing.

In part **I** the results of the measurements and their analysis are presented, with only so much experimental detail as is needed to understand the measurement and certain features of the signals. To this end the detection setup and the photon counting module are treated in detail, but the atom source is only sketched.

Part **II** then describes the remainder of the setup and its technical details, with special emphasis on those parts that were especially developed or adapted for the experiment present here.

Both parts can be read largely independently of one another, hopefully allowing easy access to both the scientific results and the more engineering oriented aspects of the experimental work.

I conclude with an outlook and a discussion of recommended improvements for future measurements in part **III**.

Additional technical information is available in the appendices.

*"Science is one percent inspiration, ninety-nine percent perspiration."*

Thomas Alva Edison



**Part I.**  
**Physics**



## 2. Basic Setup

The aim of my experiments has been to reliably detect single ultra-cold neutral  $^{87}\text{Rb}$  atoms that propagate freely in a 1D magnetic guide (see chapter 10). To this end we have integrated fibre optical detectors on an atom chip. I will give a brief overview of the setup in this chapter, addressing the experiment at large and the detectors in specific. The treatment here is intended to give an elementary understanding of the experimental setup as a foundation for the analysis of the measured signals and to give an understanding of the influence of peculiarities of the setup on those signals. A detailed and more technical description of the setup can be found in chapter 9.

### 2.1. Overview

The experimental cycle of our experiment can be abstracted to the basic steps depicted in fig.2.1. We first load the atoms from the background gas into a magneto-optic trap (MOT) [31–33]. Once the MOT is saturated with atoms, the trap is shifted close to the atom chip and the atoms are optically pumped into a magnetic substate compatible with magnetic trapping. Subsequently the MOT laser beams are turned off and the atoms are transferred into a magnetic trap on the atom chip. Here evaporative cooling methods may be employed to reduce the temperature of the atoms. From the chiptrap the atoms are transferred into a 1D magnetic guide in which the atoms expand towards the detection region according to their temperature. Atom detection is performed by guiding the atoms into the focus of a lensed fibre, where they are excited by light resonant to a closed transition. The fluorescent light from the excitation region is collected by a second fibre which guides the light to a photon detector.

Alternative fibre-based atom detectors are integrated on the atom chip but are not subjects of this thesis. They are described briefly in sections 2.3 and 2.4 and presented in detail in Marco Wilzbach’s thesis [30].

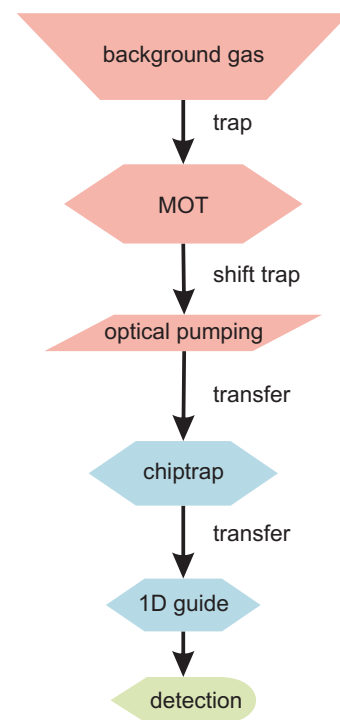


**Figure 2.1.:**  
Experimental Cycle Diagram

### 2.1.1. Atom Source Basics

Using a standard MOT setup we trap  $10^8$   $^{87}\text{Rb}$  atoms from the background gas provided by a hot Rb-Dispenser.<sup>1</sup> After polarization gradient cooling to less than  $15\ \mu\text{K}$  and optical pumping into the  $|F = 2, m_F = 2\rangle$  state about  $1 - 3 \cdot 10^6$  atoms are directly transferred into a magnetic trap on the atom chip (see fig.2.2). Here the atoms equilibrate at a temperature of  $25\ \mu\text{K}$  (transversal) before being transferred into a 1D magnetic guide, again generated by the atom chip, that leads to the fibre detector. The atoms pass the detector with a transversal temperature<sup>2</sup> of approximately  $40\ \mu\text{K}$ .

A MOT setup consists of an ultra-high vacuum (UHV) chamber, a diode laser system and copper wires in the vacuum chamber as well as external coil pairs for magnetic field generation. The atom chip is basically a gold surface on a  $\text{SiO}_2$  layer over a silicon substrate. Using lithographic techniques wires of 20 to  $100\ \mu\text{m}$  width are patterned in the gold surface. The magnetic field generated by current flowing through these wires creates, in conjunction with external magnetic fields, magnetic microtraps close to the atom chip surface.

While MOTs and wiretraps have been instrumental in achieving the results presented here a detailed understanding of their principles is not essential for the analysis and interpretation of said results. Therefore I will omit a treatment of MOTs and wiretraps, as fascinating as they are. They have been described very competently and in great detail in previous works from our group and others, e.g. references [13–15, 30–32, 34–39].

For all purposes of this work MOTs and magnetic wiretraps can be considered as black boxes, albeit possible emission of photons from these boxes has to be considered. Most notably the dispenser is a strong source of broadband black-body radiation and light from the MOT lasers might scatter into the detection fibres. For a detailed treatment of background signals see section 5.2.

Similar to most other experiments in our group we choose to work with  $^{87}\text{Rb}$  because its D-2 transition lies with  $780\ \text{nm}$  in a region that is easily accessible with commercial laser diodes and its level structure offers closed transitions<sup>3</sup> (see appendix A), making it an ideal candidate for magneto optical trapping.

### 2.1.2. Chip Layout

Of the different wire structures realized on our chip we use for the current experiments only a central Z-shaped wire and two L-shaped 1D guides (see fig. 2.3 and chapter 10).

<sup>1</sup>A Rb-Dispenser is essentially a reservoir of solid Rb embedded in a wire. Pushing a current of several amperes through the wire heats the Rb, leading to evaporation.

<sup>2</sup>Note that the atoms are not in thermal equilibrium in the guide and the collision rate after the first few ms of expansion is extremely low. Therefore a longitudinal temperature cannot be defined and a transversal temperature can only be defined approximately.

<sup>3</sup>Only once per thousand excitation cycles a  $^{87}\text{Rb}$  atom leaves the closed cycle and falls into the wrong groundstate.

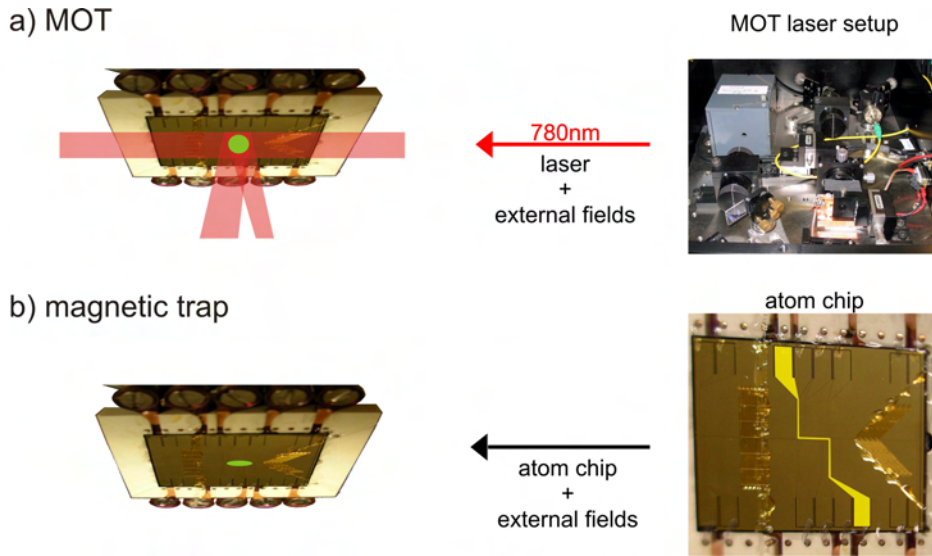


**Figure 2.2.:** Trapping Atoms Basic Procedure

A dispenser (not shown) provides a background gas of rubidium.

a) Three counterpropagating pairs of resonant laser beams combined with magnetic fields form a MOT that traps a cloud of  $^{87}\text{Rb}$  (here shown in green) from the gas. Note that two of the laser beam pairs are completed by a  $45^\circ$  reflection on the atom chip (a so-called mirror MOT [14, 30, 34]). The left column shows the atom chip in its mounting, hanging upside down to allow time of flight expansion temperature measurements when the trapping fields are turned off.

b) Current flowing through a Z-shaped wire on the atom chip (right, marked in yellow) combined with an external bias field generates a magnetic trap close to the chip [34]. Since the volume of the magnetic trap is much smaller and field gradients are much higher than in the MOT the transfer from MOT to magnetic trap involves a compression of the cloud. The atoms are now trapped at a distance  $O(100\ \mu\text{m})$  from the chip and can be manipulated and moved by changing the current through the chip wires.

The Z-wire generates the initial magnetic trap where those atoms that were successfully transferred from the MOT to the chiptrap are thermalised. The 1D guides are used to transport the atoms to the detection regions.

Transfer into one of the 1D-guides is established by ramping up the current through the guide while decreasing the current in the Z to zero. Those parts of the guide parallel to the Z generate a potential similar to the Z-trap, keeping the barrier at one end of the Z intact, while the barrier on the other end of the Z, where the guide goes straight on to the detector, is removed, so that the atoms can expand freely into the 1D-guide. Confinement of the atoms is then given only in the transversal direction.

The current in the guide-wire determines the height of the guide-potential minimum relative to the chip surface, enabling us to align the guide minimum with the detection regions given by the fibres.

Note that, were we to use both guides in parallel the overall effect would be similar to one Z, meaning we can send the atoms either to the fluorescence detection region or the absorption/cavity detection region (see figure 2.3) but not to both regions at the

same time.

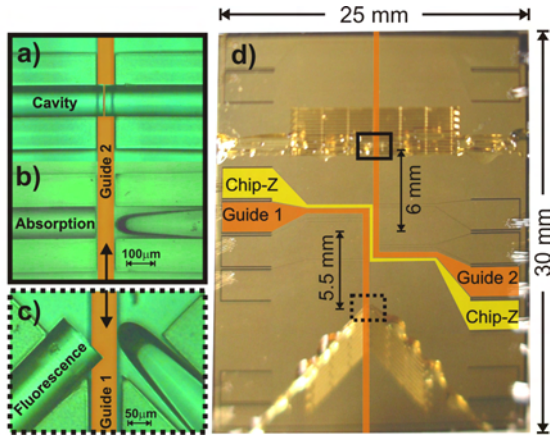


**Figure 2.3.:** The Fibre Detectors

The atoms are initially trapped by the chip-Z wire (marked yellow) and can subsequently be transferred into either one of the (orange) 1D-guides, where they will expand towards the detectors. Three different types of fibre detectors have been integrated on the atom chip. The detection regions are shown in magnification in subfigures a) to c).

a) A fibre cavity with a free-space gap for atom-photon coupling.

b) An absorption detector consisting of a tapered fibre for excitation and a multi mode fibre to collect the transmitted light.

c) A fluorescence detector consisting of a tapered fibre for excitation and a multi mode fibre to collect fluorescence light.

Note that the markings for the guide wires in subfigure d) are much thicker than the wires themselves.

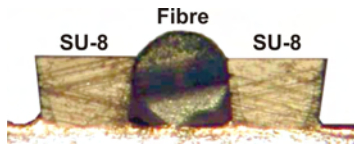


**Figure 2.4.:**

SU-8 holding structure

To test the advantages and disadvantages of different detector types three detectors have been integrated on the chip. The detectors are fully integrated on the atom chip by mounting the fibres in lithographically defined trenches. These structures are fabricated from SU-8, an epoxy based photoresist. Since all fibres employed in our setup have a diameter of  $125\ \mu\text{m}$  we use SU-8 trenches with a height of  $90\ \mu\text{m}$  and slightly undercut walls to clamp the fibres down onto the chip (see fig. 2.4). The clamping force is sufficient to keep the fibres in place. The trenches allow extremely accurate positioning of the fibres with a precision of a few ten nanometres, as well as excellent long term stability. The fibre cavity of fig. 2.3a) has shown stable alignment over more than one year under experimental conditions. For more details on the fibre holding structures see chapter 9.

## 2.2. The Fluorescence Detector

The fluorescence detector is located on guide 1 in figure 2.3, 5.5 mm from the centre of the chip-Z. The atoms trapped in the Z-trap are transferred into the 1D-guide, which leads them through the focus of a lensed excitation fibre. The fluorescence light from the interaction region is collected by a second fibre which guides the light to a photon detector (compare fig. 2.5).

As the atoms pass the detector they are excited by laser light resonant to a closed

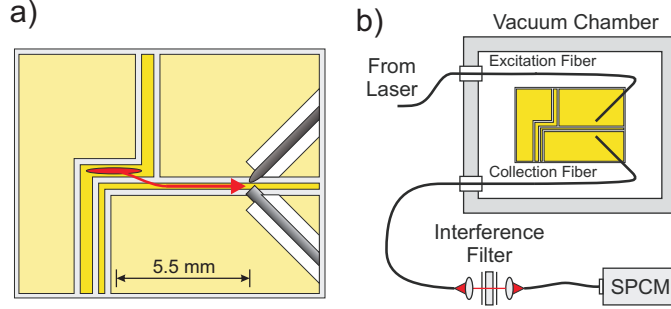


**Figure 2.5.:** Schematic Setup of the Fluorescence Detector

- a) The atoms are transferred from the Z-trap into a 1D-guide, which leads them to the integrated fibre detector.
- b) Excitation laser light is delivered to the atoms via a tapered fibre. The scattered light is collected in a second fibre and guided out of the vacuum chamber, through an interference filter, and into a single photon counting module (SPCM) for detection.

transition. The light is delivered via a single mode tapered lensed fibre<sup>4</sup> to the excitation region. The lensing effect of the tapered lensed fibre is achieved by the taper of the fibre tip, introduced during production by precisely controlled pulling and heating of the fibre. Hence, from this point on, I will refer to tapered lensed fibres simply as tapered fibres. Our tapered fibres have an outer diameter of  $125 \pm 1 \mu\text{m}$  and feature a focal length of  $40 \pm 1 \mu\text{m}$  with a waist<sup>5</sup> of  $5 \mu\text{m}$ . Correspondingly saturation intensity (see section 3.1.4) is reached in the focus at a power of  $P_{\text{sat}} = 325 \text{ pW}$ . The focus of the tapered fibre defines the excitation region, located  $62.5 \mu\text{m}$  (half a fibre diameter) above the guide-wire. The height of the 1D guide potential minimum can be aligned to the excitation region by adjusting the current in the guide-wire (see chapter 10).

The fluorescence light is collected by a commercial multi mode fibre<sup>6</sup> with outer diameter  $125 \pm 1 \mu\text{m}$  and core diameter  $d_c = 62.5 \pm 3 \mu\text{m}$ . The multi mode fibre has a limited field of view, given by its numerical aperture of  $\text{NA} = 0.275 \pm 0.015$ . Only light hitting the core at angles up to maximally  $\arcsin(\text{NA}) = 16^\circ \pm 0.9^\circ$  will be collected [40]. This defines a detection cone which is marked dark blue in figure 2.6. But due to the limited size of the core of the detection fibre only atoms in the light blue cone can exploit the full NA of the detection fibre. For atoms beyond the tip of the cone the solid angle of the detection fibre decreases as  $(d_c/x)^2$  where  $x$  is the distance from atom to fibre [41]. Photons from atoms left and right of the cone will hit the core mostly at angles larger than  $\arcsin(\text{NA})$ . Hence the region of maximum collection efficiency for the atomic signal is given by the intersection of the excitation mode field (red) and the full NA cone. This defines the detection region, which is depicted yellow in figure 2.6.

<sup>4</sup>The tapered fibres have been manufactured by Nanonics ([www.nanonics.co.il](http://www.nanonics.co.il)).

<sup>5</sup>The focus waist is here defined as the *diameter* of the focal spot.

<sup>6</sup>Thorlabs GIF-625 graded index multi mode (MM) fibre.

For the given NA a maximum photon collection efficiency of  $\eta_{\text{coll}} = 1.9\%$  can be determined (see appendix B). Figure 2.7 shows the photon collection efficiency as a function of position for an atom passing the detector.

The height of the detection region is automatically aligned to the excitation region since the outer diameters of the fibres match. By aligning the MM fibre such that the collection cone defined by the numerical aperture overlaps with the excitation region we reach both a highly selective excitation of the atoms and a matched collection region.

The angle between the tapered (excitation) and the multi mode (detection) fibre has been chosen to be  $90^\circ$ . This leads to an excellent geometrical suppression of stray light. Of each nanowatt of excitation light only about 60 photons per second are collected by the detection fibre, corresponding to a stray light suppression of approximately  $10^{-8}$  (see section 5.2). The fluorescence signal itself is of course independent of the chosen angle, since the fluorescence should be isotropically in  $4\pi$ .<sup>7</sup> The detection setup has been positioned such that both fibres are at  $45^\circ$  to the guide to avoid blocking of the guide.

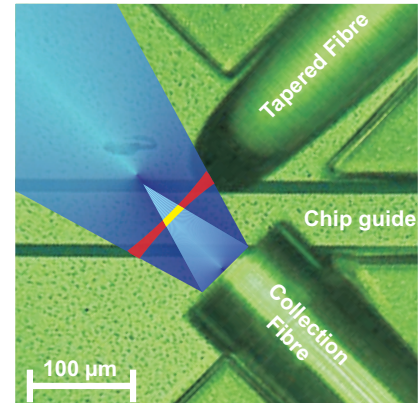


**Fig-**

**ure 2.6.:** The Detection Region The atoms are excited selectively in the focus of the tapered lensed fibre. The mode-field of the excitation light is indicated in red and cuts the field of view (blue) of the MM fibre which is given by its NA, defining the detection region (yellow) where maximum collection efficiency is achieved.

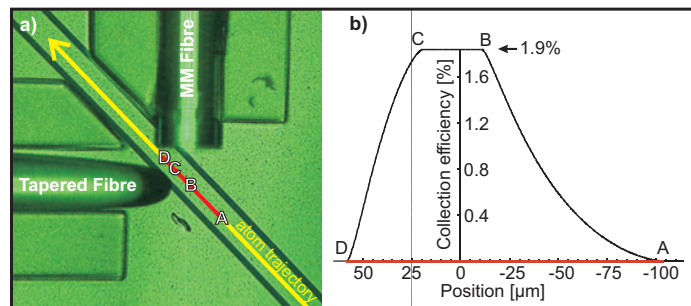


**Figure 2.7.:** Collection Efficiency as a Function of Position in the Guide [30]

Due to the limited NA of the MM collection fibre photons from atoms passing the detector can be collected with an efficiency that depends on the position of the atom in the guide. The trajectory of an atom in the guide minimum passing the detector is shown in yellow and marked with 4 points (ABCD). The maximum collection efficiency of  $1.9\%$  is achieved for photons scattered from atoms between B and C. Photons scattered beyond A and D are not collected. The position is given relative to the intersection of the centerlines of the excitation and collection fibres.

The multi mode detection fibre sends the collected photons outside the vacuum chamber through an interference filter to the single photon counting module(s) (SPCM) as

<sup>7</sup>I will neglect possible reflections of fluorescence photons from the chip surface and similar effects.



depicted in figure 2.5b). As described in section 2.5 photon detection setups employing a single SPCM have been used for maximum efficiency single atom detection, while setups with two SPCMs in Hanbury Brown-Twiss configuration have been used for correlation measurements.

### 2.2.1. Transit Signal

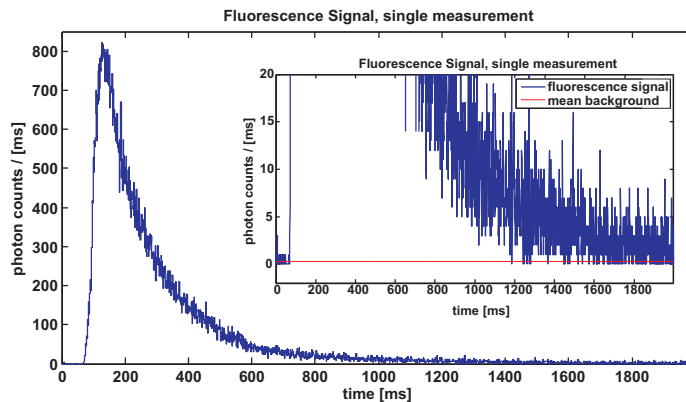


**Figure 2.8.:**

The fluorescence signal from a single measurement, showing the transit of the the atoms. The depicted signal has been arbitrarily chosen out of a series of 1545 consecutive shots<sup>8</sup> at 0.4 nW excitation power, recorded with a single SPCM. No background correction or smoothing has been applied to the signal other than a 1 ms binning for the plot.

Inset: The red line indicates the mean signal level during the first 50 ms. During this time there are no atoms in the guide, hence the red line corresponds to the background level. Even 2 s after the start of the measurement the mean signal level in the detector is significantly above background, indicating that atoms are still arriving.

A typical transit signal from a single measurement is shown in figure 2.8. During the first 50 ms of the measurement the Z-trap is still closed and no atoms reach the detector. Hence this region represents a background measurement for the detector. The fluorescence signal shows a sharp rise when the fastest atoms arrive at the detector, reaches a maximum at  $t = 140$  ms when the atoms with the most likely velocity arrive and then slowly drops again, giving a faithful representation of the transit of the atom pulse. As will be shown in chapter 5 the transit signal resembles closely a Boltzman-distribution plotted over time, since the velocities of the atoms in the Z-trap are Boltzman-distributed. For now we note only that the inset of figure 2.8 shows that even 2 s after opening of the Z-trap the mean single-shot signal in the detector is still significantly higher than the background, indicating the presence of atoms. Those atoms have travelled with a velocity of 2.8 mm/s.

<sup>8</sup>Shot number 1 of dataset 20071205Wed\_F3\_resonant\_guide2\_05V\_429pW

## 2.3. The Absorption Detector

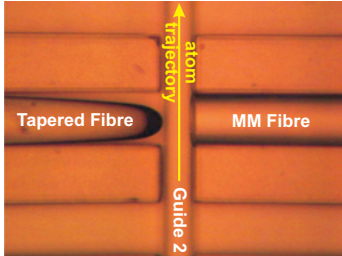


**Figure 2.9.:**

The Absorption Detector  
The tapered excitation fibre is facing the MM collection fibre at a distance of 75  $\mu\text{m}$ .

To enable us to directly compare absorption and fluorescence detection schemes in identical settings an absorption detector was integrated on the atom chip as well. It is composed of the same set of fibres as the fluorescence detector. One tapered lensed fibre is used to deliver excitation light and one MM fibre to collect the signal. Both are integrated on the chip using similar SU-8 holders. The difference is that here the detection fibre is oriented at  $0^\circ$  to the excitation fibre, i.e. the fibres are facing one another at a distance of 75  $\mu\text{m}$ . The tip of the tapered fibre is positioned 40  $\mu\text{m}$  from the centre of the guide wire, so that the atoms transferred from the Z-trap into the guide leading to the absorption detector (compare figure 2.3) are guided through the focus of the tapered fibre. There they are excited by resonant light emitted from the tapered fibre and re-emit fluorescence photons in  $4\pi$ . The attenuated transmitted light is collected by the MM collection fibre with an efficiency of  $\eta_{\text{coll}} = 0.95$ . The collected photons are guided outside the vacuum chamber to the same filter and photon detection setup as used for the fluorescence detector and described in section 2.5.

Since the fibres are aligned orthogonal to the guide and have a rather large separation there is no blocking of the guide and the atoms pass the absorption detector unhindered if the excitation light is not present. In the presence of excitation light the detection scheme is destructive, heating the atoms out of the 1D-guide by repeated scattering of photons or transferring them into magnetically untrapped states.

Since the fibres are aligned orthogonal to the guide and have a rather large separation there is no blocking of the guide and the atoms pass the absorption detector unhindered if the excitation light is not present. In the presence of excitation light the detection scheme is destructive, heating the atoms out of the 1D-guide by repeated scattering of photons or transferring them into magnetically untrapped states.

### 2.3.1. Transit Signal

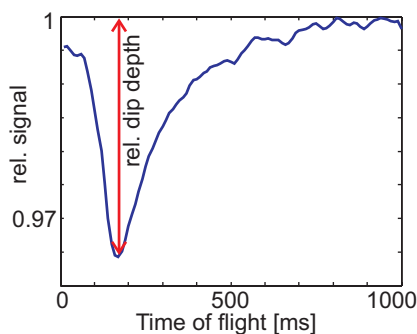


**Figure 2.10.:** Absorption signal, showing the transit of the atoms. This plot shows an average over several consecutive measurements. While the shape is similar to the (inverted) fluorescence signal, the signal (dip) has a relative strength of only a few percent. [30]

Figure 2.10 shows a typical absorption signal as recorded in our measurements [30]. The transit of the atom pulse through the detection region is marked by a dip in transmitted intensity that has the same shape as the (inverted) fluorescence signal. Due to the high light level of the transmitted beam constant background light is

of little relevance to the performance of the absorption detector. The challenge of absorption detection is that, instead of measuring a weak signal on background as it is the case for the fluorescence signal, here we have to measure a small relative change in intensity of a strong beam. The problems connected with this are briefly discussed in section 3.5 where absorption and fluorescence schemes will be compared according to their suitability for detecting low atomic densities.

For a detailed analysis of the absorption measurements see M. Wilzbach's thesis [30].

## 2.4. The Fibre Cavity

To examine cavity enhanced absorption detection and test the feasibility of simple fibre cavities for later experiments in the strong coupling regime or non-destructive detection schemes (e.g. phase contrast imaging) a fibre cavity was integrated on the atom chip as well. This cavity is located on the chip beyond the absorption detector so that atoms will have to first pass the absorption detector before entering the cavity. The fibre cavity was fabricated in our group [41] and consists of microscopic mirrors inserted into a single mode (SM) fibre at a distance of approximately 10 cm length. To allow coupling between the atoms and the mode field within the cavity a small gap of 5  $\mu\text{m}$  width has been cut into the fibre cavity and was positioned over the guide wire.

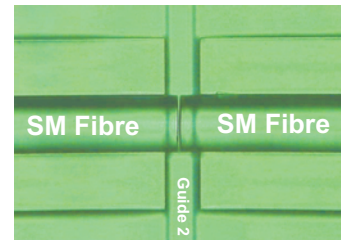


**Figure 2.11.:**

The Fibre Cavity

A gap of 5  $\mu\text{m}$  has been cut into the fibre cavity to allow passage of ultracold atoms.

Due to the extremely small size of the gap and the comparable large temperatures of the atoms used in our experiments initial tries to channel the atoms into the cavity have not been successful [30]. Further investigations have meanwhile produced several viable approaches to increase the gap size [42].

Due to its sensitivity to misalignments the cavity has been an important tool for us to examine the stability of the holding structures as well as measure thermal expansions of the chip. The cavity has shown long term stability over more than one year under experimental conditions, which is quite remarkable considering it is only passively stabilized in the SU-8 trenches. Additionally heating of the atom chip during the experimental cycle leads to an expansion of the chip, which we could measure using the cavity transmission as a sensitive probe. This leads us to believe that the alignment precision and stability of the SU-8 trenches is sufficient for all imaginable fibre integrations on the atom chip.

The cavity integration and our measurements on it have been extensively described by Marco Wilzbach [30] and therefore the cavity will not be treated any further in this thesis.

## 2.5. Photon Detection Setup

To achieve fluorescence detection of small numbers of atoms a signal consisting of only a few photons has to be separated from background. Background sources can be divided into resonant background, having the same wavelength as the fluorescence signal, and non-resonant background of different wavelength.

Resonant background originates mainly from lasers and even though only the probe laser is used during measurements a good shielding of the vacuum chamber against stray light from shutters, acousto-optical modulators and beamblocks is necessary to reduce background. Stray light from the probe laser is suppressed efficiently by a factor  $10^{-8}$  by the geometrical arrangement of the fibres as described in section 2.2.

Non-resonant background on the other hand, e.g. black body radiation from the dispensers or room light, can be efficiently removed by means of a narrow bandgap interference filter. To achieve this we employ a filter setup, depicted in figure 2.13, where the light from the detection fibre is collimated into a free-space beam by a fibre-coupler, sent through an interference filter to be coupled again into a MM fibre which then guides the light to an APD type single photon counting module (SPCM)<sup>9</sup>. For the fibre leading to the SPCM we have chosen metal-shielded GIF-625<sup>10</sup> fibres, since standard PVC shieldings offer only insufficient shielding from ambient light. The interference filter<sup>11</sup> has a transmission of 99.5899 % at 780 nm with a bandwidth (FWHM) of 3 nm [43] as shown in figure 2.12. The SPCM is presented in detail in chapter 4, its photon detection efficiency at 780 nm is  $\eta_{\text{SPCM}} = 56.4 \%$ .

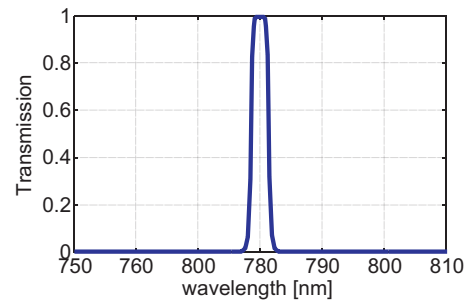


**Figure 2.12.:** Theoretical Design Spectrum of the Semrock interference filter [43]. Here only a narrow part of the design spectrum is shown. With the exception of the 3 nm wide window at 780 nm the filter offers a suppression better than  $10^{-6}$  in the range 600 to 1200 nm.

The photon counts generated by the SPCM are recorded and timestamped at 1 ns resolution by a multichannel counter card<sup>12</sup> in a dedicated computer, see section 9.6.2.

### 2.5.1. Single Counter

For high efficiency atom detection a single SPCM has been employed to count the photons collected by the MM fibre (fig. 2.13). The filter setup consists of two fibre couplers, two mirrors and the interference filter itself. Since long term stability and high coupling efficiency is desired we have chosen to use high quality mirrors on stable

<sup>9</sup>Perkin Elmer SPCM-AQR-12-FC

<sup>10</sup>Thorlabs GIF-625 graded index multi mode (MM) fibre.

<sup>11</sup>Semrock LL01-780 MaxLine laser line filter, [www.semrock.com](http://www.semrock.com).

<sup>12</sup>FAST ComTec P7888 Multiscaler

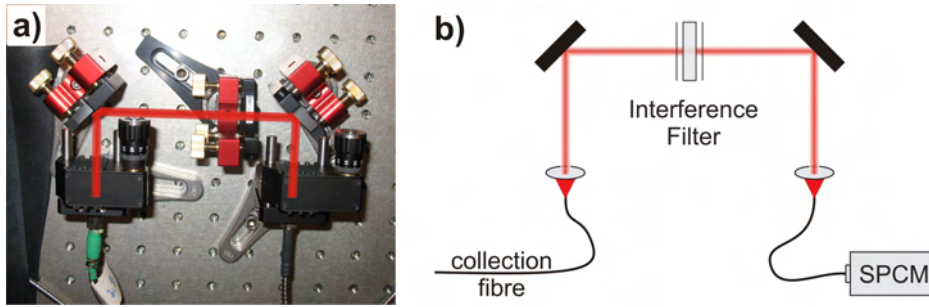


**Figure 2.13.:** Single SPCM Photon Detection Setup

- a) Photo of the actual setup used with superimposed beam path.  
 b) Schematic drawing of the beam path. The light from the collection fibre is filtered by a narrow bandgap interference filter and counted in a single SPCM.

mounts in the filter gap together with fibre couplers that allow adjusting the collimation. The fibre couplers are constructed from lenses chosen to match the NA of the fibres<sup>13</sup> and mounted in a translation stage<sup>14</sup> to allow focus fine adjustment. With this setup we measure a coupling efficiency from MM to MM fibre at the theoretical limit given by two Fresnel reflection losses at the fibre facets. The fibres have an index of refraction of  $n = 1.496$ , corresponding to an approximate loss of 4 % per facet<sup>15</sup>.

The total efficiency  $\eta_{\text{ph}}$  to detect photons emitted from atoms in the detection region is then limited mainly by the collection efficiency  $\eta_{\text{coll}}$  of the MM fibre and the SPCM photon detection efficiency  $\eta_{\text{SPCM}} = 0.56$ .

losses in photon detection		
<i>loss channel</i>	<i>efficiency / transmission</i>	<i>comment</i>
collection efficiency of the MM fibre	$\eta_{\text{coll}} = 0.019$	geometrical effect limited by NA
Fresnel loss MM	0.960	reflection at collection
filter gap	0.960	reflection at outcoupling and incoupling facet
Filter transmission	0.995899	at 780 nm
SPCM detection efficiency	$\eta_{\text{SPCM}} = 0.564$	
total photon detection efficiency	$\eta_{\text{ph}} = 0.00909$	

Hence the total photon detection efficiency for this setup is  $\eta_{\text{ph}} > 0.90 \%$ .

This setup has been employed very successfully to observe transit signals of the atom pulse, perform atom detection and examine statistical fluctuations from shot to shot (see chapter 6), but its temporal resolution is limited by the dead time of the SPCM (typically 50 ns).

<sup>13</sup>Thorlabs C240-TM, [www.thorlabs.com](http://www.thorlabs.com).

<sup>14</sup>Thorlabs SM1Z, [www.thorlabs.com](http://www.thorlabs.com).

<sup>15</sup>Assuming flat facets.

## 2.5.2. HBT Setup

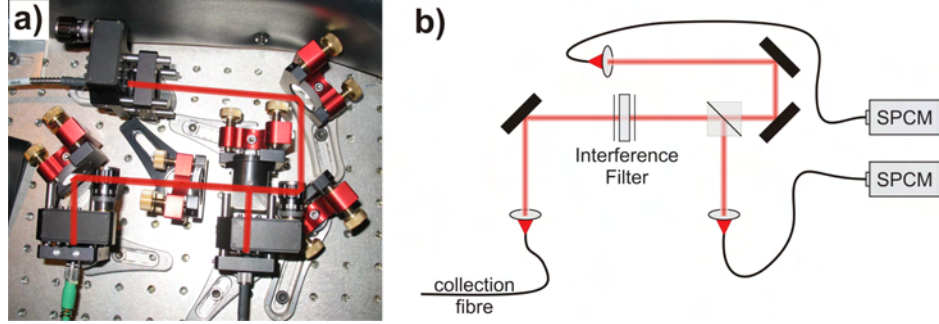


**Figure 2.14.:** Hanbury Brown-Twiss (HBT) Photon Detection Setup

- a) Photo of the actual setup used with superimposed beam path.  
 b) Schematic drawing of the beam path. The light from the collection fibre is filtered by a narrow bandgap interference filter and split into two beams to be counted by independent SPCMs.

**Two Fibre Setup** As an alternative we use a Hanbury Brown-Twiss (HBT) type setup shown in figure 2.14. In order to use the full 1 ns resolution of the counter-card the filtered beam is now split into two equal parts by a 50/50 beam splitter<sup>16</sup> and guided by identical fibres to two independent SPCMs for detection. The counter card registers the events from both counters with nanosecond precision timestamps. This allows recording events with temporal distances smaller than the dead time of the detectors (see chapter 4) and enables us to examine nonclassical correlations of photons emitted from a single atom.

The introduction of the beam splitter, two additional mirrors and the second fibre coupler leads to an overall decrease in coupling efficiency. Since the divergences of the three fibre couplers could not be matched perfectly to one another the theoretical limit could not be reached in this setup.<sup>17</sup> Instead, the coupling efficiency (including filter transmission) has been measured to  $\eta_{\text{gap}} = 0.84$ .

losses in photon detection		
<i>loss channel</i>	<i>efficiency (transmission)</i>	<i>comment</i>
collection efficiency of the MM fibre	$\eta_{\text{coll}} = 0.019$	geometrical effect limited by NA
Fresnel loss MM	0.960	reflection at collection
filter gap	$\eta_{\text{gap}} = 0.840$	including filter transmission
SPCM detection efficiency	$\eta_{\text{SPCM}} = 0.564$	
total photon detection efficiency	$\eta_{\text{ph}} = 0.00864$	

<sup>16</sup>In fact the true splitting ratio, including fibre coupling efficiencies, has been measured to  $39.3 \pm 0.3\%$  to counter 1 and  $60.7 \pm 0.3\%$  to counter 2.

<sup>17</sup>The second fibre coupler uses a Thorlabs C220-TM lens.

Hence the total efficiency to detect photons emitted from the atoms in the detection region is  $\eta_{\text{ph}} > 0.86\%$  for this setup.

**Fibre-Y Setup** As an alternative a second HBT-like setup has been tested where the filter gap setup of the single counters has been used, but instead of a single MM fibre a 1-2 fibre coupler<sup>18</sup> (fibre-Y) has been connected to the output fibre coupler of the filter gap (see figure 2.15). The fibre-Y is fabricated from the same fibre type (GIF-625) as the other MM fibres employed.

This setup has shown intolerably high losses and was therefore not used for scientific measurements, even though its reduced complexity compared to the above

described setup and the possibility to interchange between single detector and two detector measurements makes a fibre-Y solution very attractive. An interesting characterization measurement using the fibre-Y setup will be shown in chapter 4.

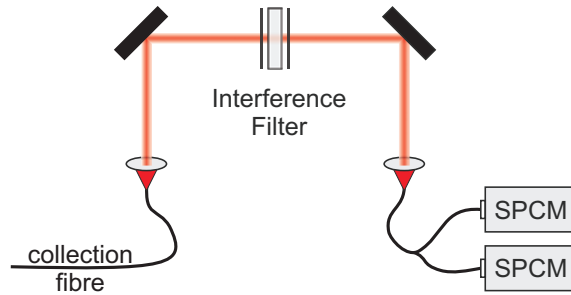


**Figure 2.15.:** Fibre-Y SPCM detection setup  
The light from the collection fibre is filtered by a narrow bandgap interference filter and split into two beams to be counted by independent SPCMs.

<sup>18</sup>Thorlabs FCMM625-50A-FC





## 3. Single Atom Detection

Atom detection can be realized by illuminating a detection region with a probing light field and measuring the absorption or phase shift introduced by the atoms or by observing their fluorescence [35]. Alternatively, sensitive cavities allow measuring the change in index of refraction caused by the presence of atoms in the resonator [17, 19]. The latter method, as well as phase contrast imaging can be non-destructive, i.e. leaving the quantum state of the atom unchanged, whereas absorption and fluorescence detection are destructive by their very nature, often even expelling the atom from the detection region.

Albeit ultra-cold and magnetically trapped atomic gases are typically studied via absorption and phase contrast imaging [18, 35] our method of choice is fluorescence imaging. After giving a review of the relevant atom light interactions I will compare these imaging methods in the following sections and motivate our choice.

### 3.1. Atom Light Interaction

The photon scattering cross section  $\sigma$  and total photon scattering rate  $\gamma$  of  $^{87}\text{Rb}$ -atoms illuminated by probe light (on the D-2-line) are needed to get quantitative estimates of the expected signals strengths. Therefore I will introduce them here, following in my discussion the excellent review of D. Steck [44], before advancing to a comparison of the detection schemes.

#### 3.1.1. Resonant Photon Scattering Cross Section

The selection rules for optical transitions offer cyclic transitions on the D-2 line, e.g.  $5^2\text{S}_{1/2}, |F = 2, m_F = \pm 2\rangle \rightarrow 5^2\text{P}_{3/2}, |F = 3, m_F = \pm 3\rangle$ , where spontaneous emission into the 6.8 GHz lower  $F = 1$  ground state is forbidden. Therefore the atom-light interaction can there be approximated by treating the atom as a two-level system consisting only of the ground state and the excited state. This approximation is well justified for the employed probe laser linewidths of  $\Delta\nu < 1$  MHz due to the smallest spacing between adjacent excited hyperfine-states of the  $^{87}\text{Rb}$ -D-2 line being larger than 72 MHz. The D-1 line is of no concern, since the fine-structure-splitting is approximately 15 nm. Please see appendix A for details on the level structure and level spacing of  $^{87}\text{Rb}$ .

In the two level system approximation the resonant photon scattering cross section  $\sigma_0$  in the limit of weak pumping light is then given by

$$\sigma_0 = \frac{\hbar\omega_0\Gamma}{2I_{\text{sat}}} \quad (3.1) \quad \begin{aligned} \omega_0 &= (E_2 - E_1)/\hbar \\ \Gamma &= 1/\tau \approx 2\pi \cdot 6 \text{ MHz} \end{aligned}$$

where  $E_1$  and  $E_2$  are the ground and excited state energies respectively and hence  $\omega_0$  is the resonance frequency of the D-2-transition.  $\Gamma$  is the natural line width (FWHM) of the transition with lifetime  $\tau = 26.24$  ns. The saturation intensity  $I_{\text{sat}}$  will be defined in section 3.1.4.

### 3.1.2. Detuning

In the presence of a magnetic field of strength  $B$  the energy  $E_{F,m_F}$  of a state  $|F, m_F\rangle$  is shifted by an amount

$$\Delta E_{F,m_F} = m_F g_F \mu_B B$$

from its field-free value, where  $g_F$  is the hyperfine Landé factor,  $m_F$  the magnetic quantum number and  $\mu_B$  the Bohr magneton. Hence the transition frequency from  $|F, m_F\rangle$  to  $|F', m_{F'}\rangle$  is shifted by

$$\Delta\omega_B = \frac{(m_{F'} g_{F'} - m_F g_F) \mu_B}{\hbar B}$$

Additionally movement of the atoms with velocity  $\vec{v}$  relative to the probe field with wavevector  $\vec{k}$  leads to a Doppler shift  $\Delta\omega_D = \vec{k} \cdot \vec{v}$  with  $|\vec{k}| = 2\pi/\lambda_f$ , where  $\lambda_f$  is the wavelength of the probe field. For an incident probe field at frequency  $\omega$  the total detuning  $\delta$  is then given by the following expression.

$$\delta = \underbrace{\omega - \omega_0}_{\text{probe detuning}} - \overbrace{\vec{k} \cdot \vec{v}}^{\text{Doppler-shift}} + \underbrace{(m_{F'} g_{F'} - m_F g_F) \frac{\mu_B}{\hbar} B}_{\text{Zeeman-shift}}$$

The scattering cross section  $\sigma(\delta, I)$  as function of probe light detuning  $\delta$  and intensity  $I$  is given by

$$\sigma(\delta, I) = \frac{\sigma_0}{1 + \left(\frac{2\delta}{\Gamma}\right)^2 + \frac{I}{I_{\text{sat}}}} \quad (3.2)$$

$$\sigma(\delta=0, I=I_{\text{sat}}) = \sigma_0/2$$

The total photon scattering rate  $\gamma(\delta, I)$ , integrated over all directions and frequencies is given by

$$\gamma(\delta, I) = \frac{\Gamma}{2} \frac{I/I_{\text{sat}}}{1 + \left(\frac{2\delta}{\Gamma}\right)^2 + \frac{I}{I_{\text{sat}}}} \quad (3.3)$$

$$\gamma(\delta=0, I=I_{\text{sat}}) = \Gamma/4$$

Note that the resonant scattering cross section is  $\sigma_0/2$  at saturation intensity, whereas the total scattering rate is there  $\Gamma/4$  and approaches  $\Gamma/2$  for strong light fields ( $I \rightarrow \infty$ ).

### 3.1.3. Illumination Under an Angle

If the electric field vector of the probe field is not aligned to the atomic dipole moment but incident under an angle  $\theta$  then the scattering cross section is reduced by a factor  $\cos^2 \theta$  [40].

$$\sigma(\theta) = \sigma(0^\circ) \cos^2(\theta) \quad (3.4)$$

With

$$\sigma \propto \frac{\gamma}{I} \quad \text{and} \quad \cos^2(45^\circ) = \frac{1}{2}$$

we get the following important relations.

$$\sigma(45^\circ) = \frac{\sigma(0^\circ)}{2} \quad \text{and} \quad \gamma(45^\circ) = \frac{\gamma(0^\circ)}{2} \quad (3.5)$$

### 3.1.4. Saturation Intensity

The saturation intensity can be written as

$$I_{\text{sat}} = \frac{c \epsilon_0 \Gamma^2 \hbar^2}{4 |\hat{p} \cdot \vec{d}|^2} \quad (3.6)$$

where  $\epsilon_0$  is the vacuum permittivity,  $\hat{p}$  the unit polarization vector of the probe field and  $\vec{d}$  the atomic dipole moment.

The saturation parameter  $s$  is a commonly used shorthand notation of the incident intensity  $I$  in units of the saturation intensity  $I_{\text{sat}}$ .

$$s = \frac{I}{I_{\text{sat}}} \quad (3.7)$$

Note that the saturation intensity, and thus the scattering rate and the scattering cross section, depend on polarization and atomic alignment. Therefore the values given here and in appendix A have to be understood as maximal steady state values for scattering cross section and scattering rate and minimal value for saturation intensity. Note as well that for weak pumping fields the settling time into the steady state can be long, leading to time-dependent effective dipole moments.

Keeping this in mind the on-resonance saturation intensity and scattering cross section in the 2-level-system approximation for circularly polarized light ( $\sigma^\pm$ ) with the atomic quantization axis aligned to the light propagation direction are given by

$$I_{\text{sat},\sigma^\pm} = \frac{\hbar \omega_0^3 \Gamma}{12\pi c^2} \quad \sigma_{0,\sigma^\pm} = \frac{3\lambda_f^2}{2\pi} \quad (3.8)$$

Inserting the corresponding values for the  $^{87}\text{Rb}$  D-2 transition from appendix A we get  $I_{\text{sat},\sigma^\pm} = 1.669 \frac{\text{mW}}{\text{cm}^2}$  and  $\sigma_{0,\sigma^\pm} = 0.29 \mu\text{m}^2$ .

### 3.1.5. Rabi Frequency

A convenient measure of the atom-light interaction strength is the Rabi frequency, which is basically the interaction energy converted to frequency.

$$\Omega(t) = -\frac{d \cdot E_0(t)}{\hbar} \quad (3.9)$$

Here  $d$  is the component of the transition dipole moment along the direction of the electric field  $\vec{E}(t) = \vec{E}_0(t) \cos(\omega t)$  at the location of the atom [45]. For a two-state system the probability to excite an atom of the lower state into the higher state by irradiating the system with a pulse of resonant radiation is given by:

$$P(t) = \left[ \sin \frac{A(t)}{2} \right]^2 = \frac{1}{2} [1 + \cos A(t)]$$

where  $A(t)$  is the pulse area up to time  $t$ .

$$A(t) = \int_{-\infty}^t \Omega(t') dt'$$

For continuous illumination the population of the upper state undergoes sinusoidal oscillations between 0% and 100% with the Rabi Frequency  $\Omega$ .

The Rabi frequency can be expressed in terms of the linewidth  $\Gamma$  and the incident intensity  $I$  using equation 3.7 [44].

$$\begin{aligned} s &= \frac{I}{I_{\text{sat}}} = 2 \left( \frac{\Omega}{\Gamma} \right)^2 \\ \Rightarrow \Omega(s) &= \sqrt{\frac{s}{2}} \Gamma \end{aligned} \quad (3.10)$$

### 3.1.6. Electric Susceptibility

Light traversing through a medium interacts with the atoms by aligning the atomic dipole moments to the electric field vector of the light. The polarizability of the medium is described by the frequency dependent electric susceptibility  $\chi(\omega)$ . The total polarization  $\vec{P}$  is consequently given by

$$\vec{P} = \epsilon_0 \chi(\omega) \vec{E}$$

The speed of light in vacuum is fixed by the the vacuum permittivity  $\epsilon_0$  and the vacuum permeability  $\mu_0$ .

$$c = \frac{1}{\sqrt{\epsilon_0 \mu_0}} = 299\,792\,458 \frac{\text{m}}{\text{s}} \quad \begin{array}{l} \epsilon_0 = 8.85 \cdot 10^{-12} \frac{\text{C}^2}{\text{N} \cdot \text{m}^2} \\ \mu_0 = 1.25 \cdot 10^{-6} \frac{\text{kg} \cdot \text{m}}{\text{C}^2} \end{array}$$

When passing through a medium with susceptibility  $\chi(\omega)$  the permittivity is no longer the vacuum permittivity  $\epsilon_0$ , but instead

$$\epsilon(\omega) = \epsilon_0(1 + \chi(\omega))$$

Thus, through interaction with the medium, the speed of light inside a medium  $c_{\text{med}}$  is reduced by a factor  $\frac{1}{\sqrt{1+\chi}}$  with respect to  $c$ .

$$c_{\text{med}} = \frac{1}{\sqrt{\epsilon(\omega)\mu_0}} = \frac{c}{n}, \quad n = \sqrt{\frac{\epsilon}{\epsilon_0}} = \sqrt{1 + \chi} \quad (3.11)$$

This relation defines the refractive index  $n$  of a medium. In dielectric materials that absorb light  $\chi$  has a complex value

$$\chi = \chi' + i \cdot \chi''$$

leading to a complex refractive index

$$n(\omega) = n_r + i \cdot \frac{\alpha}{2\frac{\omega}{c}} \quad (3.12)$$

### 3.1.7. Dispersion and Absorption

The wave propagation in the medium is then given by [46]

$$\vec{E}(\vec{r}, t) = \vec{E}_0 e^{-i(\omega t - n_r \vec{k} \cdot \vec{r})} e^{-(\alpha/(2\frac{\omega}{c})) \cdot \vec{k} \cdot \vec{r}} \quad (3.13)$$

where  $\text{Re}(n) = n_r$  is responsible for dispersion and  $\alpha = \frac{2\omega}{c} \text{Im}(n)$  is the absorption coefficient leading to a damping of the intensity  $I$  ( $I \sim E^2$ ), e.g. for propagation in z-direction:  $I(z) = I(0)e^{-\alpha z}$ .

$$\text{Dispersion} \quad n_r = \text{Re}(n)$$

$$\text{Absorption} \quad \alpha = \frac{2\omega}{c} \text{Im}(n)$$

With the Lorentz-model for the interaction of light and matter [46, 47] the dispersion relation can in general be written (for one atomic resonance) as

$$n(\omega) = 1 + \frac{n_e q_e^2}{2\epsilon_0 m_e ((\omega_0^2 - \omega^2) - i\rho\omega)} \quad (3.14)$$

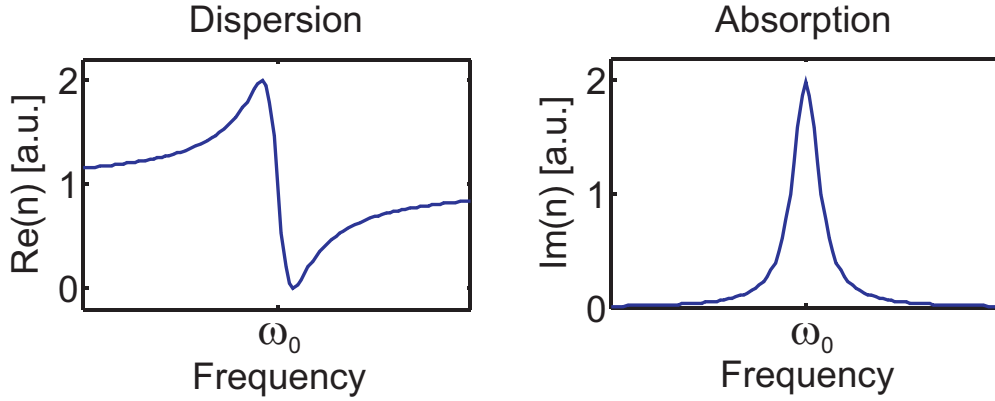


**Figure 3.1.:** Real and Imaginary part of the complex refractive index (arbitrary units) The real part (left), responsible for dispersion, and the imaginary part of the refractive index (right), responsible for absorption, plotted in the vicinity of an atomic resonance  $\omega_0$ .

Here  $q_e$  and  $m_e$  are the electron charge and mass, respectively,  $n_e$  is the number of electrons per unit volume,  $\omega_0$  the resonance frequency and  $\rho$  the damping factor of the electron oscillations.

Figure 3.1 shows the real and imaginary part of the complex refractive index near an atomic resonance  $\omega_0$ . The sign of the dispersion curve changes from normal dispersion ( $n$  grows with  $\omega$ ) far away from the resonance to anomalous dispersion ( $n$  decreases while  $\omega$  increases) on resonance. Normal dispersion can be exploited to slow and even stop a pulse of light (see e.g. my diploma thesis [48] and references therein).

As expected absorption ( $\text{Im}(n)$ ) becomes dominant close to resonance ( $\omega \approx \omega_0$ ).

## 3.2. Absorption Detection

The absorption of resonant probe light by atoms in the detection region is a standard imaging method to detect atoms and estimate atom densities in magnetic or magneto-optic traps [17, 35].

For illumination on resonance but below saturation ( $\delta = 0$ ,  $I_0 < I_{\text{sat}}$ ) Lambert-Beer's law can be used to estimate the absorption.

$$I_{\text{trans}} = I \cdot e^{-\rho_{\text{at}}\sigma_0} \quad , \quad \rho_{\text{at}} = n_{\text{at}}/A$$

Here  $\sigma_0$  is the resonant scattering cross section from section 3.1.1,  $I$  the incident intensity,  $I_{\text{trans}}$  the transmitted intensity and  $\rho_{\text{at}}$  the column density of  $n_{\text{at}}$  atoms over the area  $A$ .

With the maximum cross section  $\sigma_0 = 0.29 \mu\text{m}^2$  for the  $^{87}\text{Rb}$ -D-2 line this means that 1 atom/ $\mu\text{m}^2$  leads to a maximal absorption of approximately 25%. Assuming a

roughly cylindrical interaction region<sup>1</sup> of the probe light with the atoms of cross section  $A = 20 \mu\text{m}^2$  we expect approximately 1.5% absorption per atom in the interaction region.

Since we are interested in the detection of small numbers of atoms I will use in the following the assumption  $\rho_{\text{at}}\sigma_0 \ll 1$ . In this limit the transmitted intensity  $I_{\text{trans}}$  is simply given by

$$\frac{I_{\text{trans}}}{I} \approx 1 - \rho_{\text{at}}\sigma_0$$

Note that this approximation holds only for very small atom numbers. Assuming again ideal absorption and  $A = 20 \mu\text{m}^2$  the relative error is larger than 1% for 4 and larger than 10% for 10 atoms in the interaction region.

If we can assume the incoming intensity  $I$  to be fixed and known then the signal noise is determined by the measurement of the transmitted intensity  $I_{\text{trans}}$ . These measurements cannot be more precise than the shot noise limit. For the discussion of the signal to noise ratio (SNR) the intensity is best described in terms of the incoming photon flux  $j = n_{\text{ph}}/T$  which is connected to the incoming intensity via the following relation ( $T$  is the total measurement time,  $E$  the energy).

$$\begin{aligned} I &= \frac{E}{T A} = \frac{n_{\text{ph}} h c}{T \lambda_f A} \\ &= j \frac{h c}{\lambda_f A} \end{aligned}$$

The signal to noise ratio for the absorption signal ( $\text{SNR}_{\text{abs}}$ ) is

$$\begin{aligned} \text{SNR}_{\text{abs}} &= \frac{I \cdot T - I_{\text{trans}} \cdot T}{\sqrt{I_{\text{trans}} \cdot T}} = \frac{j T (1 - e^{-\rho_{\text{at}} \sigma_0})}{\sqrt{j T e^{-\rho_{\text{at}} \sigma_0}}} \\ &= \sqrt{j T} \frac{1 - e^{-\rho_{\text{at}} \sigma_0}}{\sqrt{e^{-\rho_{\text{at}} \sigma_0}}} \end{aligned}$$

which reduces in the above approximation to

$$\boxed{\text{SNR}_{\text{abs}} \approx \rho_{\text{at}} \sigma_0 \sqrt{j T} = n_{\text{at}} \frac{\sigma_0}{A} \sqrt{j T}} \quad (3.15)$$

The above relation demonstrates that for absorption measurements the  $\text{SNR}_{\text{abs}}$  scales with the number of atoms  $n_{\text{at}}$  in the detection region.

<sup>1</sup>The probe light is focused in our setup to a spot of  $5 \mu\text{m}$  diameter with a Rayleigh length of  $25 \mu\text{m}$ .

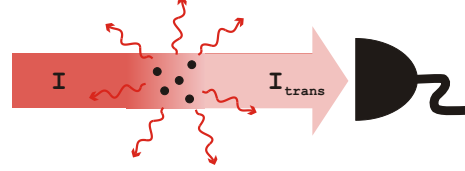


**Figure 3.2.:**

Absorption detection principle

An incoming light field of intensity  $I$  is attenuated by absorption. The intensity  $I_{\text{trans}}$  of the transmitted beam is measured to estimate the column density of atoms  $\rho_{\text{at}}$  in the beam path.

The minimal number of atoms that can be detected with  $\text{SNR}_{\text{abs}} = 1$  is consequently given by

$$n_{\text{at}}^{\text{min}} \approx \frac{A}{\sigma_0} \frac{1}{\sqrt{jT}} \quad (3.16)$$

To increase the sensitivity of an absorption detector it seems therefore worthwhile to decrease  $A$ , e.g. by stronger focusing of the probe beam. Unfortunately it has been shown that the spot size has a critical limit beyond which the coupling to the atom degrades due to a mismatch between the electric field and the radiation pattern of the atomic dipole [49–51].

Alternatively one might try to increase the interaction time  $T$ . Scattering will then heat the atoms and ultimately expel them from the interaction region, setting a natural, and rather low, limit on the maximum interaction time. But in combination with dipole traps [4, 52, 53] or for ions [54, 55] this is a very successful strategy.

For atom counting applications the atom number uncertainty  $\Delta n_{\text{at}}$  is given by the ratio of the shot noise of the transmitted intensity and the number of photons  $m$  scattered per atom.

$$\Delta n_{\text{at}} = \frac{\text{photon shot noise}}{\text{signal per atom}} = \frac{\sqrt{jT}}{m} \quad (3.17)$$

Surprisingly  $\Delta n_{\text{at}}$  is independent of the actual atom number, but, due to the full shot noise of the transmitted beam entering the uncertainty, usually not small enough to distinguish single atoms. In the strong coupling regime, where the signal per atom can be increased drastically, absorption detection is a viable choice for atom counting.

Hence, absorption detectors are excellent choices for counting high numbers of atoms with precision. Additionally equations 3.16 and 3.17 show that there is no fundamental limit to the detection efficiency of an absorption detector for single atoms, albeit an increase in detection efficiency is at the expense of atom number resolution due to the necessary increase in interaction time.

### 3.3. Phase Contrast Detection

As has been shown in section 3.1.7 the real part of the refractive index results in dispersion. On resonance absorption dominates, but a far-off detuned light field experiences a phase shift  $\phi$  [56].

$$\phi = \frac{\rho_{\text{at}} \sigma_0}{4 \delta / \Gamma} \quad (3.18)$$

With the aid of an interferometer this phase shift can be exploited for minimal- or even non-destructive atom detection at the cost of increased complexity.



From the weak field limit scattering cross section of equation 3.2

$$\sigma(\delta, I) = \frac{\sigma_0}{1 + \left(\frac{2\delta}{\Gamma}\right)^2}$$

we see that absorption decreases with  $1/\delta^2$ , whereas the phase shift (equation 3.18) decreases with only  $1/\delta$ .

Neglecting absorption, the minimal detectable phase shift  $\Delta\phi^{\min}$  is given by the number/phase uncertainty where we assume the uncertainty in photon number in the transmitted beam to be limited by shot noise.

$$\Delta\phi^{\min} = \frac{1}{\sqrt{jT}} \quad (3.19)$$

In the limit of optically thin clouds the signal to noise ratio of phase contrast imaging [17]

$$\text{SNR}_{\text{pc}} \approx \frac{\rho_{\text{at}} \sigma_0 \sqrt{jT}}{4 \delta/\Gamma} \quad (3.20)$$

can be shown to be the same as the optimal achievable SNR for resonant absorption detection [56, 57].

Hence for high atom numbers and large detunings (i.e.  $\delta/\Gamma \ll 1$ ), where absorption becomes negligible, phase contrast imaging is the method of choice. Minimal destructive, almost shot-noise limited, imaging of optically dense ensembles has been demonstrated [58]. In combination with cavities non-destructive and shot noise limited detection becomes possible [16]. Alas, for very small atom numbers phase contrast imaging is not more sensitive than absorption techniques.

### 3.4. Fluorescence Detection

In fluorescence detection a resonant light field of intensity  $I$  irradiates  $n_{\text{at}}$  atoms, driving the transition to the excited state, just as for absorption detection. Due to the short lifetime of the excited state<sup>2</sup> all excited atoms will spontaneously re-emit the absorbed photons randomly into the full solid angle  $4\pi$  during the measurement period  $T$ .

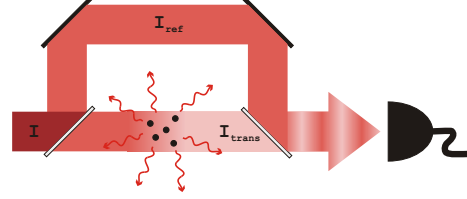


**Figure 3.3.:**

**Phase Contrast Detection Principle**  
An incoming light field of intensity  $I$  is split into a reference beam  $I_{\text{ref}}$  and a probe beam which experiences absorption via  $\text{Im}(n)$  and a phase-shift via  $\text{Re}(n)$ . After recombination of the probe and the transmitted beam the phase shift can be measured to estimate the column density of atoms  $\rho_{\text{at}}$  in the beam path.

<sup>2</sup> $\tau = 26.24$  ns for the  $^{87}\text{Rb-D-2}$  line

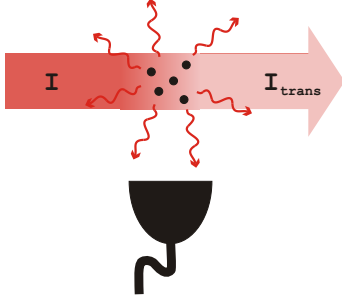


**Figure 3.4.:**

**Fluorescence Detection Principle**  
A resonant light field of intensity  $I$  irradiates an ensemble of atoms. Due to absorption and re-emission  $n_{\text{ph}}^{\text{scat}}$  fluorescence photons are emitted of which a fraction  $\eta_{\text{coll}}$  is collected.

In absorption detection the number of absorbed photons is estimated by measuring the transmitted intensity  $I_{\text{trans}}$ . In fluorescence detection a fraction  $\eta_{\text{coll}}$  of the scattered photons is collected to estimate the total number of scattered/absorbed photons  $n_{\text{ph}}^{\text{scat}}$ .

Expressing again the incident intensity  $I$  as a photon flux  $j = AI\lambda_f/(hc)$  and limiting the discussion to very low atom numbers (see sec.3.2) the total number of scattered photons is given by

$$n_{\text{ph}}^{\text{scat}} = jT(1 - e^{-\sigma_0 \frac{n_{\text{at}}}{A}}) \approx jT n_{\text{at}} \frac{\sigma_0}{A}$$

from which we get the number of fluorescence photons collected  $n_{\text{ph}}^{\text{fluo}} = \eta_{\text{coll}} n_{\text{ph}}^{\text{scat}}$ .

$$n_{\text{ph}}^{\text{fluo}} = \eta_{\text{coll}} jT(1 - e^{-\sigma_0 \frac{n_{\text{at}}}{A}}) \approx \eta_{\text{coll}} jT n_{\text{at}} \frac{\sigma_0}{A}$$

If no other light source is present the number of background photons  $n_{\text{ph}}^{\text{bg}}$  is given by the fraction  $f_{\text{bg}}$  of the incident photons that are scattered by anything else but the atoms in the detection region.

$$n_{\text{ph}}^{\text{bg}} = \eta_{\text{coll}} f_{\text{bg}} jT$$

The signal to noise ratio  $\text{SNR}_{\text{fluo}}$  of the fluorescence measurement can then be estimated by

$$\text{SNR}_{\text{fluo}} \approx \frac{n_{\text{ph}}^{\text{fluo}}}{\sqrt{n_{\text{ph}}^{\text{fluo}} + n_{\text{ph}}^{\text{bg}}}} = \frac{n_{\text{at}}}{\sqrt{n_{\text{at}} + \frac{A}{\sigma_0} f_{\text{bg}}}} \sqrt{\eta_{\text{coll}} jT \frac{\sigma_0}{A}} \quad (3.21)$$

which reduces in the background free ( $f_{\text{bg}} = 0$ ) case to the optimal  $\text{SNR}_{\text{fluo}}^{\text{opt}}$ .

$$\text{SNR}_{\text{fluo}}^{\text{opt}} \approx \sqrt{n_{\text{at}}} \sqrt{\eta_{\text{coll}} jT \frac{\sigma_0}{A}}$$

Note that for fluorescence measurements the  $\text{SNR}_{\text{fluo}} \propto \sqrt{n_{\text{at}}}$  scales with the square root of the number of atoms in the detection region.

The minimal number of atoms that can be detected with  $\text{SNR}_{\text{fluo}} = 1$  is consequently given by

$$n_{\text{at}}^{\text{min}} \approx \frac{A}{\sigma_0 \eta_{\text{coll}} jT} \quad (3.22)$$

For atom counting applications the atom number uncertainty  $\Delta n_{\text{at}}$  is given by the ratio of the shot noise of the total signal and the signal per atom  $\eta_{\text{coll}} m$ .

$$\Delta n_{\text{at}} = \frac{\text{photon shot noise}}{\text{signal per atom}} = \frac{\sqrt{\eta_{\text{coll}} n_{\text{at}} m}}{\eta_{\text{coll}} m}$$

$$\boxed{\Delta n_{\text{at}} = \sqrt{\frac{n_{\text{at}}}{\eta_{\text{coll}} m}}} \quad (3.23)$$

The atom number resolution  $\Delta n_{\text{at}} \propto \sqrt{n_{\text{at}}}$  is proportional to the square root of the atom number, making fluorescence detection good at resolving few atoms.

As it was already the case for absorption detectors, there is no fundamental limit to the detection efficiency of a fluorescence detector, as long as the interaction time can be increased arbitrarily and the background is well suppressed. These may seem to be contradicting requirements, but I intend to demonstrate in the remaining parts of this thesis that detection efficiencies high enough for all practical purposes can very well be achieved with finite interaction times.

The real strength of fluorescence detectors is of a technical nature: since the direct probe beam does not hit the detector, very sensitive photon detectors can be used. If background noise can be suppressed the fluorescence detector is excellent at examining low atom numbers, which may be, due to the limited collection efficiency, counter-intuitive.

Equations 3.21 and 3.22 show that the sensitivity of a fluorescence detector depends mainly on two factors: our ability to suppress the background  $n_{\text{ph}}^{\text{bg}}$  and the limited collection efficiency  $\eta_{\text{coll}}$ . Similar to absorption detection the number of photons  $m$  scattered per atom should be as high as possible. To this end the probe field should drive a closed transition and the same strategies as in section 3.2 to increase the interaction time  $T$  (dipole traps, etc) or decrease  $A$  apply.

In a beautiful experiment at the MPI for quantum optics in Garching Bondo et al [59] have observed the fluorescence of single, freely falling atoms with a geometrical collection efficiency of  $\eta_{\text{coll}} = 0.8$  using a shell of curved mirrors around the detection region. Here on average  $m = 20$  photons/atom could be collected in an interaction time of  $T = 60 \mu\text{s}$ . Observing the fluorescence of single dye molecules fixated in a solid matrix Wrigge et al could examine the coherent and incoherent part of the fluorescent radiation separately and measure nonclassical correlations [60].

**Resonator Assisted Detection** Resonator enhanced detection schemes have proven successful observation of small numbers of atoms in recent experiments [5–9, 11, 12].

In absorption detection employing a cavity increases the interaction between the probe light and the atoms by the number of round trips of the photons in the cavity. Hence the signal is increased by the cavity finesse and the signal to noise ratio is enhanced by the cooperativity parameter [16].

In fluorescence detection the emission of fluorescence photons in the direction of the cavity is enhanced by the Purcell factor [40], increasing the signal strength and correspondingly the signal to noise ratio.

Nonetheless cavity based detection schemes will not be considered in this discussion due to the need for active stabilization and precise alignment disagreeing with our

requirement of a robust and simple detector. For more information on cavity based detection schemes see e.g. [16, 17, 30].

As will be shown in chapters 6 to 8 single atom sensitivity can be reached in a simple, cavity-free fluorescence setup.

### 3.5. Why Fluorescence Detection

Which of the above methods is best suited to construct a fully integrated, robust and reliable single atom detector ?

Fluorescence detection shares its main disadvantage with absorption detection. Both are destructive measurements, altering the state of the atom and most likely expelling it from the detection region. But non-destructive methods, like phase contrast imaging, have to be excluded due to their inherent complexity of the setup.

Faced with the choice between absorption and fluorescence detection most experimentalists working with ultra-cold atoms tend to prefer absorption imaging. This bias is well justified for optically dense ensembles, which are the typical objects of interests in the magnetic trapping and BEC community. Here absorption imaging offers excellent performance with the signal to noise ratio proportional to the atom number and the counting resolution being independent of atom number. The minimal detectable atom number, on the other hand is inversely proportional to the probe intensity. This is the key to understanding the major drawback of absorption detection for our application. The absorption signal is a small difference (about 1.5 % per atom in the interaction region) of two large numbers, namely the incident and transmitted intensity. Every fluctuation might hide the signal. Additionally, since the full intensities have to be measured, highly sensitive photon detectors cannot be employed to full effect.

Fluorescence imaging, on the other hand is disliked in typical magnetic trapping and BEC experiments because it is very sensitive to background noise. Add to that the fact that the detection optics are typically outside of the vacuum chamber which leads to low collection efficiency, and image a rather macroscopic area which increases the background problem, and it becomes obvious why fluorescence imaging is usually not the method of choice. Both problems are removed by integration of both the probe light source and the detection optics on the atom chip. Here a highly selective excitation of the atoms, reducing stray light, and collection of light only from a very specific detection region, efficiently suppressing other background sources is possible.

Comparing equations 3.16 and 3.22

$$n_{\text{at,fluo}}^{\text{min}} \approx \frac{A}{\sigma_0 \eta_{\text{coll}} j T} \quad , \quad n_{\text{at,abs}}^{\text{min}} \approx \frac{A}{\sigma_0} \frac{1}{\sqrt{j T}}$$

$$n_{\text{at,fluo}}^{\text{min}} = \frac{1}{\eta_{\text{coll}} \sqrt{j T}} n_{\text{at,abs}}^{\text{min}}$$

Absorption	Fluorescence
$\text{SNR} \approx n_{\text{at}} \frac{\sigma_0}{A} \sqrt{jT}$	$\text{SNR} \approx \sqrt{n_{\text{at}}} \sqrt{\eta_{\text{coll}} j T \frac{\sigma_0}{A}}$
$\text{SNR} \propto n_{\text{at}}$	$\text{SNR} \propto \sqrt{n_{\text{at}}}$
$\Delta n_{\text{at}} = \frac{\sqrt{jT}}{m}$	$\Delta n_{\text{at}} = \sqrt{\frac{n_{\text{at}}}{\eta_{\text{coll}} m}}$
$n_{\text{at}}^{\text{min}} \approx \frac{A}{\sigma_0} \frac{1}{\sqrt{jT}}$	$n_{\text{at}}^{\text{min}} \approx \frac{A}{\sigma_0} \frac{1}{\eta_{\text{coll}} j T}$

$$n_{\text{at,abs}}^{\text{min}} = \eta_{\text{coll}} \sqrt{jT} n_{\text{at,fluo}}^{\text{min}}$$
**Table 3.1.:** Comparing Absorption and Fluorescence

As discussed in the previous section resonator assisted detection enhances the absorption SNR by the cooperativity parameter [16], while the fluorescence SNR is increased by the Purcell factor [40].

we see that the minimal number of atoms that can be detected in fluorescence with  $\text{SNR} = 1$  is smaller than in absorption by a factor of  $1/\sqrt{jT}$ . Meaning for a fixed minimal atom number higher probe intensities can be employed in fluorescence, leading to higher scattering rates  $\gamma$  (see equation 3.3) and thus to an increased signal per atom. It should be noted, though, that compared to absorption detection the minimal detectable atom number is increased by the finite collection efficiency, emphasizing again that the collection efficiency should be increased wherever possible.

Comparing the counting resolutions  $\Delta n_{\text{at}}$  delivers similar results (see table 3.1). In absorption detection the counting resolution suffers from a proportionality to the probe intensity, whereas the fluorescence resolution increases the smaller the number of atoms in the detection region. Even though, again, the fluorescence resolution is reduced by the finite collection efficiency, fluorescence detection presents itself as an excellent tool to count small numbers of atoms.

For typical experimental parameters of  $I \cdot A = 1\text{mW}$ , interaction time  $T = 25\ \mu\text{s}$ ,  $j \cdot T \approx 196000$ , and a measured signal strength of  $m = 120$  photons/atom (see chapter 6)<sup>3</sup> we receive even in our simple setup, where  $\eta_{\text{coll}} = 1.9\%$  for  $n_{\text{at}} = 1$ , for absorption detection a resolution of

$$\Delta n_{\text{at}}^{\text{abs}} = 3.68$$

while fluorescence detection gives

$$\Delta n_{\text{at}}^{\text{fluo}} = 0.96$$

<sup>3</sup>Theoretically expected would be a signal strength of  $m = 240$  photons/atom at saturation under ideal conditions and  $m = 120$  photons/atom for illumination under  $45^\circ$ .

While the signal to noise ratio of fluorescence detection is proportional to the square root of the number of atoms in the detection region, it should not be overlooked that fluorescence detection has no inherent background, unlike absorption detection. In principle a single detected photon is enough to detect an atom if the background is completely suppressed. Used solely to detect presence or absence of atoms in the detection region a fluorescence detector can have arbitrarily high SNR.

In our measurements in Heidelberg Marco Wilzbach and I performed a thorough comparison of our integrated fluorescence and absorption detectors (for details see [30]). While for typical atomic densities the fluorescence signal was clearly visible with  $\text{SNR} \gg 1$  even in a single shot, the absorption signal in a single shot tended to have  $\text{SNR} \approx 1$  or below. For typical peak atomic densities of 7 atoms/5  $\mu\text{m}$  the absorption signal was no larger than 2.5%.<sup>4</sup> Comparing this number with the expected absorption signal of  $7 \cdot 1.5\% = 10.5\%$  under ideal conditions demonstrates the reduction in scattering cross section for real measurements.

Even with intensity stabilized probe lasers fluctuations are likely to wash out absorption signals on the few percent level, especially in the low density tail of the atomic signal. This problem is pronounced by the relatively strong signal in the detector which necessitates the use of less sensitive (and less stable) detectors or operation of sensitive detectors near saturation. Fluorescence imaging has the advantage that the signal depends only weakly on the incident probe intensity  $I$  if we are working in the regime  $I \geq I_{\text{sat}}$  since here the scattering rate  $\gamma$  changes only slowly.

It follows that, for an integrated single atom detector and counter, fluorescence detection is the method of choice.

---

<sup>4</sup>The detection region has a diameter of approximately 5  $\mu\text{m}$ .

# 4. Photon Detector Characterization

## 4.1. APD Operation Principle

Avalanche photodiodes (APDs) are widely used for highly sensitive and fast photodetection. They are usually fabricated from silicon or germanium. Indeed silicon based avalanche photodiodes are the most sensitive photodetectors available in the mid-visible to near infrared ( $\approx 1 \mu\text{m}$ ) range. An APD is essentially a p-n junction operated under reverse bias close to the breakdown voltage  $V_B$  to achieve high gain. Light incident on the depletion region creates electron-hole pairs through the photo effect. The electric field generated by the voltage drop accelerates charge carriers injected in the depletion region until they can multiply by impact ionization, creating an avalanche. Typical values for  $V_B$  in silicon based detectors are 100 to 200 V.



**Figure 4.1.:**  
Avalanche photodiode (APD), photo from [lasercomponents.com](http://lasercomponents.com)

For single photon detection APDs are operated at  $V > V_B$ , in the so-called Geiger-mode. The name derives, in analogy to the Geiger counter, from the fact that here the bias field is so high that a single charge carrier injected into the depletion region generates a self-sustaining avalanche. An APD designed for use in Geiger-mode is often referred to as single-photon avalanche diode (SPAD). While Si-based APDs reach gain factors of 100, a single charge carrier in a SPAD can be multiplied within less than a nanosecond into a current of several milliamp [61]. The trade-off for this extremely high sensitivity is the loss of information on the intensity of the impinging light field. While for an APD the output signal is proportional to the light intensity, SPADs deliver an all-or-nothing signal. This limits the use of SPADs to extremely low light levels where multiple photon events are very unlikely.

**Passive Quenching** In SPAD mode the amplification is infinite, leading to a complete breakdown of the diode. To protect the diode the current has to be limited, which is achieved by quenching the avalanche through lowering the bias voltage below breakdown.

A simple, straightforward way to achieve this is to use a large resistor (typically 100 k $\Omega$ ) in series with the SPAD. On breakdown the voltage drop across the resistor quenches the avalanche, leading to a self limiting current [62]. This approach is known

as passive quenching but has only limited applications, due to the rather long time until the voltage recovers its original value, given by the recharge time of the diode capacitance in the resulting RC circuit (typically 1  $\mu$ s). Photons arriving during this time cannot be detected, hence it is referred to as dead time.

An added difficulty in analysing count distributions from passively quenched detectors is that the sensitivity increases at the end of the dead time parallel to the recharging curve of the RC circuit, instead of switching abruptly between quenched and active mode.

**Active Quenching** Accepting the necessity of quenching, one would ideally like to have a quenching circuit that is able to [61]

1. sense the leading edge of an avalanche
2. generate a standard output pulse (TTL, NIM, ...) synchronized with the edge
3. quench the avalanche by setting  $V < V_B$  for a predetermined time  $t_{\text{dead}}$
4. restore the bias voltage rapidly to operational level at the end of the dead time

The last two requirements lead to a step-like sensitivity characteristic with the detector being 'off' for the dead time  $t_{\text{dead}}$  after an event, followed by a sudden switch to the full sensitivity at the end of the dead time. Unlike the sensitivity characteristic of passively quenched SPADs this step-like characteristic with fixed dead time leads to a predictable distortion of the count distribution.

Quenching circuits adhering to the above requirements are known as active quenching circuits, due to the first requirement. Using active quenching dead times smaller than 50 ns can be realized [63, 64]. Numerous implementations of active quenching circuits exist, reference [65] gives a good starting point to get an overview.

Quenching leads with a low probability to secondary pulses at the end of the dead time, these afterpulses are treated later in this chapter as well as avalanches ignited by thermally activated electrons, so called dark counts.

Most modern single photon counting devices, including the modules employed for our measurements, use active quenching.

**Temperature Dependence** It should be stressed that the breakdown voltage of an APD varies rapidly with its temperature  $T_C$ . A typical relation has been measured by Brown et al. [62].

$$\frac{V_B}{T_C} = 0.75 \frac{\text{V}}{^\circ\text{C}}$$

Therefore the excess voltage  $V - V_B$ , determining the gain, is temperature dependent, too. This influences directly the dark count rate, afterpulsing probability and detection efficiency of a SPAD [61], which is a major problem for reliable measurements of photon counting statistics, since the power dissipation during a pulse is significant. A variation



of the bias voltage by  $\Delta V_B = 0.1$  V or drift in temperature of  $\Delta T_C = 0.004^\circ\text{C}$  leads to a 1% change in countrate. Hence SPADs require a good thermal stabilization, often realized using peltier elements and a large thermal reservoir. In the case of the modules used for our experiments the thermal reservoir was the optical table itself (several hundred kilograms of honeycombed steel).

The complete bundle of a SPAD with active quenching circuit, internal bias voltage generation and stabilization, thermal stabilization and electrical and optical connectors is often referred to as a single photon counting module (SPCM) and I will use this term from now on to label our photon detector.

**Applications** The ability to detect single photons is of interest to a diverse range of scientific fields and correspondingly SPCMs have found widespread use. Aside from single atom and single molecule detection applications include, but are not limited to, photon correlation studies, quantum communication and cryptography, astronomy, fluorescence decay studies, laser range finders, fibre optic telecommunication as well as several military applications [61].

## 4.2. Specifications

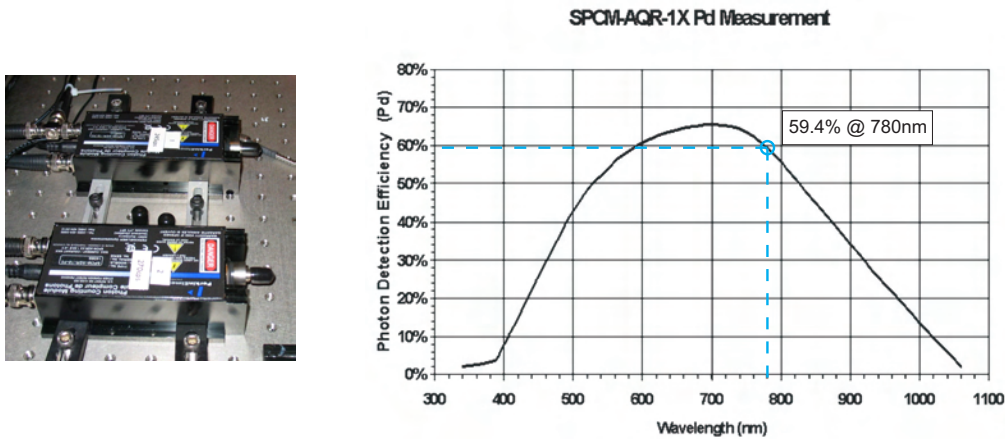


**Figure 4.2.:** Single Photon Counting Modules

**left:** The single photon counting modules in our setup

**right:** Photon detection efficiency vs wavelength from [66].

For the measurements presented here two PerkinElmer SPCM-AQR-12-FC single photon counting modules have been used. In addition to the above described active quenching capabilities they offer an FC/PC fibre coupling as well as an external gating of the high voltage bias. The latter feature is essential for our experiments, since the SPCM has to be protected from light scattered into the detection fibre during the MOT phase. The total power of the MOT laser beams is approximately 300 mW, of

which 200 mW are reflected off the atom chip in the mirror MOT setup leading to unacceptable high light levels in the detector.<sup>1</sup> Hence the SPCM is gated to low bias voltage during MOT-phase and primed to high bias voltage operation only during the magnetic trapping phase, when the MOT lasers are blocked.

In our experience one artificial count is always generated when the gating primes the detector.

PerkinElmer specifies a photon detection efficiency of 59.4 % at 780 nm for the SPCM-AQR-12 modules (see figure 4.2). The fibre connectorization reduces this by a factor 0.95 for our modules, yielding a photon detection efficiency of  $\eta_{\text{SPCM}} = 56.4$  %.

<b>Manufacturer Specifications</b>	
PD efficiency at 780 nm	$59.4\% \cdot 0.95 = 56.4\%$
dark counts	$< 500$ counts/s
average dark count variation at constant case temperature (6h at 25°C)	$\pm 10\%$
dead time (typical)	50 ns
afterpulsing probability $p_{\text{ap}}$	0.5 %
saturation count rate	15 Megacounts/s
output pulse width (TTL)	35 ns
peak light intensity in a 1 ns pulse	$10^4$ photons/pulse

	<b>Counter 1</b>		<b>Counter 2</b>	
	(Module No. 14067)		(Module No. 14069)	
	<i>specified</i>	<i>measured</i>	<i>specified</i>	<i>measured</i>
dark counts	244 cps	$245 \pm 10$ cps	270 cps	$304 \pm 12$ cps
dead time	55.2 ns	52 ns	49.2 ns	47.5 ns
$p_{\text{ap}}$	0.5 %	$2.6 \pm 0.1$ %	0.5 %	$1.0 \pm 0.1$ %

**Table 4.1.:** Manufacturer specifications and corresponding measured values for the employed SPCM-AQR-12-FC single photon counting modules.

Table 4.1 lists the specifications of the employed SPCMs, as well as the corresponding

<sup>1</sup>On a side note: this leads to a heating of the atom chip that can be measured with the integrated fibre cavity [30].

results from my own calibrations. The unit cps (counts per second) denotes the number of events generated by the SPCM and counted by the counter card per second. The saturation count rate is the maximum instantaneous event rate that the SPCM will produce. The detector response is not a linear function of the photon arrival rate due to dead time effects. Thus correction factors have to be applied for count rates above 1 Mcps (Megacounts per second). This is fortunately of no concern for our measurements. The output pulse width has been confirmed by my own measurements. The peak light intensity given is limited by heating of the SPCM and should not be exceeded. Dark counts, dead time and afterpulses will be discussed in the following sections.

## 4.3. Signal Artefacts

The analysis of statistical properties of a measured value is very sensitive to distortions of the statistical distribution by detector effects. For this reason I will now examine signal artefacts introduced by the photon detector and present corrections, where possible.

### 4.3.1. Dark counts

Dark counts are events generated by thermally activated electrons in the depletion region. The use of a bias voltage  $V$  larger than the breakdown voltage  $V_B$  makes SPCMs extremely sensitive to this effect. Obviously the dark count rate rises with increasing excess voltage  $V - V_B$  and temperature  $T_C$  [62], demanding cooling and temperature stabilization of the APD. But since both the dark count rate and the quantum efficiency depend on  $T_C$  and excess voltage usually a trade-off between low dark count rate and high quantum efficiency has to be made.

Typical dark count rates for the detectors employed are 300 cps (counts per second), but detectors with dark count rates below 25 cps are available, albeit at significantly higher price.<sup>2</sup>

**Statistical Distribution** Dark counts are generated independently from one another<sup>3</sup>, hence they should follow a Poisson distribution. But since the mean value of the dark counts may vary by  $\pm 10\%$  over 6 h at constant case temperature the distribution may be disturbed. The deviation from a Poisson distribution is small and will be examined in detail when discussing afterpulse effects.

Bistabilities of the dark count rate (a sudden jump from one mean value to another, typically a factor 1.5 to 2 higher) have been a common problem in early SPCM generations. They have not been observed in our detectors.

---

<sup>2</sup>PerkinElmer SPCM-AQR-16

<sup>3</sup>Neglecting second order effects like afterpulses generated by dark counts.

**Measurements** The dark count rates have been measured on disconnected counters with the fibre receptacles blocked.

	<i>dark count rate</i>	<i>specification</i>
counter 1	$245 \pm 10$ cps	244
counter 2	$304 \pm 12$ cps	270

For counter 1 the specification could be confirmed perfectly,<sup>4</sup> while the dark count rate of counter 2 exceeds the specifications.<sup>5</sup> Further measurements showed that counter 2 was prone to collect a small fraction of the ambient light, even when covered with multiple layers of black foil. Thus it has to be assumed that the deviation of the dark count rate of counter 2 from its specifications are caused by insufficient shielding of the fibre receptacle.

### 4.3.2. Dead Time

Each detection of a photon is followed by a dead time  $t_{\text{dead}}$ , given by the active quenching circuit that lowers the bias voltage below the breakdown voltage to quench the avalanche (see section 4.1). Photons arriving during this time will not be counted, leading to an underestimation of the count rate.

A time interval histogram, i.e. a histogram of the nearest neighbour distances of the recorded counts, allows measuring the dead time directly. Normalizing the time interval histogram by the total number of counts yields the probability distribution of temporal distances. The measurements show that both counters are actually faster than specified. Counter 1 exhibits a dead time of 52 ns (specification was 55.2 ns) and counter 2 was measured to have a dead time of 47.5 ns (specification was 49.2 ns).

**Correction** If the photon number in the incident signal is Poisson distributed, then the distances between the photons will follow an exponential distribution as will be derived in chapter 7. If  $\lambda$  denotes the mean photon rate, then the probability for two photons to arrive with a temporal distance  $d$  is given by  $p_{\text{dist}}(d) = e^{-\lambda \cdot d}$ . The fraction of missed photons is then given by the total probability to miss a photon during the dead time (assuming the intensity is low enough to miss at most one photon)  $p_{\text{miss}} = 1 - p_{\text{dist}}(t_{\text{dead}}) = 1 - e^{-\lambda \cdot t_{\text{dead}}}$ .

Using this as a correction factor to the total count rate the true count rate can be approximated. It should be noted, though, that dark counts and background counts

<sup>4</sup>Dataset 20071210Mon\_Darkcounts\_both, 198 shots

<sup>5</sup>Dataset 20071122\_Darkcounts\_2s\_noroomlight, 83 shots

<sup>6</sup>Dataset 20071215Sat\_F3\_2Fbr\_Disp\_Off\_background, measurement of Poissonian background, 1770 shots of 2s each.

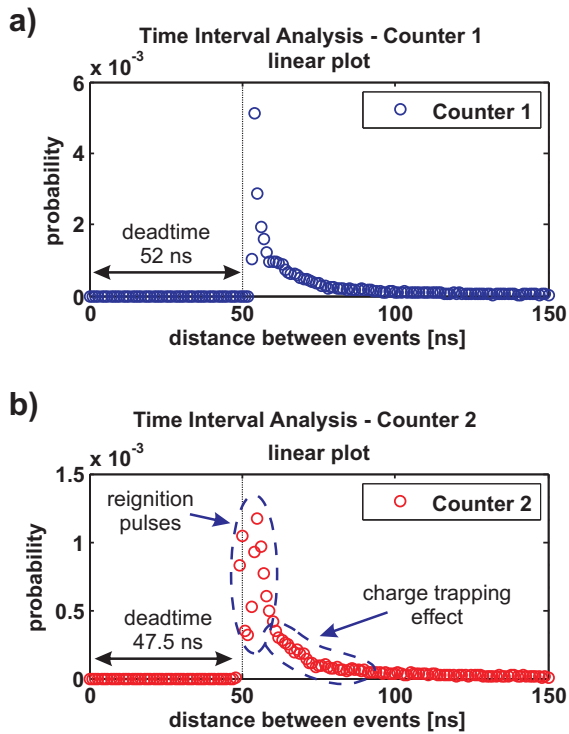


**Figure 4.3.:** Time Interval Histograms for the events from a single counter allow measuring the dead time as the smallest time interval that occurs with non-zero probability. A reference line at 50 ns is included for comparison.<sup>6</sup>

a) The histogram for counter 1 shows no events with a distance smaller than 52 ns.

b) For counter 2 the dead time is measured to 47.5 ns. Here additionally afterpulse distortions have been marked. The strong peak at the end of the dead time is due to reignition pulses, whereas the long slope is caused by charge trapping effects.

lead of course to dead time as well. The effect of dead time on the counting statistics has been examined and several different approaches to correct the counting statistics exist [67–69]. But it is worth pointing out that, while the total count rate and count histograms may be corrected for dead time, the information about correlations shorter than the dead time is lost. Hence correlation studies employing a single SPCM are limited in time resolution by the dead time.

### 4.3.3. Afterpulses

Afterpulses are those events that occur not independently of previous events, but at a certain time after an initial event. They are caused either by charge trapping or as a side-effect of the active quenching circuit.

#### Sources of Afterpulses

**Reignition Pulses** Active quenching can generate afterpulses during reignition of the detector at the end of the dead time. If a previous discharge current has been quenched incompletely a new avalanche will be triggered when the bias voltage is ramped above breakdown voltage again. Hence reignition pulses occur directly after the dead time, leading to a sharp over-representation of the event-distance  $\Delta t \approx t_{\text{dead}}$  in the time interval histogram.

Photons arriving at the end of the dead time present a special problem. If a photon arrives at the detector just when the bias voltage is being ramped up again then the afterpulsing probability is increased. For a detector with approximately 50 ns dead time only the photons arriving in the last 10 ns before recovery increase the afterpulsing probability. Interestingly avalanches initiated via this process are strongly delayed (up to approximately 10 ns for 50 ns dead time). The closer the arrival of the photon towards the end of the dead time, the shorter the delay. This effect is usually suppressed by an adapted quenching circuit [70].

**Charge Trapping** Charge trapping describes the process where an electron of the avalanche is trapped in the potential well around an impurity site. These sites are created by imperfect doping of the diode. Since doping is necessary to create the band gap needed for high quantum efficiency at the desired wavelength, charge trapping is an unavoidable side effect of avalanche photo diode production.

The trapped electron can be released by thermal excitation. If this occurs at a time  $t > t_{\text{dead}}$ , then it will create a new avalanche, the afterpulse. The lifetime of the trapped state depends on temperature and may be as high as several milliseconds or even a second [68], but is typically on the order of 100 ns [64]. Since the lifetime follows an exponential decay, charge trapping will result in an exponential time interval distribution that is added on top of the signal time interval distribution.

The measured distribution is distorted in addition by reignition pulses as discussed above and shown in figure 4.3. Reignition pulses appear in a narrow time frame of few nanoseconds after the end of the dead time, allowing to estimate the charge trapping lifetime from the distribution at larger time distances.

A single exponential decay does not describe the measured distribution for  $\Delta t > 60$  ns, even though reignition pulses should be of little relevance here. Additional analysis shows, that the region  $\Delta t = 60 \dots 80$  ns of fig.4.3 can be well approximated by a single exponential decay with  $1/e$  lifetime of  $\tau_{ct1} = 11 \dots 13$  ns for both counters. A fit to the region  $\Delta t = 80 \dots 150$  ns yields  $\tau_{ct2} = 47 \dots 50$  ns, again with a good fit to both counters.

The increased slope for the region  $< 80$  ns may be caused reignition pulses or be an indication for different trapping states. A distinction between these two explanations cannot be made from the current analysis and since it is of no deeper significance for our work this question will not be pursued further here. We note, though, that the  $1/e$  lifetime of the charge trapping states is  $< 50$  ns. This result will be of relevance in chapter 7, where it will allow us to treat the time interval histogram for time distances larger than a few hundred nanoseconds as being virtually unaffected by afterpulsing effects.

**Tardy Detection Events** An additional delay of up to 2 ns between the arrival of the photon and the generation of the output pulse may occur when the photons hit

the edge of the sensitive area of the APD. Here the APD responds more slowly and is usually less sensitive [70].

In our measurements tardy detection events are not expected, since we use a 62.5  $\mu\text{m}$  core diameter fibre with fibre connectors designed to fully illuminate the APD if 100  $\mu\text{m}$  core diameter fibres are employed [71]. Additionally the PerkinElmer SPCMs employed in our experiments contain APDs designed to exhibit a homogeneous sensitivity over the whole surface [66].

### Total Afterpulse Probability

**Total Afterpulse Probability from Probability Density Functions** As has been mentioned before the time interval distribution can be normalized by the total number of counts to become a probability density function  $p_{\text{dist}}(d)$  describing the likelihood to measure two events at temporal distance between  $d \cdot t_b$  and  $(d + 1) \cdot t_b$ . Here  $t_b$  is the size of the bins on which the probability density function is based. A natural minimum bin size is 1 ns, the resolution of our counter card, but for many applications a larger bin size will be used to be able to perform time interval analysis with a reasonable amount of statistics per bin.

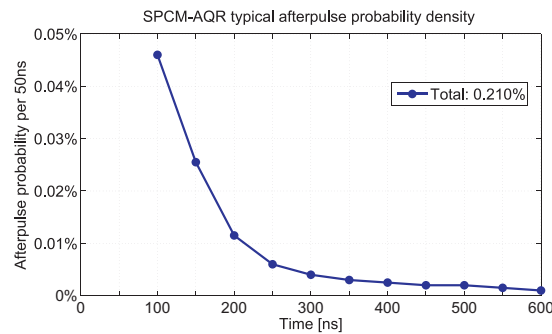


Figure 4.4.: SPCM Typical Afterpulse Probability, from [66]

PerkinElmer specifies a typical total afterpulse probability of  $p_{\text{ap}} = 0.5 \%$  and supplies a typical afterpulse probability density based on a 50 ns binning (fig.4.4). The total afterpulse probability  $p_{\text{ap}}$  can be approximated as the sum of  $p_{\text{dist}}(d)$  for temporal separations smaller than 600 ns.<sup>7</sup> Doing this for the specified typical distribution results in  $p_{\text{ap}}^{\text{spec}} = 0.21 \%$ . The difference between the two specified values may result from the fact that the provided probability density contains no data for the region  $t < 100$  ns.

Calculating the total afterpulsing probability from measured probability density functions for several different datasets yields consistently  $p_{\text{ap}}^{\text{meas}} = 2.6 \pm 0.1 \%$  for counter 1 and  $p_{\text{ap}}^{\text{meas}} = 1.0 \pm 0.1 \%$  for counter 2. Since this seems to be in disagreement with the

<sup>7</sup>At larger separations the afterpulse probability is low enough to be neglected.

**Table 4.2.: Total Afterpulse Probability for  $t < 600$  ns**

from integration of the measured probability density function from fig.4.3. The last two lines have been corrected for the contribution of the Poissonian source measured. The second and fourth line regard only the interval [100 600] ns to exclude reignition pulses. The indicated specified total afterpulsing probability has been calculated similarly as the integral of the provided probability density of figure 4.4.

specified total afterpulsing probability: 0.21 %		
<i>uncorrected</i>	<i>counter 1</i>	<i>counter 2</i>
<hr/>	<hr/>	<hr/>
$p_{\text{ap}}, \text{ total}$	: 2.69 %	1.03 %
$p_{\text{ap}}, t \geq 100 \text{ ns}$	: 0.65 %	0.26 %
 <i>Poisson corrected</i>	 <i>counter 1</i>	 <i>counter 2</i>
<hr/>	<hr/>	<hr/>
$p_{\text{ap}}, \text{ total}$	: 2.68 %	1.01 %
$p_{\text{ap}}, t \geq 100 \text{ ns}$	: 0.63 %	0.25 %

specification of typical 0.21 % (0.5 %) total afterpulsing probability we will examine it in detail here.

We have measured Poisson distributed sources which lead, if counted without distortions, to an exponential time interval distribution and hence  $p_{\text{dist}}^{\text{poiss}}(d) = e^{-\lambda \cdot d}$ , where  $\lambda$  denotes the mean count rate per bin (see chapter 7). To retrieve the total afterpulse probability from the measured distribution  $p_{\text{dist}}(d)$  the contribution of  $p_{\text{dist}}^{\text{poiss}}(d)$  for  $t < 600$  ns has to be subtracted. This is done for all evaluations presented in this work, but for the results of this section the mean count rate was so low that the total contribution from the Poisson source was approximately 0.01 % in the region  $t < 600$  ns and can therefore be neglected.

Table 4.2 summarizes the results of our total afterpulsing evaluation by integrating the measured probability density functions. It shows that counter 2 agrees well with the specification of 0.21 % total afterpulsing probability if only events with  $t \geq 100$  ns are considered. Counter 1 shows significantly higher afterpulsing probabilities. An independent study performed at the CalTech [72] using the same detector model (SPCM-AQR-12) measured a total afterpulsing probability of 1.2 % for their SPCM.

**Total Afterpulse Probability from Count Histograms** Campbell [73] has pointed out that the total afterpulse probability can as well be calculated from count histograms. His approach assumes that the following conditions are met.

1. Counts produced by light and noise are Poisson distributed.
2. The total afterpulse probability is independent of the light level and of previous events.
3. All afterpulses occur in the same bin as the initiating event.



The first condition was tested and is fulfilled in good approximation, the last condition can be met by choosing a bin size of at least 600 ns when creating the count histograms.

Let  $\lambda$  be the event rate,  $t_b > 600$  ns the bin size,  $p_{\text{ap}}$  as usual the total afterpulse probability (in this context the probability to have any number of afterpulses following one event) and  $p_{\text{ap}1}$  the probability that only a single afterpulse occurs. If one then generates a normalized histogram of the counts per bin, one gets  $p'_{\text{cts}}(n)$  the measured probability distribution to have  $n$  counts per bin. The original distribution to generate  $n$  counts per bin before distortions by afterpulsing will be labelled  $p_{\text{cts}}(n)$  and is given, due to condition 1, by the following expression.

$$p_{\text{cts}}(n) = \frac{(\lambda \cdot t_b)^n}{n!} e^{-\lambda \cdot t_b}$$

Note that  $p'_{\text{cts}}(0)$ , the probability to have 0 counts per bin, remains unchanged by afterpulsing and is therefore given by  $p'_{\text{cts}}(0) = p_{\text{cts}}(0) = e^{-\lambda \cdot t_b}$  from which follows:

$$\lambda = -\frac{1}{t_b} \log p'_{\text{cts}}(0) \quad \Rightarrow \quad p_{\text{cts}}(n) = \frac{(\lambda \cdot t_b)^n}{n!} p_{\text{cts}}(0) \quad (4.1)$$

One count per bin can only be measured if no afterpulse occurred, thus  $p_{\text{ap}}$  reduces  $p'_{\text{cts}}(1)$  to

$$p'_{\text{cts}}(1) = p_{\text{cts}}(1) \cdot (1 - p_{\text{ap}}) = \lambda \cdot t_b \cdot p'_{\text{cts}}(0) \cdot (1 - p_{\text{ap}})$$

which allows us to calculate the total afterpulse probability from measured values.

$$p_{\text{ap}} = 1 - \frac{p'_{\text{cts}}(1)}{\lambda \cdot t_b \cdot p'_{\text{cts}}(0)} \quad (4.2)$$

Similarly, realizing that the probability to measure two counts in a bin is composed of having two original counts without afterpulses  $p_{\text{cts}}(2) \cdot (1 - p_{\text{ap}})^2$  and one original count followed by a single afterpulse  $p_{\text{cts}}(1) \cdot p_{\text{ap}1}$ , we can express  $p_{\text{ap}1}$  by measured values.

$$p_{\text{ap}1} = \left[ \frac{p'_{\text{cts}}(2)}{p_{\text{cts}}(0)} - \frac{1}{2} (\lambda \cdot t_b)^2 (1 - p_{\text{ap}})^2 \right]^2 \frac{1}{\lambda \cdot t_b} \quad (4.3)$$

Count histograms of several background measurements have been build and analysed using the procedure outlined above. Figure 4.5 shows a typical result. The total afterpulse probability for counter 1 was estimated to  $p_{\text{ap}} = 2.70 \pm 0.10$  %, the single afterpulse probability to  $p_{\text{ap}1} = 2.66 \pm 0.10$  %, demonstrating that two afterpulse events can be neglected for counter 1. Counter 2 shows similar results with  $p_{\text{ap}} = 1.18 \pm 0.10$  % and  $p_{\text{ap}1} = 1.18 \pm 0.10$  %. Both values for the total afterpulsing probability confirm the afterpulse probabilities derived from the probability density functions.

The calculated count rates from the count histograms via equation 4.1 (counter 1:  $\lambda = 242$ , counter 2:  $\lambda = 306$ ) agree well within errors with the mean count rates measured directly (counter 1:  $248 \pm 16$ , counter 2:  $310 \pm 17$ ).

<sup>8</sup>Dataset 20071122\_Darkcounts\_2s\_roomlight, 26 shots of 2 s each.

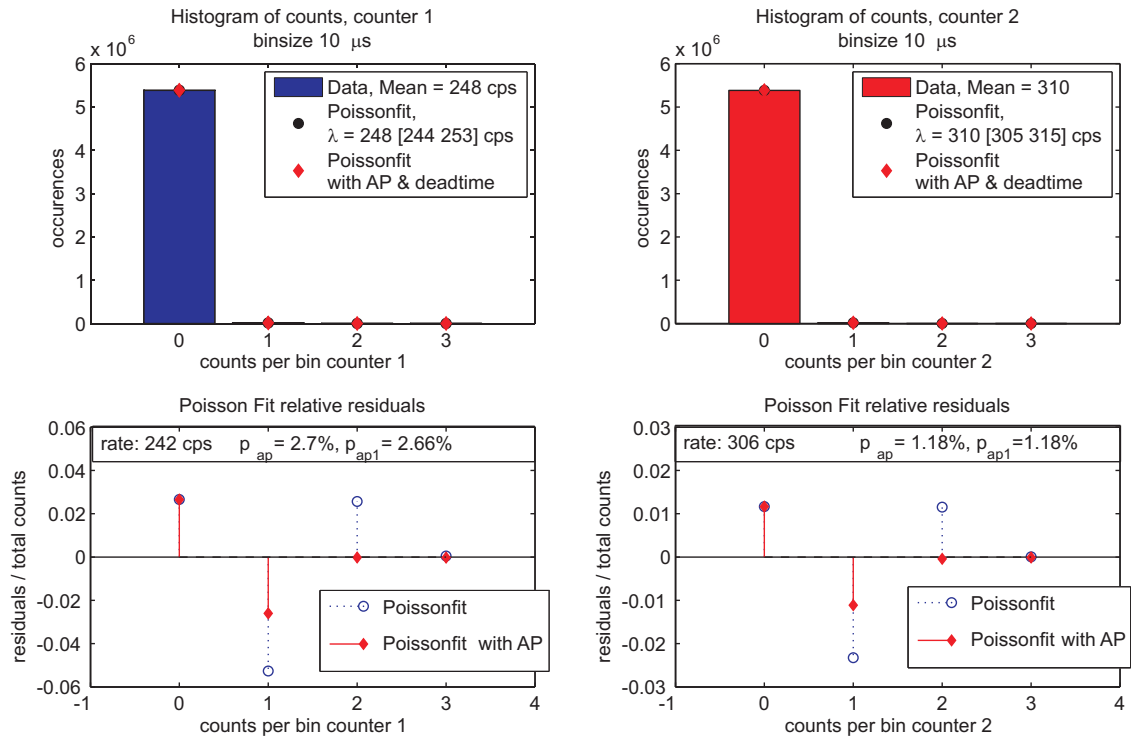


**Figure 4.5.:** Total Afterpulse Probability from Count Histograms

The upper graphs show histograms of the number of counts in 10  $\mu$ s bins for counter 1 (left) and counter 2 (right)<sup>8</sup>. Total afterpulsing probabilities, single afterpulse probabilities and count rates are calculated from the histograms and shown as insets in the lower graphs.

A fit of the count histograms to a Poisson distribution delivers a perfect agreement between the fit parameter and the mean count rate. An analysis of the fit residuals (blue open circles in lower left and lower right graph) shows systematic deviations from the Poisson distribution caused by afterpulsing and dead time effects. Correction of the fitted Poisson distributions for measured afterpulsing probabilities yields smaller residuals (red diamonds in lower left and lower right graph). The remaining deviations are most likely caused by dead time effects (increasing the chance to get 0 counts per bin at expense of (mostly) 1 count per bin).

A Poisson fit to the count histograms shows small but systematic deviations in the residuals, caused by afterpulsing and dead time distortion of the recorded counts. Correcting the fitted Poisson distribution for afterpulsing effects up to second order reduces the residuals, leaving only discrepancies between Poisson fit and measured distribution for 0 and 1 counts per 10  $\mu\text{s}$  bin. These are very likely caused by dead time effects, which increase the number of 0 counts per bin at the expense of (mostly, due to the low count rate) 1 count per bin.

In summary, two independent methods showed that the total afterpulsing probabilities are approximately 2.7 % and 1.1 % for counter 1 and counter 2 respectively. Both values are significantly higher than the specified values.

It appears therefore that  $p_{\text{ap}}$  as specified by PerkinElmer neglects reignition pulses, and includes only charge trapping effects. Which renders the specification quite useless.

### Correction

Regardless of the source, afterpulses are highly detrimental to our experiments and therefore have to be corrected for.

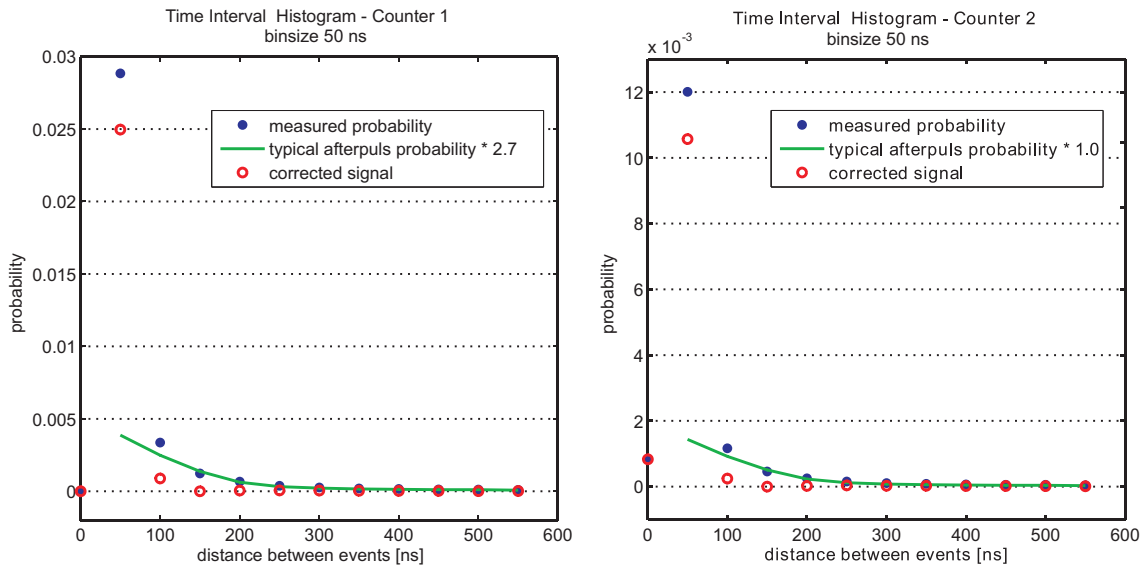


**Figure 4.6.:** Afterpulse correction of the time interval distribution

The measured normalized time interval distribution (blue dots, bin size 50 ns) for counter 1 (left) and counter 2 (right) can be corrected for afterpulse distortions using a multiple spline fit expanded version of the specified total afterpulse probability density (green line). The correction (red open circles) is very good for  $t > 100$  ns but fails for smaller time intervals due to uncompensated reignition pulses. Note that the entry at  $t = 0$  ns is non zero for counter 2 because the chosen binning of 50 ns is larger than the dead time.

The true number of total counts  $n_{\text{counts}}$  can be estimated from the measured number of total counts  $n'_{\text{counts}}$  simply via the total afterpulse probability  $p_{\text{ap}}$  if dead time effects,

i.e. counts missed due to afterpulses, are neglected.

$$n'_{\text{counts}} = (1 + p_{\text{ap}}) \cdot n_{\text{counts}}$$

Here we will concern ourselves with the correction of time interval distributions [68]. If the probability density of the afterpulses is known it can be used to correct the normalized time interval distribution. In figure 4.6 the results of such a correction are shown. Here the specified total probability density from figure 4.4 has been used for correction, after it has been extended to the region  $t = 50 \cdots 100$  ns by a non-linear multiple spline fit and scaled with a fixed factor to accommodate for the fact that our counters show higher afterpulsing probabilities than specified. Optimal scaling factors are 2.7 for counter 1 and 1.0 for counter 2, close to the ratio measured to specified afterpulse probability in the region  $> 100$  ns. A good correction is achieved for  $t > 100$  ns, but the entries up to  $t = 100$  ns remain undercompensated, due to non-corrected reignition pulse contributions.

The afterpulse probability densities from background measurements, e.g. figure 4.3, unfortunately do not deliver a better correction for  $t < 100$  ns. While the charge trapping induced afterpulses can be corrected for very well using either a scaled version of the specified afterpulse probability density (fig.4.4) or a measured probability density, the reignition part is often over- or undercompensated. A possible explanation for this failure is that the reignition pulse probability might depend on the light intensity, likely via an increased chance of photon arrivals at the end of the dead time.

In autocorrelations afterpulses lead to a strong peak at 50-100 ns, dominating all other structures. Correlation functions will be discussed in chapter 8. Afterpulses, as well as dead time effects, are eliminated if cross correlations between two detectors in a Hanbury Brown-Twiss type setup are examined, instead of autocorrelations of a single detector. However, the signal strength is reduced by a factor 2. Several approaches exist to correct count histograms for afterpulsing effects [68, 73], but of interest to us is a correction method of the second order correlation function proposed by Zhao et al. [74].

Starting from the assumption that, if  $p_{\text{ap}}(t)$  is the afterpulsing probability at time  $t$  after the initial event, the recorded intensity  $I'$  is related to the true intensity  $I$  via

$$I'(t) = I(t) + \int_0^\infty p_{\text{ap}}(t') \cdot I(t - t') dt'$$

the following relation between the measured intensity correlation function  $g^{(2)'}(d)$  and the true intensity correlation function  $g^{(2)}(d)$  can be derived.

$$g^{(2)'}(d) = g^{(2)}(d) + \frac{t_b}{\lambda_b} p_{\text{ap}}(d) \quad (4.4)$$

Here  $t_b$  denotes the bin size and  $\lambda_b$  the mean count rate per bin. The lag  $d$  is the temporal distance.

Equation 4.4 is valid for small afterpulsing probability and sources that are approximately Poisson distributed, under the condition that  $g^{(2)}(d)$  decays slowly compared to  $p_{\text{ap}}(d)$ .

$p_{\text{ap}}(d)$  can be retrieved from a background measurement with an uncorrelated source (mean count rate per bin  $\lambda_{bg}$ ), since then the following relation holds.

$$g_{bg}^{(2)'}(d) = 1 + \frac{t_b}{\lambda_{bg}} p_{\text{ap}}(d) \quad (4.5)$$

Once  $p_{\text{ap}}(d)$  is known relation 4.4 can simply be inverted to calculate the true correlation function from the measured  $g^{(2)'}(d)$ .

This scheme works well if  $p_{\text{ap}}(d)$  is known with high precision and is independent of the count rate. Unfortunately, as has been mentioned before, the latter was not the case for our detectors. Therefore afterpulse correction of the correlation functions has delivered only unsatisfactory results for our data. An added difficulty here is the strength of the distortion, leading to high sensitivity to errors in  $p_{\text{ap}}(d)$ .

The next section will demonstrate that a similar scheme can be employed much more successfully to correct cross correlations for secondary emission effects.

#### 4.3.4. Secondary Emission

Silicon SPADs are known to emit a pulse of light when recovering from an avalanche. This light can be reflected back on the APD or enter nearby APDs, creating additional counts.

**Source** These secondary emissions are linked in shape and timing to the current in the APD. The spectrum of the breakdown flash however does not depend on the frequency of the incident light field, but shows instead a broad spectral range as shown in figure 4.7 [75]. The emission reaches its peak with a rise time of 1 to 2 ns, followed by an exponential decay with a timeconstant of approximately 3 ns (following the discharge current quenching) [75]. As a rule of thumb, according to Dravins et al. [63], typically 100 photons are emitted per avalanche. Kurtsiefer et al. [75] measured that  $B = 2 \cdot 10^{-3}$  photons/(sr ·  $\mu\text{m}^2$ ) are emitted from the sensitive area of the APD, of which  $n_r \approx B \omega_0^2 \Theta^2 \pi^2/4 = 1.3 \cdot 10^{-3}$  photons/event are coupled back into a fibre with mode diameter  $\omega_0$  and divergence  $\Theta$ .

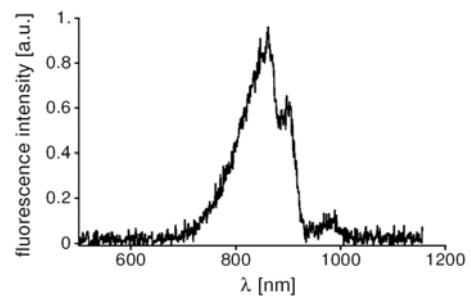


**Figure 4.7.:** Normalized breakdown flash (secondary emission) spectrum of a silicon APD. The spectrum is independent on the incident light frequency and peaked at 850 nm. From [75].

**Effect** Secondary emission (SE) of light will distort our measurements if it is somehow reflected back into the APD or manages to enter the second APD.

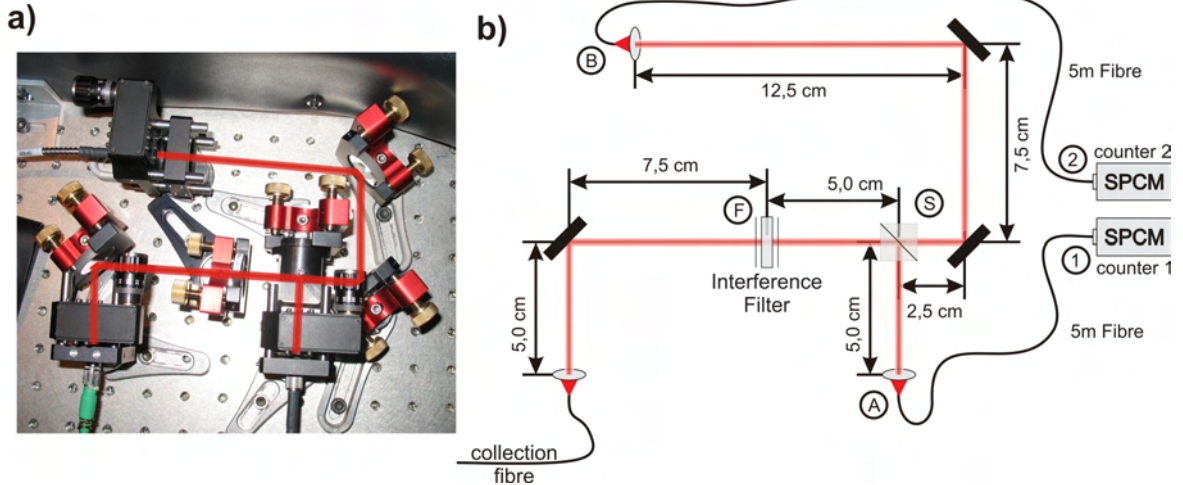


**Figure 4.8.:** The photon detection setup in Hanbury Brown-Twiss configuration

a) Photo of the actual setup used with superimposed beam path.

b) Schematic drawing of the beam path. The length of the sections of the path have been marked, as well as specific points. For secondary emission of counter 1 to reach counter 2 it will have to travel from counter 1 (1) through 5 m of MM fibre to the fibre coupler (A), be reflected on the 50/50 beam splitter (S), be reflected in the interference filter (F), pass the beam splitter (S) enter the fibre coupler (B) and travel another 5 m of MM fibre to counter 2 (2). On the total path 1ASFSB2 it will then have travelled 10 m in the fibre at  $n = 1.456$  and 37.5 cm in free space at  $n = 1$ . This corresponds to 51 ns travel time.

Most backreflections can be neglected since dead time prevents them from being counted. For example the most likely reflections, i.e. on the APD window<sup>9</sup> or on the fibre facet close to the APD, return to the APD after only a few picoseconds. More critical is a ringing reflection in the MM fibre leading from the filter gap to the APD (see figure 4.8). We employ identical graded index multi mode fibres of 5 m length each with core index of refraction  $n = 1.496$  to guide the light from the filter gap to the photon detectors. Secondary emission from counter 2 that enters the MM fibre and is backreflected on the far facet (point marked B in fig.4.8) will return to the APD after  $t = 2 \cdot 5 \text{ m} / (c/n) = 50 \text{ ns}$ . While for counter 1 this would still be suppressed by dead time, counter 2 would be counting its own secondary emissions. Autocorrelations in counter 2 e.g. would show strong correlation at 50ns. Again, this effect can be avoided by employing fibres with at least one angle polished (APC) facet.

Relevant to our analysis is a third possibility that appears at first unlikely. If secondary emission from counter 2 (at position (2) in fig.4.8) manages to enter the fibre and leaves it at position (B) it has a 50/50 chance to be transmitted at the beam splitter (B).

<sup>9</sup>The window of the APD is not anti-reflection coated. [71]

<sup>10</sup>Dataset 20071211Tue\_2Fiber\_Efficiency\_2, shots 800-1533, 2 s each.

<sup>11</sup>Dataset 20071211Tue\_2Fiber\_Efficiency, 107 shots, 2 s each.

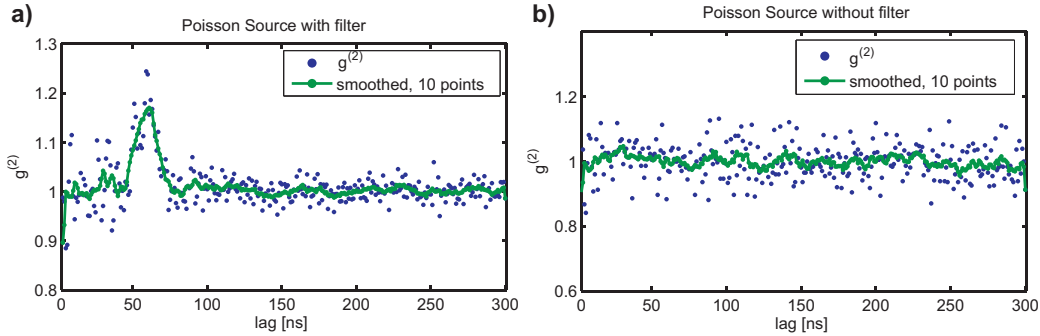


**Figure 4.9.:** Secondary Emission

Cross Correlation of a Poissonian Source (blue dots).

The green line is a 10 point moving average smoothing of the data to guide the eye.

a) The measurement shows a distortion due to secondary emissions entering the opposite counter.

Delay is  $60 \pm 5$  ns.<sup>10</sup>

b) Removing the filter removes the distortion as well.<sup>11</sup>

Light reflected on the beam splitter is dumped and need not concern us, but if the light is transmitted through the beam splitter it will reach the interference filter at position (F). Figure 4.7 showed that the SE spectrum is broadband, which leads to most light being *reflected* on the interference filter, back towards the beam splitter (B). If it is now reflected here this time it will enter the second MM fibre at (A) to be guided to counter 1 (1). The total length of fibre travelled is the same as in the previous example ( $10 \text{ m} \hat{=} 50 \text{ ns}$ ) but here an additional free space path (BSFSA) of  $37.5 \text{ cm} \hat{=} 1 \text{ ns}$  is added. Combined with an expected pulse length of approximately 5 ns this leads to counts in counter 2 generating correlated counts in counter 1 with temporal distance approximately 51 to 56 ns. Even though this number may be considered just a rough estimate (e.g. possible delays in the secondary emission production have not been taken into consideration) its value is quite alarming. Since we intend to measure nonclassical correlations in photons generated by a single atom with excited state lifetime of  $\tau = 26 \text{ ns}$ , the SE distortion is with approximately  $2 \cdot \tau$  precisely in the region of interest. Hence a correction of secondary emission distortions is, at least for cross correlations measurements, of paramount importance.

One can easily imagine more complicated beam paths, involving multiple passes through the fibres leading to higher order distortions that would produce delays of multiples of the above estimated 51 to 56 ns.

A measurement of a Poissonian signal with the Hanbury Brown-Twiss type photon detection setup as described in section 2.5 and figure 4.8 shows indeed a correlation between counts from the two counters for a lag (time difference) of  $60 \pm 5 \text{ ns}$  (see fig.4.9a)). This time difference agrees well with the expected time difference for secondary emission caused distortions. In order to exclude other sources we perform two relatively simple tests. First we remove the interference filter from the setup and perform the measurement under otherwise identical conditions. The result is shown in figure 4.9b) and proves already that the broad spectrum of the secondary emissions is

effectively reflected on the filter.

As a second test we perform a similar measurement of a Poissonian signal in the alternative Hanbury Brown-Twiss setup using a fibre-Y as described in section 2.5. Each leg of the fibre-Y has a length of 1 m, so that a secondary emission pulse will have to travel  $2 \cdot 2$  m in the fibre to enter the opposite detector. Together with the free space path to the filter and back we expect to see correlations at a lag of approximately 21 ns in this setup. The results of the measurements, presented in figure 4.10, show a correlation at  $28 \pm 4$  ns. This is close to the expected value and only half of the lag measured in the standard setup, confirming that the distortions observed are indeed caused by secondary emissions.

The total probability to generate a count caused by secondary emission from the other counter was measured to  $p_{se} = 1.46$  % in the standard filter gap setup.

**Correction** Since secondary emission leads to the same kind of distortion in cross correlations of neighbouring detectors as afterpulsing does in autocorrelations a correction of the cross correlation functions for secondary emission effects can be achieved by employing very similar schemes.

In the last section the correction scheme for autocorrelation functions proposed by Zhao et al.[74] was introduced. The difference here is that we do not have one mean count rate  $\lambda$ , but two for two different counters. If  $\lambda_1$  is the mean count rate per second in counter 1 and  $\lambda_2$  correspondingly for counter 2, then the relation between the measured second order correlation function  $g^{(2)'}(d)$  and the true second order correlation function  $g^{(2)}(d)$  can be expressed as

$$g^{(2)}(d) = g^{(2)'}(d) - \frac{c_{SE}(d)}{\lambda_1 \lambda_2} \quad (4.6)$$

Where  $d$  is again the temporal distance and  $c_{SE}$  is the secondary emission correction factor, derived from a background measurement of an uncorrelated source in analogy to equation 4.5.

$$g_{bg}^{(2)'}(d) = 1 + \frac{f_n}{\lambda_{bg1} \lambda_{bg2}} c_{SE}(d)$$

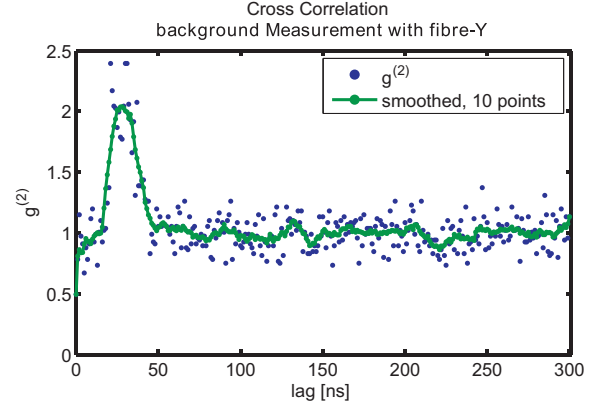


**Figure 4.10.:**

**Secondary Emissions in the Fibre-Y Setup** The correlation function measured employing a fibre-Y beam splitter<sup>12</sup> shows a distortion peak at  $28 \pm 4$  ns. The blue dots are the measured cross correlations from a Poissonian source, the green line is the result of a 10 point moving average smoothing to guide the eye.

<sup>12</sup>Dataset 20071125\_LED\_Y\_2s\_4, 10 shots, 2 s each.



The terms  $\lambda_{bg1}$  and  $\lambda_{bg2}$  denote the mean count rates in the background measurement and  $f_n$  is a normalization factor<sup>13</sup>

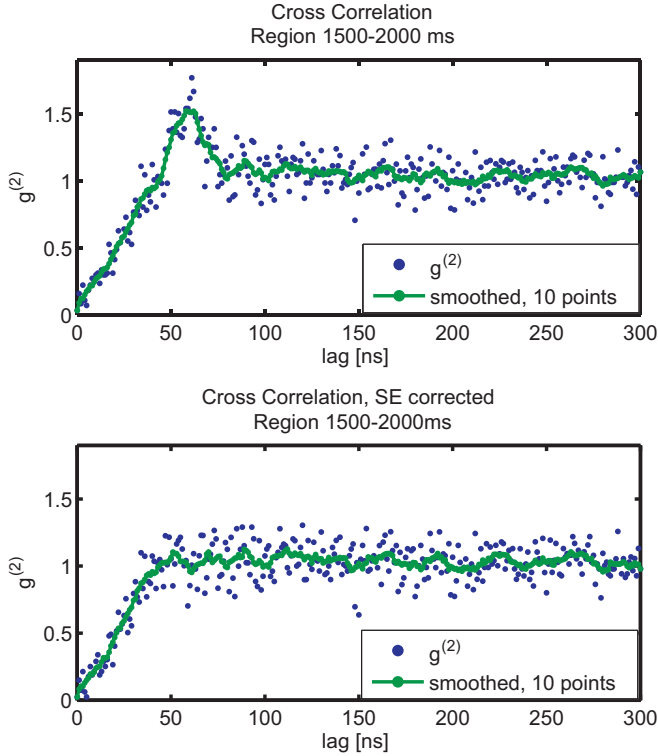


**Figure 4.11.:** Secondary emission correction demonstrated on a cross correlation measurement of an atomic signal.<sup>14</sup> The region 1500 to 2000 ms after opening of the Z trap was chosen to examine low atomic densities. The upper graph shows the uncorrected normalized intensity correlation function  $g^{(2)}$  exhibiting a strong secondary emission distortion exactly in that region where Rabi oscillations might be expected. The lower graph shows the secondary emission corrected correlation function. In both graphs the blue points represent the actual datapoints measured. The green points are included to guide the eye and have been produced by a 10 point moving average smoothing of the measured correlation function.

### 4.3.5. Mandel Q Factor

The Mandel Q factor is so to speak a quick test of how a given distribution  $k$  compares to a Poisson distribution. Using angular brackets to denote mean values it can be defined by

$$\begin{aligned}
 Q &= \frac{\text{Var}(k) - \langle k \rangle}{\langle k \rangle} \\
 &= \frac{\text{Var}(k)}{\langle k \rangle} - 1 \\
 &= \frac{\langle k^2 \rangle - \langle k \rangle^2}{\langle k \rangle} - 1
 \end{aligned} \tag{4.7}$$

For Poisson distributed  $k$  the variance equals the mean  $\text{Var}(k) = \langle k \rangle$ , therefore  $Q = 0$ . We can now distinguish three different regimes.

- $Q = 0$  Poisson distribution
- $Q < 0$  sub-Poissonian behaviour
- $Q > 0$  super-Poissonian behaviour

<sup>13</sup>  $f_n = 2.5$  has produced very good corrections for us.

<sup>14</sup> Dataset 20071220Thu\_F3\_resonant\_412mV, 4409 shots, Region 1500-2000ms.

Light has a Poissonian photon number distribution. If now a constant light source illuminates the detector afterpulses will broaden the distribution, leading to super-Poissonian behaviour and dead time will narrow the distribution, resulting in sub-Poissonian behaviour. The combined effect of a detector with afterpulse probability  $p_{\text{ap}}$  and dead time  $t_{\text{dead}}$  on the photon count distribution is given by

$$Q = 2 p_{\text{ap}} - 2 \lambda t_{\text{dead}} \quad (4.8)$$

where  $\lambda$  is the mean count rate. Plotting  $Q$  versus the count rate for purely Poissonian illumination results in a linear relation with slope  $-2 t_{\text{dead}}$  and y-intercept  $2 p_{\text{ap}}$  [69].

In figure 4.12 the Mandel  $Q$  factor is plotted against count rate for a third PerkinElmer SPCM-AQR-12-FC.<sup>15</sup> This module was characterized during our measurements in Heidelberg, but not used for scientific measurements. The linear fit to the measured  $Q$  parameter yields a dead time of  $t_{\text{dead}} = 60 \pm 5$  ns, agreeing with the specified value of 55.2 ns within errors. The total afterpulse probability, indicated by the y-intercept, is estimated to  $p_{\text{ap}} = 1.6 \pm 0.3$  %, fitting well into the range of total afterpulsing probabilities measured for the other modules.

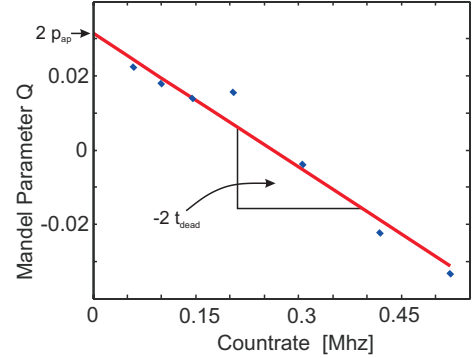


**Figure 4.12.:** Mandel  $Q$  Factor plotted vs count rate with linear fit. The slope corresponds to a dead time of  $t_{\text{dead}} = 60 \pm 5$  ns, the y-intercept indicates  $p_{\text{ap}} = 1.6 \pm 0.3$  %. [30]

<sup>15</sup>PerkinElmer SPCM-AQR-12-FC, module no. 14068

# 5. Signal & Background

In this chapter I will derive the shape of the transit signal produced by an atom pulse passing the fluorescence detector and show typical measurements. After establishing the signal strength for our experimental parameters, the background signal will be discussed. The discussion in this chapter will be limited to the single detector setup, but is equally valid for the two detector setup. If two detectors are employed the signal and background light will be distributed to the detectors according to the splitting ratio of the photon detection setup (see chapter 9).

## 5.1. Signal

During preparation the atoms thermalize in the magnetic Z-trap generated by the chip. As long as the temperature does not fall below the critical temperature for Bose-Einstein condensation the deBroglie wavelengths of the atoms will not overlap. Thermalization can then be described classically and the velocities of the atoms will be Boltzman-distributed.<sup>1</sup>

### 5.1.1. Boltzman Distribution of velocities

**Velocity Distribution in 1D** The one-dimensional Boltzman velocity distribution<sup>2</sup>  $F_{1D}(v)$  depends on the mass  $m_{\text{Rb}}$  of the atoms and their temperature  $T$  [47].

$$F_{1D}(v) = \sqrt{\frac{m_{\text{Rb}}}{2\pi k_B T}} e^{-\frac{m_{\text{Rb}} v^2}{2k_B T}} \quad (5.1)$$

The probability  $p(v)$  to find a particle with velocity  $v$  between  $v_1$  and  $v_2$  is then given by

$$p(v) = \int_{v_1}^{v_2} F_{1D}(v) dv$$

from which we get the the number of atoms  $n_v(v)$  in the velocity interval  $dv$  via the total number of atoms  $N$ .

$$n_v(v) dv = N p(v) = N \int_{v_1}^{v_2} F_{1D}(v) dv$$

---

<sup>1</sup>The deBroglie wavelength for an  $^{87}\text{Rb}$ -atom in an ensemble with  $T = 50 \text{ }\mu\text{K}$  is approximately 27 nm.

<sup>2</sup>Also known as Maxwellian velocity distribution.

The most likely velocity in the 1D Boltzman distribution is

$$\hat{v}_{1D} = \frac{dF_{1D}(v)}{dv} = 0$$

due to the symmetry of the distribution. The mean velocity, regarding only the half-space  $[0, \infty]$ , is given by the expectation value.

$$\bar{v}_{1D} = \int_0^{\infty} v F_{1D}(v) dv = \sqrt{\frac{k_B T}{2\pi m_{Rb}}}$$

**Velocity Distribution in 3D** If the mean kinetic energy  $\bar{E}_{kin} = 3/2 k_B T$  is large compared to the potential energy differences in the volume considered, then all directions are emancipated and the solution derived above for the one dimensional case holds true for the velocities  $v_x, v_y, v_z$  in the three spatial dimensions. The probability  $p(\vec{v})$  to find a particle with velocity  $\vec{v} = (v_x, v_y, v_z)$  is consequently given by the product of the single probabilities and the velocity distribution likewise.

$$\begin{aligned} F_{3D}(\vec{v}) &= F_{1D}(v_x) \cdot F_{1D}(v_y) \cdot F_{1D}(v_z) \\ F_{3D}(\vec{v}) &= \left( \frac{m_{Rb}}{2\pi k_B T} \right)^{3/2} e^{-\frac{m_{Rb} \vec{v}^2}{2k_B T}} \end{aligned} \quad (5.2)$$

The probability  $p(\mathbf{v})$  to find a particle with velocity  $\mathbf{v} = |\vec{v}|$  is given by the integration over a spherical shell with volume  $4\pi v^2 dv$ . The number of atoms  $n_v(\mathbf{v})$  in the velocity interval  $d\mathbf{v}$  is then given by

$$n_v(\mathbf{v}) d\mathbf{v} = N \int_{v_1}^{v_2} 4\pi v^2 F_{3D}(v) dv$$

The most likely velocity of the 3D Boltzman distribution is

$$\hat{v}_{3D} = \frac{dF_{3D}(v)}{d\mathbf{v}} = \sqrt{\frac{2k_B T}{m_{Rb}}}$$

and the mean velocity can again be calculated as the expectation value.

$$\begin{aligned} \bar{v}_{3D} &= \int_0^{\infty} v F_{3D}(v) 4\pi v^2 dv \\ \bar{v}_{3D} &= \sqrt{\frac{8k_B T}{\pi m_{Rb}}} \end{aligned}$$

**Table 5.1.:** Boltzman Distribution Parameters

$\hat{v}$  denotes the most likely velocity,  $\bar{v}$  the mean velocity,  $t_{\max}$  the arrival time of the peak of the atom pulse at the detector and  $T$  the temperature.

1D	3D
$\hat{v}_{1D} = 0$	$\hat{v}_{3D} = \sqrt{\frac{2 k_B T}{m_{\text{Rb}}}}$
$\bar{v}_{1D} = \sqrt{\frac{k_B T}{2\pi m_{\text{Rb}}}}$	$\bar{v}_{3D} = \sqrt{\frac{8 k_B T}{\pi m_{\text{Rb}}}}$
$t_{\max 1D} = \frac{s}{\sqrt{2}} \sqrt{\frac{m_{\text{Rb}}}{k_B T}}$	$t_{\max 3D} = \frac{s}{2} \sqrt{\frac{m_{\text{Rb}}}{k_B T}}$
$T_{1D} = \frac{s^2}{2 t_{\max}^2} \frac{m_{\text{Rb}}}{k_B}$	$T_{3D} = \frac{s^2}{4 t_{\max}^2} \frac{m_{\text{Rb}}}{k_B}$

### 5.1.2. Boltzman Distribution of arrival times

The Fluorescence detector records the arrival times  $t$  of the atoms, not the velocities  $v$ . The distribution of arrival times  $F^t(v)$  at distance  $s$  from the initial position can be obtained from the velocity distribution  $F(v)$  by a transformation of variables  $v \rightarrow t$  with  $v = s/t$ .

$$\begin{aligned} F^t(t) dt &= F(s/t) \frac{dv}{dt} dt \\ &= F(s/t) \frac{-s}{t^2} dt \end{aligned}$$

In the calculation of the number of particles  $n_t$  that arrive between times  $t_1$  and  $t_2$  the minus sign is taken care of by reversion of the integration directions, since  $(t_2 = s/v_2) < (t_1 = s/v_1)$  for  $v_2 > v_1$ .

$$\begin{aligned} n_t = \int_{t_2}^{t_1} n_t(t) dt &= N \int_{t_1}^{t_2} F^t(t) dt = N \int_{t_1}^{t_2} F(s/t) \frac{-s}{t^2} dt \\ &= N \int_{s/t_2}^{s/t_1} F(v) dv \end{aligned}$$

The peak of the arrival time distribution (most likely arrival time) is given by

$$t_{\max} = \frac{dn_t(t)}{dt} = 0$$

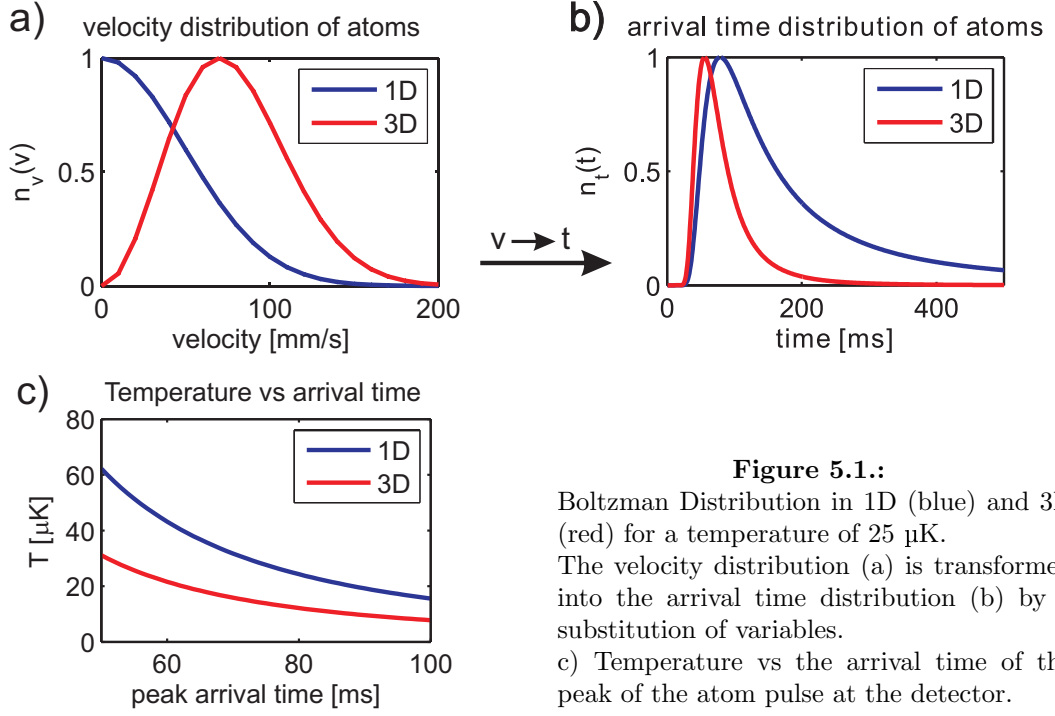


**Figure 5.1.:**

Boltzman Distribution in 1D (blue) and 3D (red) for a temperature of 25  $\mu\text{K}$ . The velocity distribution (a) is transformed into the arrival time distribution (b) by a substitution of variables. c) Temperature vs the arrival time of the peak of the atom pulse at the detector.

**Arrival Time Distribution in 1D** For the 1D Boltzman distribution the number of atoms arriving at time  $t$  is consequently given by

$$n_t(t) dt = N \sqrt{\frac{m_{\text{Rb}}}{2\pi k_B T}} e^{-\frac{m_{\text{Rb}} s^2}{2k_B T t^2}} \frac{s}{t^2} dt$$

which reaches the maximal arrival rate at  $t_{\text{max1D}}$ .

$$t_{\text{max1D}} = \frac{s}{\sqrt{2}} \sqrt{\frac{m_{\text{Rb}}}{k_B T}} \quad (5.3)$$

The above equation can be inverted, allowing us to estimate the temperature of the atomic ensemble by measuring the arrival time of the peak of the atom pulse.

$$T_{1\text{D}} = \frac{s^2}{2 t_{\text{max}}^2} \frac{m_{\text{Rb}}}{k_B}$$

**Arrival Time Distribution in 3D** Correspondingly for the 3D Boltzman distribution one gets the following relations.

$$n_t(t) dt = N 4\pi \frac{s^2}{t^2} \left( \frac{m_{\text{Rb}}}{2\pi k_B T} \right)^{3/2} e^{-\frac{m_{\text{Rb}} s^2}{2k_B T t^2}} \frac{s}{t^2} dt$$

$$t_{\text{max3D}} = \frac{s}{2} \sqrt{\frac{m_{\text{Rb}}}{k_B T}} \quad T_{3\text{D}} = \frac{s^2}{4 t_{\text{max}}^2} \frac{m_{\text{Rb}}}{k_B}$$

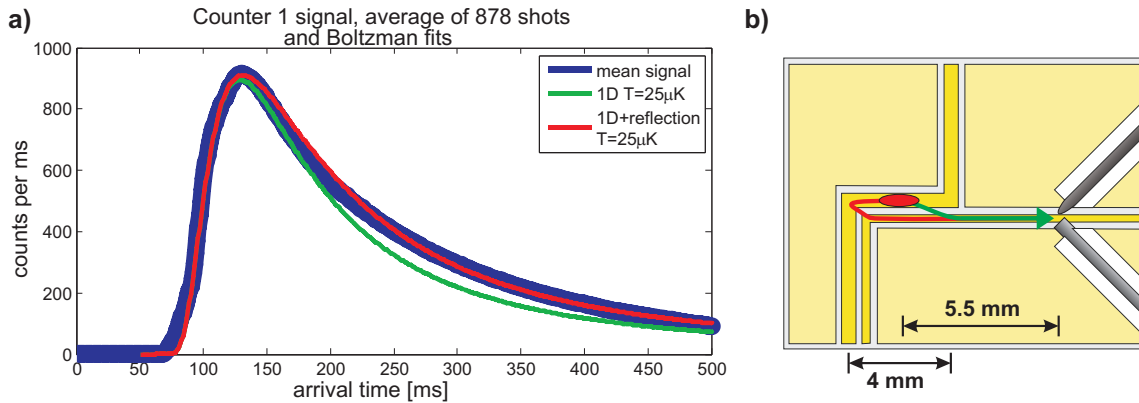


**Figure 5.2.:** Transit signal as recorded in a single counter.

a) The signal (blue) is the 1 ms binned average of 878 consecutive shots at identical parameters. The line thickness indicates the standard deviation. At  $t = 50$  ms the Z-trap is opened in 25 ms and releases the atoms into the guide. The peak of the atom pulse passes the detector at  $t = 135$  ms.

A 1D Boltzmann distribution (green) delivers a reasonably good fit to the data at a temperature of  $25 \mu\text{K}$ , but underestimates the measured distribution for arrival times between 200 and 500 ms. Taking reflections of the trapped cloud at the closed end of the guide into account a good fit is achieved (red line) at identical temperature. The remaining deviation for arrival times smaller than 100 ms is due to the non-instantaneous opening of the Z-trap.

b) Schematic view of the chip illustrating the direct path to the detector (green) assumed in the simple 1D fit (green) in a) and a path including reflection at the closed end of the guide (red) which is taken into account for the red line in a).

### 5.1.3. Transit Signal

Figure 5.2 shows a typical transit signal recorded by the fluorescence detector. The atoms are transferred from the Z-trap into the guide leading to the fluorescence detector at  $t = 50$  ms. The peak of the atom pulse passes the detector 85 ms later, corresponding to a velocity of  $65 \text{ mm/s}$ . Peak signal strength is  $916 \text{ counts per ms}$  with a total number of  $178500 \pm 5000 \text{ counts per shot}$ . The temperature of the atoms in the Z-trap has been measured with time of flight techniques to be  $25 \pm 2 \mu\text{K}$  transversal and  $31 \pm 5 \mu\text{K}$  longitudinal.

Since the Z-trap is very elongated the atoms should thermalize according to a 1D Boltzmann distribution. As can be seen from figure 5.2 the 1D model fits the measured distribution quite well. The temperature resulting from the 1D-fit is  $25 \pm 1 \mu\text{K}$ .

Notable deviations of the fit exist at the very beginning of the rising slope and on the lower part of the falling slope. The deviation in the region  $t = 50 \text{ ms}$  to  $t = 90 \text{ ms}$  can be understood as an effect of the atom release into the guide. The Z-trap is not switched off abruptly as assumed for the fit, but instead ramped down in 25 ms, slowly transferring the atoms into the guide.

The deviation between 200 and 500 ms arrival time is explained by reflection of the

<sup>2</sup>Dataset 20071205Wed\_F3\_resonant\_guide2\_05V, 878 shots of 2s each.

atoms on the closed part of the guide. As discussed in chapter 2 the guide potential allows expansion towards the detector, but presents a barrier in the opposite direction. Atoms with velocity directed away from the detector at release of the Z-trap will be reflected on that barrier and arrive at the detector with a delay given by the size of the Z-trap. Figure 5.2b) gives a schematic view of the paths.

A simple model considering the contribution of the reflected part of the cloud as an additional Boltzman distributed ensemble of identical temperature, but longer distance  $d$  from the detector yields a very good fit to the measured distribution as demonstrated in figure 5.2a). The additional distance travelled corresponds to the extension of the Z-trap. A full model would require treating the atom cloud as an extended object and calculating reflected contributions for all parts of the cloud.

To present the noise level on a single measurement a single shot atom transit is shown in figure 5.3. Fitting the same 1D+reflection Boltzman model to the single shot yields a temperatures of  $T_{1D} = 25 \mu\text{K}$ , agreeing with the previous results. The fitfunction reproduces the shape of the single shot signal always within errors.

Several other measurements<sup>3</sup> performed under similar conditions confirm both the structure of the signal and the temperatures measured. Temperature is always within  $20 - 30 \mu\text{K}$ .

#### 5.1.4. Optimal Detuning

To estimate the optimal detuning of the probe beam acceleration due to light pressure has to be taken into account [59].

For each fluorescence photon emitted one photon has to be absorbed from the probe beam. Since the atoms are illuminated only from one side this leads to a net transfer of momentum. With each absorption the atom velocity changes by an amount given by the recoil velocity  $v_{\text{rec}} = \hbar k/m_{\text{Rb}}$  [44]. The probe detuning  $\delta(t)$  and total photon scattering rate  $\gamma(\delta(t), I)$  from section 3.1.1 have to be adapted for the time-dependent

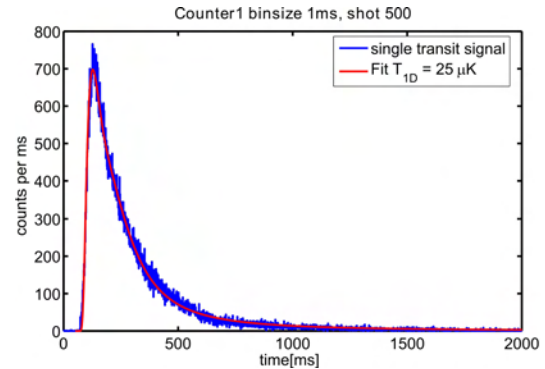


**Figure 5.3.:** Single shot atom transit signal randomly selected (shot nr. 500) from the dataset presented in fig. 5.2. The 1D fit including reflection fits within errors.

<sup>3</sup>e.g. Datasets 20071204Tue\_F3\_resonant\_guide2\_05V, 20071203Mon\_F1\_resonant\_guide2\_05V and 20071205Wed\_F3\_resonant\_guide2\_05V\_429pW.



atom velocity.

$$\gamma(\delta(t), I) = \frac{\Gamma}{2} \frac{I/I_{\text{sat}}}{1 + \left(\frac{2\delta(t)}{\Gamma}\right)^2 + \frac{I}{I_{\text{sat}}}}$$

with  $\delta(t) = \omega - \omega_0 - \vec{k} \cdot \vec{v}(t) + (m'_{F'}g_{F'} - m_F g_F) \frac{\mu_B}{\hbar} B$

Limiting the discussion to the velocity in the direction of the probe beam  $v_{\parallel}(t)$ , the velocity dependent frequency shift becomes

$$\delta_v(t) = \vec{k} \cdot \vec{v}(t) = k \cdot v_{\parallel}(t) = 2\pi/\lambda v_{\parallel}(t)$$

The acceleration due to the probe light field can then be calculated to

$$\frac{d}{dt}v_{\parallel}(t) = v_{\text{rec}} \gamma(\delta(t), I) \quad (5.4)$$

and will continue until the atom is Doppler shifted out of resonance.

The total number  $n_{\text{ph}}^{\text{scat}}$  of photons scattered during the interaction time  $t_{\text{int}}$  per atom is consequently given by integration over the scattering rate.

$$n_{\text{ph}}^{\text{scat}} = \int_0^{t_{\text{int}}} \gamma(\delta(t), I) dt \quad (5.5)$$

Since the scattering rate and the velocity at a certain time  $t$  depend on one another this relation can only be solved numerically.

An evaluation of  $n_{\text{ph}}^{\text{scat}}$  for strong probe beams, 50  $\mu\text{s}$  interaction time and atoms initially at rest ( $v_{\parallel}(0) = 0$ ) yields as optimal probe beam detuning  $\omega_{\text{opt}} = \omega - \omega_0 = 2\pi \cdot 3$  MHz (see fig.5.4). For this detuning the atoms are initially slightly off-resonant and are subsequently accelerated into resonance and beyond, emitting a total of 17500 photons.

Even though the above model completely ignores the effect of the magnetic guide and finite probe beam spot size our measurements with the fluorescence detector confirm an optimal detuning of 3 MHz on the blue side. Figure 5.5 shows the results of a combined probe beam power and probe detuning scan, demonstrating that over a large range of powers around saturation<sup>5</sup> a blue detuning of 3 MHz delivers the maximal signal strength. The effect of the remaining magnetic field in the magnetic guide (approximately 1 G in the minimum of the guide) can be seen from the two measurements with the highest powers presented here. The peak splits up into two separate peaks for high powers, caused by optical pumping between the Zeeman-sublevels. For more information about this feature see Marco Wilzbach's thesis [30].

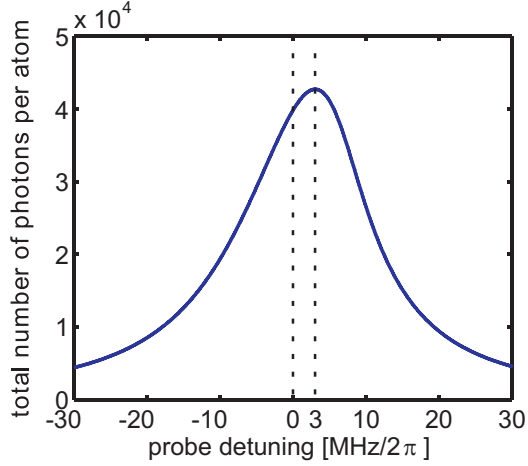


**Figure 5.4.:** Number of photons scattered as a function of probe detuning. An optimal detuning of 3 MHz is predicted.

<sup>4</sup>Dataset 20071201-Imdetscan\_guide2.05

<sup>5</sup>Saturation intensity is reached at a power of 325 pW

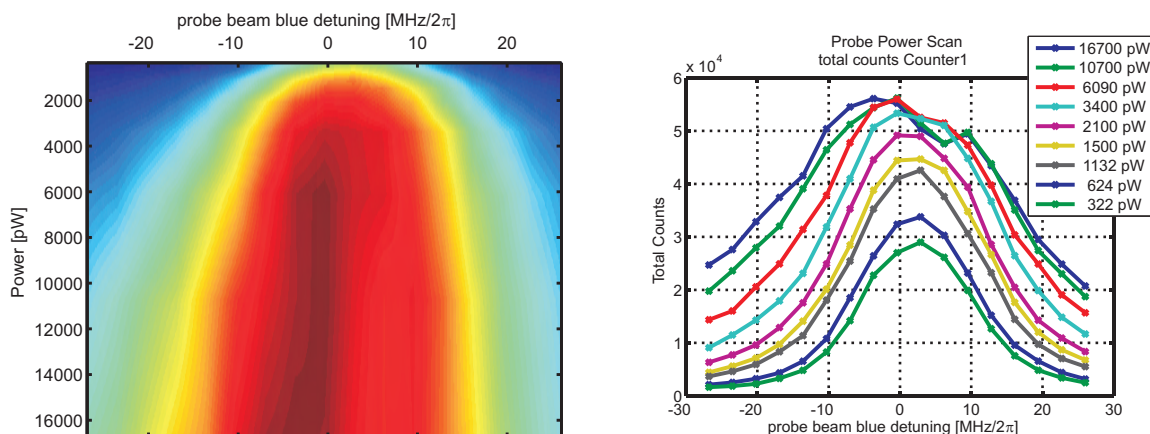


**Figure 5.5.:** Total counts recorded per shot in counter 1 in a 2D scan of probe beam power versus probe beam detuning<sup>4</sup>. An optimal detuning of 3 MHz blue is confirmed for powers in the range of 1 nW (saturation intensity is reached at 325 pW). The right graph shows the detuning scans for each power separately. The dips around resonance for the two highest powers are due to optical pumping effects.

## 5.2. Background Level

Efficient suppression of background is essential for fluorescence detection. As discussed in chapter 3 it is essentially the background level that limits the sensitivity of a fluorescence detector.

### 5.2.1. Sources

Background counts in our detector are either caused by background light or by photon detector effects. The latter have been discussed in chapter 4 and of those only the darkcount rate delivers a significant contribution to the total count rate for low light levels.

Background light can have a variety of sources as listed in table 5.2. Obviously room light and similar ambient light sources<sup>6</sup> in the lab are major sources. Fortunately the experiment can be very well shielded against sources outside of the vacuum chamber by simple means.

Sources inside the vacuum chamber are more critical. Here the hot vacuum gauge emits

Background Light Sources	
TSP	$\gg 15 \cdot 10^6$ cps
MOT beams	$\gg 15 \cdot 10^6$ cps
vacuum gauge	$0.24 \cdot 10^5$ cps
ambient light	4800 cps
<sup>87</sup> Rb-dispensers	3000 cps
probe beam	30 cps/nW

**Table 5.2.:** Background contributions, if left unshielded, listed by source

<sup>6</sup>Such as LEDs of electronic equipment, computer monitors, displays, etc.

black body radiation, as do the  $^{87}\text{Rb}$ -dispensers and of course the titan sublimation pump (TSP) during sublimations. Finally the laser beams used for the experiment might scatter light into the detection fibre and create background counts. While the setup has been designed such that scattered light from the probe beam emitted by the tapered lensed fibre is very efficiently suppressed, the MOT beams cannot be prevented from entering the fibre. The chip with all its reflective surfaces is illuminated with approximately 300 mW of trapping light during the MOT phase leading to a significant amount of photons being collected.

### 5.2.2. Reduction Strategies

Fortunately the major background sources can be removed quite easily. The titan sublimation pump is actually usually turned off. It was included in the above list to stress the fact that it absolutely has to be off when using the photon counters, otherwise the SPCMs will be destroyed.

Since the same holds true for the MOT lasers the SPCMs are operated in gated mode, ramping the bias voltage above breakdown only when the MOT beams are already shuttered. Nonetheless scattered light from the MOT beams has to be shielded as well. To achieve this, several stages of metal and cloth separation walls are introduced between the laser shutters and the vacuum chamber reducing stray light in the detector to non-measurable values.

The vacuum gauge can as well simply be turned off. Ambient light was suppressed by surrounding the optical table from all six sides by optically dense materials.

**Pulsed Dispensers** To reduce the contribution from the dispensers pulsed operation can be considered. Due to the high temperature during operation the dispensers need either a long time or active cooling to reduce their emission significantly since for pulsed operation their current has to be increased significantly to reach the same background pressure as in continuous operation. To reach a 10 % reduction of the dispenser contribution to the background by pulsed operation a cooldown time of 2 s in a 20 s experimental cycle has been necessary.

Since the background in the current setup is dominated by the dark count contribution from the single photon counting module (see table 5.3) we abstained from pulsing the dispensers.

**Optical Bandpass** To further reduce background light contributions we use an optical bandpass interference filter<sup>7</sup> with 99.5899 % transmission at 780 nm and 3 nm bandwidth (FWHM)[43], as described in section 2.5. The effect of the filter and the remaining background signal is summarized in table 5.3.

---

<sup>7</sup>Semrock LL01-780 MaxLine laser line filter

**Table 5.3.:** Background Contributions with and without interference filter

<i>source</i>	<i>without filter</i>	<i>with filter</i>
ambient light	4800 cps	0 cps
<sup>87</sup> Rb-dispensers	3000 cps	36 cps
probe beam	30 cps/nW	30 cps/nW
total background at 1 nW		66 cps

Use of the interference filter setup allows continuous operation of the dispensers as well as normal lab operation including monitors and room light without influence on the measurements.

### 5.2.3. Total Background

The total background rate  $bg$  for a typical measurement with a single counter is given by the sum of the above background light contribution and the dark counts of the detector  $bg = (66 + 245) \text{ cps} = 311 \text{ cps}$ .

During the approximately  $t = 20 \text{ }\mu\text{s}$  interaction time of the atoms with the probe field in the fluorescence detector the atoms should scatter  $t \cdot \Gamma/4 = 190$  photons at saturation under ideal conditions. With the total photon detection efficiency of 0.9 % from section 2.5 and an additional factor 1/2 due to the geometry (see chapter 3) this leads to an expected mean atomic signal of 0.85 counts per 20  $\mu\text{s}$ . The measured background rate is, with  $6.2 \cdot 10^{-2}$  counts per 20  $\mu\text{s}$ , significantly smaller leading us to expect a favourable signal to noise ratio.

In order to estimate the effect of background on the statistical distribution of counts the distribution of the background counts needs to be known. The counting statistics of all above background sources have been measured to be in good approximation Poissonian.

A Fourier transform of the recorded counts was used to verify that measurement system is free from period noise.<sup>8</sup>

### Reduced Background

For possible extensions of the measurements presented here it is important to stress that this setup can be upgraded to a total background of less than 91 cps simply by

<sup>8</sup>Since the counts are recorded in a PCI computer card the network connection of this computer is prone to introduce ground loops into the setup. To eliminate these oscillations the counter computer was built into the experimental setup and connected to the analysis and experiment control computers via WLAN.

replacing the SPCM with a more costly module of the same series. In this regime it will become interesting to eliminate the dispenser contribution to background by pulsed operation or by replacing the atom source, e.g. by LIAD methods [76–79], reducing the background to below 55 cps.

#### 5.2.4. Suppression of Scattered Light

The suppression of stray light from the probe beam emitted by the tapered lensed fibre was estimated by measuring the background count rate as a function of the probe beam power. Accounting for the dark count rate of 245 cps we record 30 cps per nanowatt of probe beam light. Correcting for the finite filter gap transmission (84 % since this measurement was performed in the two counter setup) and the SPCM detection efficiency of  $\eta_{\text{SPCM}} = 56.4\%$  this corresponds to 63 photons collected by the MM fibre per nW of excitation light. Hence the geometrical suppression of the probe light can be estimated to approximately  $10^{-8}$ .

In summary, with ambient light eliminated as a background source, stray light from the probe beam suppressed by  $10^{-8}$  and only a small contribution from the dispensers, the background of our detector is now dominated by the dark count rate of the SPCM.

The achieved background count rate of 311 cps translates into a mean distance between background counts of 3.2 ms. In chapter 3 the importance of background suppression for fluorescence detection has been pointed out. In chapter 8 I will show that besides many other interesting measurements, the currently achieved background count rate allows us to measure non-classical correlations between photons emitted from a single atom.



## 6. Variance Analysis

In this chapter I will introduce a statistical analysis of the atom transit signals based on the ratio of variance over mean of a series of measurements, where variance and mean are taken over the consecutive measurements for a fixed arrival time.

This ensemble averaging method allows retrieving the number of atoms, signal strength per atom and interaction time of the atoms with the probe field from a shot-to-shot analysis of a series of measurements taken under identical parameters.

As a check of the results of the statistical methods I will first derive the signal strength per atom via an independent method.

### 6.1. Atom Number

The atomic density in the detection region and the number of atoms in the guide are important parameters for our experiments. The total number of atoms in the guide can be determined by:

1. standard absorption and fluorescence imaging employing external cameras,
2. measuring the total number of counts generated when probing the cloud on the  $5^2S_{1/2}|F = 2\rangle \rightarrow 5^2P_{3/2}|F' = 1\rangle$  transition or
3. by statistical analysis of the ensemble variations in a series of measurements.

In our analysis of the measurements performed in Heidelberg we have demonstrated the equivalence of these methods for our setup [30].

#### 6.1.1. Absorption & Fluorescence Imaging

External absorption and fluorescence time of flight imaging is the standard method to observe ultra-cold atomic clouds in magnetic microtraps [35, 36]. Here an imaging probe beam is sent into the vacuum chamber at a small angle (typically  $8^\circ$ ) to the chip surface. One CCD Camera on the opposite side of the chamber measures the transmitted beam for absorption imaging. A second camera is mounted orthogonal to the plane of the chip, at  $90^\circ$  to the probe beam, to collect a fraction of the fluorescent light emitted by the atoms (see figure 6.1).

Using time of flight measurements the atom number at the end of the Z-trapping phase, right before transfer into the 1D-guide, has been estimated to  $(2.0 \pm 0.2) \cdot 10^6$  atoms.<sup>1</sup> Of these  $2 \cdot 10^6$  atoms approximately 60 % are transferred into the guide.

### 6.1.2. The $F' = 1$ Transition

Standard imaging is not well suited to measure the atom number in the 1D guide. Rapid spreading of the cloud along the guide leads to low densities over a large area, making time of flight atom number measurements rather unreliable. Indeed it turns out that the integrated fluorescence detector is a superior tool, even for such a relatively simple task. Its advantages are the highly selective detection region and its integration, giving it the possibility to measure unobstructed in-situ.

If the total number  $m$  of photons emitted per atom and the photon detection efficiency  $\eta_{\text{ph}}$  are known, then the number of atoms  $n_{\text{at}}$  in the detection region can be calculated from the total number of counts  $n_{\text{cts}}$ .

$$n_{\text{at}} = \frac{n_{\text{cts}}}{m \cdot \eta_{\text{ph}}} \quad (6.1)$$

The photon detection efficiency is known from the numerical aperture of the collection fibre and measured transmission losses to be  $\eta_{\text{ph}} = 0.909 \%$  (see section 2.5). In order to exploit the above relation for atom number estimation a transition is needed where the number of photons emitted per atom is known, preferably independent of interaction time. Ideally, an atom should be excited absorbing one photon from the probe beam, re-emit a single photon and subsequently be removed from the detection cycle to minimize effects of interaction time on the signal strength.

### Number of Photons per Atom

$^{87}\text{Rb}$  offers with the  $5^2\text{S}_{1/2}|F = 2\rangle \rightarrow 5^2\text{P}_{3/2}|F' = 1\rangle$  transition depicted in figure 6.2 an ideal candidate for the above described procedure. An atom excited to the  $F' = 1$  level can relax to the  $F = 1$  or  $F = 2$  ground state. Although there are three transitions back to the  $F = 2$  level, they are much weaker than the two strong transitions to the  $F = 1$  level. Once the atom enters the  $F = 1$  ground-state the probe laser will not be able to excite it any more due to a hyperfine-splitting of 6.8 GHz between the  $F = 2$  and  $F = 1$  ground-states. For each of the magnetic sublevels of the  $F' = 1$  state the sum of the relative strengths of the transitions to  $F = 1$  is  $2 \cdot 25$  while the sum of the

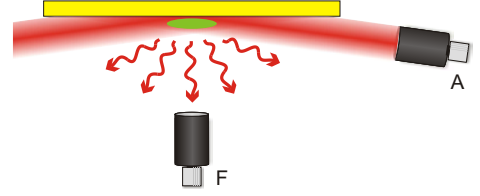


**Figure 6.1.:** Standard Imaging

The atom cloud (green) is illuminated by a probe beam that hits the chip under a small angle ( $8^\circ$ ). Camera A detects the transmitted beam for absorption imaging, while camera F is oriented at  $90^\circ$  to the beam to collect the fluorescence light from the atoms.

<sup>1</sup>Dataset 20071203Mon\_endofZ\_fluo



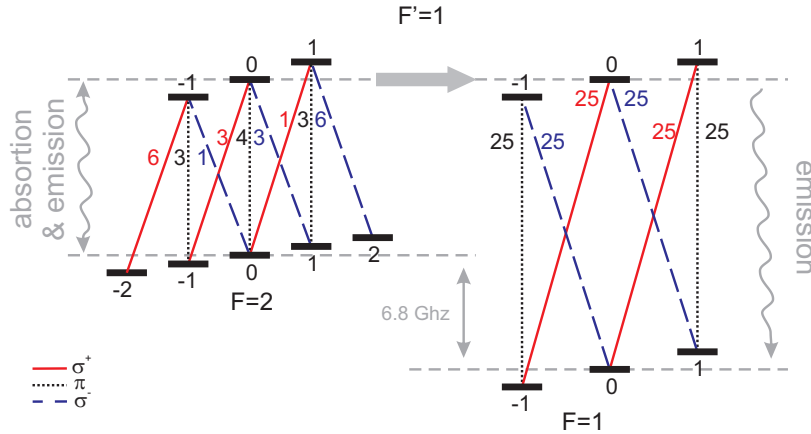


**Figure 6.2.:** Energy Levels and Transition Strengths of the  $F = 2 \rightarrow F' = 1$  Transition

The magnetically trapped atoms in the  $F = 2$  level are excited by the probe beam into the  $F' = 1$  level from which they can decay back into  $F = 2$  (left diagram) or into  $F = 1$  (right diagram). The two hyperfine states are separated by 6.8 GHz, thus a re-excitation from the  $F = 1$  level is highly unlikely.

The relative transition strengths indicated beside the transitions have been derived from the corresponding values in [44].

transition strengths to  $F = 2$  is 10. Hence for each excitation the chance to fall back to  $F = 2$  and emit more than one photon is  $p = 1/6$ . The mean number  $m$  of photons per atom is then given by the expectation value.

$$m = \sum_{n=1}^{\infty} n \cdot p^{n-1} = \frac{1}{p} \sum_{n=1}^{\infty} n \cdot p^n$$

$$\text{with } \sum_{n=1}^{\infty} n \cdot p^n = \frac{p}{(1-p)^2}, \quad \forall |p| < 1 \quad (\text{first derivative of the geometrical series})$$

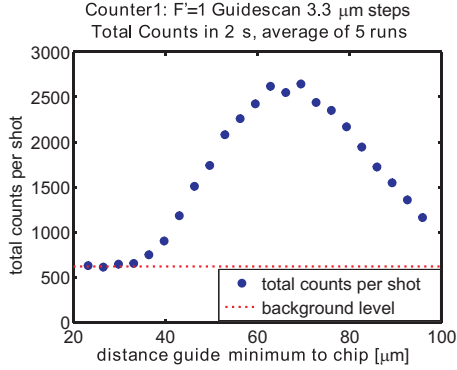
$$m = \frac{1}{(1-p)^2}$$

$$m = 1.44 \text{ photons/atom} \quad (6.2)$$

## Total Number of Atoms in the Guide

The detector was designed to selectively probe an only 5  $\mu\text{m}$  wide region in the guide. If the guide potential is shifted relative to the excitation fibre different slices through the guide can be probed. A full picture of the atom distribution in the guide is achieved by collecting a series of measurements during which the guide current is increased from shot to shot, shifting the minimum of the guide away from the chip surface (see sections 10.3 and chapter 10 for details).

<sup>2</sup>Dataset 20071203\_Guidescans\F1\



distance to chip	total counts in 2s
23.2 $\mu\text{m}$	630
62.5 $\mu\text{m}$	2610
96.0 $\mu\text{m}$	1160

**Figure 6.3.:** Guidescan of the  $F' = 1$  transition in 3.3  $\mu\text{m}$  steps.<sup>2</sup>

A scan of the distance between guide minimum and chip surface from 23.2  $\mu\text{m}$  to 96  $\mu\text{m}$  in steps of 3.3  $\mu\text{m}$  (see figure 6.3) shows the extension of the atomic ensemble in the guide. For most measurements presented here we chose to probe the guide in its potential minimum, corresponding to a distance of 62.5  $\mu\text{m}$  between guide minimum and chip surface. Atoms in the minimum of the guide potential populate the lowest energy mode of the guide and should correspondingly represent the coolest part of the ensemble. The total number of atoms  $n_{\text{at}}$  in the probed mode of the guide can be estimated from the background corrected total number of  $n_{\text{cts}} = 2013 \pm 100$  counts in 2 s. Using equation 6.1 together with the above derived  $m = 1.44$  photons/atom emitted on the  $F' = 1$  transition we can estimate the total number of atoms in the probed mode of the guide to be

$$n_{\text{at}} \approx 1.54 \pm 0.07 \cdot 10^5 \text{ atoms}$$

### Number of Photons per Atom on the $F' = 3$ transition

In the last section I have demonstrated the use of equation 6.1 to calculate the number of atoms in the probed mode of the guide using a transition where  $m$ , the mean number of photons per atom, is known. Obviously this relation can be inverted to retrieve  $m$  for any transition from a measurement where the number of atoms  $n_{\text{at}}$  is known.

Even knowledge of the atom number is not necessary if a comparison measurement at the same atom number on a transition with known  $m$  is available. This I will use here to derive  $m_{\text{F3}}$  the number of photons per atom emitted when probing on the  $F' = 3$  transition. The ratio of the number of counts generated by probing on the  $F' = 3$  and  $F' = 1$  transitions yields directly the ratio of number of photons per atom.

$$\begin{aligned} \frac{n_{\text{ctsF3}}}{n_{\text{ctsF1}}} &= \frac{n_{\text{at}} \cdot m_{\text{F3}} \cdot \eta_{\text{ph}}}{n_{\text{at}} \cdot m_{\text{F1}} \cdot \eta_{\text{ph}}} \\ m_{\text{F3}} &= \frac{n_{\text{ctsF3}}}{n_{\text{ctsF1}}} \cdot m_{\text{F1}} \end{aligned} \quad (6.3)$$

Using  $m_{F1} = 1.44$  as derived above with a background corrected value of  $n_{\text{cts}F1} = 2013 \pm 100$  total counts in 2 s and an identical measurement<sup>3</sup> on  $F' = 3$  that yields a background corrected value of  $n_{\text{cts}F3} = (1.70 \pm 0.06) \cdot 10^5$  total counts in 2 s we receive

$$m_{F3} = 122 \pm 4 \text{ photons}$$

during the interaction time. Under ideal conditions we would expect 120 photons after an interaction time of 25  $\mu\text{s}$  if illuminated with saturation intensity under 45°.

### Number of Counts per Atom

Using in addition the known photon detection efficiency of  $\eta_{\text{ph}} = 0.909 \%$  we can derive  $\alpha_{F3}$  the number of counts per atom generated under illumination on the  $F' = 3$  transition. The atomic signal strength  $\alpha$  is probably the central parameter of the detector, characterizing its sensitivity.

$$\alpha_{F3} = m_{F3} \cdot \eta_{\text{ph}}$$

$$\alpha_{F3} = 1.10 \pm 0.04 \text{ counts/atom}$$

---

<sup>3</sup>Dataset 20071203\_Guidescans\F3



### Moment Generating Function

In order to calculate the variance and mean for a given probability distribution  $p(n)$  it is often the easiest approach to use moment generating functions  $G(x)$  which give the  $k$ -th moment of  $p(n)$  as their  $k$ -th derivative evaluated at  $x = 0$  [81].

$$\langle n^k \rangle = \left. \frac{d^k G(x)}{dx^k} \right|_{x=0} \quad (6.7)$$

This is achieved by defining  $G(x)$  as the Laplace transform of  $p(n)$ . In a Laplace transform the probability distribution is convoluted with the exponential function  $e^{xn}$ . Now the Taylor expansion of the exponential function takes care of sorting out the  $k$ -th moment in the  $k$ -th derivative.

$$\begin{aligned} G(x) &= \sum_{n=0}^{\infty} p(n) e^{xn} \\ &= \sum_{n=0}^{\infty} \left( \sum_{s=0}^{\infty} \frac{(xn)^s}{s!} \right) p(n) \\ &= \sum_{n=0}^{\infty} \left( 1 + xn + \frac{x^2 n^2}{2} + \frac{x^3 n^3}{3!} + \dots \right) p(n) \\ &= 1 + x \langle n \rangle + \frac{x^2}{2} \langle n^2 \rangle + \frac{x^3}{3!} \langle n^3 \rangle + \dots \end{aligned} \quad (6.8)$$

If the variable  $Y = X + Z$  is the sum of independent random variables, the moment generating function of  $Y$  is given by the product of the moment generating functions of  $X$  and  $Z$  [81].

The moment generating function of the atom count distribution can be calculated using equations 6.6 and 6.8.

$$\begin{aligned} G(x) &= \sum_{n=0}^{\infty} p_{\text{cts,at}}(n) e^{xn} \\ &= \sum_{n=0}^{\infty} \left( \sum_{a=0}^{\infty} p_{\text{at}}(a, \langle n_{\text{at}} \rangle) \cdot \frac{(n_{\text{at}} \cdot \alpha)^n}{n!} e^{-n_{\text{at}} \cdot \alpha} \right) e^{xn} \\ &= \sum_{a=0}^{\infty} p_{\text{at}}(a, \langle n_{\text{at}} \rangle) e^{-n_{\text{at}} \cdot \alpha} \sum_{n=0}^{\infty} \frac{(n_{\text{at}} \cdot \alpha \cdot e^x)^n}{n!} \\ G(x) &= \sum_{a=0}^{\infty} p_{\text{at}}(a, \langle n_{\text{at}} \rangle) e^{n_{\text{at}} \cdot \alpha \cdot (e^x - 1)} \end{aligned} \quad (6.9)$$

### Variance and Mean

From the moment generating function defined in equation 6.9 the mean can be calculated as the first derivative evaluated at  $x = 0$ .

$$\begin{aligned}\langle n \rangle &= \left. \frac{dG(x)}{dx} \right|_{x=0} \\ &= \sum_{a=0}^{\infty} p_{\text{at}}(a, \langle n_{\text{at}} \rangle) n_{\text{at}} \alpha \\ \langle n \rangle &= \alpha \langle n_{\text{at}} \rangle\end{aligned}\tag{6.10}$$

Likewise the second moment is given by the second derivative and can be calculated to

$$\langle n^2 \rangle = \alpha^2 \langle n_{\text{at}}^2 \rangle + \alpha \langle n_{\text{at}} \rangle\tag{6.11}$$

Hence the ratio of the variance of the counts over their mean value is given by the following simple expression, regardless of the shape of the atom number distribution.

$$\begin{aligned}\frac{\text{Var}(n)}{\langle n \rangle} &= \frac{\langle n^2 \rangle - \langle n \rangle^2}{\langle n \rangle} \\ &= \frac{\alpha^2 \langle n_{\text{at}}^2 \rangle + \alpha \langle n_{\text{at}} \rangle - \alpha^2 \langle n_{\text{at}} \rangle^2}{\alpha \langle n_{\text{at}} \rangle} \\ &= 1 + \alpha \frac{\langle n_{\text{at}}^2 \rangle - \langle n_{\text{at}} \rangle^2}{\langle n_{\text{at}} \rangle}\end{aligned}$$

In summary, the ratio of the variance of the counts at a certain bin and the corresponding mean in an ensemble average varies from 1 by  $\alpha$ , the signal per atom, times the ratio of variance and mean of the atom number.

$$\boxed{\frac{\text{Var}(n)}{\langle n \rangle} = 1 + \alpha \frac{\text{Var}(n_{\text{at}})}{\langle n_{\text{at}} \rangle}}\tag{6.12}$$

It is worth noting that the above relation is independent of the actual atom number. For a purely Poisson distributed signal, such as the background if no atoms are present, the variance equals the mean (see appendix C) and the ratio  $\text{Var}(n)/\langle n \rangle$  will consequently be 1.

The presence of atoms in the detection region and their statistical distribution determines the deviation of the measured count statistic from the Poissonian case. Assuming a Poissonian atom number distribution, i.e.  $\text{Var}(n_{\text{at}}) = \langle n_{\text{at}} \rangle$ ,  $\alpha$  can be measured as the slope of a variance versus mean plot.

$$\frac{\text{Var}(n)}{\langle n \rangle} = 1 + \alpha \quad (\text{for Poisson distributed atoms})\tag{6.13}$$

Conversely, if  $\alpha$  is known relation 6.12 allows measuring the statistical distribution of the atoms from variance over mean of the counts.

### 6.2.2. Effect of Binning on the Statistics

The counts are recorded and timestamped with a resolution of 1 ns by a multichannel counter card. But for analysis usually a much higher binning, typically several hundred  $\mu$ s is used. Therefore it is important to understand the effect of the binning on the variance and mean.

A binning of  $b$  neighbouring data points decreases the size of a dataset  $X$  from  $N$  to  $N/b$ . The binned dataset  ${}_bX$  can be written in terms of the entries  $X_i$  of the unbinned dataset  $X$ .

$${}_bX = \left\{ \sum_{i=1}^b X_i, \sum_{i=b+1}^{2b} X_i, \dots, \sum_{i=N-b+1}^N X_i \right\}$$

But it is more instructive to view binning as adding  $b$  datasets of size  $N/b$ .

$$\begin{aligned} {}_bX &= (X^{(1)} + X^{(2)} + \dots + X^{(b)}) \\ X^{(1)} &= \{X_1, X_{b+1}, X_{2b+1}, \dots\} \\ X^{(2)} &= \{X_2, X_{b+2}, X_{2b+2}, \dots\} \\ &\vdots \end{aligned}$$

Then variance and mean can be calculated following standard rules for datasets composed of several random variables [81]. Generally the variance of a random variable  $Z = Y + W$  is given by  $\text{Var}(Z) = \text{Var}(Y) + \text{Var}(W) + \text{Covar}(Y, W)$ . The covariance vanishes for independent datasets  $Y$  and  $W$ . The mean of  $Z$  is similarly given by the sum of the means of  $Y$  and  $W$ . Since our counts are assumed to be independent from one another for the timescales considered in this chapter the variance and mean of a binned dataset can be expressed as follows.

$$\begin{aligned} \langle {}_bX \rangle &= \langle X^{(1)} + X^{(2)} + \dots + X^{(b)} \rangle \\ &= \langle X^{(1)} \rangle + \langle X^{(2)} \rangle + \dots + \langle X^{(b)} \rangle \\ \langle {}_bX \rangle &= b \langle X \rangle \end{aligned}$$

$$\begin{aligned} \text{Var}({}_bX) &= \text{Var}(X^{(1)} + X^{(2)} + \dots + X^{(b)}) \\ &= \text{Var}(X^{(1)}) + \text{Var}(X^{(2)}) + \dots + \text{Var}(X^{(b)}) \end{aligned}$$

$$\text{Var}({}_bX) = b \text{Var}(X)$$

Hence for uncorrelated datapoints the ratio of variance over mean remains unchanged for all binnings.

$$\frac{\text{Var}({}_bX)}{\langle {}_bX \rangle} = \frac{\text{Var}(X)}{\langle X \rangle} \quad \forall b$$

**Poisson Distributed Datasets** For Poisson distributed datasets this can be seen even more simply by realizing that a binning of  $b$  neighbouring datapoints changes the mean  $\lambda$  to  ${}_b\lambda = b\lambda$ . It follows then directly from the fundamental properties of the Poisson distribution that  $\langle {}_bX \rangle = b\lambda = b\langle X \rangle$  and  $\text{Var}({}_bX) = b\lambda = b\text{Var}(X)$ .

### 6.2.3. Background Effect

The measured signal is composed of background and atomic counts. The background sources present in our experiment and discussed in chapter 5 have a non-negligible effect on the measured counting statistics. Defining  $p_{\text{bg}}(b)$  as the probability to generate  $b$  background counts the total probability  $p_{\text{cts}}(n)$  to measure  $n$  counts is given by the following relation.

$$p_{\text{cts}}(n) = p_{\text{cts,at}}(n - b) \cdot p_{\text{bg}}(b)$$

The mean and variance of the background can be measured to high precision in background measurements. If we assume background counts  $n_{\text{cts,bg}}$  and atom induced counts  $n_{\text{cts,at}}$  to be independent random variables, then the variance and mean of the resulting total counts are the sums of the contributing variances and means.<sup>4</sup>

$$\begin{aligned} \frac{\text{Var}(n)}{\langle n \rangle} &= \frac{\text{Var}(n_{\text{cts,at}}) + \text{Var}(n_{\text{cts,bg}})}{\langle n_{\text{cts,at}} \rangle + \langle n_{\text{cts,bg}} \rangle} \\ \frac{\text{Var}(n)}{\langle n \rangle} &= \frac{\alpha^2 \text{Var}(n_{\text{at}}) + \alpha \langle n_{\text{at}} \rangle + \text{Var}(n_{\text{cts,bg}})}{\alpha \langle n_{\text{at}} \rangle + \langle n_{\text{cts,bg}} \rangle} \end{aligned} \quad (6.14)$$

If the distribution of the background or the atom counts is known equation 6.14 can be simplified.

**Poissonian Background** The background has been thoroughly tested and found to be in good approximation Poisson distributed (see section 5.2). Assuming a Poisson distributed background with  $\text{Var}(n_{\text{cts,bg}}) = \langle n_{\text{cts,bg}} \rangle$  equation 6.14 is reduced to

$$\frac{\text{Var}(n)}{\langle n \rangle} = 1 + \alpha \frac{\text{Var}(n_{\text{at}})}{\langle n_{\text{at}} \rangle + \langle n_{\text{cts,bg}} \rangle / \alpha} \quad (6.15)$$

<sup>4</sup>Note that this assumption ignores afterpulses which are treated here as second order effects and are neglected.



For a strong signal, i.e.  $\alpha \cdot \langle n_{\text{at}} \rangle \gg \langle n_{\text{cts,bg}} \rangle$  we get

$$\frac{\text{Var}(n)}{\langle n \rangle} \rightarrow 1 + \alpha \frac{\text{Var}(n_{\text{at}})}{\langle n_{\text{at}} \rangle}$$

which is equivalent to equation 6.12 in the limiting case of strong signal.

**Poissonian Atoms** Thermal atoms far from the BEC crossover will populate multiple modes in the magnetic guide and can thus be considered independent from one another. Hence the atom distribution can be approximated by a Poisson distribution as well. Using  $\text{Var}(n_{\text{at}}) = \langle n_{\text{at}} \rangle$  equation 6.14 simplifies to the following relation.

$$\frac{\text{Var}(n)}{\langle n \rangle} = \frac{(1 + \alpha)\alpha \langle n_{\text{at}} \rangle + \text{Var}(n_{\text{cts,bg}})}{\alpha \langle n_{\text{at}} \rangle + \langle n_{\text{cts,bg}} \rangle} \quad (6.16)$$

If additionally the signal is much stronger than the background, i.e.  $\alpha \cdot \langle n_{\text{at}} \rangle \gg \langle n_{\text{cts,bg}} \rangle$ , then background can again be neglected and the simple relation

$$\frac{\text{Var}(n)}{\langle n \rangle} \rightarrow 1 + \alpha$$

holds.

**Background and Atoms Poisson Distributed** Assuming that both the background and the atoms are Poisson distributed equation 6.14 can be written as

$$\boxed{\frac{\text{Var}(n)}{\langle n \rangle} = \frac{(1 + \alpha)\alpha \langle n_{\text{at}} \rangle + \langle n_{\text{cts,bg}} \rangle}{\alpha \langle n_{\text{at}} \rangle + \langle n_{\text{cts,bg}} \rangle}} \quad (6.17)$$

where the equality of variance and mean of Poissonian distributions has been used to simplify the equation.

As motivated above both assumptions are fulfilled in good approximation in the measurements presented in this thesis, hence equation 6.17 will generally be used to estimate  $\alpha$ , the number of counts per atom.

### Measuring $\alpha$

We are finally in a position to understand the full signal generated by the atom pulse passing the fluorescence detector. Figure 6.4 shows the result of a typical measurement for a binning of 200  $\mu\text{s}$ . For the first 50 ms the Z-trap is closed and no atoms are in the guide. The statistical analysis of variance over mean shows only Poissonian background with variance/mean equal to 1. When the first atoms arrive variance/mean suddenly jumps from 1 to a higher value, as predicted by equation 6.17. As the atom density drops the background starts to become relevant and variance/mean is reduced towards later detection times.

<sup>5</sup>Dataset 20071204Tue\_F3\_resonant\_guide2\_05V, 601 shots.

<sup>6</sup>Dataset 20071204Tue\_F3\_resonant\_guide2\_05V, 601 shots.

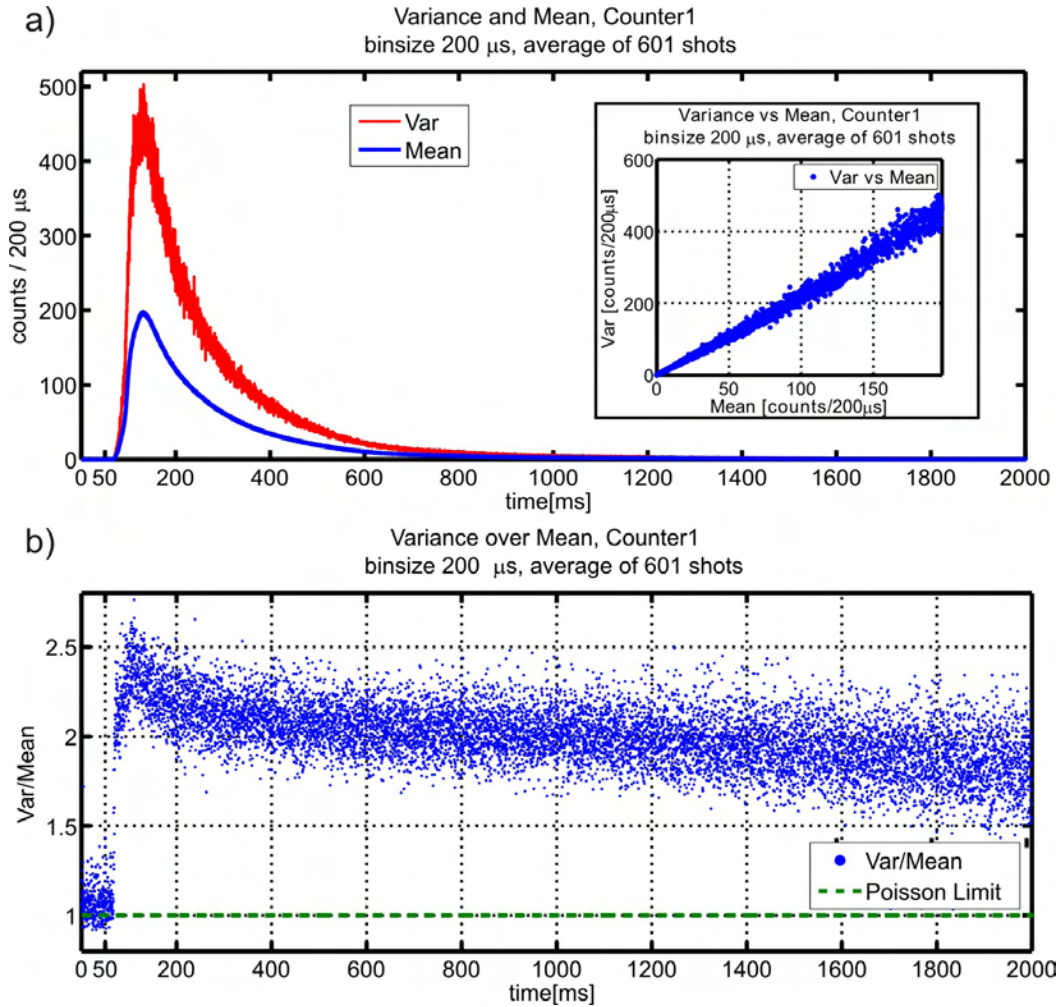


**Figure 6.4.:** Variance and Mean of the Transit Signal

a) Mean (blue) and variance (red) calculated from 601 shots at identical parameters using a binning of 200  $\mu\text{s}$ .<sup>5</sup> The inset shows a plot of the variance as a function of the mean values, indicating a linear relation over the full range.

b) The ratio variance/mean shows a Poissonian background with variance/mean=1 during the first 50 ms when no atoms are present in the detector. When the atoms arrive a sudden jump in variance/mean is observed as predicted. The decrease for lower atomic densities is explained by background contributions.

Note that the initial overshoot in variance/mean for arrival time < 170 ms are analysis artefacts caused by the extreme steepness of the atom transit signal. Very small fluctuations in arrival time of the atoms cause significant changes in atom number from shot to shot in a bin of 200  $\mu\text{s}$  width. This artefact is removed if smaller bin sizes are considered.

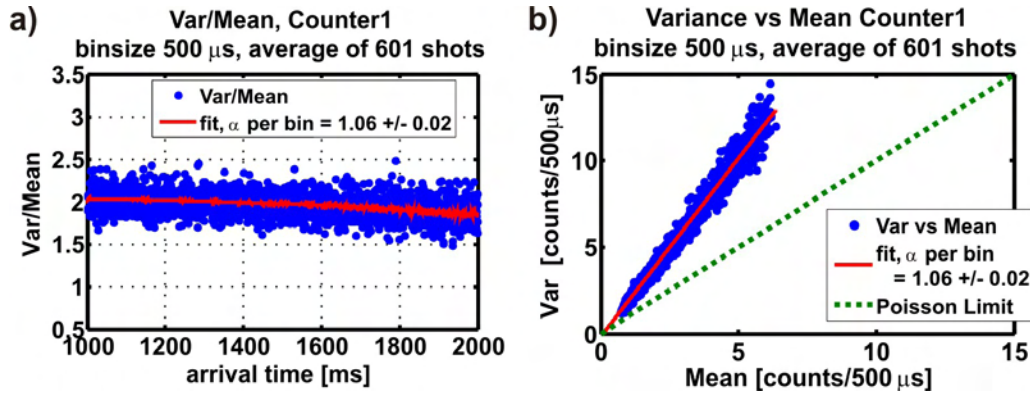


**Figure 6.5.:** Fitting Variance/Mean

a) The ratio variance/mean for 1000 to 2000 ms<sup>6</sup>, showing clearly the drop of variance/mean for low atomic densities. The red curve is the fit derived from b).

b) Variance plotted as a function of the mean values shows a behaviour as predicted by equation 6.17, which is approximately linear. A fit to the measured data yields  $\alpha = 1.06 \pm 0.02$  counts per atom.

**Number of counts per atom** A fit based on equation 6.17 for the time 1000 to 2000 ms presented in figure 6.5 yields a signal strength of  $\alpha = 1.06 \pm 0.02$  counts per atom. An analysis of all available datasets together with the results of section 6.3 leads to a final result of

$$\alpha = 1.08 \pm 0.01 \text{ counts/atom}$$

corresponding to  $119 \pm 1$  photons per atom, which confirms the signal strength estimation of section 6.1.2.

With known signal strength  $\alpha$  the atom density in the guide can be calculate from the mean number of counts per ms.

$$n_{\text{at}} = \frac{n_{\text{cts}}}{\alpha}$$

Figure 6.6 shows the corresponding atom density profile of an atom pulse passing the detector and the mean temporal separation between the atoms as function of the arrival time.

## 6.3. Interaction Time

While binning does not change the statistics of the measured signal the bin size does have an effect on the measurement of  $\alpha$ . The number of photons emitted per atom  $m$  is determined by the fluorescence rate  $\gamma$  (see equation 3.3) and the interaction time  $t_{\text{int}}$  of the atoms with the light field.

$$m = \gamma \cdot t_{\text{int}} \quad \Rightarrow \quad \alpha = \eta_{\text{ph}} \cdot \gamma \cdot t_{\text{int}}$$

<sup>6</sup>Dataset 20071204Tue\_F3\_resonant\_guide2\_05V, 601 shots.

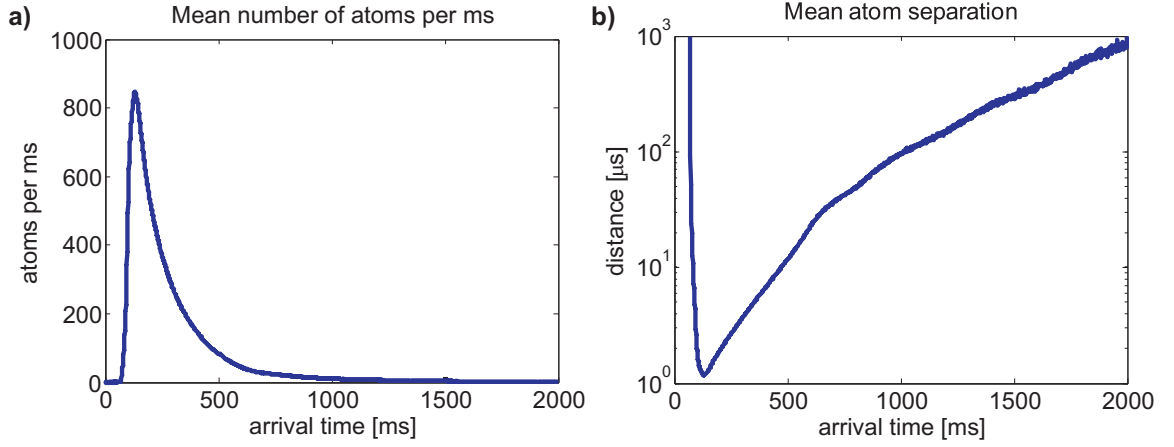


**Figure 6.6.:** Atom Density Profile of an Atom Pulse Passing the Detector

- a) Atom density calculated from the mean number of counts via the measured signal strength  $\alpha = 1.08$ .  
 b) Mean distance between the atoms as function of the arrival time.

The fluorescence rate is given by the probe intensity and detuning, taking into account the  $45^\circ$  geometry (see chapter 3) we expect a rate of  $\Gamma/8 \approx 5$  photons per microsecond per atom at saturation, corresponding to  $\alpha_{\text{theo}} = 0.045$  counts per atom per microsecond.

The interaction time can be limited by either the transit time through the interaction region or loss of atoms, e.g. by heating. The atoms in the peak of the transit pulse arrive at the detection region with a speed of 65 mm/s, while those towards the end of the recorded signal have a longitudinal speed of 2.8 mm/s. This corresponds to 58  $\mu\text{s}$ , respective 1.7 ms spent in the 5  $\mu\text{m}$  wide detection region. Likely the interaction time will be much shorter due to atoms being heated out of the trap or shifted out of resonance by photon recoil induced Doppler shifts.

Obviously, if the bin size  $t_b$  is chosen to be smaller than the interaction time not all counts from a single atom will be collected in the same bin, thus  $\alpha$  will be reduced for small bin sizes. Assuming an exponential decay for the time an atom spends in the detection region with the interaction time  $t_{\text{int}}$  defined as the decay constant we can express  $\alpha$  as a function of the bin size.

$$\alpha(t_b) = \eta_{\text{ph}} \int_0^{t_b} \gamma e^{-t/t_{\text{int}}} dt$$

$$\alpha(t_b) = \eta_{\text{ph}} \gamma t_{\text{int}} (1 - e^{-t_b/t_{\text{int}}}) \quad (6.18)$$

Figure 6.7 shows an evaluation of the number of counts per atom as a function of the bin size to measure the interaction time. The measured decay can be approximated by the exponential shape of equation 6.18 in the region 2 to 25  $\mu\text{s}$ . The simple exponential

<sup>7</sup>Dataset 20071205Wed\_F3\_resonant\_guide2\_05V, 878 shots.

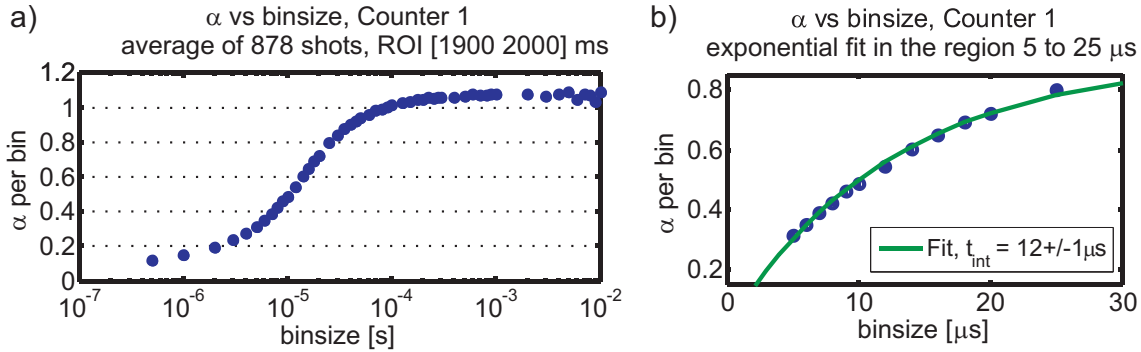


**Figure 6.7.:** Alpha vs Binning

Signal per atom per bin in the region 1900 to 2000 ms after the start of the measurement plotted versus the bin size (a).<sup>7</sup> Fitting an exponential decay to the region 2 to 25  $\mu$ s yields an interaction time of  $12 \pm 1 \mu$ s (b), but a bin size of larger than 300  $\mu$ s is necessary to record the full signal.

model breaks down for very large and very small bin sizes due a time-varying scattering rate caused by photon recoil induced Doppler-shifts. A fit yields a  $1/e$  interaction time of

$$t_{\text{int}} = 12 \pm 1 \mu\text{s}$$

but figure 6.7 demonstrates as well that a bin size of more than 300  $\mu$ s is needed to collect all  $1.08 \pm 0.01$  counts from a single atom. In most applications though it will be advantageous to work at a slightly lower detection efficiency. For example only 45  $\mu$ s are needed to collect already  $\alpha = 0.92$  counts per atom and bin. The trade-off between detection efficiency and collection time will be discussed in section 6.5.

Taking both Doppler shift due to photon recoil and the  $45^\circ$  geometry into account we expect at saturation approximately 62 photons in 12  $\mu$ s interaction time. With the total photon detection efficiency of  $\eta_{\text{ph}} = 0.909 \%$  this leads to an expected signal strength of  $\alpha_{\text{theo}} = 0.56$  counts per atom in 12  $\mu$ s. The measurement depicted in figure 6.7 yields  $\alpha = 0.54 \pm 0.01$  counts per atom and bin for a binsize of 12  $\mu$ s, agreeing with the theoretical prediction.

## 6.4. Examination of Alpha

### 6.4.1. Alpha as Function of Atom Density

To test whether the signal per atom depends on the atomic density the density profile of the atomic pulse was exploited. Since the peak of the atom distribution passes the detector 170 ms after the start of the measurement the atom density in the detection region drops continuously for later arrival times, therefore arrival time can be used as an indicator of atomic density.

Figure 6.8 shows the result of an evaluation of the number of counts per atom and bin for a fixed bin size of 300  $\mu\text{s}$  at various arrival times. An analysis with a bin size of 50  $\mu\text{s}$  reveals that the increase in measured  $\alpha$  in the region 50 to 600 ms cannot be attributed to an atomic density dependence of  $\alpha$  but is indeed caused by the steepness of the transit pulse profile. Here even very small fluctuations in peak arrival time lead to an increase in the variance, distorting the measurement of  $\alpha$  for large bins.

The region 600 to 2000 ms is unaffected by small changes in the arrival time. Between the arrival times of 600 and 2000 ms the atomic density is decreased by a factor of 34 but  $\alpha$  remains constant.

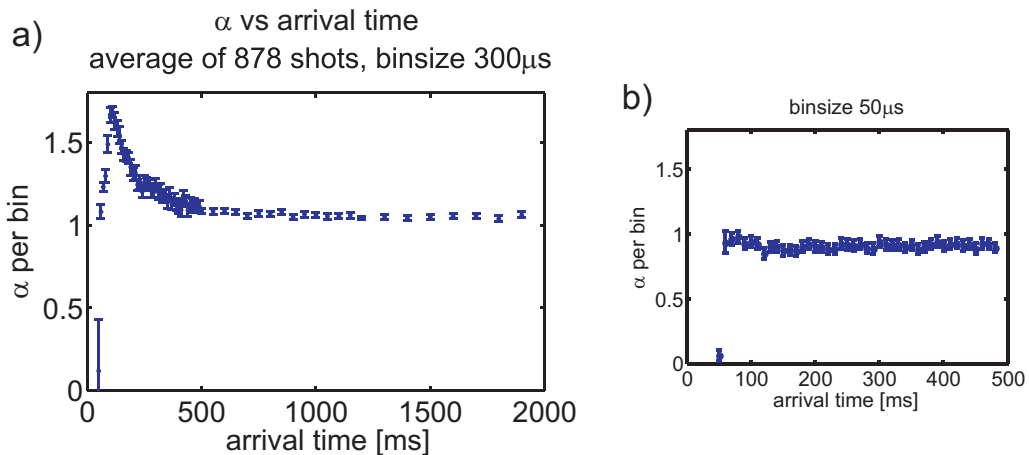


**Figure 6.8.:** Alpha versus arrival time (atom density)<sup>8</sup>

a) Overview of the full signal for 300  $\mu\text{s}$  bins. b) The region 50 to 500 ms with a bin size of 50  $\mu\text{s}$ , demonstrating that the peak for arrival time < 500 ms is due to arrival time fluctuations. Error bars indicate 95% confidence intervals.

<sup>8</sup>Dataset 20071205Wed\_F3\_resonant\_guide2\_05V, 878 shots.

### 6.4.2. Alpha as Function of Guideheight

For all standard measurements the guide is adjusted such that the guide minimum overlaps with the detection region. Under these conditions the coldest atoms which reside in the lowest energy mode of the guide should be observed preferably. Atoms with more transversal energy will reach higher regions in the guide, further away from the chip surface.

To test the effect of transversal energy on the signal strength four different guide heights have been examined as shown in figure 6.9. While changes of up to 10  $\mu\text{m}$  show only a small decrease in  $\alpha$ , a change of 25  $\mu\text{m}$  results in a significantly reduced signal strength  $\alpha$ .

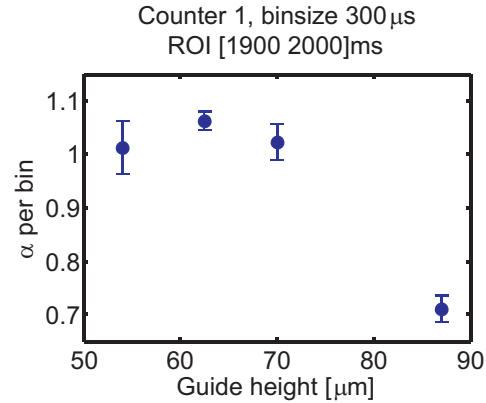


**Figure 6.9.:** Alpha vs Guide Height<sup>9</sup>  
Error bars mark 95% confidence intervals.

The interaction time was measured to be identical for all guide heights. Thus the reduction in signal strength is most likely caused by a detuning induced by the magnetic guiding field. The further the atoms run upwards the potential barrier the more they will feel the Zeeman-detuning, resulting in a reduced signal.

### 6.4.3. Alpha as Function of Probe Detuning

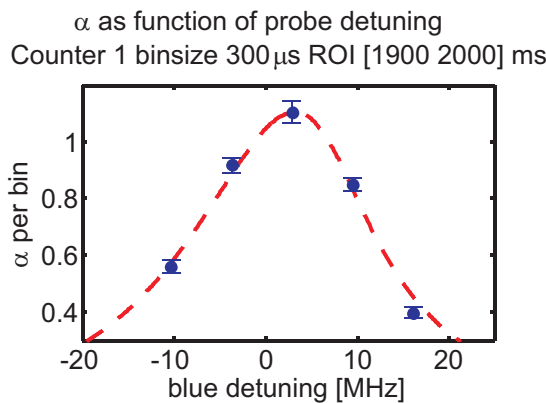


**Figure 6.10.:** Alpha as function of the Probe detuning.<sup>10</sup>  
Error bars mark 95% confidence intervals. The red line is the expected fluorescence rate, scaled to fit to the shown count rate.

As has already been discussed, the maximum signal is retrieved from the atoms if the probe beam is slightly blue detuned to compensate for photon recoil induced Doppler shift. Figure 6.10 confirms the results of section 3.1.1 where an optimal detuning of 3 MHz was derived. Both for red detuned and further blue detuned probe light the

<sup>9</sup>Datasets 20071205Wed\_F3\_resonant\_guide2\_05V, 878 shots  
and 20071205Wed\_Guidescan\_stat, 3 times 200 shots

<sup>10</sup>Dataset 20071203\_FrequencyScan, 878 shots.

signal strength is reduced in accordance with the theoretically expected reduction in total number of fluorescence photons at saturation, taking photon recoil into account, given by the red line.

This supports the assumption of the previous section that Zeeman-detuning is responsible for the reduced signal at larger guide heights.

The interaction times have been measured to be independent of the probe detuning.

#### 6.4.4. Alpha as Function of Magnetic Guiding Field

Magnetic traps can trap only specific Zeeman-substates. To prevent the atoms from performing Majorana-spinflips, i.e. spontaneously changing their magnetic substate, a non-zero guide field has to be present at all times to define a quantization axis. For the magnetic trap configuration used in the experiments presented here this field is usually labelled anti-Ioffe field.

Figure 6.11 shows a measurement for three different anti-Ioffe fields at identical guide-heights. As expected from the previous two sections here again the signal per atom decreases in higher/lower magnetic fields due to the mismatch between probe beam frequency and induced Zeeman-shift.

The remaining measurements presented in this thesis have been carried out at an anti-Ioffe field of 1 G.

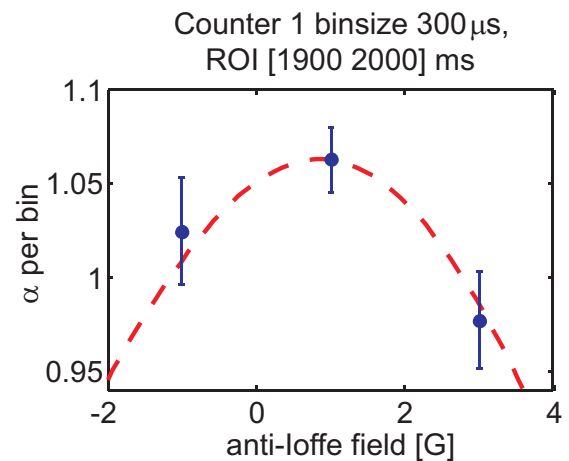


**Figure 6.11.:**  $\alpha$  as function of the magnetic guiding field.<sup>11</sup> Error bars mark 95% confidence intervals. The red line is the expected fluorescence rate, scaled to fit to the shown countrate.

<sup>11</sup>Datasets 20071205Wed\_F3\_resonant\_guide2\_05V, 878 shots; 20071204Tue\_Ioffe1, 364 shots and 20071204Tue\_Ioffe5, 347 shots



## 6.5. Single Atom Detection Efficiency

number of atoms	total counts expected in 300 $\mu\text{s}$	atom detection efficiency	
		$\eta_{\text{at},1}$	$\eta_{\text{at},2}$
0	0.093 (0.016)	8.9 (1.6) %	0.4 (0.01) %
1	$1.08 \pm 0.1$	$66.0 \pm 0.4$ %	$29.4 \pm 0.4$ %
2	$2.16 \pm 0.2$	$88.5 \pm 0.2$ %	$63.6 \pm 0.5$ %
3	$3.24 \pm 0.3$	$96.1 \pm 0.1$ %	$83.4 \pm 0.4$ %
4	$4.32 \pm 0.4$	$98.7 \pm 0.1$ %	$92.9 \pm 0.2$ %
5	$5.40 \pm 0.5$	$99.55 \pm 0.02$ %	$97.1 \pm 0.1$ %

**Table 6.1.:** Overview of the atom detection efficiency

Based on the number of counts per atom expected in 300  $\mu\text{s}$  the atom detection efficiencies for two different detection thresholds are presented. The first line gives the false detection probabilities if no atoms are present (values in brackets are for a reduced background rate of 55 cps). In the following lines the probability to detect the presence of atoms from the signal of a fixed number of atoms is given.

For  $\eta_{\text{at},1}$  the threshold was set to 1 count, leading to a false positive detection probability of 8.9 % due to a background count rate of 311 cps. A threshold of 2 counts in 300  $\mu\text{s}$  leads to a reduction in detection efficiency  $\eta_{\text{at},2}$  (rightmost column) but suppresses the false detection probability to 0.4 %.

To distinguish counts generated by atoms from background counts a detection threshold  $c_{\text{th}}$  has to be defined. If at least  $c_{\text{th}}$  counts are collected in a bin of size  $t_b = 300 \mu\text{s}$  an atom is assumed to be present.

If  $p_{\text{cts,at}}(n)$  denotes the probability to measure a signal of  $n$  counts from the atoms then the atom detection efficiency  $\eta_{\text{at}}$  can be calculated depending on the detection threshold  $c_{\text{th}}$ .

$$\eta_{\text{at}}(c_{\text{th}}) = 1 - \sum_{n=1}^{c_{\text{th}}} p_{\text{cts,at}}(n) \quad (6.19)$$

The counts generated by the atoms under the condition that  $n_{\text{at}}$  atoms are present in the detection region are Poisson distributed according to

$$p_{\text{cts,at}}(n)|_{n_{\text{at}}} = \frac{(n_{\text{at}} \alpha)^n}{n!} e^{-n_{\text{at}} \alpha}$$

For an ideal, background free detector the threshold can be set to  $c_{\text{th}} = 1$ . This choice yields the atom detection efficiencies  $\eta_{\text{at},1}$  listed in table 6.1 according to equation 6.19. A single atom is then detected with an efficiency of

$$\begin{aligned} \eta_{\text{at}} &= 1 - e^{-\alpha} \\ \eta_{\text{at}} &= 66.0 \pm 0.4 \text{ \%} \end{aligned}$$

The efficiency to detect the presence of atoms increases of course with the number of atoms in the detection region, so that five or more atoms are detected almost with certainty ( $> 99.55 \pm 0.02$  %). The presence of a background of 311 counts per second (see chapter 5) leads to a false detection probability of  $p_{\text{false1}} = 8.9$  %, where background counts are identified as atoms.

This number can be reduced to  $p_{\text{false}} = 0.4$  % if a treshold of 2 counts per bin is chosen, albeit at the expense of a reduced atom detection efficiency of  $\eta_{\text{at}} = 29.4 \pm 0.4$  % for the current setup. If the background is minimized to less than 55 cps by pulsing the dispensers and replacing the single photon counting module by a commercially available low noise model then the false detection probabilities reduce to 1.64 (0.01) % for a detection threshold of 1 (2) counts per bin. A projected improvement of the atom detection sensitivity in the next generation of integrated fluorescence detectors is discussed in chapter 13.

**Bit Error Rate** For a binary single atom detector that detects only presence or absence of atoms but does not resolve the number of atoms a bit error rate can be defined as benchmark for its performance [40]. If  $p_{\text{false0}} = e^{-\alpha}$  denotes the probability of failure to detect an atom and  $p_{\text{false1}}$  the probability of false detection in the presence of background, then the bit error rate (BER) can be defined by

$$\text{BER} = \frac{n_{\text{cts,at}}}{n_{\text{cts,at}} + n_{\text{cts,bg}}} p_{\text{false0}} + \frac{n_{\text{cts,bg}}}{n_{\text{cts,at}} + n_{\text{cts,bg}}} p_{\text{false1}} \quad (6.20)$$

where  $n_{\text{cts,bg}} = 311 (55) \cdot t_{\text{int}} = 0.933 (0.016)$  denotes the number of background counts and  $n_{\text{cts,at}}$  the number of counts due to atoms. Obviously the bit error rate depends on the atomic density. For an atom signal strength of  $\alpha = 1.08$  and typical experimental parameters (1 nW probe power) the maximum measured fluorescence count rate was 887579 cps, while a small atom signal, that can still be seen in a single shot, would have 66 cps. With

$$p_{\text{false0}} = 33.6 \text{ \% and } p_{\text{false1}} = 8.9 (1.6) \text{ \%}$$

for the current setup (background reduced setup) the BER rates listed in table 6.2 are achieved.

**Signal to Noise Ratio** For very low atomic densities the BER is dominated by false positive detections due to background counts. In this domain a trade-off between signal to noise ratio (SNR) and detection efficiency becomes possible by using the fact that the instantaneous count rate from atoms is much higher than the background if atoms are present.

The signal to noise ratio for a given detection window (bin size) of width  $t_b$  is given by the ratio of signal strength per bin to the number of background counts per bin  $n_{\text{cts,bg}}$ .

$$\text{SNR} = \frac{\alpha(t_b)}{n_{\text{cts,bg}}} \quad (6.21)$$

Bit Error Rates		
Single Atom Detector		
	$bg = 311$ cps	$bg = 55$ cps
$n_{\text{cts,at}} = 887579$ cps	0.34	0.34
$n_{\text{cts,at}} = 66$ cps	0.13	0.19
5 Atom Detector		
	$bg = 311$ cps	$bg = 55$ cps
$n_{\text{cts,at}} = 887579$ cps	0.005	0.005
$n_{\text{cts,at}} = 66$ cps	0.074	0.010

**Table 6.2.:** Bit Error Rates for typical experimental parameters at 1 nW probe beam power. The first row gives BERs for strong atomic signals, while the second row shows BERs for low atomic densities. In the first column the current experimental setup is shown and in the second column corresponding values for a background reduced setup are given. The first section lists BERs for a single atom detector while the second considers the case of an detectors that distinguished between less than 5 and at least 5 atoms. In both cases the detection threshold was set to 1 count.

The relation between signal strength per atom and bin size has already been shown in figure 6.7. The number of background counts per bin is given by the background rate  $bg = 311$  cps for the current setup or  $bg = 55$  cps for the background reduced setup described above via  $n_{\text{cts,bg}} = bg \cdot t_b$ .

As figure 6.12 demonstrates  $\alpha$  varies much slower with bin size than the number of background counts per bin, making small detection windows attractive for high SNR detection at the expense of detection efficiency. With the current setup a signal to noise ratio of 100 is reached at a detection window of 25  $\mu\text{s}$ , the atom detection efficiency at that point is still 55%. As can be seen from the following table a SNR of 1000 is possible if a background reduced setup is employed.

Signal to Noise Ratio				
SNR	100		1000	
Background	311 cps	55 cps	311 cps	55 cps
$t_b$	25 $\mu\text{s}$	175 $\mu\text{s}$	< 500 ns	7 $\mu\text{s}$
$\alpha$	0.80	1.05		0.39
$\eta_{\text{at},1}$	55 %	65 %		32 %
$p_{\text{false}1}$	0.8 %	1 %		0.03 %

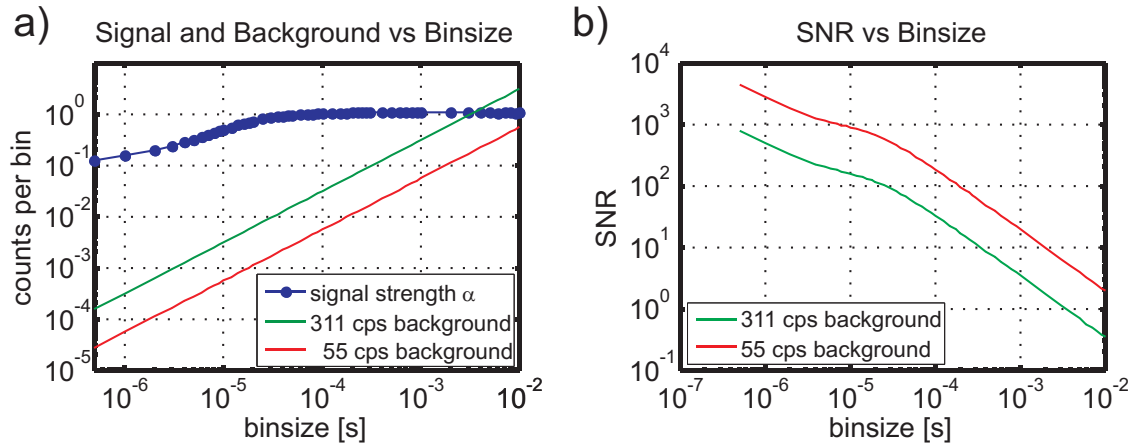


**Figure 6.12.:** Signal to noise ratio as function of the bin size

a) Double-logarithmic plot of the signal strength  $\alpha$  (blue), and background counts per bin (green 311 cps, red 55 cps background rate) versus bin size. Clearly  $\alpha$  always varies much slower with bin size than the number of background counts, even in the region 5 to 100  $\mu$ s where  $\alpha$  increases dramatically.

b) Signal to noise ratio versus bin size for a background rate of 311 cps (green) and 55 cps (red).

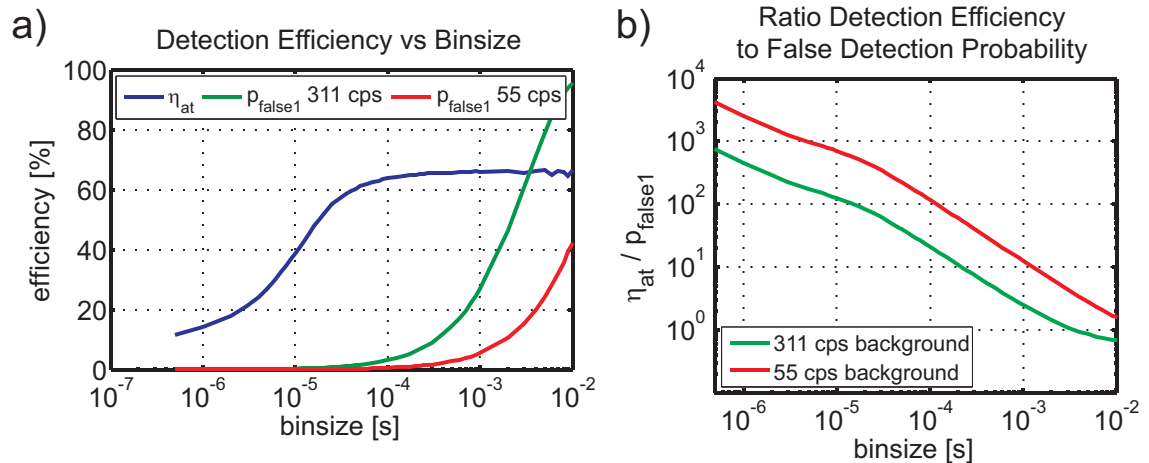


**Figure 6.13.:** Detection Efficiency vs Bin Size

a) The detection efficiency (blue) and false positive detection probabilities for a background rate of 311 cps (green) and 55 cps (red) versus bin size. b) The ratio of detection efficiency to false detection probability reveals that suppression of false positive detections by a factor 100 or even 1000 is achieved at realistic parameters.

Comparing the single atom detection efficiency to the false positive detection probability as function of the detection window demonstrates that operation of the detector at the highest efficiency is undesirable for most applications (see figure 6.13).  $\alpha$  remains almost constant over more than two order of magnitude in bin size, while the number of background counts per bin decreases linearly with bin size. This can be exploited to reach a single atom detection efficiency of 60 % with a false detection probability of only 1.4 (0.2) % for a background of 311 (55) cps instead of a false detection rate of 8.9 % if operated at highest efficiency.

Single Atom Detection				
$\eta_{\text{at},1}$	42 %	50 %	60 %	66.0 %
$t_b$	12 $\mu\text{s}$	20 $\mu\text{s}$	45 $\mu\text{s}$	300 $\mu\text{s}$
$\alpha$	0.55	0.72	0.92	1.08
$p_{\text{false}1}$ 311 cps	0.37 %	0.6 %	1.4 %	8.9 %
$p_{\text{false}1}$ 55 cps	0.07 %	0.1 %	0.2 %	1.6 %

## 6.6. Summary

In this chapter a statistical method was introduced that allows extraction of important parameters of the detector from an analysis of shot to shot variations in the signal.

The signal strength  $\alpha$  per atom was determined to  $\alpha = 1.08 \pm 0.01$  counts per atom, corresponding to  $m = 119 \pm 1$  photons per atom via the statistical approach and confirmed by an independent relative measurement of the signal strength on the  $F' = 1$  and  $F' = 3$  transitions.

The  $1/e$  interaction time could be estimated to  $12 \pm 1 \mu\text{s}$  via the statistical method. It was shown as well that a bin size  $t_b = 300 \mu\text{s}$  is needed to collect the full  $\alpha = 1.08$  counts per atom.

The achieved signal strength in 12  $\mu\text{s}$   $1/e$  interaction time of  $\alpha = 0.54 \pm 0.01$  counts per atom compares favourably to the theoretical expected maximal value of  $\alpha = 0.56$  counts per atom in 12  $\mu\text{s}$ .

The signal strength has been demonstrated to be constant over atomic densities differing by a factor of 34. Guide height and magnetic field influence the signal strength only insofar as they introduce a Zeeman-detuning, reducing the scattering rate.

It has been shown, that the fluorescence detector presented here can be operated as a single atom detector with an atom detection efficiency of  $66.0 \pm 0.4 \%$  at a false negative detection probability (missed atoms) of  $p_{\text{false}0} = 33.6 \%$  and a false positive detection probability of  $p_{\text{false}1} = 8.9 \%$ . The false positive detection rate can be reduced

to 1.6 % by replacing the single photon detection module with a commercially available low noise version and by pulsing the dispensers.

For high SNR atom detection operation at reduced detection efficiency but higher bandwidth and less background is possible with SNR as high as 1000. False positive detection probabilities can be suppressed to e.g. 0.1 % at a single atom detection efficiency of 50 %. This corresponds to 1 false detection in 15 s while detecting single atoms with 50 % efficiency at 50 kHz bandwidth.

If the statistical distribution of the atoms is known the variance analysis method can be used to measure the signal strength  $\alpha$  from the measurements as demonstrated here. Conversely, if  $\alpha$  is known the method presented here can be used to extract the ratio variance over mean of the atom number distribution from a series of measurements. This allows to distinguish unambiguously between independent atom distributions such as thermal atoms populating multiple modes of the guide which follow a Poisson distribution, and condensed atoms, such as BECs, following a Bose distribution. Even differentiating between Bose-Einstein condensed atoms [82] and 1D condensates (Tonks-Girardeau Gases, following Fermi statistics) [83] seems possible.

*"A physicist is just an atom's way of looking at itself."*

Niels Bohr

# 7. Time Interval Analysis

Time interval analysis (TIA) examines the temporal distances between neighbouring events to draw conclusion on the statistical distribution of the atoms. In contrast to the variance over mean analysis presented in chapter 6 TIA does not require a series of measurements, but extracts statistical information from a single measurement.

## 7.1. TIA Basics

The photon detection setup delivers an array of counts per time bin.

Bin	1	2	3	4	5	6	7	8	9	...
Counts	0	1	0	0	1	1	0	2	0	...

### 7.1.1. Probability Distribution of Distances

TIA uses the fact that the probability  $p_0$  to have no counts in a time bin of size  $t_b$  is well known for most probability distributions. We denote the probability to generate  $n$  counts in a certain bin as  $p(n)$ . In the following we will assume that we analyse counts generated by a photon source of constant intensity emitting independent photons, so that  $p_0 = p(0)$  is constant.

Note that the distribution of the recorded counts is equivalent to the distribution of the photons, even if recorded by a photon detector with limited photon detection efficiency  $\eta_{\text{ph}}$  [40].

For each event we count the number of empty time bins to the next event to create a histogram of distances  $d$  between neighbouring events. If the dataset considered is sufficiently large, the histogram can be normalized by the total number of distances to deliver the probability distribution  $p_{\text{dist}}(d)$  of distances  $d$ . Using the known probability  $p_0$  to get zero counts in a bin the probability of having counts in directly neighbouring bins (distance  $d = 0$ ) is given by  $p_{\text{dist}}(0) = 1 - p_0$ , while the probability to measure a distance of  $d$  bins is given by the probability to find  $d$  empty bins followed by an event.

$$p_{\text{dist}}(d) = p_0^d \cdot (1 - p_0) \quad (7.1)$$

The probability to have a start event does not enter  $p_{\text{dist}}(d)$  since we start counting only when there is an event, thus  $p_{\text{start}} = 1$  by default.

Note that it does not matter how many counts are recorded in a bin. We stop counting as soon as we encounter a non-empty bin. Hence only  $p_0$  needs to be known.

### Measuring $p_0$

The natural logarithm of the probability distribution of distances is given by

$$\log p_{\text{dist}}(d) = d \cdot \log p_0 + \log(1 - p_0) \quad (7.2)$$

Thus we should find a linear relationship between  $\log p_{\text{dist}}(d)$  and  $d$  if the probabilities are independent of previous results.

Note that the slope is always negative, since  $p_0 < 1$ . As soon as there is a bunching or anti-bunching effect, influencing the probabilities to find events in nearby bins, it will show up as a deviation from the linear relationship between  $\log p_{\text{dist}}(d)$  and  $d$ .

Extracting the slope of a measured distribution  $\log p_{\text{dist}}(d)$  yields  $p_0$  while the term  $\log(1 - p_0)$  only shifts the linear relationship.

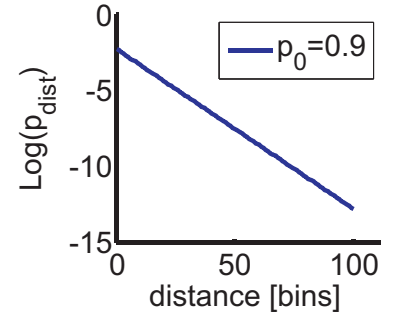


**Figure 7.1.:**  
Logarithm of the Probability Distribution of Distances

### 7.1.2. Poisson Distributed Sources

A special case of an independent probability distribution is the Poisson distribution with mean value  $\lambda$  counts per bin, where the probability to have  $k$  events in a certain bin is given by

$$p(k) = \frac{\lambda^k}{k!} e^{-\lambda} \quad (7.3)$$

where  $\lambda$  equals both the mean and the variance of the distribution (see appendix C). Thus the probability to have zero counts in a certain bin becomes

$$p_0 = e^{-\lambda}$$

transforming eq. 7.1 for the probability to find a certain distance  $d$  to

$$p_{\text{dist}}(d) = e^{-d\lambda} \cdot (1 - e^{-\lambda}) \quad (7.4)$$

and the natural logarithm of the probability distribution from eq.7.2 becomes

$$\log p_{\text{dist}}(d) = -d \cdot \lambda + \log(1 - e^{-\lambda}) \quad (7.5)$$

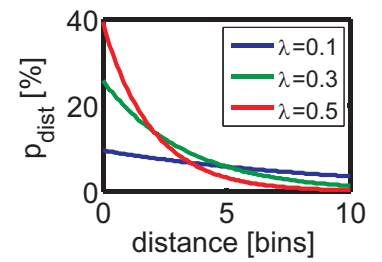


**Figure 7.2.:**  
Poisson Probability Distribution for different values of  $\lambda$ .



which can be approximated for  $e^{-\lambda} \ll 1$  by

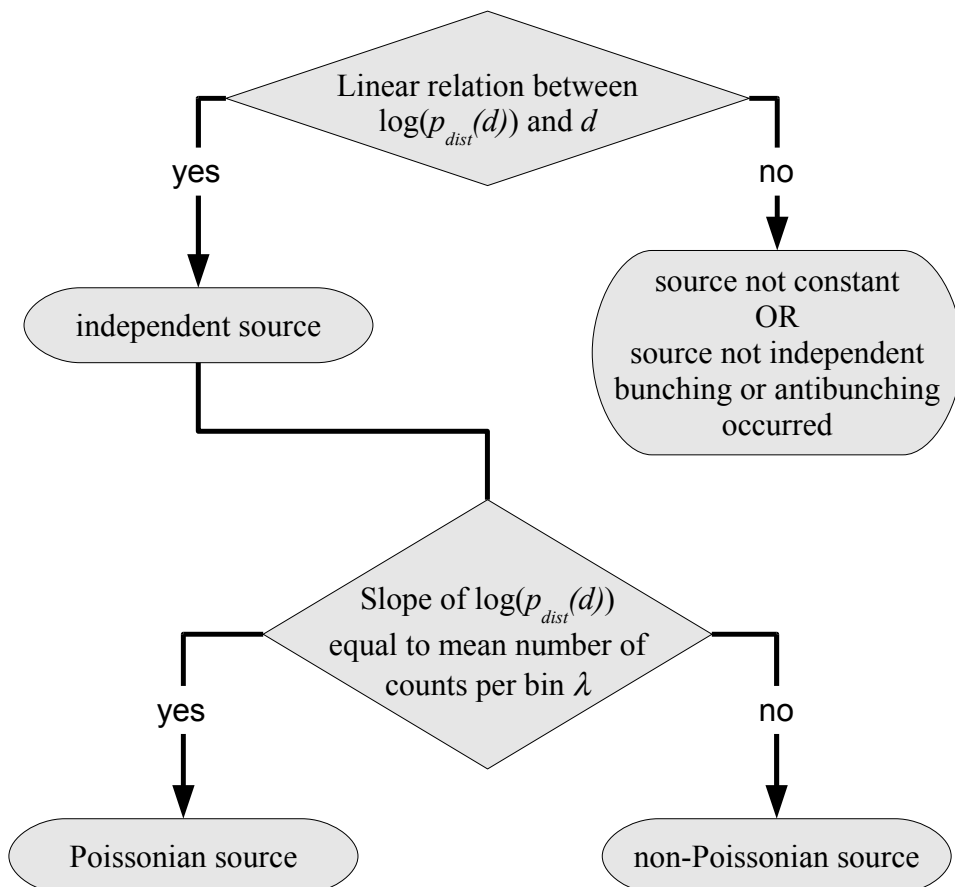
$$\log p_{\text{dist}}(d) = -d \cdot \lambda + \log \lambda \quad (7.6)$$

Note that this approximation does not hold for our application, since we have sparsely distributed light sources with  $\lambda$  typically 0.1 or less. See fig 7.2 for  $p_{\text{dist}}(\lambda)$  for Poisson distributed sources.

### Identifying Poisson Distributed Sources

Emissions from a source following any independent number distribution will produce a linear relationship between  $\log p_{\text{dist}}(d)$  and  $d$  if the source intensity is constant, as derived in eq.7.2. Nonetheless it is still possible to unambiguously identify Poisson distributed sources as outlined in figure 7.3. Only for a Poissonian distribution of counts the slope of  $\log p_{\text{dist}}(d)$  versus  $d$  equals the mean number of counts per bin  $\lambda$ .

Figure 7.3.: Identifying Poisson Distributed Sources from TIA



## 7.2. Atomic Source

The equations derived in the previous section are applicable for constant light sources emitting a stream of uncorrelated photons. For our measurements, where the sources of the fluorescence photons are the atoms, we have to take a non-constant atom number  $n_{\text{at}}$  into account.

Let  $p_{\text{at}}(a)$  be the atom number distribution and  $p_{\text{cts}}(n, a)$  the probability to measure  $n$  counts per bin if  $a$  atoms are present in the detection region. Then the probability to measure no counts in a certain bin is given by

$$p_0 = \underbrace{p_{\text{at}}(0)}_{\text{no atoms}} + \underbrace{\sum_{a=1}^{\infty} p_{\text{at}}(a) p_{\text{cts}}(0, a)}_{\text{atoms, but no counts}}$$

$$p_0 = p_{\text{at}}(0) + \sum_{a=1}^{\infty} p_{\text{at}}(a) e^{-a\alpha} \quad (7.7)$$

when background counts are neglected.

This complicates the treatment significantly, but an inspection of a measured time interval distribution as presented in figure 7.4 reveals that the instantaneous fluorescence rate when atoms are present and the atom arrival rate  $r_{\text{at}}$  are on completely different timescales for the measurements presented here. Hence we can separate the time interval distribution into two separate regions. Firstly the short time intervals up to the order of magnitude of the interaction time  $t_{\text{int}}$  which are determined by the rate of fluorescence emissions from a single atom. And secondly the long time intervals which are determined by the atom flux.

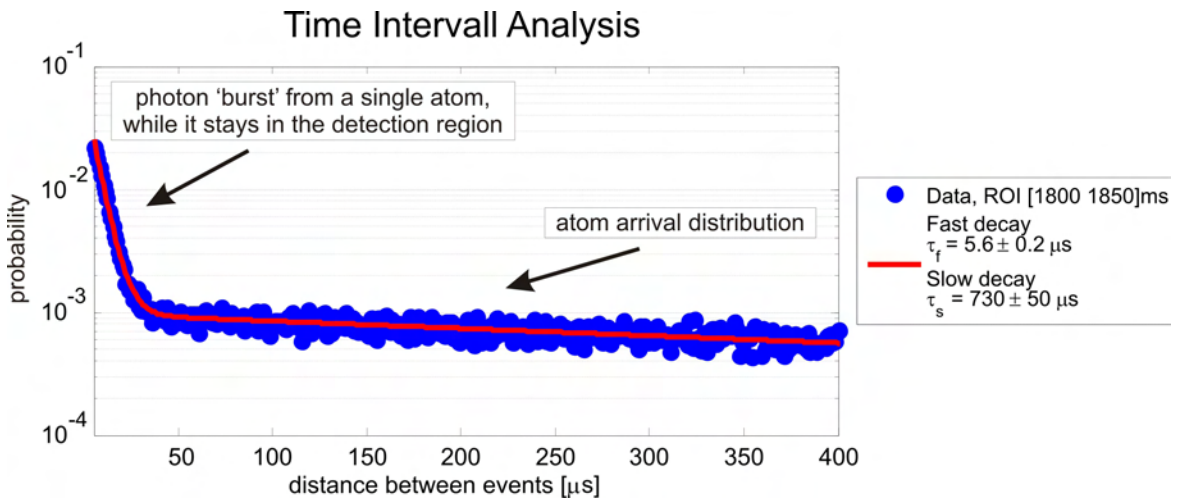


**Figure 7.4.:** Time Interval Distribution for constant atom flux<sup>1</sup>, showing that the distribution is composed of two separate exponentials decaying on different timescales.

If the constant atom flux is composed of stochastically independent atoms one can describe the time interval distribution as a sum of two independent exponentials with different decay times.<sup>2</sup> Figure 7.4 shows the result of a corresponding fit to the time interval distribution, yielding decay times of  $\tau_f = 5.6 \pm 0.2 \mu\text{s}$  and  $\tau_s = 730 \pm 50 \mu\text{s}$ , the meaning of which will be discussed in the following sections.

The two distinct regions of time intervals  $\delta t$  smaller than the interaction time  $t_{\text{int}}$  and time intervals large compared to  $t_{\text{int}}$  will be treated separately.

Note that the procedure outline in figure 7.3 is valid for both regions. For long time intervals the distribution of the atom arrival times can be tested while for short time intervals  $p_0$  is related to the instantaneous photon rate. Background counts will be neglected for the remainder of the chapter.

### 7.2.1. Long Time Intervals

We first consider the region  $\delta t \gg t_{\text{int}}$ . The maximum distance between photons emitted from one single atom is given by the interaction time. Therefore the rate of fluorescence emission from a single atom does not determine the time interval histogram in this region. Instead, neglecting background counts, we can assume the event separations to represent the distances between atoms that generated at least one count.

For  $\alpha \gg 1$  each atom will be detected (generate at least one count) and the rate of detected atoms  $r_{\text{det}}$  can be considered to be equal to the rate of atom arrivals  $r_{\text{at}}$ . Generally the atom detection rate is reduced by the finite detection efficiency  $\eta_{\text{at}}$  (see equation 6.19).

$$r_{\text{det}} = \eta_{\text{at}} \cdot r_{\text{at}} = (1 - e^{-\alpha}) \cdot r_{\text{at}} \quad (7.8)$$

#### Poisson Distributed Atoms

The logarithm of the time interval distribution for long time intervals can be extremely well approximated by a linear fit, as has been demonstrated in figure 7.4. This already

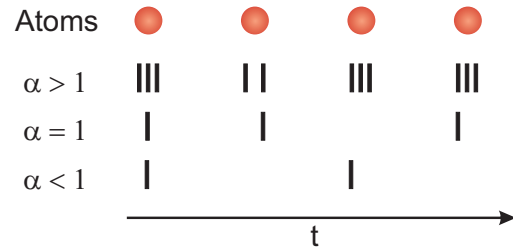


**Figure 7.5.:** Counts generated due to the presence of atoms for different values of  $\alpha$ . The smaller  $\alpha$  the higher the chance that an atom does not generate any counts and remains undetected. Note that even for  $\alpha \geq 1$  not all atoms will be detected due to the poissonian distribution of counts around  $\alpha$ .

<sup>1</sup>Dataset 20071205Wed\_F3\_resonant\_guide2\_05V, Region of Interest 1800 to 1850ms.

<sup>2</sup>If the atoms do not arrive independently of one another, then equation 7.2 does not apply and thus the slope of  $\log p_{\text{dist}}(d)$  will not be linear for long time intervals. The exponential approximation may still apply for the short time intervals, though, depending on whether the atom distribution shows significant bunching or anti-bunching on timescales of the interaction time or not.

confirms that the atoms arrive independently from one another at the detection region, allowing us to assume a fixed probability  $p_0$  to measure zero events at a certain time. According to equation 7.1 the probability for a certain distance  $\delta t = d \cdot t_b$  decays exponentially with the logarithm of  $p_0$ .

$$p_{\text{dist}}(\delta t) \propto p_0^{\delta t/t_b}$$

$$p_{\text{dist}}(\delta t) \propto e^{\delta t/t_b \cdot \log p_0}$$

The exponential decay with  $1/e$  decay time  $\tau_s$  observed in figure 7.4 can now be identified via

$$e^{\delta t/t_b \cdot \log p_0} = e^{\delta t/(t_b \tau_s)}$$

Hence we find the logarithm of the probability to have no events in a certain bin from the  $1/e$  time of the slow decay, if the decay is indeed exponential, confirming that the atoms arrive stochastically independent.

$$\log p_0 = 1/\tau_s \quad (\text{stochastically independent atoms})$$

Only for a Poisson distribution the logarithm of  $p_0$  equals the mean of the distribution. The mean rate of detected atoms is denoted  $r_{\text{det}}$ . Consequently, if the atoms are not only stochastically independent, but even Poisson distributed, the following relation should hold true.

$$\log p_0 = 1/\tau_s = r_{\text{det}} \quad (\text{Poisson distributed atoms})$$

We measure photon counts with a mean rate of  $\alpha$  photons per atom arriving at the detector.<sup>3</sup> Thus the mean count rate is given by the atom *arrival* rate.

$$\langle n_{\text{cts}} \rangle = \alpha \cdot r_{\text{at}} \quad (7.9)$$

With the relation between atom detection rate and actual rate of atoms arriving at the detector given by equation 7.8 the mean number of counts can then easily be expressed in terms of the atom detection rate.

$$\langle n_{\text{cts}} \rangle = \frac{\alpha}{\eta_{\text{at}}} r_{\text{det}} = \frac{\alpha}{1 - e^{-\alpha}} r_{\text{det}} \quad (\text{Poisson distributed atoms}) \quad (7.10)$$

To check if the atoms arrivals followed a Poisson distribution it is therefore sufficient to test whether  $r_{\text{det}} = 1/\tau_s$  fulfils the above equation.

The measurement presented in figure 7.4 yields a decay time of  $\tau_s = 730 \pm 50 \mu\text{s}$  leading to a calculated number of counts of  $\langle n_{\text{cts}} \rangle_{\tau_s} = 2240 \pm 153$  cps. An actual measurement of the background corrected mean number of counts yields  $\langle n_{\text{cts}} \rangle = 2044 \pm 271$  cps in full agreement with a Poissonian distribution of atoms.

We are examining a thermal ensemble of atoms well above the condensation threshold. Hence the atoms in a single mode of the guide follow a Boltzman distribution. Nonetheless we observe here Poisson distributed atoms since the atoms populate several modes of the guide and atoms in different modes arrive independently of one another.

<sup>3</sup>Here the full  $\alpha = 1.08$  for arbitrarily large bin sizes has to be considered, see chapter 6.

### Signal Strength $\alpha$

With equations 7.9 and 7.8 we see that  $\alpha$  can be measured from the ratio of the mean total number of counts measured to the slope  $r_{\text{det}}$  of  $\log p_{\text{dist}}(\delta t)$ .

$$\begin{aligned}\frac{\langle n_{\text{cts}} \rangle}{r_{\text{det}}} &= \frac{\alpha \cdot r_{\text{at}}}{\eta_{\text{at}} \cdot r_{\text{at}}} \\ \frac{\langle n_{\text{cts}} \rangle}{r_{\text{det}}} &= \frac{\alpha}{\eta_{\text{at}}} \\ \frac{\langle n_{\text{cts}} \rangle}{r_{\text{det}}} &= \frac{\alpha}{1 - e^{-\alpha}}\end{aligned}\tag{7.11}$$

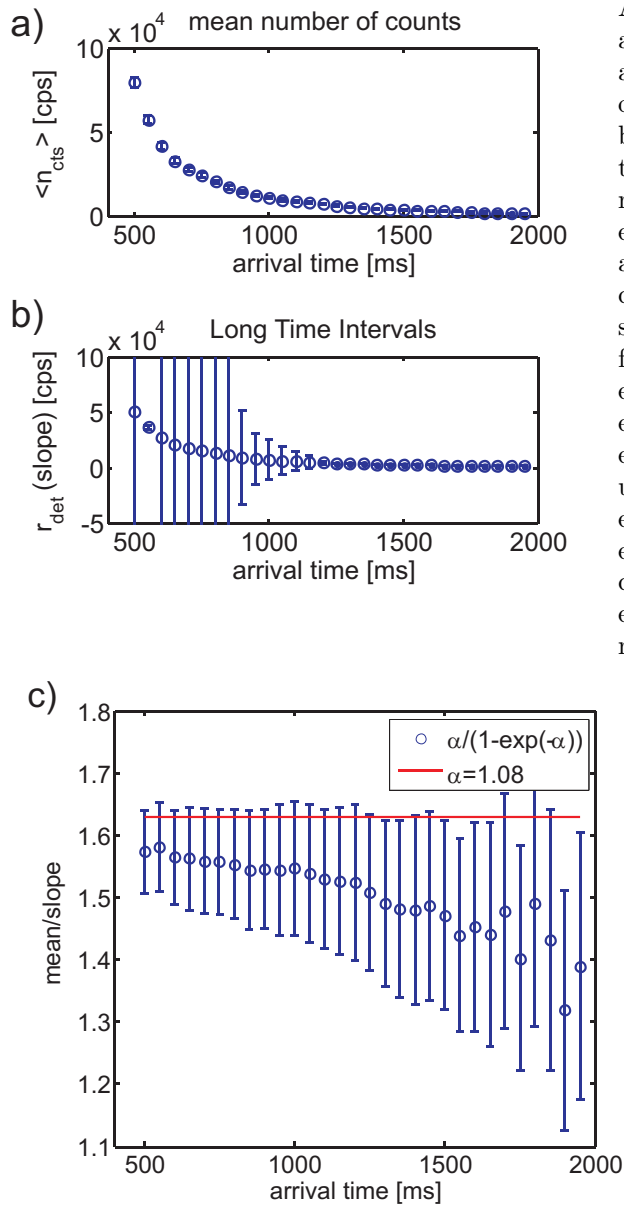
Unfortunately this relation cannot be solved analytically for  $\alpha$ . Therefore it is not conveniently used as the main approach to retrieve  $\alpha$  from the measured data, but may very well serve as an independent check of an  $\alpha$  acquired via different means.

The ratio of mean counts to slope was measured to be in first approximation constant over two orders of magnitude in mean count rate (figure 7.6). Each single measured value for  $\alpha/(1 - e^{-\alpha})$  is within a 95 % confidence interval reach of the expected value but the general trend is an underestimation of the ratio, caused by background effects leading to an artificial increase in slope (see section 7.2.3). The extracted mean value for the signal strength is  $\alpha = 0.88 \pm 0.10$  counts per atom, which is within two sigma of the expected value of  $\alpha = 1.08$  counts per atom.

More importantly we learn from the analysis that the slope of the time interval distribution for  $\delta t \gg t_{\text{int}}$  corresponds to the atom detection rate and is consequently determined by the atom flux through the detection region according to equation 7.8.

---

<sup>4</sup>Dataset 20071205Wed\_F3\_resonant\_guide2\_05V

**Figure 7.6.:**

Analysis of the Long Time Intervals<sup>4</sup>

a) Mean number of counts per second, evaluated for 50 ms region of interests, as function of the arrival time.

b) The slope of the logarithm of the time interval distribution for  $\delta t \gg t_{\text{int}}$ , giving the rate of atom detections. The large errors for early arrival times are due to non-constant atom flux during the region of interest.

c) & d) The ratio of mean count rate over slope is in first approximation constant as function of arrival time or count rate (see equation 7.11). The red line indicates the expected value of  $\alpha = 1.08$ . Even though the expected value is within errors a trend for underestimation exists, caused by an overestimation of the slope due to background effects (see sec.7.2.3). Since these effects become more important for low atom flux this explains as well the drop-off towards late arrival times.

### 7.2.2. Short Time Intervals

If an atom is present in the detection region it will fluoresce with an instantaneous rate of approximately  $\Gamma/8 = 4.7$  MHz, taking the  $45^\circ$  geometry into account (see chapter 3). Hence time intervals shorter than the  $1/e$  interaction time will be completely dominated by the instantaneous fluorescence rate and the atom arrival rate does not play a role. For time intervals  $\delta t$  larger than a few hundred nanoseconds, where no photon anti-bunching is expected, the photon counts generated by the fluorescence of  $n_{\text{at}}$  atoms in the detection region can very well be assumed to be Poissonian distributed with an instantaneous mean rate of  $\lambda$ .

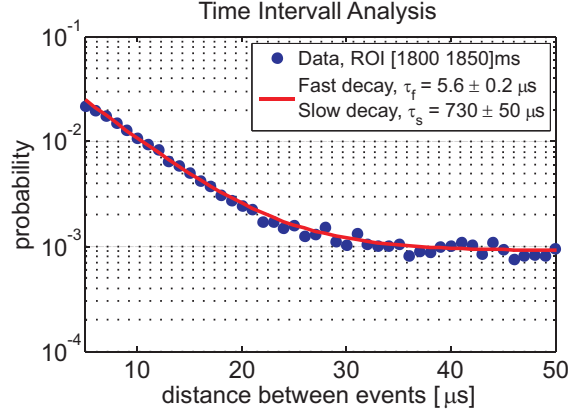


**Figure 7.7.:** Time Interval Distribution for constant atom flux from figure 7.4, zoomed on the short time interval part.

$$\lambda = n_{\text{at}} \cdot \alpha_{\text{inst}}$$

Here  $\alpha_{\text{inst}}$  is the instantaneous rate of counts generated per atom.

As discussed in equation 7.2 the slope of  $\log p_{\text{dist}}(\delta t)$  equals the logarithm of the probability  $p_0$  to measure no counts in a certain bin. For a Poissonian source this is given by the mean of the Poissonian (see eq.7.5). Consequently the slope of the short time interval part is given by

$$\log p_{\text{dist}}(\delta t) \propto \log p_0 = \lambda = \frac{1}{\tau_f}$$

Hence the slope will be proportional to the number of atoms present in the detection region.

The decay time  $\tau_f = 1/\lambda$  should not be confused with the  $1/e$  interaction time of an atom with the light field. While  $\lambda$  is the instantaneous rate of counts, the time an atom spends in the interaction region follows an exponential decay with  $1/e$  time  $t_{\text{int}}$ .

Similarly  $\alpha_{\text{inst}}$  is the instantaneous count rate per atom, i.e. the signal strength  $\alpha$  is calculated by the integral of  $\alpha_{\text{inst}}$  convoluted with the survival probability of the atoms.

$$\alpha = \int \alpha_{\text{inst}} \cdot e^{-t/t_{\text{int}}} dt$$

Additionally we know already from chapter 3 that the fluorescence rate of the atoms is not constant during the interaction time but is reduced with time due to photon recoil and magnetic field induced detuning. As a rough approximation we take the

time varying fluorescence rate into account by integrating not to infinity but only to the  $1/e$  interaction time.

$$\alpha = \int_{t=0}^{t_{\text{int}}} \alpha_{\text{inst}} \cdot e^{-t/t_{\text{int}}} dt = \alpha_{\text{inst}} t_{\text{int}} (1 - 1/e) \quad (7.12)$$

Defining  $t' = t_{\text{int}} (1 - 1/e)$  the instantaneous count rate  $\lambda = 1/\tau_f$  can be approximated to

$$\lambda = 1/\tau_f = n_{\text{at}} \cdot \frac{\alpha}{t'}$$

The actual number of atoms  $n_{\text{at}}$  will vary stochastically according to the atom number distribution  $p_{\text{at}}(n_{\text{at}})$ . As a first order approximation we will fix the atom number to its mean value during interaction  $\langle n_{\text{at}} \rangle_{\text{int}}$  [84]. Neglecting background at least one atom has to be in the detection region to generate counts. Thus the mean number of atoms during interaction has to be evaluated under the condition that atoms are present. The conditional probability distribution  $p_{\text{at}}(a)|_{a>0}$  is calculated using Bayes theorem [81].

$$p(A|B) = \frac{p(A \cap B)}{p(B)}$$

$$p_{\text{at}}(a)|_{a>0} = \frac{p_{\text{at}}(a)}{1 - p_{\text{at}}(0)}$$

The mean number of atoms during interaction is consequently given by

$$\langle n_{\text{at}} \rangle_{\text{int}} = \sum_{a>0}^{\infty} a \cdot \frac{p_{\text{at}}(a)}{1 - p_{\text{at}}(0)}$$

$$\langle n_{\text{at}} \rangle_{\text{int}} = \frac{\langle n_{\text{at}} \rangle}{1 - p_{\text{at}}(0)} \quad (7.13)$$

which can be simplified to the following expression if Poissonian distributed atoms with arrival rate  $r_{\text{at}}$  are assumed.

$$\langle n_{\text{at}} \rangle_{\text{int}} = \frac{r_{\text{at}} \cdot t'}{1 - e^{-r_{\text{at}} \cdot t'}} \quad (7.14)$$

$$\langle n_{\text{at}} \rangle_{\text{int}} = \begin{cases} r_{\text{at}} \cdot t' & , \text{for } r_{\text{at}} \cdot t' \gg 1 \\ 1 & , \text{for } r_{\text{at}} \cdot t' \ll 1 \end{cases}$$

Note that here an additional simplification has been made by assuming the atom number to be constant during the interaction time, which requires co-instantaneous arrival and departure of the atoms.

The slope  $\lambda$  can now be expressed in terms of the time  $t'$  and atom arrival rate.

$$\lambda = \frac{r_{\text{at}} \cdot t'}{1 - e^{-r_{\text{at}} \cdot t'}} \cdot \frac{\alpha}{t'} \quad (7.15)$$



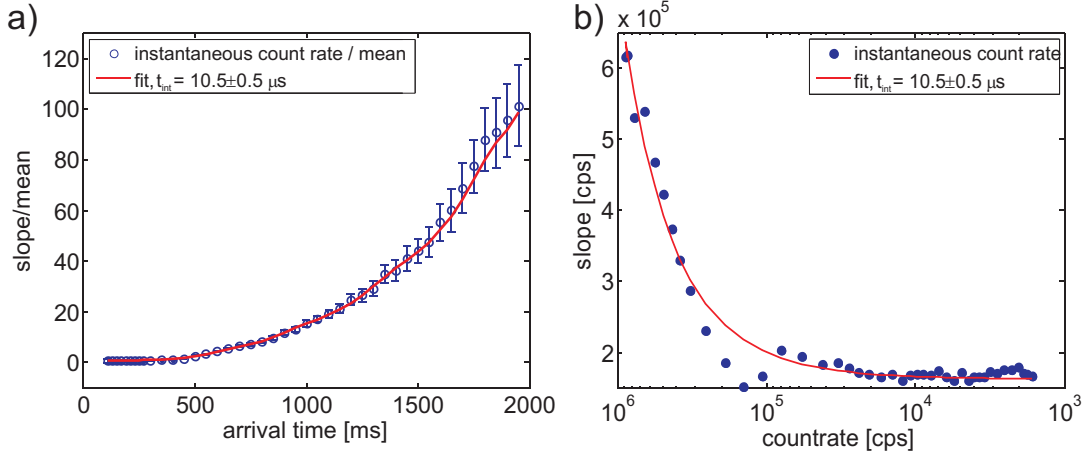


**Figure 7.8.:** Analysis of the Short Time Intervals<sup>5</sup>

a) The slope of the logarithm of the time interval distribution for short time intervals gives the instantaneous count rate in the presence of atoms. Here the ratio of slope to mean number of counts is plotted as function of the arrival time. For a high flux of atoms (early arrival times) the ratio levels out to 1, while for low flux of atoms the ratio increases inversely proportional to the atom flux (see equation 7.17).

b) The slope (instantaneous count rate) is plotted as a function of mean count rate. The instantaneous count rate is proportional to the atom flux for high flux, but levels out to a constant value for low flux where no more than 1 atom is present in the detection region (see equation 7.16).

The red line in both plots is a fit to the instantaneous count rate  $\lambda$  given in equation 7.15, yielding a  $1/e$  interaction time of  $t_{\text{int}} = 10.5 \pm 0.5 \mu\text{s}$ .

The approximation used for the fit breaks down in the region  $r_{\text{at}} \cdot t' \approx 1$  corresponding to count rates of approximately  $2 \cdot 10^5$ , reached around 400 ms. Therefore the fit over-estimates the slope in this region, but fits the limiting cases very well.

## Interaction Time

As before an analysis of the slope as a function of the atom flux is possible by evaluating the slope for different arrival times, corresponding to different densities in the atom pulse passing the detector. Figure 7.8 shows the result of such an analysis. The slope, representing the instantaneous count rate in the presence of atoms, levels out for low flux of atoms to a constant value  $\alpha/t'$  as predicted by equation 7.15. In this regime no more than one atom is present in the detection region at the same time. For high atom flux on the other hand the slope is proportional to the flux (see subfigure (b)).

$$\lambda \rightarrow \begin{cases} r_{\text{at}} \cdot \alpha & , \text{for } r_{\text{at}} \cdot t' \gg 1 \\ \frac{\alpha}{t'} & , \text{for } r_{\text{at}} \cdot t' \ll 1 \end{cases} \quad (7.16)$$

In figure 7.8b) the slope is fitted as a function of mean count rate according to equation 7.15, using the relation between atom arrival rate and mean count rate detailed in

<sup>5</sup>Dataset 20071205Wed\_F3\_resonant\_guide2\_05V

equation 7.9. For the ratio of slope  $\lambda$  to mean number of counts  $\langle n_{\text{cts}} \rangle$  we get the following limiting cases

$$\frac{\lambda}{\langle n_{\text{cts}} \rangle} = \frac{\lambda}{\alpha \cdot r_{\text{at}}} \rightarrow \begin{cases} 1 & , \text{for } r_{\text{at}} \cdot t' \gg 1 \\ \frac{1}{r_{\text{at}} \cdot t'} & , \text{for } r_{\text{at}} \cdot t' \ll 1 \end{cases} \quad (7.17)$$

The fit reproduces the limiting cases very well and allows extracting an estimate for the interaction time of

$$t_{\text{int}} = 10.5 \pm 0.5 \mu\text{s}$$

Note as well that the approximations of fixed atom number during interaction and co-instantaneous arrival and departure of atoms break down in the region  $r_{\text{at}} \cdot t' \approx 1$  (arrival times around 400 ms, corresponding to count rates of approximately  $2 \cdot 10^5$ ). Here the fit overestimates the slope significantly, albeit without reducing the quality of the overall fit.

The interaction time estimated from the fit agrees within errors with the value of  $t_{\text{int}} = 12 \pm 1 \mu\text{s}$  gained from variance over mean analysis in chapter 6. Due to the number of assumptions necessary to retrieve the results presented here it has to be noted, though, that an interaction time estimation from TIA can only be used as an independent check of a previously acquired value, not as a stand-alone measurement of interaction time.

### 7.2.3. Regarding Background Counts

For a first order approximation background counts can be treated as being independent of fluorescence counts and of one another, if afterpulsing is neglected. They have been proven to be in good approximation Poisson distributed around a mean value of 311 cps. Hence they too will contribute an exponential decay to the time interval distribution, superimposed on the two exponential decays caused by the atom flux and instantaneous count rate. Neglecting background counts leads consequently to an overestimation of the slopes of the remaining two exponential decays.

Since the mean distance of background counts is 3.2 ms the background contribution to the time interval histogram has only small effect on the measured decay times in the long time interval region and can be completely neglected for the short time interval region dominated by an instantaneous count rate of the order of MHz.

### 7.3. Summary

Time interval analysis is an important and powerful tool that allows us to draw conclusions on the statistics of the atoms from a single measurement.

With the signal strength  $\alpha$  and the interaction time  $t_{\text{int}}$  the fundamental parameters determining the performance of the detector can be acquired from TIA.

The signal strength per atom has been proven to conform with the previous result of  $\alpha = 1.08$  counts per atom and the interaction has been measured to  $t_{\text{int}} = 10.5 \pm 0.5 \mu\text{s}$  agreeing within errors with the result of the variance over mean analysis.

While both parameters can be retrieved more reliably from variance over mean analysis of a series of measurements at identical parameters it has to be pointed out that TIA allows retrieving estimates for these parameters from a single measurement. Since only nearest neighbour distances are evaluated only  $O(N)$  operations are necessary if  $N$  counts are recorded. With a typical cycle time of the experiment of 20 s TIA can be easily performed by modern computers in 'real time', even including advanced fitting routines, before the next cycle starts.

Thus, changes in  $\alpha$  or interaction time relative to a known, previously acquired value can be monitored directly with only a single measurement necessary. This makes it possible to get a live feedback of the influence of experimental parameters on the statistical distribution of the atoms.

The figures presented in this chapter are the results of an analysis of 878 consecutive measurements at identical parameters to enhance the clarity of the presentation. To demonstrate that a single measurement is sufficient to retrieve reliable estimates figure 7.9 shows the results of an identical, automated analysis of a randomly selected single measurement<sup>6</sup>, yielding an identical result of  $t_{\text{int}} = 10.5 \mu\text{s}$  for the interaction time, albeit at larger errors ( $\pm 1.1 \mu\text{s}$ ).

But most importantly time interval analysis allows identification of the statistical distribution of the atoms without previous assumptions. It has been shown that for the atomic densities and temperatures employed for the measurements presented in this thesis the atoms arrive independently from one another in the detection region.

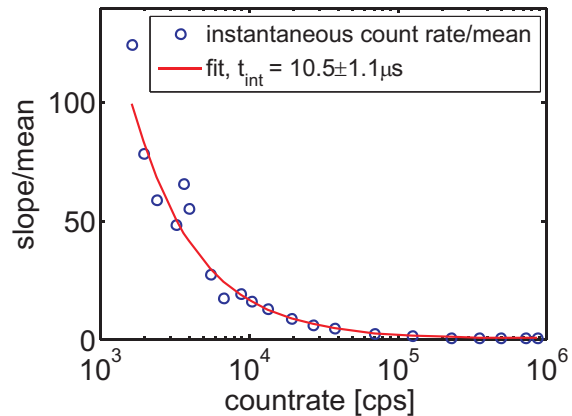


**Figure 7.9.:**

Time Interval Distribution of a single measurement, evaluating the slope for small time intervals (instantaneous count rate) versus the count rate to retrieve an estimate for the interaction time.

<sup>6</sup>Shot number 100 of Dataset 20071205Wed\_F3\_resonant\_guide2\_05V

Even more, the atom numbers follow a Poisson distribution, since we observe multiple modes of a thermal ensemble.

Time interval analysis allows distinction between stochastically independent, bunched or anti-bunched distributions opening a vast field of applications in the monitoring of ultra-cold atomic gases. The integration of the detector allows e.g. 'watching' BEC transitions or even 1D condensation (transition to a Tonks-Girardeau Gas) in-situ with high signal to noise ratio as an alternative to the commonly used time of flight method [82, 83] where only the greatly expanded cloud can be observed.

*"If your experiment needs statistics, you ought to have done a better experiment."*

Ernest Rutherford

# 8. Correlation Analysis

Coherence of light at two points in space or time is defined as its capability to interfere. Two superimposed light fields will interfere if a fixed phase relation between the fields exists. Coherence can thus be understood as a measure for the memory of the light emission process.

## 8.1. Theoretical Introduction

Correlation functions can be used to measure coherence properties of optical fields. The degree of coherence of a classical field  $E(\vec{r}, t)$  can be defined as the value of the normalized first order correlation function [40, 85, 86].

$$g^{(1)}(\vec{r}_1, t_1; \vec{r}_2, t_2) = \frac{\langle E^*(\vec{r}_1, t_1) E(\vec{r}_2, t_2) \rangle}{[\langle |E(\vec{r}_1, t_1)|^2 \rangle \langle |E(\vec{r}_2, t_2)|^2 \rangle]^{1/2}}$$

Where the angular brackets denote ensemble averages.

In the following discussion I will concern myself only with temporal coherence, since the geometry of the detector automatically samples the fields at a fixed, common point  $\vec{r} = \vec{r}_1 = \vec{r}_2$  in space. The correlation function becomes then a function of the time difference  $\delta t = t_2 - t_1$  alone. In correlation analysis the time difference at which the correlation is evaluated is usually denoted as *lag*.

The temporal resolution of the photon detection setup is with 1 ns significantly smaller than the lifetime  $\tau = 26.24$  ns [44] of the excited state. This enables us to examine the coherence properties of the fluorescence emission of the atoms in the detection region. Since the analysis of the previous chapters has shown that the integrated fluorescence detector is capable of observing the fluorescence of single atoms, non-classical behaviour of the emission is expected if the atom flux is low enough to warrant that at a given time at most one atom will be in the detection region.

### 8.1.1. Coherence Time

In an ideal monochromatic light wave the electric field has a fixed phase relation over all temporal distances. For most light sources the memory of the emission process is not unlimited and coherence will break down beyond a critical distance. Light that is

emitted with a separation greater than this distance has no phase relation and cannot interfere.

The correlation function is positive for all values of  $\delta t$  and the value of the correlation function for a given lag  $\delta t$  is a measure of the influence of the electric field at time  $t$  on the electric field value at time  $t + \delta t$ . This interpretation of the correlation function motivates the definition of the coherence time  $\tau_c$  as power equivalent width of the correlation function  $g(\delta t)$ .

$$\tau_c = \int_{-\infty}^{\infty} |g(\delta t)|^2 d\delta t \quad (8.1)$$

An evaluation of this integral shows that this definition is equivalent to the  $1/e$  time of exponentially decaying correlation functions  $g(\delta t) \propto e^{-|\delta t|/\tau_c}$  or the width of Gaussian shaped correlation functions  $g(\delta t) \propto e^{-\pi \delta t^2 / (2\tau_c^2)}$  correspondingly [40].

Light is considered to be completely coherent for all practical purposes if the coherence length  $l_c = c \cdot \tau_c$  is larger than all optical path lengths in the system. The ideal, monochromatic wave with infinite coherence length has already been mentioned above. Generally speaking the coherence time is shorter the larger the linewidth of the light. Note though, that the coherence of a light field is a property of the field and not of the source. Coherence can be increased using filters at the expense of intensity [40].

### 8.1.2. Second Order Correlation Function

Usually the intensity  $I = \langle E^* E \rangle$  of a field  $E$  is measured, instead of the field strength itself. Hence we will consider now the second order intensity correlation function  $g^{(2)}(\delta t)$ .

The labelling *first* and *second* order refers to the order of the field measured, even though it may be misleading due to first order correlation functions involving squares of field amplitudes and second order correlation functions being fourth order in the field.

#### Classical Fields

The second order intensity correlation function  $g^{(2)}(\delta t)$  is defined by [40, 87]

$$g^{(2)}(t, \delta t) = \frac{\langle E^*(t) E^*(t + \delta t) E(t) E(t + \delta t) \rangle}{\langle |E(t)|^2 \rangle \langle |E(t + \delta t)|^2 \rangle} \quad (8.2)$$

which can be reordered if we are dealing with classical fields to express  $g^{(2)}(\delta t)$  in terms of intensities.

$$g^{(2)}(t, \delta t) = \frac{\langle I(t) I(t + \delta t) \rangle}{\langle I(t) \rangle \langle I(t + \delta t) \rangle}$$

I will limit myself in this discussion to the stationary case of constant intensity  $\langle I(t) \rangle = \langle I(t + \delta t) \rangle$ . Here  $g^{(2)}(\delta t)$  becomes a function of the lag  $\delta t$  alone.

$$g^{(2)}(\delta t) = \frac{\langle I(t) I(t + \delta t) \rangle}{\langle I(t) \rangle^2} \quad (8.3)$$

**Coherent Light** Perfectly coherent light, e.g. an ideal laser emitting a single frequency, yields  $g^{(2)}(\delta t) = 1$  as displayed in figure 8.1.

$$g^{(2)}(\delta t) = 1 \quad \text{coherent light}$$

**Chaotic Light** The shape of the second order correlation function of chaotic light, i.e. thermal radiation<sup>1</sup>, depends on the light source [85]. Chaotic light follows a Bose-Einstein statistic instead of a Poissonian photon number distribution. Hence the photons tend to arrive bunched together with small temporal separations. This behaviour has been termed *photon bunching*. Correspondingly the ratio of variance of the photon number over its mean is for small separations super-Poissonian, i.e. larger than the Poissonian limit of 1.

If the source is dominantly collision broadened we speak of Lorentzian chaotic light. In the limit of large atom numbers  $g^{(2)}(\delta t)$  can be expressed as a simple function of the line width  $\gamma_L$ .

$$g^{(2)}(\delta t) = 1 + e^{-2\gamma_L \delta t} \quad \text{Lorentzian chaotic light}$$

Gaussian chaotic light, on the other hand, describes light sources dominantly broadened by the Doppler effect. Here, too,  $g^{(2)}(\delta t)$  can be given as simple function of the Doppler width  $\gamma_D$  in the many atom limit.

$$g^{(2)}(\delta t) = 1 + e^{-\gamma_D^2 \delta t^2} \quad \text{Gaussian chaotic light}$$

**Characteristics of the Correlation Function** From the definition of the correlation function in eq.8.3 we see that  $g^{(2)}(\delta t)$  is an even function.

$$g^{(2)}(\delta t) = g^{(2)}(-\delta t)$$

<sup>1</sup>I follow the definition of chaotic light given by Loudon [85].

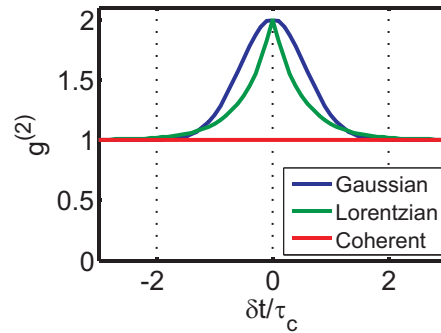


**Figure 8.1.:** Second order correlation function  $g^{(2)}(\delta t)$  as function of the lag  $\delta t$  in units of the coherence time  $\tau_c$  for classical fields. The red curve shows  $g^{(2)}(\delta t)$  for light of a single frequency. The green curve gives  $g^{(2)}(\delta t)$  for Lorentzian chaotic light, while the blue curve describes Gaussian chaotic light. The chaotic light follows super-Poissonian statistics and displays photon bunching.

For classical fields the correlation function takes values between 1 and  $\infty$  at  $\delta t = 0$ , while for larger temporal distances it might drop to 0, but always remains positive [85].

#### Classical Fields

$$\begin{aligned} 1 &\leq g^{(2)}(0) \leq \infty & g^{(2)}(\delta t)|_{\delta t > 0} &\leq g^{(2)}(0) \\ 0 &\leq g^{(2)}(\delta t)|_{\delta t > 0} \leq \infty \end{aligned}$$

For all types of chaotic light the behaviour of the first order correlation function yields the following additional relations (see Loudon [85]).

#### Chaotic Light

$$\begin{aligned} g^{(2)}(\delta t) &= 1 + |g^{(1)}(\delta t)|^2 & g^{(2)}(0) &= 2 \\ & & g^{(2)}(\delta t)|_{\delta t > 0} &= 1 \end{aligned}$$

Note that for temporal separations  $\delta t$  long compared to the coherence time  $\tau_c$  the numerator in equation 8.3 factorizes because the intensity at time  $t + \delta t$  becomes independent of the intensity at time  $t$  and  $g^{(2)}(\delta t)$  settles on 1.

$$\begin{aligned} \langle I(t) I(t + \delta t) \rangle &\rightarrow \langle I(t) \rangle \langle I(t + \delta t) \rangle \\ \Rightarrow g^{(2)}(\delta t \rightarrow \infty) &= 1 \end{aligned}$$

### Quantum Fields

In order to examine quantum effects the electromagnetic fields  $E^*$  and  $E$  in equation 8.2 have to be replaced by the corresponding field operators  $\hat{E}^-$  and  $\hat{E}^+$  with the intensity operator  $\hat{I} = \hat{E}^+ \hat{E}^-$ .

$$g^{(2)}(t, \delta t) = \frac{\langle \hat{E}^-(t) \hat{E}^-(t + \delta t) \hat{E}^+(t) \hat{E}^+(t + \delta t) \rangle}{|\langle \hat{E}^-(t) \hat{E}^+(t) \rangle|^2} \quad (8.4)$$

**Fock States** For a single mode field at  $\delta t = 0$  the above relation can be significantly simplified and the second order correlation function can be written using the creation and annihilator operators  $\hat{a}^\dagger$  and  $\hat{a}$  [85].

$$g^{(2)}(0) = \frac{\langle \hat{a}^\dagger \hat{a}^\dagger \hat{a} \hat{a} \rangle}{\langle \hat{a}^\dagger \hat{a} \rangle^2} \quad \text{with} \quad \begin{aligned} [\hat{a}, \hat{a}^\dagger] &= 1 \\ \hat{a}^\dagger \hat{a} &= \hat{a} \hat{a}^\dagger - 1 \\ \hat{n} &= \hat{a}^\dagger \hat{a} \end{aligned} \quad (8.5)$$



In this notation the photon number operator  $\hat{n}$  is the measure of intensity. Using  $\hat{n} = \hat{a}^\dagger \hat{a}$  and the commutator relations outlined above the second order correlation function can be rewritten.

$$\begin{aligned} g^{(2)}(0) &= \frac{\langle \hat{a}^\dagger (\hat{a} \hat{a}^\dagger - 1) \hat{a} \rangle}{\langle \hat{a}^\dagger \hat{a} \rangle^2} \\ g^{(2)}(0) &= \frac{\langle \hat{n} (\hat{n} - 1) \rangle}{\langle \hat{n} \rangle^2} \end{aligned} \quad (8.6)$$

Equation 8.6 gives now an interesting insight into the quantum nature of the measurement. The detection of a photon requires its annihilation. To examine the correlation two measurements are performed at times  $t_1$  and  $t_2$ , and since the first measurement already removes one of the  $n$  photons, the second measurement has to be performed on  $n - 1$  photons [85].

For a Fock state  $|n\rangle$  with fixed photon number  $n$  we receive therefore the following important relation.

$$g^{(2)}(0) = \frac{n^2 - n}{n^2} = 1 - \frac{1}{n} \quad ; \quad g^{(2)}(0) = \begin{cases} 0 & \text{for } n = 1 \\ \frac{1}{2} & \text{for } n = 2 \\ \vdots & \\ 1 & \text{for } n \rightarrow \infty \end{cases} \quad (8.7)$$

Note that  $g^{(2)}(0)$  for a state with well defined photon number is therefore always smaller than the classical limit of  $g^{(2)}(0) = 1$ , showing a clear signature of quantum effects. Thus in quantum theory

$$0 \leq g^{(2)}(\delta t) \leq \infty$$

holds true for all  $\delta t$ , including  $\delta t = 0$ . Comparing this behaviour with the discussion of classical fields above, we can establish an exclusive range that can be reached only by quantum effects.

$$0 \leq g^{(2)}(0) < 1$$

A behaviour of this type, with a correlation smaller than 1, is referred to as photon *anti-bunching*, since here the photons are unlikely to arrive together, while normally, being bosons, the photons would prefer to bunch. Perfect anti-bunching is achieved at  $g^{(2)}(0) = 0$ , where no two photons arrive at the same time.

**Coherent State** For very large photon number  $n$  the results given in equation 8.7 approach those of a coherent state. The coherent state  $|\alpha\rangle$  is an appropriate description

of a laser mode and can be defined in a Fock basis as a superposition of all possible photon numbers [85].

$$|\alpha\rangle = e^{-|\alpha|^2/2} \sum_{n=0}^{\infty} \frac{\alpha^n}{n!} |n\rangle \quad (8.8)$$

The coherent state is an eigenstate of the annihilation operator

$$\hat{a}|\alpha\rangle = \alpha|\alpha\rangle$$

meaning, unlike the Fock state, the coherent state is unchanged by the detection of a photon. The probability to measure  $n$  photons

$$p(n) = |\langle n|\alpha\rangle|^2 = \frac{|\alpha|^{2n}}{n!} e^{-|\alpha|^2}$$

is Poisson distributed, in agreement with classical observations.

The second order correlation function at  $\delta t = 0$  for the coherent state can be calculated from

$$\begin{aligned} g^{(2)}(0) &= \frac{\langle \alpha | \hat{a}^\dagger \hat{a}^\dagger \hat{a} \hat{a} | \alpha \rangle}{\langle \alpha | \hat{a}^\dagger \hat{a} | \alpha \rangle^2} = \frac{\alpha^* \alpha^* \alpha \alpha}{(|\alpha|^2)^2} = \frac{|\alpha|^4}{|\alpha|^4} \\ g^{(2)}(0) &= 1 \end{aligned}$$

### Emission from a single atom

Of substantial interest for the analysis of the measurements presented in this thesis is the fluorescence emission of a single atom. For resonant illumination on a cyclic transition the atom can be approximated as a two-level system.

The second order coherence function of the emission of a single 2-level atom depends on the nature of the illumination and the broadening processes influencing the emission of fluorescent light. A complete derivation of the following relations is given in Loudon [85].

**Broadband Illumination** In the case of broadband illumination and large collision or Doppler broadening of the line  $g^{(2)}(\delta t)$  can be approximated by

$$g^{(2)}(\delta t) = 1 - e^{-2\Gamma \delta t} \quad (8.9)$$

where  $\Gamma$  is again the radiative decay rate of the excited state.

**Weak Single Mode Coherent Illumination** In our experiments the atomic sample is illuminated not by a broadband source but a resonant laser, usually referred to as the probe beam. In the case of resonant illumination by a single mode field Doppler broadening does not influence the coherence characteristics of the fluorescence emission, hence we will only consider collisional broadening.

For weak, coherent illumination with a single mode probe beam with Rabi frequency  $\Omega \ll \Gamma$  the scattered light is completely coherent in the absence of collisional broadening. For resonant illumination the second order correlation function is then given by the following approximation.

$$g^{(2)}(\delta t) = (1 - e^{-\Gamma \delta t})^2 \quad (8.10)$$

In the limit of large collisional broadening, but still weak single mode coherent probe beam, the same approximation as for broadband illumination holds.

$$g^{(2)}(\delta t) = 1 - e^{-2\Gamma \delta t} \quad (8.11)$$

**Single Mode Coherent Illumination without Collisional Broadening** The atomic density in the guide is at least for arrival times larger than 1000 ns (after the peak of the atom distribution has passed) so low that collisional broadening can be completely neglected. In this regime an approximation for  $g^{(2)}(\delta t)$  for arbitrary probe beam powers can be given if the illumination is on resonance [85].

$$g^{(2)}(\delta t) = 1 - \left( \cos \zeta \delta t + \frac{3\Gamma}{2\zeta} \sin \zeta \delta t \right) e^{-3/2\Gamma \delta t} \quad \text{with} \quad \zeta = \sqrt{\Omega^2 - \frac{1}{4}\Gamma^2} \quad (8.12)$$

$\zeta$  can here be interpreted as an effective Rabi frequency. In the absence of spontaneous emission ( $\Gamma = 0$ ) the population of the upper state would exhibit Rabi oscillations. The spontaneous emission rate  $\Gamma$  acts as a damping term on these oscillations, reducing the effective Rabi frequency from  $\Omega$  to  $\zeta$  [85].

For  $\Omega \leq \Gamma/2$  the oscillations are completely damped out and the excited state population approximates its steady state value without overshoot.

Figure 8.2 shows the resulting second order correlation function for different values of the saturation parameter  $s = I/I_{\text{sat}}$  (see chapter 3), using  $1/\Gamma = 26.24$  ns.<sup>2</sup> Note that for  $\Omega > \Gamma/2$ , where  $\zeta$  is real,  $g^{(2)}(\delta t)$  shows oscillatory behaviour.

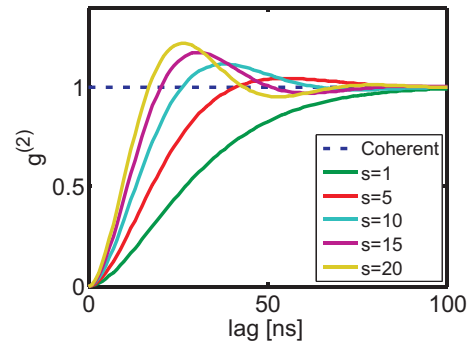


**Figure 8.2.:**

Second order correlation function for different values of the saturation parameter  $s$  and  $1/\Gamma = 26.24$  ns.

<sup>2</sup> $1/\Gamma = 26.24$  ns is the lifetime of the cyclic  $^{87}\text{Rb}$  transition used for probing the atoms.

**Photon Anti-bunching** As mentioned above light is said to be bunched for  $g^{(2)}(0) > 1$  and anti-bunched for  $g^{(2)}(0) < 1$ . The latter can be explained only by quantum effects. In the case of single two level atom the reason for anti-bunching of the fluorescence emission is easily understood.

Once the atom has emitted one photon it has dropped to the ground state and cannot emit a second photon before it is excited again. The transfer of the atom into the excited state takes a time of the order of the lifetime of the excited state, hence anti-bunching of the emission will occur for times shorter than this timescale. Note that in figure 8.2 the first peak of the correlation function for strong pumping is reached approximately after a time of  $1/\Gamma$ .

## 8.2. Measuring the Correlation Function

Measurements of the correlation function are subject to a number of limitations arising from finite measurements time, measurement resolution and background disturbances. The influence of these disturbances on a measurement of  $g^{(2)}(\delta t)$  will be discussed in sections 8.2.1 to 8.2.5, following the excellent presentation in A.Boca's thesis [87].

To simplify the notation the following discussion will be based on the second order correlation function for classical fields as given in equation 8.3, but you will find that all results are equally valid for quantum fields.

### 8.2.1. Finite Sampling

If the light fields are ergodic then the ensemble averages can be replaced by averages over the measurement time  $T$ .

$$\langle I(t) I(t + \delta t) \rangle = \lim_{T \rightarrow \infty} \frac{1}{T} \int_{-T/2}^{T/2} I(t) I(t + \delta t) dt$$

$$\langle I(t) \rangle = \lim_{T \rightarrow \infty} \frac{1}{T} \int_{-T/2}^{T/2} I(t) dt$$

The above relations hold true when the signal can be sampled for an infinitely long measurement time  $T$ . In this case the second order correlation function of a coherent signal of constant intensity  $I_0$  will be measured faithfully to  $g^{(2)}(\delta t) = 1$  for all lags (see figure 8.3a).

If the same signal is sampled only for a finite time  $T_0$  the ergodic means are replaced by signal averages.

$$\langle I(t) I(t + \delta t) \rangle = \frac{1}{T_0} \int_{-T_0/2}^{T_0/2} I(t) I(t + \delta t) dt$$

$$\langle I(t) \rangle = \frac{1}{T_0} \int_{-T_0/2}^{T_0/2} I(t) dt$$

However, when calculating  $g^{(2)}(\delta t)$  from the measured signal it will be considered equal to 0 for times larger than  $T_0$ . Hence the constant signal has become a square pulse with length  $T_0$  and the second order correlation function acquires a triangular shape.

$$g^{(2)}(\delta t)_{T_0} = 1 - \frac{|\delta t|}{T_0} \quad \text{for a constant coherent signal} \quad (8.13)$$

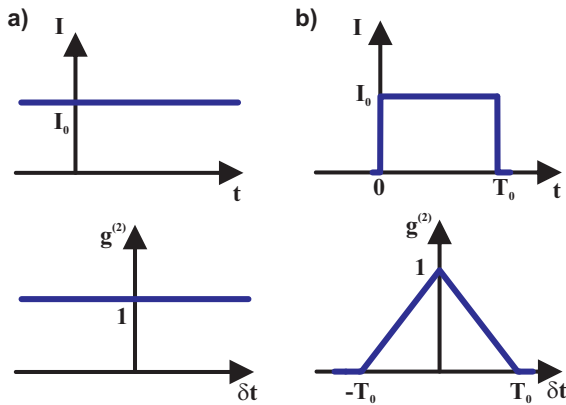


**Figure 8.3.:** Finite Sampling Effect on the Measurement of the Second Order Correlation Function

a) If a coherent signal of constant intensity  $I_0$  is measured for an infinite time  $T$  the resulting second order correlation function is  $g^{(2)}(\delta t) = 1$  for all lags.

b) If the same signal is measured only for a finite time  $T_0$  then the effective signal shape is a square pulse of length  $T_0$  and  $g^{(2)}(\delta t)$  acquires a triangular shape.

This triangular shape of  $g^{(2)}(\delta t)$  cannot be avoided in finite sampling, since the zero intensity outside of the measured range  $T_0$  pulls  $g^{(2)}(\delta t)$  down to zero. The second order correlation function can be corrected for this effect by multiplication with a factor  $T_0/(T_0 - |\delta t|)$ . Note though, that the latter correction leads to increasing fluctuations at  $|\delta t| = T_0$  where the correction factor diverges.

$$g^{(2)}(\delta t)_{T_0, \text{corr}} = g^{(2)}(\delta t)_{T_0} \cdot \frac{T_0}{T_0 - |\delta t|}$$

If  $T_0$  is chosen large compared to the examined lags (as is done for our measurements) the effect of finite sampling time can be neglected.

### 8.2.2. Discretization

In a real measurement the arrival times of the photons are always recorded with a finite time resolution  $t_b$ . This leads to a discretization of the time axis for a measurement of  $T_0$  into  $N = T_0/t_b$  bins of size  $t_b$ . The lag can then be expressed in terms of the bin size  $\delta t = j \cdot t_b$ . With  $a_k$  denoting the number of photon counts recorded in the  $k$ th bin the second order correlation function sampled at  $N$  points can then be expressed

as follows.

$$g^{(2)}(j \cdot t_b)_N = \frac{\langle I(t) I(t + \delta t) \rangle_N}{\langle I(t) \rangle_N^2}$$

$$\langle I(t) I(t + \delta t) \rangle_N = \frac{1}{N} \sum_{k=1}^N a_k a_{k+j}$$

$$\langle I(t) \rangle_N = \langle I(t + \delta t) \rangle_N = \frac{1}{N} \sum_{k=1}^N a_k$$

**Autocorrelation and Afterpulsing** As discussed in chapter 4 and demonstrated in figure 8.4, single counter autocorrelation measurements suffer from detector afterpulsing leading to strong correlations for lags corresponding approximately to the detector dead time of 52 ns. Correction strategies for afterpulsing effects as well as the reason for their failure have been discussed in chapter 4 as well.

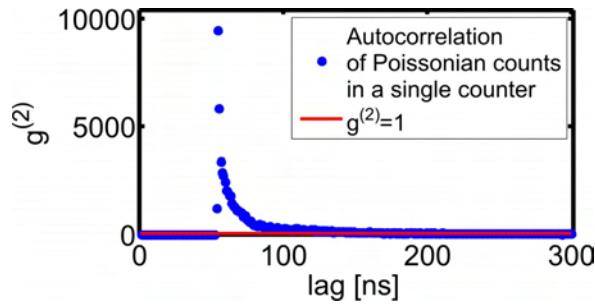


**Figure 8.4.:** Autocorrelation Function of a Poissonian Background<sup>3</sup>, distorted by detector afterpulsing.

**Cross-Correlation and Secondary Emission** To prevent afterpulse distortions the correlation analysis presented in this chapter has been performed on cross-correlations measured between two separate photon counters in a Hanbury Brown-Twiss type setup as described in chapter 2. Use of cross-correlations instead of autocorrelations avoids afterpulsing distortions at the expense of a reduction in measurement statistics.

But, as discussed extensively in chapter 4, the specific cross-correlation setup employed leads to a distortion of the second order correlation function caused by secondary emissions. It was shown that, unlike afterpulses, these can be successfully corrected for. Figure 8.5 reproduces figure 4.11, showing a measurement of Poissonian distributed background before and after secondary emission correction.

<sup>3</sup>Dataset 20071206Thu\_F3\_resonant\_Displ\_Off\_fieldsOff, 1090 shots, measuring the Poisson distributed background.

<sup>4</sup>Dataset 20071220Thu\_F3\_resonant\_412mV, 4409 shots, Region 1500-2000ms.

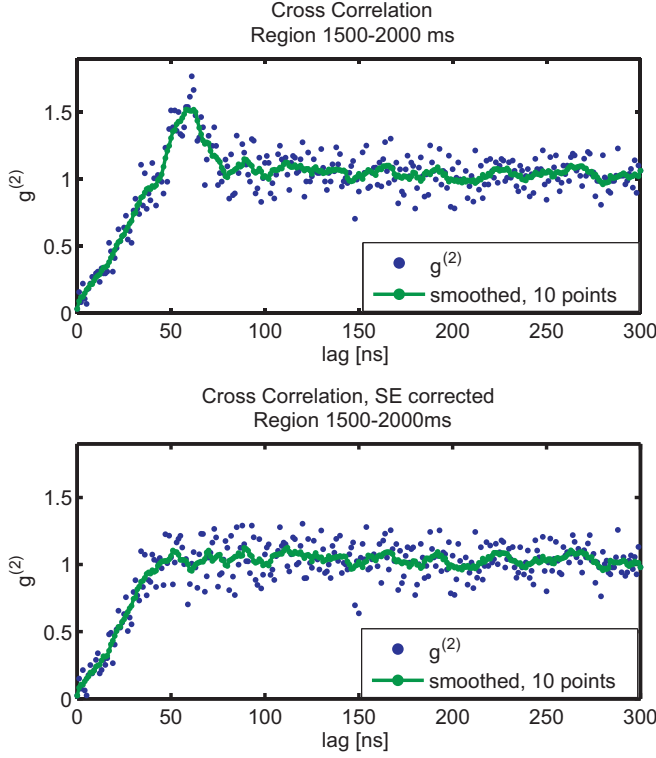


**Figure 8.5.:**

Secondary emission correction demonstrated on a cross correlation measurement of an atomic signal.<sup>4</sup>

The upper graph shows the uncorrected normalized intensity correlation function  $g^{(2)}$  exhibiting a strong secondary emission distortion exactly in that region where Rabi-oscillations might be expected. The lower graph shows the secondary emission corrected correlation function.

In both graphs the blue points represent the actual datapoints measured. The green points are included to guide the eye and have been produced by a 10 point moving average smoothing of the measured correlation function.

**Discretization of Cross-Correlation Measurements** In cross-correlation analysis we deal with two counters and hence  $a_k$  counted photons per bin in the first and  $b_k$  counted photons per bin in the second detector. It follows, that

$$\langle I_A(t) I_B(t + j t_b) \rangle = \frac{1}{N} \sum_{k=1}^N a_k b_{k+j}$$

$$\langle I_A(t) \rangle = \frac{1}{N} \sum_{k=1}^N a_k$$

$$\langle I_B(t) \rangle = \frac{1}{N} \sum_{k=1}^N b_k$$

Using  $A$  and  $B$  as abbreviations for the total number of counts in all  $N$  bins for the corresponding counter and labelling the unnormalized correlations  $G^{(2)}(j t_b)_N$  the second order cross-correlation function can be written as follows.

$$g^{(2)}(j t_b)_N = N \frac{\sum_{k=1}^N a_k b_{k+j}}{(\sum_{k=1}^N a_k) (\sum_{k=1}^N b_k)}$$

$$g^{(2)}(j t_b)_N = N^2 \frac{G^{(2)}(j t_b)_N}{A \cdot B} \tag{8.14}$$

The unnormalized correlation function  $G^{(2)}(j t_b)_N$  can be measured most conveniently if the bin size  $t_b$  is chosen small enough to warrant that there is at most one count

per detector in each bin. Under these conditions  $a_k$  and  $b_k$  can only have the values 0 or 1. This requirement is fulfilled automatically if  $t_b$  is chosen to be smaller than the dead time of the detectors.<sup>5</sup> In this case  $G^{(2)}(j t_b)_N$  is given by the histogram of time intervals between adjacent counts [88].

It is worth pointing out that this is not the time interval distribution examined in chapter 7. In performing time interval analysis *all* pairwise distances have been considered, while a faithful representation of  $g^{(2)}(\delta t)$  is achieved if only nearest neighbour distances are measured. A simple, unnormalized example illustrates the difference (figure 8.6). Consider a dataset consisting of counts with a period of two bins. Here we expect a strong correlation for a lag of 2. A histogram of nearest neighbour separations displays just that, while a histogram of all pairwise distances will show correlations for all lags that are integer multiples of 2.

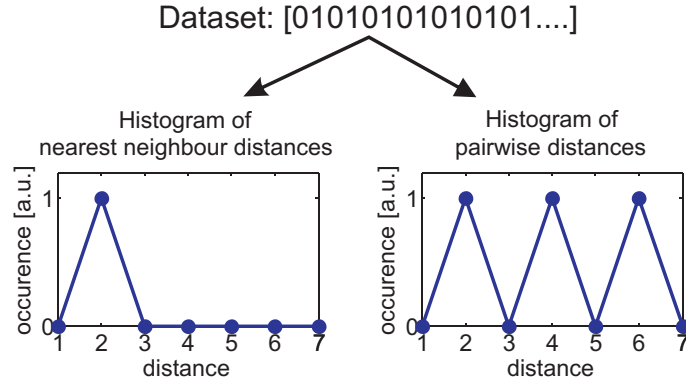


**Figure 8.6.:** Retrieving the Second Order Correlation from Time Interval Histograms

### 8.2.3. Background Correction

In measuring correlations we have to deal with an unavoidable background of counts originating mainly from dark counts generated by the photon detectors (see chapter 4 for a detailed discussion). We assume uncorrelated, constant background rates for the two detectors and label the total number of background counts accumulated during the measurement time  $T_0$   $A_b$  and  $B_b$  for the corresponding counters. Let  $a_k$  and  $b_k$  denote the measured counts in bin  $k$  then the true number of photon counts originating from fluorescence  $a_k^s$  and  $b_k^s$  can be estimated.

$$a_k^s = a_k - \frac{A_b}{N} \quad b_k^s = b_k - \frac{B_b}{N}$$

<sup>5</sup>In our measurements the photon counts were recorded with a bin size of  $t_b = 1$  ns on detectors with 52 ns and 47 ns dead times.



Likewise the unnormalized correlations from fluorescence counts  $G^{(2)}(j t_b)^s$  can be calculated from the measured unnormalized correlations and total counts

$$G^{(2)}(j t_b) = \frac{1}{N} \sum_{k=1}^N a_k b_{k+j} \quad , \quad A = \sum_{k=1}^N a_k \quad , \quad B = \sum_{k=1}^N b_k$$

defined in equation 8.14 (the index  $N$ , denoting discretization, has been dropped to simplify the notation).

$$\begin{aligned} G^{(2)}(j t_b)^s &= \frac{1}{N} \sum_{k=1}^N a_k^s b_{k+j}^s \\ &= \frac{1}{N} \sum_{k=1}^N \left( a_k - \frac{A}{N} \right) \left( b_{k+j} - \frac{B}{N} \right) \\ &= G^{(2)}(j t_b) - \frac{1}{N^2} (A_b B + A B_b - A_b B_b) \\ G^{(2)}(j t_b)^s &= \frac{1}{N^2} (N^2 \cdot G^{(2)}(j t_b) - G_b) \end{aligned} \tag{8.15}$$

The background contribution has been summarized into the term  $G_b$ .

$$G_b = A_b B + A B_b - A_b B_b$$

The normalization factor is calculated similarly,

$$\begin{aligned} \left( \frac{1}{N} \sum_{k=1}^N a_k^s \right) \left( \frac{1}{N} \sum_{k=1}^N b_k^s \right) &= \frac{1}{N^2} \left( \sum_{k=1}^N (a_k) - A_b \right) \left( \sum_{k=1}^N (b_k) - B_b \right) \\ &= \frac{1}{N^2} (A - A_b)(B - B_b) \\ &= \frac{1}{N^2} (A B - G_b) \end{aligned}$$

leading to the background corrected second order correlation function  $g^{(2)}(\delta t)^s$ .

$$g^{(2)}(\delta t)^s = \frac{N^2 \cdot G^{(2)}(\delta t) - G_b}{A B - G_b} \tag{8.16}$$

Interestingly, brief calculations show that a Poissonian background does not change the value of the second order correlation function if  $g^{(2)}(\delta t)^s = 1$ , but a super- or sub-Poissonian character of the measured correlation  $g^{(2)}(\delta t)$  is enhanced if the background is removed.

$$\begin{aligned} g^{(2)}(\delta t) = 1 &\quad \Rightarrow \quad g^{(2)}(\delta t)^s = 1 \\ g^{(2)}(\delta t) < 1 &\quad \Rightarrow \quad g^{(2)}(\delta t)^s < g^{(2)}(\delta t) \\ g^{(2)}(\delta t) > 1 &\quad \Rightarrow \quad g^{(2)}(\delta t)^s > g^{(2)}(\delta t) \end{aligned}$$

In a real measurement source fluctuations, background contributions and, in the case of a two-detector setup, non-equal splitting ratios have to be taken into account for normalization of  $g^{(2)}(\delta t)$ . Different strategies exist to achieve this [4, 88], we follow in our work the above outlined procedure [87].

### 8.2.4. Multiple Measurements

To increase the measurement statistics usually not one but several hundred measurements are performed at identical parameters and combined for the analysis. Several different strategies exist how to combine  $N_p$  consecutive datasets of length  $T_0$  and achieve a consistent normalization.

**Concatenation** The most straightforward strategy is to concatenate the single measurements into one measurement of length  $N_p \cdot T_0$  and use the equations derived above. Unfortunately the required computations are very demanding in terms of computer memory needed.

**Mean of Correlation Function** A second obvious approach consists of building the correlation functions for each of the  $N_p$  shots separately and retrieve  $g^{(2)}(\delta t)$  as the mean of the single correlation functions.

$$g^{(2)}(\delta t) = \frac{1}{N_p} \sum_{i=1}^{N_p} g_i^{(2)}(\delta t)$$

The problem here lies in the sparsity of the count record. Both the time interval histograms and the normalizations will consist of small numbers. The ratio of those two small numbers will fluctuate, washing out the interesting signals.

**Weighted Mean of Correlation Functions** The latter problem can be avoided by weighting the single correlation functions according to their total number of photon counts, so that correlation functions acquired from stronger signals are weighted more.

**Common Histogram** Alternatively one can build a common histogram of time intervals and divide by a proper normalization constant.

$$G^{(2)}(\delta t) = \sum_{i=1}^{N_p} G_i^{(2)}(\delta t)$$

In analogy to the normalization of a single measurement given in equation 8.14 the normalization is found to be given by the sum of the product of total counts from counter 1 and 2.

$$g^{(2)}(\delta t) = N^2 \frac{G^{(2)}(\delta t)}{\sum_{i=1}^{N_p} A_i \cdot B_i} \quad (8.17)$$

Here  $A_i$  and  $B_i$  denote the total number of counts in detector 1 and 2 respectively for the  $i$ th measurement. This approach can be shown to be similar to building the weighted mean.

**Background Correction** We have used in our analysis the latter approach for which the background correction can be found following the same line of calculations as above to be

$$g^{(2)}(\delta t)^s = \frac{N^2 \cdot G^{(2)}(\delta t) - G_b}{\sum_{i=1}^{N_p} (A_i \cdot B_i) - G_b} \quad (8.18)$$

with the background contribution now given by

$$G_b = \sum_{i=1}^{N_p} G_{b,i} = A_b \sum_{i=1}^{N_p} B_i + B_b \sum_{i=1}^{N_p} A_i - N_p A_b B_b \quad (8.19)$$

### 8.2.5. Error Estimation

Error estimates for the above expressions can be found by using Gauss' principle to propagate the measurement uncertainties under the assumption that  $G^{(2)}(\delta t)$ ,  $A_i$  and  $B_i$  are independent Poisson variables, i.e. that the variance equals the mean. The derivations of the following relations have been omitted to enhance the clarity of the presentation, but are straightforward results of Gaussian error propagation.

The relative error for the the uncorrected second order correlation function given in equation 8.17 is

$$\left( \frac{\Delta g^{(2)}}{g^{(2)}(\delta t)} \right)^2 = \frac{1}{G^{(2)}(\delta t)} + \frac{\sum_{i=1}^{N_p} A_i \cdot B_i (A_i + B_i)}{\left( \sum_{i=1}^{N_p} A_i \cdot B_i \right)^2} \quad (8.20)$$

while the relative error of the background corrected  $g^{(2)}(\delta t)^s$  given in equation 8.18 is

$$\left( \frac{\Delta g^{(2)}}{g^{(2)}(\delta t)^s} \right)^2 = \frac{N^4 G^{(2)}(\delta t) + G_b}{(N^2 \cdot G^{(2)}(\delta t) - G_b)^2} + \frac{G_b + \sum_{i=1}^{N_p} A_i B_i (A_i + B_i)}{\left( \sum_{i=1}^{N_p} (A_i \cdot B_i) - G_b \right)^2} \quad (8.21)$$

and finally the absolute error of the background contribution given in equation 8.19.

$$\begin{aligned} \Delta G_b^2 &= T_0 \left( \frac{A_b}{T_0} \left( \sum_{i=1}^{N_p} B_i \right)^2 + T_0 \frac{A_b^2}{T_0^2} \sum_{i=1}^{N_p} B_i \dots \right. \\ &\quad \left. + \frac{B_b}{T_0} \left( \sum_{i=1}^{N_p} A_i \right)^2 + T_0 \frac{B_b^2}{T_0^2} \sum_{i=1}^{N_p} A_i \dots \right. \\ &\quad \left. + N_p^2 T_0^2 \frac{A_b}{T_0} \frac{B_b}{T_0} \left( \frac{A_b}{T_0} + \frac{B_b}{T_0} \right)^2 \right) \quad (8.22) \end{aligned}$$

Further corrections of the correlation function due to transit time effects have been introduced by Kimble, Dagenais and Mandel [89], but can be neglected in this discussion since the lifetime of the excited state is  $1/\Gamma = 26.24$  ns while the interaction time is  $O(10 \mu\text{s})$ .

### 8.3. Measurements

Photon anti-bunching has first been observed by Kimble, Dagenais and Mandel [90] in the resonance fluorescence of a beam of sodium atoms. While a pioneering work, perfect anti-bunching for zero lag ( $g^{(2)}(0) = 0$ ) could be distilled from the measurements only after a significant amount of background analysis and taking fluctuating atom numbers into account [91]. Diedrich and Walther were the first to measure non-classical fluorescence emission of a single magnesium ion stored in a Paul trap [2]. More recently the group of Grangier measured anti-bunching in the fluorescence emission of a rubidium atom stored in a dipole trap [92].

In contrast to ion or dipole trap experiments, where arbitrary long interaction times can be achieved to collect many photons, we examine here the case of single neutral atoms propagating in a one-dimensional magnetic guide, leading to finite interaction times of the order of  $O(10 \mu\text{s})$ . As will be shown in the following we are able to observe perfect anti-bunching in the fluorescence emission of single atoms from a signal of only 1.08 counts per atom on average as derived in chapter 6.

#### 8.3.1. Autocorrelation

For the measurements presented in chapters 6 and 7 a single photon detector setup was used as detailed in chapter 2. The second order auto-correlation function can be built from the counts recorded by the single photon counter.

##### Short Time Intervals

As has been discussed before auto-correlations suffer from both dead time, effectively blinding the detector for correlations at lags smaller than 52 ns, and afterpulsing, resulting in a strong correlation peak from 52 ns to approximately 150 ns, obscuring all non-classical correlations.

Figure 8.7 shows an autocorrelation, built from one of the measurements analysed in chapters 6 and 7. Due to the dead time all information for lags smaller than 52 ns is lost. Combined with the strong afterpulsing peak no signature of the atoms can be observed in the short timescale correlation signal. In fact, looking only at this

---

<sup>6</sup>Dataset 20071205Wed\_F3\_resonant\_guide2\_05V, 878 shots, region of interest 1500 to 2000 ms.

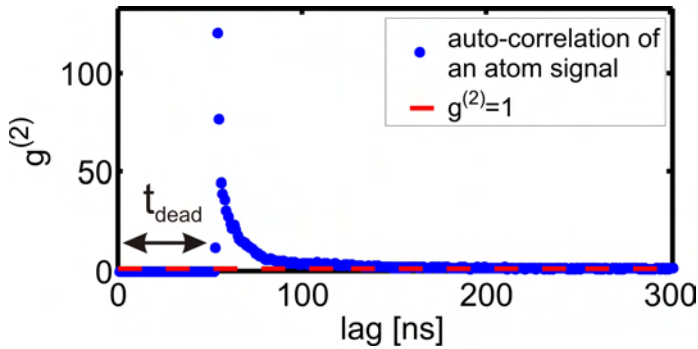


**Figure 8.7.:** Autocorrelation of an Atom Signal<sup>6</sup> Anti-bunching cannot be observed due to the detector dead time  $t_{\text{dead}}$  and strong afterpulsing.

region the second order correlation function cannot easily be distinguished from the autocorrelation of Poissonian background, depicted in figure 8.4.

Even though the afterpulsing peak could be suppressed by artificially extending the dead time in the analysis to e.g. 200 ns, no insight into the characteristics of the fluorescence emission can be gained by this procedure. Reason being that with a lifetime of 26.24 ns of the excited state all interesting non-classical correlations take place for lags smaller than 100 ns, as can be seen from figure 8.2.

### Interaction Time

For large lags the autocorrelation function  $g^{(2)}(\delta t)$  is limited by the atoms leaving the detection region. The interaction time  $t_{\text{int}}$  can be measured from  $g^{(2)}(\delta t)$  for lags from 500 ns to 50  $\mu\text{s}$ , assuming an exponential decay.

$$t_{\text{int}} = 11.5 \pm 1.0 \mu\text{s}$$

As demonstrated in figure 8.8 a simple exponential decay (red line) alone does not deliver a satisfactory fit to the autocorrelation function. The point spread function of the MM detection fibre has to be taken into account as well. The broken orange line shows that modelling the point spread function by a Gaussian function yields a much better fit, using an identical decay time of  $t_{\text{int}} = 11.5 \mu\text{s}$ .

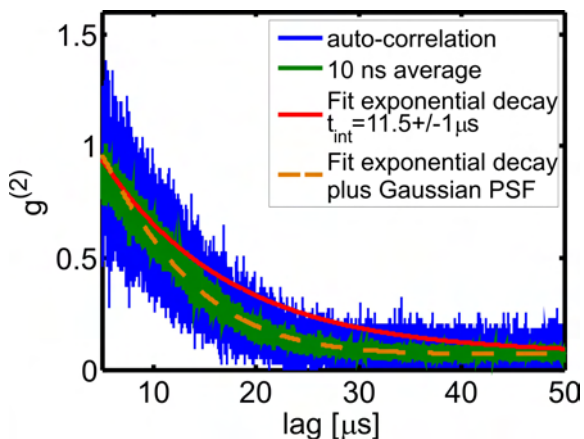


**Figure 8.8.:** Autocorrelation of the Atom Signal shown in fig.8.7 examined for lags from 5 to 50  $\mu\text{s}$ . The decay of correlations is due to atoms leaving the interaction region. A simple exponential decay does not give an estimate of the  $1/e$  interaction time, but has to be expanded with a Gaussian function, representing the point spread function of the detection fibre, to model the shape of the correlation function.

The measured  $1/e$  interaction time of  $t_{\text{int}} = 11.5 \pm 1.0 \mu\text{s}$  agrees well with the results of  $12 \pm 1 \mu\text{s}$  and  $10.5 \pm 0.5 \mu\text{s}$  obtained via independent methods in chapters 6 and 7, correspondingly.

### 8.3.2. Cross Correlation

To avoid both afterpulsing distortions and loss of information due to detector dead time the measurements analysed in this chapter have been performed using two single photon counters in a Hanbury Brown-Twiss type setup. The signal gathered by the detection fibre is split evenly by a 50/50 beam splitter after passing the interference filter. See chapter 2 for further information. Random partitioning of the beam does not influence the photon number statistics measured by the single photon counting modules [40].

As discussed in chapter 4 this detection setup leads to a secondary emission caused distortion of the correlation function, similar in effect to afterpulsing distortions but, unlike afterpulsing, secondary emission effects can be successfully compensated for, as demonstrated in chapter 4 as well.

As was the case for autocorrelations the interaction time can be measured from the coherence time of the cross correlations, yielding identical results.

#### Effects of the Corrections

We built  $g^{(2)}(\delta t)$  from a dataset consisting of 4409 consecutive measurements of 2 s each at resonant illumination.<sup>7</sup> To demonstrate the effect of background and secondary emission corrections the uncorrected  $g^{(2)}(\delta t)$  is displayed together with the corrected cross-correlation functions in figure 8.9.

The effects of the corrections on  $g^{(2)}(0)$  are listed below for arrival times between 1500 and 1600 ms. Secondary emission has of course no influence on the measured correlations at lag 0. The corrected value is given here to demonstrate that errors introduced by the correction algorithm are negligible as compared to the uncertainty of the measurement.

	$g^{(2)}(0)$
uncorrected	0.0490 $\pm$ 0.0490
<b>background corrected</b>	<b>0.0005 <math>\pm</math>0.0010</b>
secondary emission corrected	0.0444 $\pm$ 0.0490
background and secondary emission corrected	-0.0004 $\pm$ 0.0010

<sup>7</sup>Dataset 20071220Thu\_F3\_resonant\_412mV, 4409 shots

<sup>8</sup>Dataset specified in the main text, region of interest 1600 to 2000 ms arrival time.

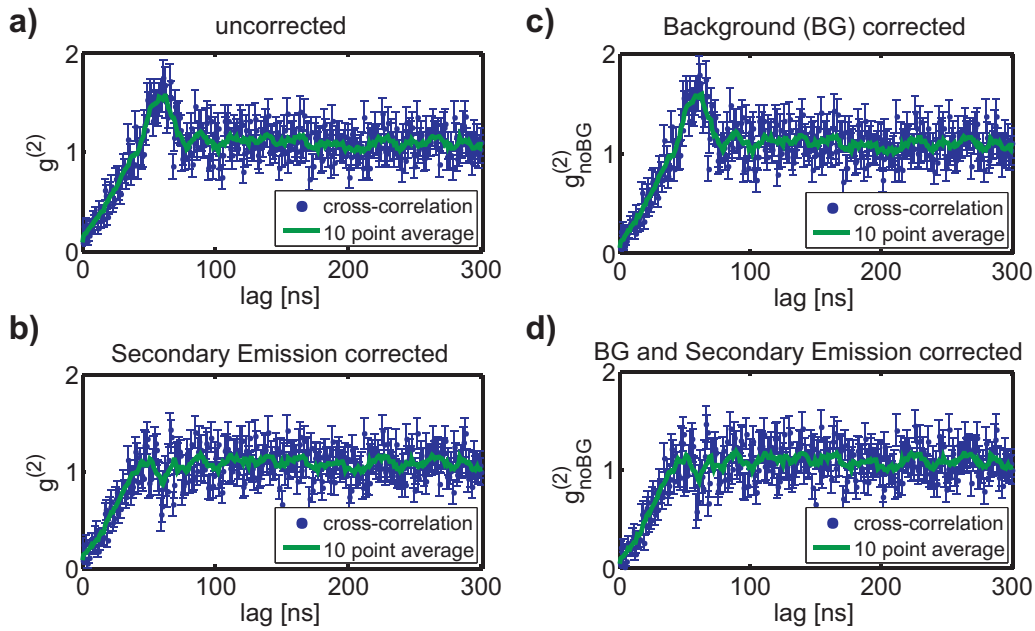


**Figure 8.9.:** Effect of the corrections on  $g^{(2)}(\delta t)$ .<sup>8</sup>

a) The uncorrected second order cross-correlation function exhibits a secondary emission peak around 60 ns.

b) Correcting for the secondary emission by using a background measurement, as described in chapter 4, results in the expected shape of  $g^{(2)}(\delta t)$ .

c) & d) The likelihood of the measured time intervals can be corrected for the known background count rate, albeit this has only a small effect on  $g^{(2)}(\delta t)$  due to the already good background suppression of our detector. Hence the background corrected correlation functions in c) and d) are very similar to the results in a) and b).

The correlation functions are shown with error estimates calculated according to section 8.2.5. The green line is the result of a ten point moving average smoothing to guide the eye.

### 8.3.3. Non-Classical Correlations

#### Anti-bunching for Zero Lag

We measure a background corrected anti-bunching of  $g^{(2)}(0) = 0.0005 \pm 0.0010$  for arrival times between 1500 and 1600 ms. Thus the fluorescence displays perfect anti-bunching corresponding to  $g^{(2)}(0) = 0$  within one standard deviation. The results have been confirmed by separate analyses on arrival times between 1500 and 2000 ms, always resulting in values for  $g^{(2)}(0)$  within one standard deviation of 0.

It is worth noting, that due to the low background of our detector even the directly measured  $g^{(2)}(0)$  without background correction is within one standard deviation of  $g^{(2)}(0) = 0$ .

**Mean Number of Photons** The above results confirm that we are deep into the non-classical regime and have to good approximation at most one atom in the detection region at all times. As discussed previously the  $^{87}\text{Rb}$  atom can be approximated very well by a two-level system on the used transition. Thus, with a single  $^{87}\text{Rb}$  atom in the detection region only photon states with exactly 0 or 1 photons should be observed. To increase the mean photon number beyond 1 necessarily more than one atom has to have been present in the detection region.

From equation 8.7 we can estimate the mean number of photons  $n$ .

$$n = \frac{1}{1 - g^{(2)}(0)} \quad (8.23)$$

With a background corrected value of  $g^{(2)}(0) = 0.0005 \pm 0.0010$  we get  $n = 1.0005 \pm 0.0010$  photons, and even the raw, uncorrected value of  $g^{(2)}(0) = 0.049 \pm 0.049$  yields  $n = 1.05 \pm 0.05$  photons. Both the uncorrected and the background corrected result agree within one standard deviation with the hypothesis of a pure single photon state.

coincident photon number $n$	
uncorrected	1.05 $\pm$ 0.05
background corrected	1.0005 $\pm$ 0.0010

The mean distance between the atoms for the measurement presented here (arrival times between 1500 and 1600 ms) can be calculated to 360  $\mu\text{s}$  from the recorded count rate. Since this is much larger than the  $1/e$  interaction time  $t_{\text{int}} = 12 \pm 1 \mu\text{s}$  we do indeed expect at most one atom to be present in the interaction region at all times.



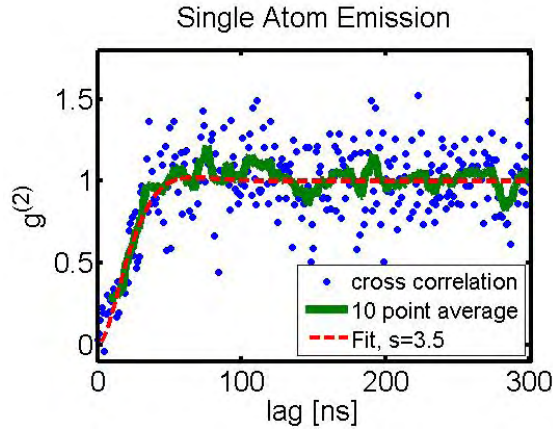


**Figure 8.10.:**  $g^{(2)}(\delta t)$  of the fluorescence emission of a single atom.<sup>9</sup> The green line is again the result of a 10 point moving average. The broken red line is a fit according to eq.8.12, yielding a saturation parameter of  $s = 3.5 \pm 0.5$ .

### Anti-bunching as Function of the Lag

The photon anti-bunching in the fluorescence emission of a single atom under resonant single mode illumination is described by equation 8.12. The measured  $g^{(2)}(\delta t)$  for arrival times between 1500 and 1600 ms is shown together with a fit according to equation 8.12 in figure 8.10. Note that the usual 10 point moving average used to guide the eye starts at a lag of 10 ns, since obviously for the first 9 points no moving average of 10 points can be constructed.

The fit shows excellent agreement to the measurement with the probe beam intensity of  $3.5 \pm 0.5$  saturation intensity as only free parameter. The lifetime of the excited state was assumed to be 26.24 ns [44]. Saturation is in our setup achieved at a power of approximately 325 pW. For the measurements presented here the probe beam was externally stabilized to a power of 1 nW, corresponding to 3.1 times the saturation intensity.<sup>10</sup>

### Rabi Oscillations

From equation 8.12 we expect Rabi oscillations to emerge if the atoms are illuminated with more than 5 times the saturation intensity. The resulting theoretical shape of the second order correlation function of fluorescence emitted by a single atom under resonant illumination was given in figure 8.2.

To examine this we have probed the atoms with Rabi frequencies ranging from  $0.7\Gamma$  to  $2.3\Gamma$ , corresponding to 1 to 11 times saturation intensity. Figure 8.11 presents the resulting correlation functions together with the theoretical models, showing excellent agreement.

<sup>9</sup>Dataset as above 20071220Thu\_F3\_resonant\_412mV, 4409 shots, region of interest 1500 to 1600 ms arrival time.

<sup>10</sup>See chapter 9 for details of the probe intensity stabilization.

<sup>11</sup>a) Dataset 20071214Fri\_F3\_2Fbr\_resonant\_130mV, 1054 shots, 1500-2000 ms arrival time

b) Dataset 20071214Fri\_F3\_2Fbr\_resonant\_276mV, 1041 shots, 1500-2000 ms arrival time

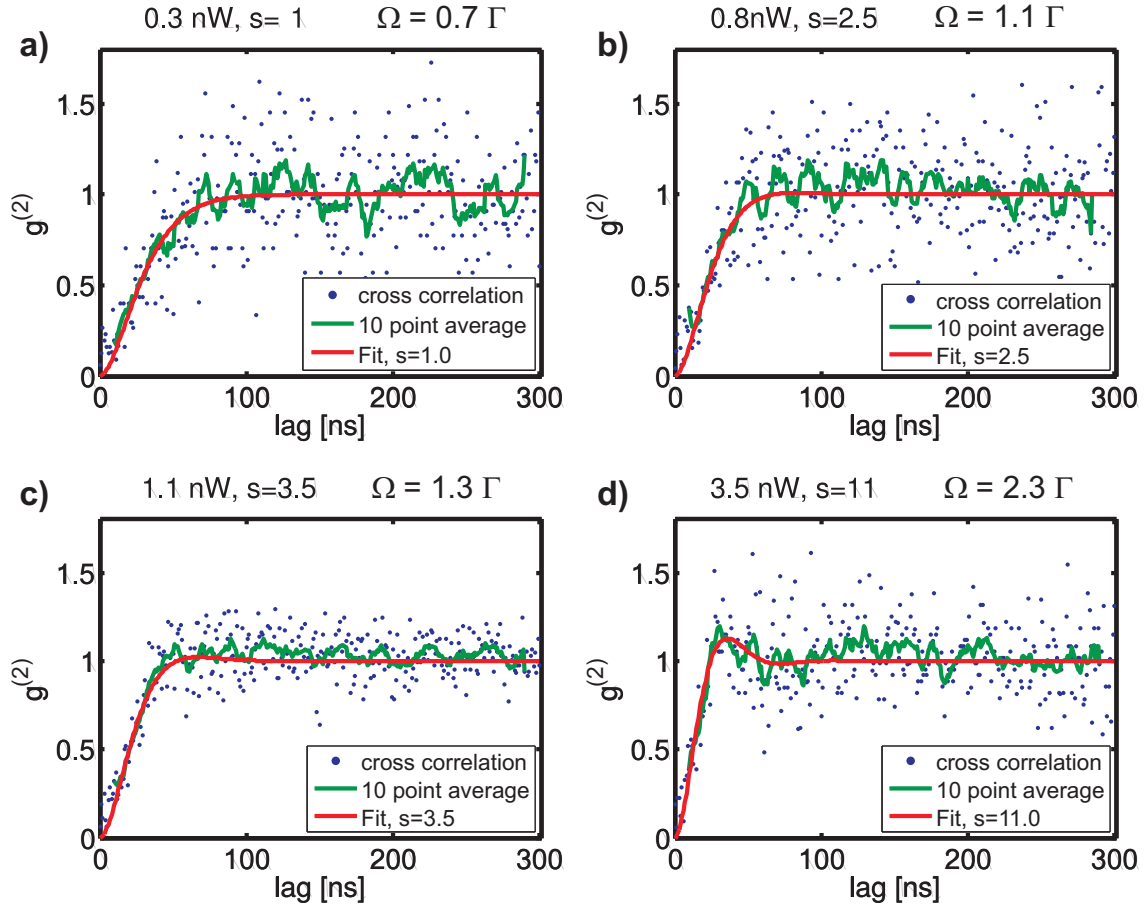


**Figure 8.11.:**

Rabi Oscillations in the Cross-Correlation Function  
 Cross-correlation functions showing the fluorescence emissions of single atoms for four different probe beam powers.<sup>11</sup>

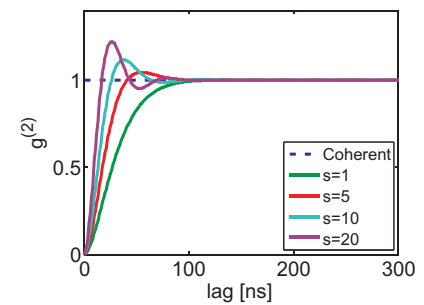
a) Illuminated with saturation power the correlations of the fluorescence do not exhibit Rabi oscillations, but slowly approach  $g^{(2)}(\delta t)=1$ . The final value is reached after approximately 4 times the lifetime of the excited state.

b) With a probe beam power 2.5 times the saturation power the final value is approached much faster, but still no Rabi oscillations are induced.

c) At 3.5 times saturation power a very slight overshoot emerges.

d) At 11 times saturation power a clear Rabi oscillation emerges, as predicted by theory.

In all four graphs the green lines were produced by a 10 point moving average and the red lines are theoretical models corresponding to equation 8.12 with the probe beam power as only free parameter.



Theoretically expected second order correlation function for different values of the saturation parameter  $s$  and  $1/\Gamma = 26.24$  ns, as shown in figure 8.2.

### Correlations as Function of Atomic Density

Due to the passage of the atomic pulse through the detection region we expect to see more than one atom co-instantaneously in the detection region for early arrival times when the atomic density is high. Higher atomic densities will lead to  $g^{(2)}(0) > 0$  since then two photons can be emitted simultaneously by two atoms in the detection region.

An analysis of the non-classical correlations as function of the arrival time shows that for arrival times later than 1000 ms the atomic density is low enough to guarantee that no more than one atom is in the detection region at every given time. At arrival times earlier than 1000 ms the density of atoms is high enough to increase  $g^{(2)}(\delta t)$  significantly above 0, indicating the presence of more than one atom in the detection region.

Unfortunately saturation effects in the P7888 FAST ComTec counter card falsify the measurement of  $g^{(2)}(0)$  for high atom densities. As can be seen from figure 8.12c)  $g^{(2)}(0)$  is limited to 0.5 for peak densities, since for high count rates data loss in channel two of the counter card occurs (see section 9.6.2).

The card has been thoroughly tested to faithfully record count rates below 10 kcps, corresponding to arrival times later than 1000 ms. Figures 8.12e) and 8.12f) depict  $g^{(2)}(0)$  and the corresponding photon numbers calculated via equation 8.7 from the reliable  $g^{(2)}(0)$  for  $t > 1000$  ms. At late arrival times pure single photon states are detected.

Comparing the mean distance between atoms depicted in figure 8.12b) with the correlation at vanishing lag given in figure 8.12c) we note that  $g^{(2)}(0)$  deviates significantly from zero when the mean separation becomes much smaller than the interaction time.<sup>13</sup>

The density dependence of the correlation function can be examined despite the distortion of  $g^{(2)}(0)$ . In figure 8.12d) equation 8.7 is applied to  $g^{(2)}(1 \text{ ns})$  to calculate an upper limit to the photon number  $n$ . Strictly speaking equation 8.7 applies only to  $g^{(2)}(0)$  of a Fock state, but an examination of  $g^{(2)}(1 \text{ ns})$  corresponds basically to a measurement with a detector with reduced temporal resolution.

The photon number is proportional to the number of atoms in the detection region, hence the calculated mean photon number  $n$  should be proportional to the atom density  $\rho$ . We start evaluating the correlation function when one photon has been detected. Hence the minimal photon number is 1. The probability to generate a second photon count is proportional to the atom density. With the proportionality factor  $a$  the mean photon number  $n$  is therefore given by

$$n = 1 + a \cdot \rho \quad (8.24)$$

c) Dataset 20071220Thu\_F3\_resonant\_412mV, 4409 shots, 1500-2000 ms arrival time

d) Dataset 20071219Wed\_F3\_resonant\_2000mV, 1757 shots, 1500-2000 ms arrival time

<sup>12</sup>Dataset 20071220Thu\_F3\_resonant\_412mV, 4409 shots.

<sup>13</sup>The  $1/e$  interaction time was measured to  $12 \pm 1 \mu\text{s}$ , but approximately 300  $\mu\text{s}$  are needed to collect all emissions from a single atom.

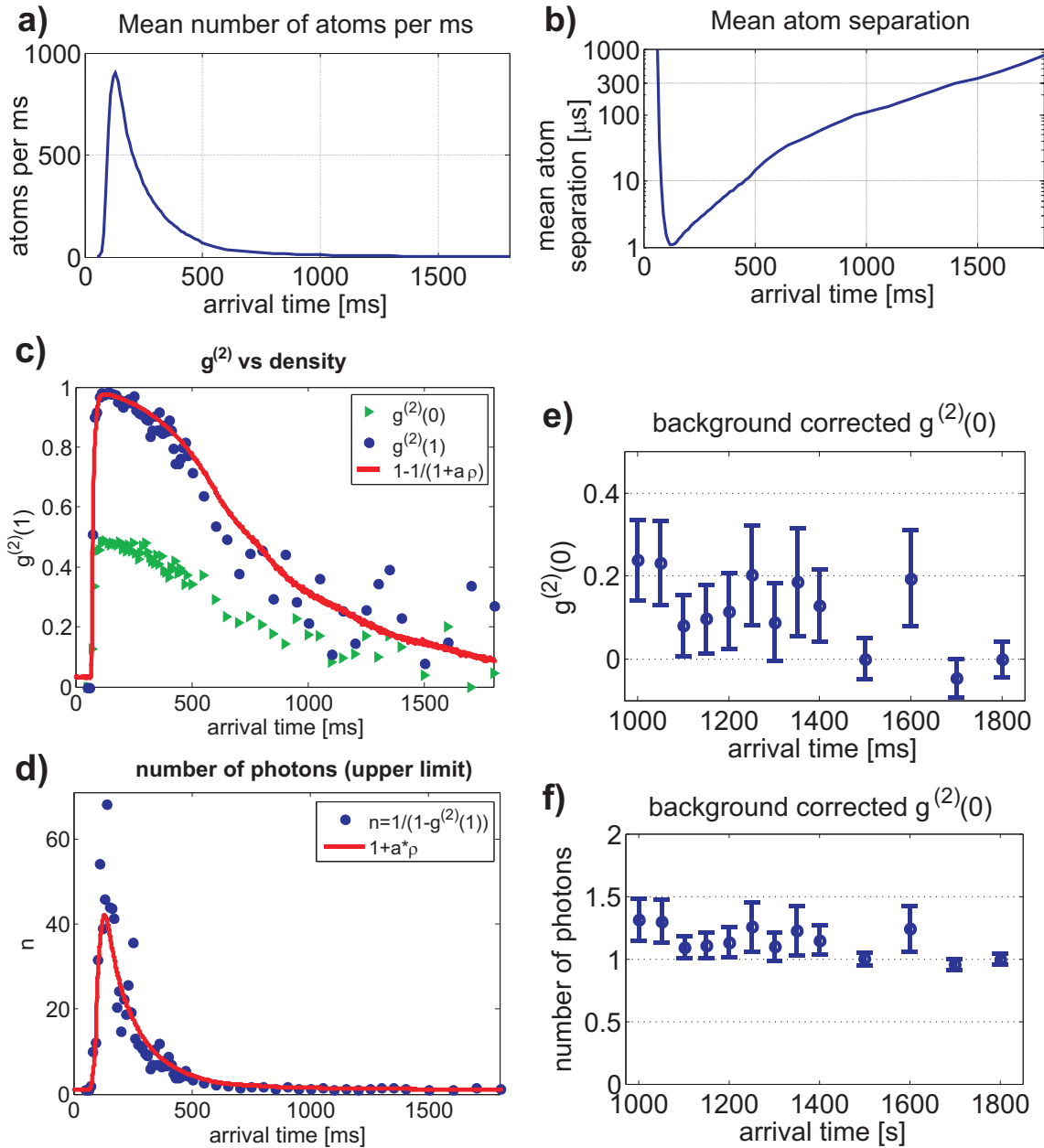


**Figure 8.12.:** Non-classical Correlation as Function of the Atom Density<sup>12</sup>

- a) Atom Density  $\rho$  as function of arrival time.  
b) Mean temporal distance between the atoms versus arrival time.  
c) The uncorrected value of  $g^{(2)}(i)$ s plotted versus the arrival time, which is proportional to the atomic density.  $g^{(2)}(0) > 0$  indicates presence of more than one atom in the detection region. Counting card effects distort  $g^{(2)}(0)$  for high atom densities, limiting it to  $g^{(2)}(0) = 0.5$  (see main text).  $g^{(2)}(1 \text{ ns})$  is proportional to the atom density  $\rho$  over almost 3 orders of magnitude in  $\rho$ .  
d) An upper limit of the mean number of photons emitted simultaneously is calculated from the uncorrected  $g^{(2)}(1 \text{ ns})$ . The photon number is proportional to atom density over three orders of magnitude in density. The deviation for high densities is discussed in the main text.  
e) Background corrected values of  $g^{(2)}(0)$  for arrival times later than 1000 ms.  
f) Mean number of simultaneously emitted photons calculated from the background corrected values of  $g^{(2)}(0)$ . Errors bars in d) and e) indicate one standard deviation.

Using the measured atom density  $\rho$  shown in figure 8.12a) we can demonstrate that  $n$  shows the expected proportionality to atom density.

The deviations for peak atom densities around 130 ms arrival time are explained by an additional artefact of the counter card. In addition to data loss for coincident counts at high count rates the P7888 card has a small probability to timestamp coincident events with a time difference of 1 ns. If that occurs, channel 2 will always receive the later timestamp, indicating an electronic delay as the most likely cause of error (see section 9.6.2). Therefore at the highest densities a timing jitter of 1 ns for coincident counts exists, leading to some coincident counts being recorded with 1 ns lag. This results in the overshoot of the measured distribution for peak densities.

Inserting relation 8.24 into equation 8.7  $g^{(2)}(0)$  can be described as function of the atom density.

$$g^{(2)}(0) = 1 - \frac{1}{1 + a \cdot \rho}$$

As shown in figure 8.12c), using the above relation with the proportionality factor  $a$  derived from the fit to photon number in figure 8.12d), the correlation at lag 1 ns can be described as function of the measured atom density  $\rho$  over almost three orders of magnitude in  $\rho$ .

To the best of our knowledge this is the first observation of fluorescence emission anti-bunching over a large range in atom density.

## 8.4. Summary

Using two single photon detectors in a Hanbury Brown and Twiss type configuration fluorescence signals from atoms passing the detector were recorded with 1 ns temporal resolution. It has been demonstrated that detector artefacts can be successfully removed from the measured signal for low atomic densities.

Correlation analysis of the recorded photon counts reveals non-classical second order intensity correlations. This is a direct observation of photon anti-bunching in the fluorescence emission of single atoms passing the integrated detector.

The coherence time is limited by the interaction time of the atoms with the probing light field. An interaction time of  $t_{\text{int}} = 11.5 \pm 1.0 \mu\text{s}$  was measured, in good agreement with the previously obtained measurements of  $t_{\text{int}} = 12 \pm 1 \mu\text{s}$  from variance over mean analysis and  $t_{\text{int}} = 10.5 \pm 0.5 \mu\text{s}$  from time interval analysis.

We measured the anti-bunching of fluorescence photons from a single atom to  $g^{(2)}(0) = 0.049 \pm 0.049$  without background correction, corresponding to a maximum number of  $n = 1.05 \pm 0.05$  photons simultaneously emitted. Background correction reduces the correlation for zero lag to  $g^{(2)}(0) = 0.0005 \pm 0.0010$  corresponding to a maximum number of  $n = 1.0005 \pm 0.0010$  photons. Thus the fluorescence displays perfect anti-bunching corresponding to  $g^{(2)}(0) = 0$  within one standard deviation, demonstrating that at each point in time no more than one atom is present in the detection region. Consequently the photon counts indicate detection of true single photon states.

It has been confirmed that an increased atomic density in the guide leads to  $g^{(2)}(0) > 0$  due to the finite probability simultaneous presence of more than one atom in the detection region. In an unprecedented measurement it was demonstrated that the measured value of  $g^{(2)}$  for vanishing lag is proportional to atom density over three orders of magnitude in density.

Rabi oscillations of the correlation function have been observed and proven to be in excellent agreement with the theoretical expectations.

*"It is easy to lie with statistics. It is hard to tell the truth without it."*

Andrejs Dunkels

**Part II.**

**Nuts and Bolts**





## 9. Setup

An ultracold atom experiment is a quite complex merge of ultra-high vacuum technology, hundreds of opto-mechanical components, highly stabilized and interdependent laser systems, sensitive detection setups and a vast array of control electronics delivering everything from kilovolts of supply voltage to almost shot-noise limited currents in the milli- and microampere range.

Even though every last part of the setup was instrumental in achieving the results presented here, a full treatment is beyond the scope of this work. Since the experiments presented here used the ultracold atom production machine mainly as a tool to deliver single atoms to the detector I will describe these topics only superficially, just enough to give a basic understanding of how the experiment works. But for further information I will in large parts refer to previous works that can give a much deeper treatment of those subjects than is possible here.

There are two main differences between our experiments and standard ultracold atom experiments. Firstly, due to the high number of statistics needed to examine correlations, an above standard level of stability and reproducibility over hours and even days is required. Secondly, time of flight imaging (ToF), the standard method of atom observation, is only of minor importance for diagnosis. Instead the novel integrated fibre based fluorescence detector together with the associated photon detection setup is used.

An important, but conceptionally very simple, improvement of the setup was to increase the pointing stability of the laser beams. In the old setup insufficiently stable beam optic mountings and long beam paths led to day to day fluctuations and made frequent re-adjustments necessary. These problems have been avoided in the redesign of the setup in Vienna by employing exclusively one inch pillars as mounting posts in combination with high quality mirror mountings and a reduction of the beam paths by guiding the light in fibres wherever feasible.

Combining these measures with an increase in MOT laser power lead to a drastic increase in stability enabling reproducible experiments over the course of several weeks to a few months without the need for even minor re-adjustments. The laser power was increased by the introduction of the tapered amplifier system described in chapter 11.

Here I will strive to describe those parts of the setup that could not be treated in chapter 2, but are nonetheless peculiar to this experiment.

## 9.1. Overview

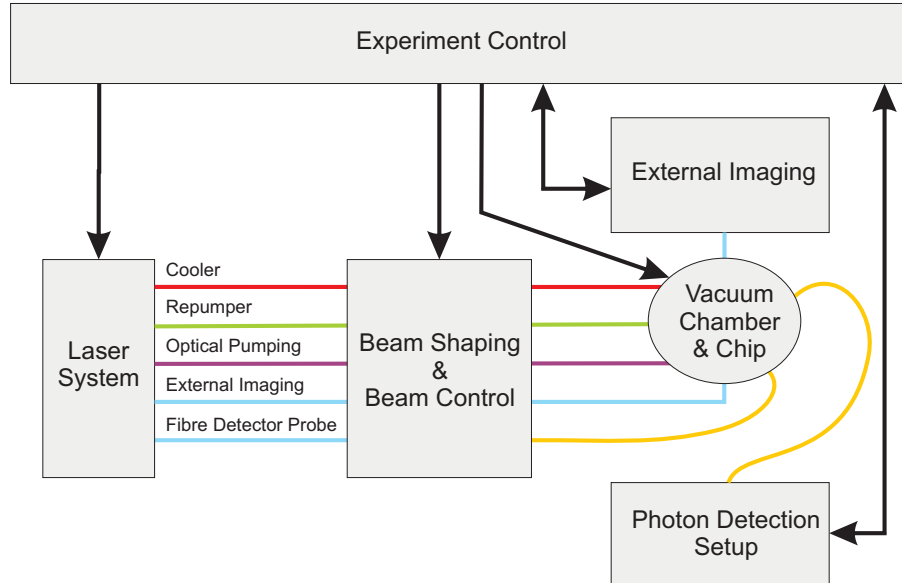


**Figure 9.1.:** Structural Overview of the Setup

The setup is subdivided into six functional elements marked by the grey boxes. The coloured lines indicate the different lasers.

The experimental setup can be broken down into six basic blocks, separated spatially and, at least to a large degree, functionally. Figure 9.1 shows a structural diagram of the setup. The six basic blocks are:

- laser system
- beam shaping and beam control optics
- vacuum chamber and chip
- external imaging (for ToF)
- photon detection setup
- experiment control

The laser system will be discussed in section 9.3.

Beam shaping and beam control follows standard procedures and consists largely of simple mirrors and lenses. Temporal control over the beam pulses is attained by switching the beams using a combination of acousto-optical modulators (AOMs) and mechanical shutters. AOMs allow fast ( $O(\mu\text{s})$ ) switching of the beams, but achieve only a suppression of approximately  $10^{-3}$ . Mechanical shutters are much slower, switching typically in 1-3 ms, but allow complete blocking of the beam.

Trapping, transfer and detection of atoms takes place in the vacuum chamber where the atom chip is mounted. Both chamber and chip have become standard technology

in our group and will be discussed briefly in section 9.4, with a focus on the fibre integration into the chip. Similarly, the external imaging will briefly be discussed in section 9.5.

The photon detection setup is central to this thesis and has been presented in section 2.5. Additional technical details of the fibre connections will be discussed in section 9.6.

To get an understanding of the experimental cycle and the interplay of the different elements we will discuss the experiment control first.

## 9.2. Experiment Control

With the move to Vienna the experiment control was expanded and adapted for autonomous execution of long series of measurements. Logging of scanned parameters was introduced as well as an enhanced interfacing with the newly written ToF camera control software, allowing for automated scanning of large, multidimensional parameter spaces with online pre-analysis capability. The automated ToF parameter scans were used for characterisation and optimisation of the initial MOT and the magnetic traps. A small part of these measurements is presented in [84].

### 9.2.1. Experimental Cycle

The experimental cycle was already briefly discussed in chapter 2. Figure 9.2 reproduces figure 2.1 with the addition of an intermediate magnetic trapping stage between the MOT and the chiptrap phase.

Using a standard Mirror-MOT setup [31–34] we trap  $10^8$   $^{87}\text{Rb}$  atoms from the background gas provided by a hot Rb-Dispenser.<sup>1</sup> Once the MOT is saturated with atoms the trap is compressed and shifted close to the atom chip by changing the magnetic trapping fields. At the new position, only 1 mm to several hundred micrometer from the chip surface, the atoms are optically pumped into the  $|F = 2, m_F = 2\rangle$  magnetic substate, compatible with magnetic trapping. At this stage polarization gradient cooling has reduced the temperature to less than 15  $\mu\text{K}$ .

Subsequently the MOT laser beams are turned off and the atoms are transferred into a magnetic trap generated by macroscopic copper wires underneath the atom chip (see figure 9.3). The magnetic trap generated by the copper structures is mode matched to the compressed MOT for optimal transfer efficiency. Here evaporative cooling methods may be employed to reduce the temperature of the atoms.

---

<sup>1</sup>A Rb-Dispenser is essentially a reservoir of solid Rb embedded in a wire. Pushing several amperes of current through the wire heats the Rb, leading to evaporation.

Once magnetically trapped the atoms can be brought even closer to the chip surface by compressing the magnetic trap. The compressed trap can in turn be mode-matched to the magnetic trap generated by the microscopic atom chip wires. At a distance of approximately 100  $\mu\text{m}$  the atom cloud can be transferred into the chiptrap.

Here the atoms equilibrate to their final temperature before being transferred into a 1D magnetic guide, again generated by the atom chip, that leads to the fibre detector. In the guide the atoms expand according to their temperature towards the detection region. Atom detection is performed by guiding the atoms into the focus of a lensed fibre, where they are excited by light resonant to a closed transition. The fluorescent light from the excitation region is collected by a second fibre which guides the light to the photon detection setup.

The intermediate magnetic trap generated by the copper structures introduced in figures 9.2 and 9.3 is needed to achieve optimal transfer efficiency from the MOT to the chiptrap. It will be instrumental in achieving Bose-Einstein condensation and, hopefully, one-dimensional condensation, but was omitted for the measurements presented here. We have transferred the atoms directly from the MOT into the chiptrap with an efficiency of about 1 %, since for the single atom experiments a low density of thermal atoms was desired.

Of the  $10^8$  atoms in the MOT  $3 \cdot 10^6$  atoms are transferred into the initial magnetic chiptrap, of which  $2 \cdot 10^6$  atoms remain after 1 s of thermalization and evaporative cooling. Approximately 800 000 atoms are finally transferred into the 1D guide which leads them to the detector. The following table gives an overview of the approximate temperature of the atoms in the separate stages of the experiment.

Temperature of the atomic ensemble	
end of Molasses	< 15 $\mu\text{K}$
chiptrap Z	25 $\mu\text{K}$ (transversal)
1d guide	$\approx$ 40 $\mu\text{K}$ (transversal)

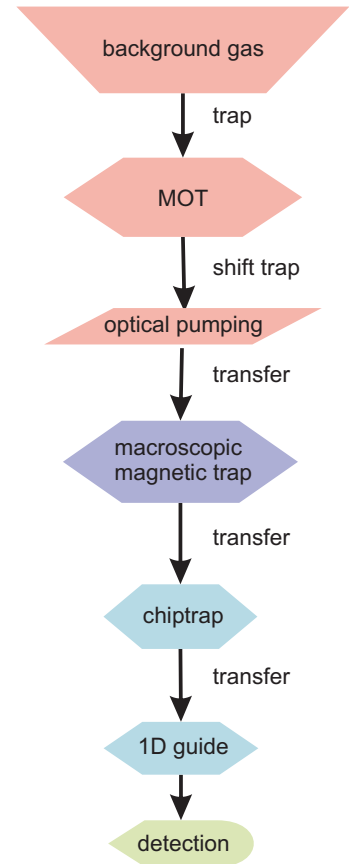
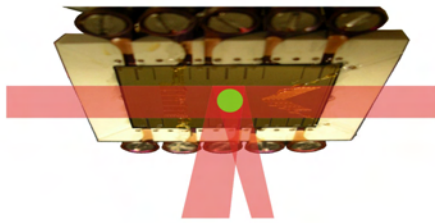


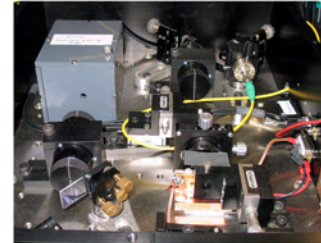
**Figure 9.2.:**  
Experiment Cycle Diagram

## a) MOT

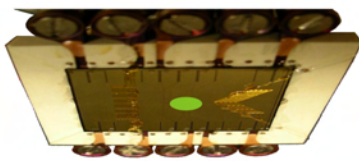


← 780nm  
laser  
+  
external fields

## MOT laser setup

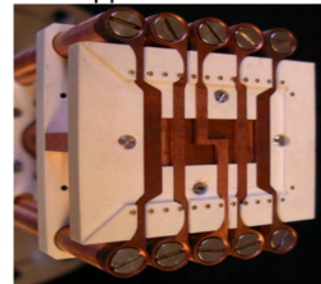


## b) macroscopic magnetic trap

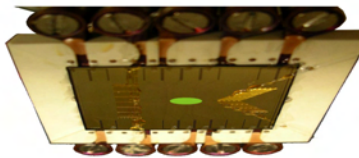


←  
copper  
structure

## copper structure



## c) chip magnetic trap



←  
atom chip

## atom chip

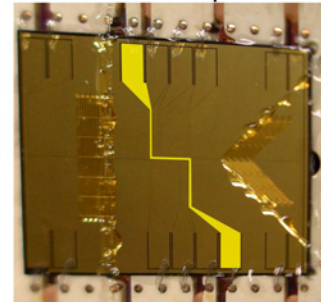


**Figure 9.3.:** Trapping Atoms Basic Procedure

A dispenser (not shown) provides a background gas of rubidium.

a) Three counterpropagating pairs of resonant laser beams combined with magnetic fields form a MOT that traps a cloud of  $^{87}\text{Rb}$  (here shown in green) from the gas. Note that two of the laser beam pairs are completed by a  $45^\circ$  reflection on the atom chip (a so-called mirror MOT [14, 30, 34]). The left column shows the atom chip in its mounting, hanging upside down to allow time of flight expansion temperature measurements when the trapping fields are turned off.

b) Current flowing through a Z-shaped copper wire under the atom chip (right) combined with an external bias field generates a magnetic trap close to the chip [34, 36]. Since the volume of the magnetic trap is much smaller and field gradients are much higher than in the MOT the transfer from the MOT to the magnetic trap involves a compression of the cloud. The atoms are now trapped at a distance  $O(1 \text{ mm})$  from the chip.

c) Compressing the magnetic trap generated by the copper wire and moving the trapped cloud close to the chip allows transfer into a magnetic trap generated by current flowing through a microscopic Z-shaped wire on the atom chip (right, marked in yellow) combined with an external bias field [34]. The atoms are now trapped at a distance  $O(100 \mu\text{m})$  from the chip and can be manipulated and moved by changing the current through the chip wires.

### 9.2.2. Signal Generation

The experiment is controlled via 16 analogue and 8 digital (TTL) signals generated by three National Instruments PCI-computer-cards<sup>2</sup> programmed in Labview plus 16 digital in-out channels provided by 2 logic boxes developed by the electronics workshop of the Physikalisches Institut, Universität Heidelberg<sup>3</sup>.

The digital National Instrument card serves as a clock for the experiment, generating a master trigger pulse that is sent to the other signal generators for synchronization of the output pulses. The control computer containing the NI-PCI cards is built into the experiment, to avoid ground loops. Access to the Labview control surface is realized via remote control over a wireless-LAN connection.<sup>4</sup> The generated signals are connected to the experiment hardware by a custom built interface, developed as well by the electronics workshop of the Physikalisches Institut. For more information about the Labview control program see [30, 93].

#### Logic Box

The FPGA's contained in the logic boxes are programmed in VHDL, but a toolbox of logic-VI's for Labview exists that allows to conveniently build logic input-output circuits. The programmed FPGA resembles a simple electronic circuit that can generate output signals conditional on the state of one or several inputs. In contrast to a custom built electronic circuit FPGA-based devices offer flexibility. The virtual electronic circuit can be changed at any time by reprogramming the FPGA. With the Labview interface it becomes even possible that one logic box changes the behaviour of several other logic boxes conditioned on the state of an experimental input signal for optimal analysis. A minor, but not to be overlooked, advantage of the logic box devices is that they allow multiple changes of the output level of a channel after a single trigger, creating the possibility to generate arbitrarily shaped TTL pulses.

A programmed logic box can for all purposes be treated as a fixed electronic circuit, hence the logic boxes offer excellent timing stability. For this reason they have been chosen to control all time-critical functions of our experiment, such as laser shutters, AOM and detector gates.

Analogue versions of the logic boxes exist as well, which can conveniently be used as programmable function generators. A prototype of these has been employed in my diploma thesis to generate arbitrarily shaped light pulses via analogue AOM control [48].

---

<sup>2</sup>One NI-6602 and two NI-6713 cards available from [www.ni.com](http://www.ni.com).

<sup>3</sup>The FPGA-based (field-programmable gate array) logic boxes are now commercially available under the trade name of *NemboX* in combination with a set of Labview-VI's for convenient programmability from W-IE-NE-R, Plein & Baus GmbH, Burscheid, Germany [www.wiener-d.com](http://www.wiener-d.com).

<sup>4</sup>Experience has shown that a direct connection of the control computer to the ethernet creates strong ground-loops.

### Timing Diagram

Figure 9.4 depicts the timing of the transfer from MOT to magnetic chiptrap. After saturating the atom number in the MOT, the trap is slowly shifted closer to the atom chip by increasing the MOT fields over 150 ms. When the atomic cloud has reached its final position the magnetic fields are switched off and the cloud is allowed to expand in the optical molasses generated by the laser beams alone for 12 ms. At the end of the molasses the laser fields are

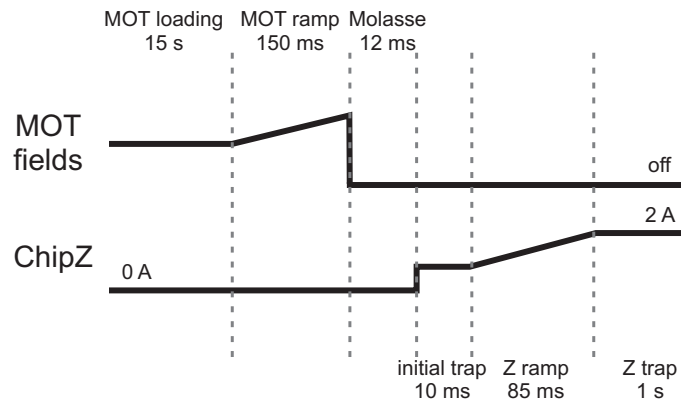


Figure 9.4.: MOT Timing

switched off and the magnetic trap is activated. For the first 10 ms the chiptrap is operated at low current to achieve a trap minimum far away from the chip. In the following 85 ms the current is slowly increase to compress the trap and bring the trap minimum closer to the chip. The trap is then held for 1 s at a bias field of 20 G and an anti-Ioffe field of 1 G. The relation between wire current, magnetic fields and distance of the trap minimum to the chip is discussed in chapter 10.

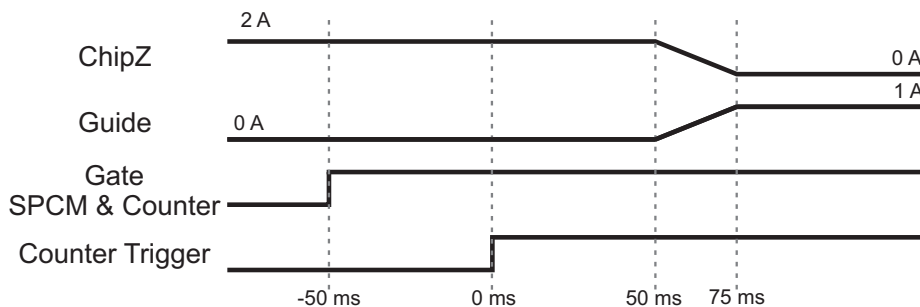


Figure 9.5.: Timing Diagram of the Detection

Figure 9.5 displays the timing of the photon detection circuit. The atoms are transferred from the chiptrap into the guide by decreasing the current in the chip-Z while simultaneously increasing the current in the guide-wire. The final guide minimum is at a distance of  $62.5 \mu\text{m}$  from the chip surface, aligned with the detection region, at a bias field of 20 G and an anti-Ioffe field of 1 G.

As soon as the Z trap is released the atoms will expand in the guide towards the detection region. Hence the single photon counting module (SPCM) and the counting card are triggered to record photon counts 50 ms before releasing the atoms to accumulate a background signal before the first atoms arrive. In order to prevent damage of the

SPCM both the SPCM and the counter card are gated 'off' during the MOT phase. The SPCM generates a false count upon receiving the gate signal and the counter card is known to exhibit a 20 ns dead time after being gated active [72]. Therefore the gate is activated 50 ms before the trigger arrives. Time indices in figure 9.5 are given relative to the start of the measurement. Once the counter is triggered it accumulates photon count arrival times for 2 s of measurement time.

## 9.3. Laser System

Diode lasers are popular light sources in atomic physics due to their low cost, flexibility and ease of operation [94]. The resonator length of a laser diode is with typically 300  $\mu\text{m}$  quite small, leading to a linewidth of several hundred MHz.

### 9.3.1. External Cavity Diode Lasers

To be of use in MOT experiments the linewidth of the lasers has to be reduced to below 1 MHz. A straightforward approach to frequency stabilize a diode laser is to increase the cavity length. Laser diodes are extremely sensitive to back-reflections, making it possible to build an external cavity around the diode that dominates the lasing behaviour. This is realized in an external cavity diode laser (ECDL) setup, where a part of the output beam is reflected back into the diode for optical feedback.

The long form of the acronym ECDL is variably given to stand for *external* cavity diode laser or *extended* cavity diode laser. In both cases the laser cavity is defined by the back facet of the diode and an external grating or mirror. Even though the terms are used as interchangeable in most of the literature a subtle difference exists. Following the definition given in [95], I use the denotation *extended* cavity diode laser for a system with anti-reflection coated diode front facet, where the cavity consists *only* of the diode back facet and the mirror or grating. The term *external* cavity diode laser applies to a system employing a not anti-reflection coated diode, as used in our experiments. Here the laser cavity is actually composed of three competing cavities, leading to notable difference in the system behaviour as compared to a anti-reflection coated diode systems.

ECDL's are usually constructed in either Littman- [96] or Littrow-configuration [97] as shown in figure 9.6, reaching linewidths of approximately 1 MHz without active stabilization. Used in conjunction with active stabilization methods, discussed later in this chapter, stabilization with a precision of a few kHz can theoretically be achieved, while in real experiments typically a few hundred kHz linewidths are reached.

In Littrow-configuration the zeroth order reflection on a holographic grating is used as output beam, while the first order diffraction is fed back into the diode for stabilization. Wavelength tuning is achieved by a rotation of the grating, leading to an angular displacement of the output beam as well.



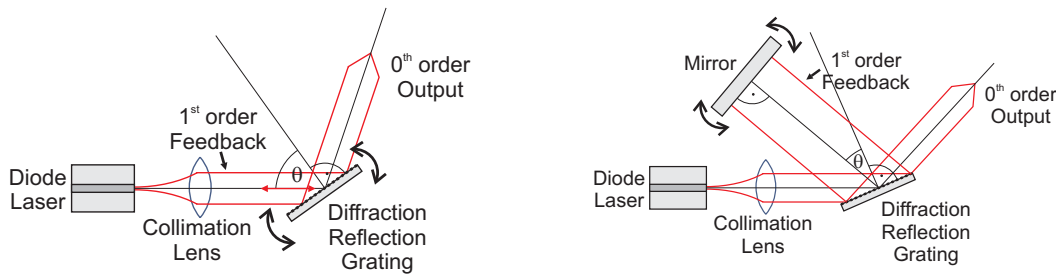


**Figure 9.6.:** Littrow and Littman ECDL Designs

Littrow configuration (left) : The first order diffraction of a holographic grating is directed back into the diode as feedback. Rotating the grating allows choosing the wavelength receiving maximum feedback. This however also causes an angular displacement of the zeroth order output beam.

Littman configuration (right): While here too the zeroth order reflection of a holographic grating is used as output beam the first order is not fed back directly into the diode but directed towards an additional mirror. Wavelength tuning is achieved by a rotation of the mirror while the grating remains fixed, leaving the direction of the output beam unchanged. To deliver feedback to the diode the first order reflected on the mirror is directed back towards the grating to be diffracted into the diode.

Figures from [42].

A Littman-configuration circumvents the latter problem by sending the first diffraction order not directly back into the diode for feedback, but retro-reflecting it on an additional mirror. Here rotating the mirrors allows selecting the wavelength receiving maximum feedback, while the grating and with it the output beam direction remains fixed. The drawback here is that the first order diffracted beam has to be diffracted on the grating again before being directed back into the diode. The zeroth order of this second diffraction is lost.

Correspondingly Littman-ECDLs typically reach only 50-70 % of the output power of a comparable Littrow-design, while offering a larger mode-hop-free scanning range.

The angular displacement during frequency scans in a Littrow-configuration can be reduced by employing an additional beam correction mirror [98], but pointing stability of Littman setups remains inherently superior.

For most applications in ultracold atomic physics experiments, though, lasers operate only in a narrow range of frequencies around a fixed point. Typical frequency changes during operation are rather of the order of 10 MHz region than in the 100 MHz region. Since small beam displacements can more easily be tolerated than a reduction in beam power we employ Littrow-configurations in most of our lasers. A notable exception is the cooler laser that will be discussed in detail in chapter 11.

We construct our own ECDL system based on a design introduced by Ricci et al [97] and described in detail e.g. in [93] and references therein. For a students guide to the construction of ECDL lasers see appendix E.

### 9.3.2. The Laser Setup

#### Transitions

For the present experiment five different laser beams are needed. An overview of the mapping of lasers to used transition is given in figure 9.7.

The trapping force in the MOT is supplied by the cooler beam, 5 – 15 MHz red detuned from the cyclic  $F = 2 \rightarrow F' = 3$  transition. Approximately once every thousand cooling cycles the atom does not fall back to the  $F = 2$ , but enters the  $F = 1$  ground state instead. Therefore a repumper laser operating on resonance to the  $F = 1 \rightarrow F' = 2$  is needed to pump those atoms back into the  $F = 2$  ground state, re-inserting them into the cooling cycle.

In the MOT all magnetic sublevels are trapped, while the magnetic traps only apply restrictive forces to the Zeeman states with positive values for  $m_F$ . To pump the atoms into the  $|F = 2, m_F = 2\rangle$  substate a  $\sigma^+$  polarized optical pumping beam is applied on the  $F = 2 \rightarrow F' = 2$  transition right before the atoms are transferred into the magnetic trap.

Last but not least the atoms should be detected. For this purpose two imaging beams are necessary. One for time of flight imaging, allowing detection in fluorescence or absorption images, and one as a probe beam in the integrated fibre detector. Since for an imaging beam strong coupling to the atoms is desired both operate on the  $F = 2 \rightarrow F' = 3$  transition.

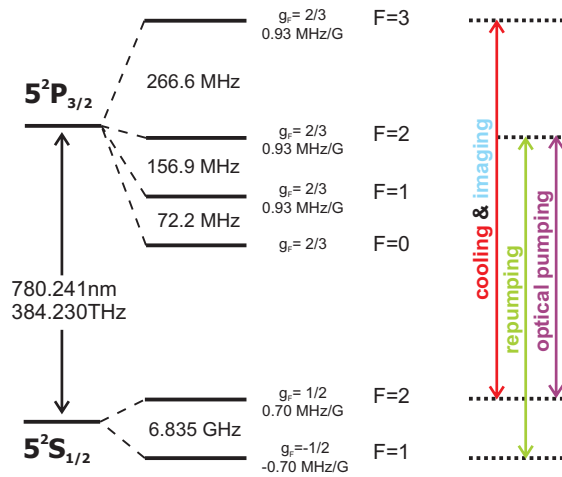


**Figure 9.7.:**

The  $^{87}\text{Rb}$  D2 Line Hyperfine Structure. The frequency splitting between adjacent energy levels is given as well as the approximate Landé- $g_F$ -factors and the Zeeman shifts between neighbouring magnetic sublevels according to [44].

On the right hand side the laser transitions are marked. The cooling (MOT) and imaging lasers operate on the cyclic transitions between  $F = 2$  and  $F' = 3$ , while the repumper laser is resonant to  $F = 1$  to  $F' = 2$ . Optical pumping into the  $F = 2, m_F = 2$  state is performed on the  $F = 2$  to  $F' = 2$  transition.

#### Laser Locking

The lasers are stabilized on the designated transitions with a precision well below 1 MHz by means of a frequency modulation (FM) technique locking relative to an atomic transition or by frequency offset (FO) locking relative to a reference laser. Both

techniques have been extensively described in the diploma theses of Markus Rückel and Marco Wilzbach [93, 99]. An overview of the corresponding lock electronics, developed in cooperation with the electronics workshop of the Physikalisches Institut, Universität Heidelberg, can be found in [30].

## Beampath

Since laser locks are sensitive to vibrations of the laser cavity, the laser setup is realized on a separate breadboard, mechanically and acoustically shielded from the rest of the experiment. In order to increase stability, and to keep the different sections of the experiment as modular as possible, the laser beams are fibre coupled.<sup>5</sup> Following the idea of modular, self-contained units the AOMs and mechanical shutters, responsible for switching the beams, have been directly integrated into the laser setup as well, where possible. Acoustical disturbances introduced by the shutters are minimized by employing miniature shutters with lightweight blades.<sup>6</sup> The cooler laser is realized with a tapered laser amplifier stage (see chapter 11). Here a short beam path to the fibre coupler to guarantee stable output power levels was deemed more important than including the AOM and shutter into the amplifier stage. Thus the cooler beam AOM and shutter are external, positioned right before the telescope needed to expand the cooler beam for MOT operation.

For a diagram of beam paths through the vacuum chamber and further information on the mirror-MOT setup please refer to [30].

Figure 9.8 gives a schematic overview of the laser setup. The five laser beams needed are derived from four lasers. The time of flight imaging beam and the fibre detector probe beam originate from the same laser, while the frequency offset lock master laser doubles as optical pumping laser.

The implementation of the scheme in the real experiment is shown in figure 9.9. While building the laser setup special attention was given to keep the beam paths short, which leads to a somewhat nested setup, but increased stability.

---

<sup>5</sup>The repumper beam is the exception to that rule. Here a commercial Toptica DL100 Laser system has been used. The already low power and beam quality of that system would have led to unacceptable high losses in the fibre coupling. The loss in pointing stability, by guiding the repumper beam in free space, was tolerable, since the MOT is rather insensitive to changes in the repumper direction and beam shape.

<sup>6</sup>E.g. Sunex CMT-SHT934 minishutters available from [www.optics-online.com](http://www.optics-online.com). We previously employed even more silent shutters. Unfortunately those are not available any more, but note that several interesting alternatives exist [100, 101].

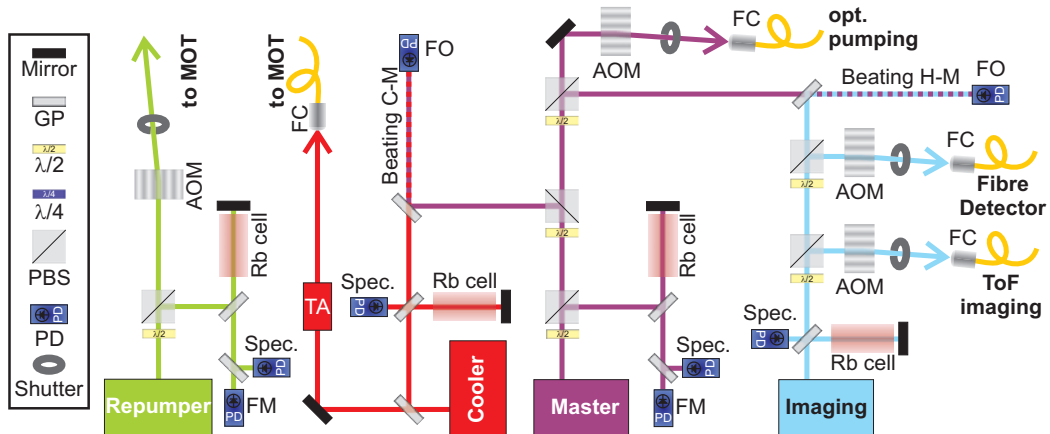


**Figure 9.8.:** Schematic View of the Laser Setup

Lenses, irides and mirrors have been omitted where not essential for the understanding. The photo diodes marked 'spec' are standard PIN type photo diodes used to observe the spectroscopy, while the photo diodes labelled 'FM' and 'FO' are fast avalanche photo diodes which are used to derive the error signal necessary for the laser locks. Note that both imaging beams are derived from the same laser. The imaging and cooler lasers are FO-locked to the master laser, which doubles as optical pumping laser. The cooler laser is sent though an amplification stage (labelled TA) that is described in chapter 11. This drawing is based on the presentation given in [30].

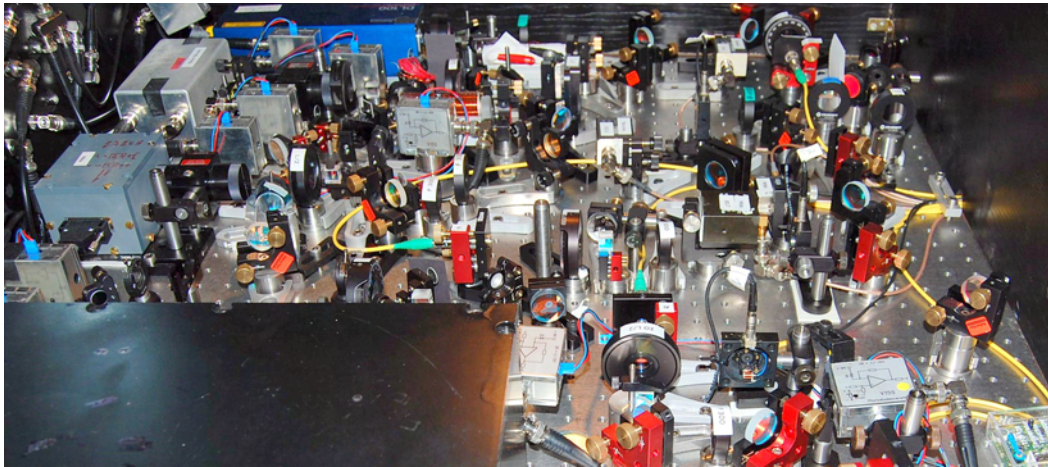
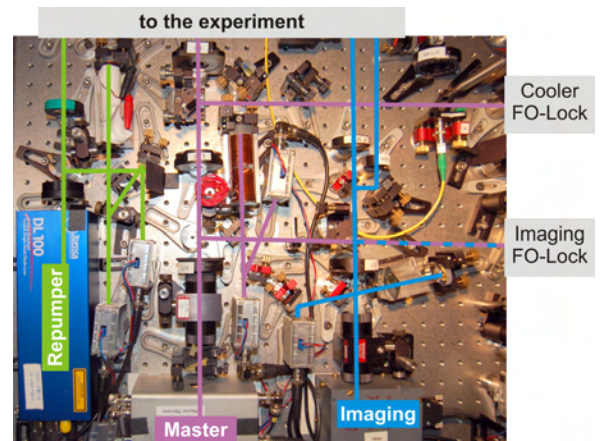


**Figure 9.9.:** The Laser Setup

In building a stable laser setup care was taken to create short beam paths. The section depicted to the right shows the spectroscopy and locking beam paths for three of the four lasers. The master laser doubles as optical pumper in the experiment and the imaging beam is split in two to serve as ToF imager and fibre detector probe beam. All beams are subsequently sent through AOMs for beam control and, with the exception of the repumper, coupled into SM fibres.



### Locking Points

An AOM consists of a radio-frequency (RF) driven piezo-element attached to a crystal. When an RF signal is applied to the piezo (typically 30 to 200 MHz) a sound wave is generated in the crystal, on which the laser beam is refracted. An AOM does not only act as a switch for the laser light but introduces additionally a frequency shift, given by the Rf frequency, on the laser light. This allows us to use beams originating from the same laser for different purposes in the experiment.

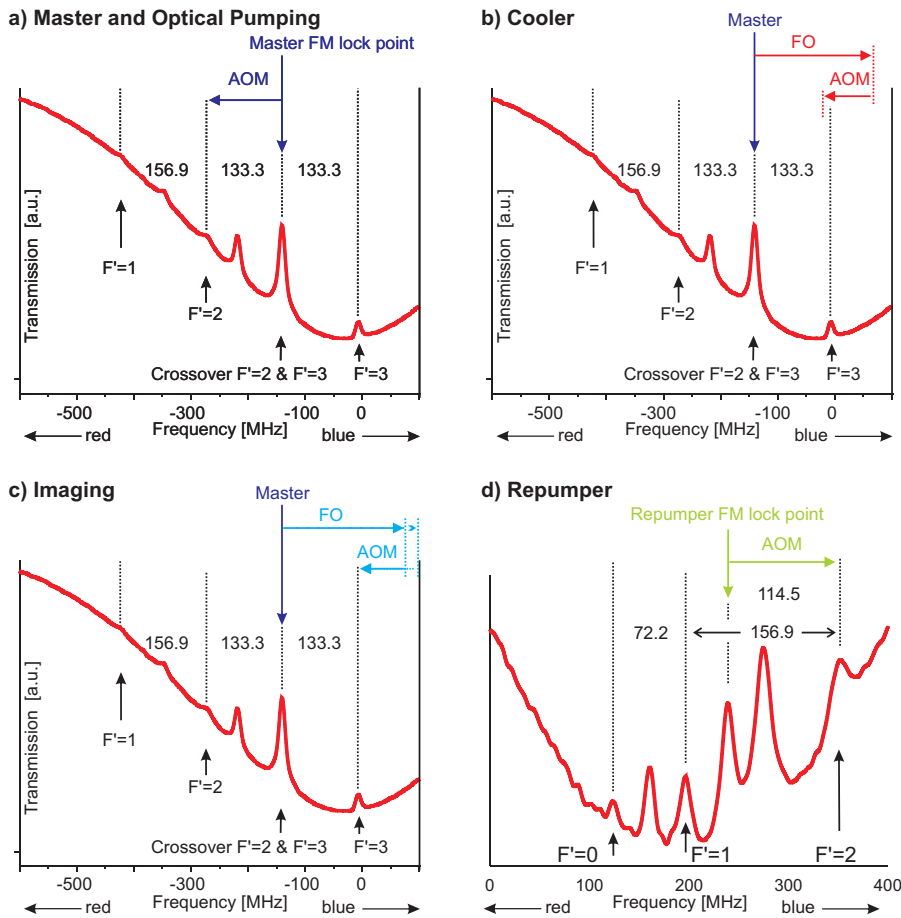


**Figure 9.10.:** Locking Points and AOM shifts

- The FO-lock frequency master is locked on the  $F' = 2$  and  $F' = 3$  crossover of the  $F = 2 \rightarrow F'$  transitions. The part of the beam serving as optical pumper is red shifted by an 133.3 MHz AOM to resonance with the  $F = 2 \rightarrow F' = 2$  transition.
- The cooler is frequency offset locked to the master and red shifted by a 92 MHz AOM. For MOT operation the cooler is locked slightly red detuned of the  $F = 2 \rightarrow F' = 3$  transition.
- The imaging probe beam is FO locked to the master and red shifted by an AOM, usually to be resonant with the  $F = 2 \rightarrow F' = 3$  transition. Note that the ToF imaging beam and the fibre detector beam have independent AOMs.
- The repumper is FM locked to the  $F = 1 \rightarrow F' = 1$  and  $F' = 2$  crossover. After being blue shifted by 114.5 MHz by an AOM it is resonant to the  $F = 1 \rightarrow F' = 2$  transition.

In the following the locking points of the separate lasers will briefly be discussed, see figure 9.10 for a schematical presentation.

The master is locked to the  $F' = 2$  and  $F' = 3$  crossover of the  $F = 2 \rightarrow F'$  transitions to serve as a reference to the cooler and imaging lasers. Since the master is employed as optical pumping laser as well, a 133.3 MHz AOM shifts a part of the beam into resonance with the  $F = 2 \rightarrow F' = 2$  transition.

The cooler is FO locked to the master and red shifted by a 92 MHz AOM. Since the cooler is typically used at 10 to 20 MHz red detuning for MOT operation this leads to a FO lock beating frequency of 205.3 to 215.3 MHz.

The imaging beam is split into two beams controlled by independent AOMs. The ToF imaging beam is red shifted by a 80.7 MHz AOM, while the fibre detector probe beam is red shifted by a 110.7 MHz AOM. This leads to FO lock beating frequencies of 214 MHz and 244 MHz correspondingly.

Even though it would have been technically possible to use identical AOM frequencies for the two imaging beams to have a common setpoint for ToF and fibre detection, it is not advisable to do so. The RF-operation of the AOM piezos tends to produce a significant amount of noise and crosstalk. Operating two AOMs close to one another at similar frequencies leads correspondingly to strong beating effects, jeopardizing intensity stability.

The repumper beam is FM locked to the  $F' = 1$  and  $F' = 2$  crossover of the  $F = 1 \rightarrow F'$  transitions. After a 114.5 MHz blue shift by its AOM it is resonant with the  $F = 1 \rightarrow F' = 2$  transition.

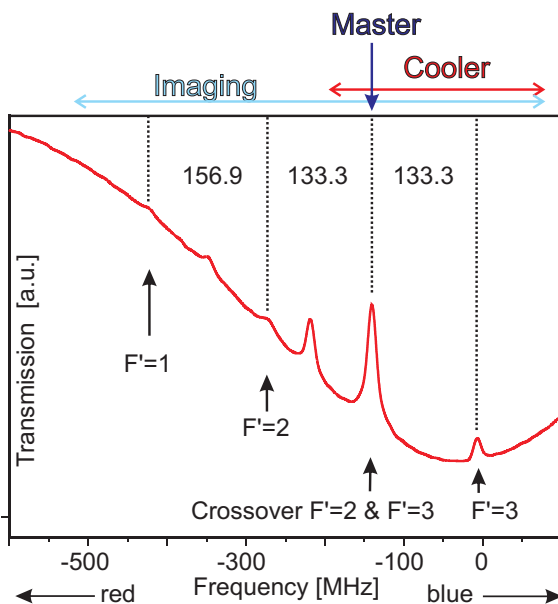


**Figure 9.11.:**

Frequency Offset Lock Accessible Range  
The spectroscopy of the  $^{87}\text{Rb}$   $F = 2 \rightarrow F'$  is shown, indicating the possible frequency offset locking points for imaging and cooler laser with the master locked on the  $F' = 3$  and  $F' = 2$  crossover.

Figure 9.11 gives an overview of the the range of locking points that can be reached with the frequency offset lock. The imaging probe beam can be locked basically

anywhere on the  $F = 2 \rightarrow F'$  transition, allowing flexible probing of the atomic example. Since the locking point is externally set via a control voltage given by the Labview experiment control program, the cooler detuning can kept on the optimal point during MOT, ramping and molasse phases of the transfer.

The following table gives an overview of the locking points and AOM frequencies used.

Laser Locking Scheme				
	Lock	AOM	FO	resonant to
Master	FM			$F = 2 \rightarrow F' = 2/3$
optical pump		-113.3 MHz		$F = 2 \rightarrow F' = 2$
cooler	FO	-92 MHz	205.3 to 215.3 MHz	$F = 2 \rightarrow F' = 3$ (10 to 20 MHz red)
Imaging ToF	FO	-80.7 MHz	214 MHz	$F = 2 \rightarrow F' = 3$
Fibre Probe	FO	-110.7 MHz	244 MHz	$F = 2 \rightarrow F' = 3$
repumper	FM	+114.5 MHz		$F = 1 \rightarrow F' = 2$

### 9.3.3. State Selective Detection

To demonstrate that the integrated fluorescence detector allows state selective detection we have measured the signal of an atom pulse passing the detector for different probe beam frequencies.

The atoms should all be in the  $|F = 2, m_F = 2\rangle$  ground state when they arrive at the detector. The strongest signal is expected for the cyclic transition  $F = 2 \rightarrow F' = 3$ . The results of our measurements, shown in figure 9.12, demonstrate that our detector can resolve the whole  $F = 2 \rightarrow F'$  transition. The flexibility of the FO lock allows us to probe a window of approximately 600 MHz width, starting 60 MHz blue detuned of the  $F' = 3$  transition and going down to more than 100 MHz red detuning of the  $F' = 1$  transition.

For this measurement a remaining magnetic field at the guide minimum of approximately 4 G was chosen. This field leads to a Zeeman-splitting of the magnetic sub-levels. The splitting between adjacent levels is much smaller than the linewidth, hence only one peak is observed for the  $F' = 1$  and  $F' = 2$  transitions. For the  $F' = 3$  transition, though the two cyclic transitions  $|F = 2, m_F = 2\rangle \rightarrow |F' = 3, m_{F'} = 3\rangle$  and  $|F = 2, m_F = -2\rangle \rightarrow |F' = 3, m_{F'} = -3\rangle$  can be clearly separated. This demonstrates, that not only can we selectively address transitions to different excited states, but magnetic substates can be resolved as well, if the magnetic field in the guide minimum is chosen correspondingly<sup>7</sup>.

<sup>7</sup>This is the so called Ioffe field, see chapter 10.

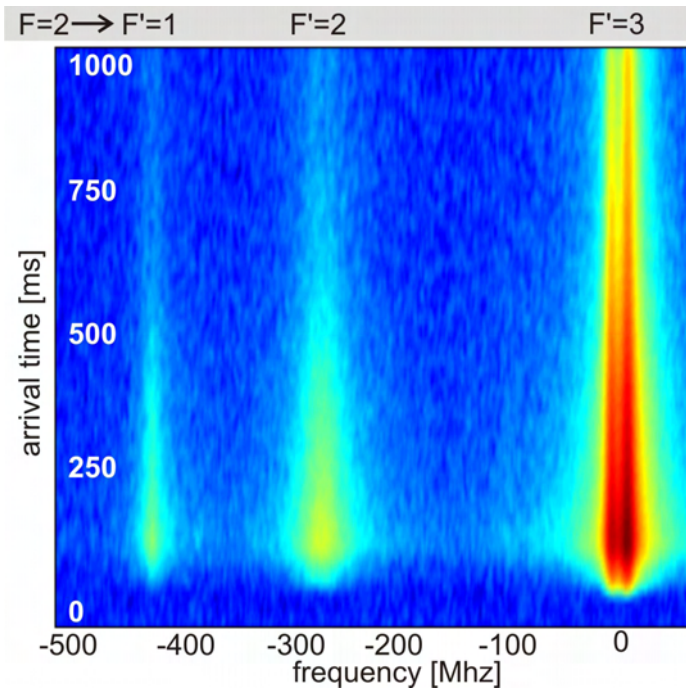


**Figure 9.12.:** Full Spectroscopy of the  $F = 2 \rightarrow F'$  transition. The signal from an atom pulse passing the detector is measured for probe beam covering a range of more than 600 MHz. The  $F' = 3$  state is split into two separate peaks due to Zeeman splitting (see main text). This graph has already been published in [30].

A more detailed analysis of the frequency dependent response is performed in [30].

In summary the integrated detector allows state selective detection with extremely high background suppression in a highly selective spatial region.

### 9.3.4. Probe Beam Stabilization

The fibre detector probe beam has to be stabilized in intensity as well as frequency. As depicted in figure 9.13 the imaging beam is coupled into a 50/50 fibre beam splitter. Half of the beam is sent through a manual fibre polarization controller<sup>8</sup>, which is used to optimize the fluorescence signal. The polarization optimized signal is coupled into the tapered excitation fibre via a mechanical fibre optical splice<sup>9</sup>. The other half of the beam is sent to a photo diode for stabilization. The photo diode signal is fed into a PID controller<sup>10</sup> which compares it to its set value and generates an error signal that is used to regulate the amplitude of the RF signal generated in the AOM driver.

Using this circuit intensity stabilization on the 10 pW level has been achieved. The set intensity is reached in less than 3 ms after the TTL control of the AOM driver is set to high. The AOM driver is controlled with the same gating pulse as the SPCM and the counting card (see figure 9.5), activating the AOM 50 ms before the measurements starts. Thus a constant probe light intensity during measurement can be guaranteed.

<sup>8</sup>Thorlabs FPC030, available from [www.thorlabs.com](http://www.thorlabs.com).

<sup>9</sup>Newport F-SK-SA, available from [www.newport.com](http://www.newport.com).

<sup>10</sup>PI-Regler A368F, electronics workshop, Physikalisches Institut, Universität Heidelberg.



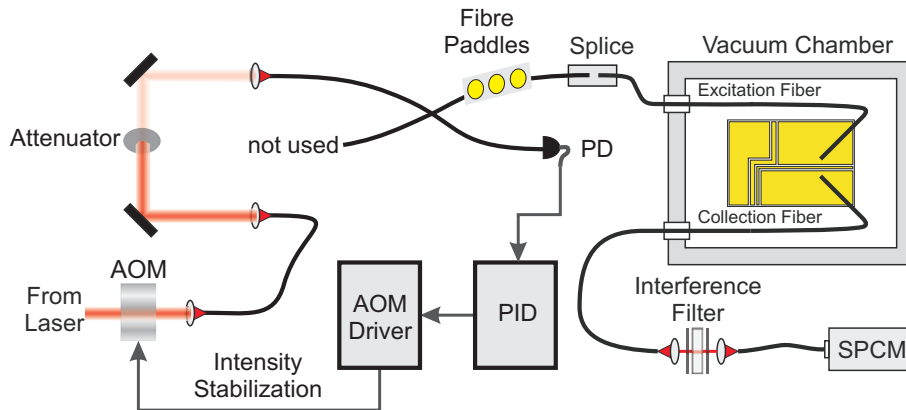


**Figure 9.13.:** Probe Beam Stabilization

The probe beam for the fibre detector is coupled into a 50/50 fibre beam splitter. One leg of the beam splitter is used for intensity stabilization. The intensity measurement of a photodiode is used as an input signal for a PID regulator. The response of the PID regulator is used as an amplitude control signal for AOM driver. The other leg is sent through fibre paddles to adjust the polarization of the probe light and then coupled to the tapered excitation fibre via a fibre splice.

**Setpoint Uncertainty** The splitting ratio of the 50/50 fibre beam splitter employed has not been measured. Experience with similar fibre beam splitters shows that the splitting ratio might deviate by 20 % (60/40 instead of 50/50) from the specified values. Additional sources of errors include the unknown coupling efficiency of the mechanical splice. Note though, that regardless of the exact splitting ratio the beam intensity is stabilized to a few picowatt around the set point, only the absolute value of the set point depends on the splitting ratio. For the calculations in the main text the splitting ratio is assumed to be 50 %.

The Rabi oscillation measurements in chapter 8 allow to estimate the absolute error in probe beam power calibration to be below 300 pW for the powers employed.

## 9.4. Vacuum Chamber and Atom Chip

The chip is mounted on a Shapal baseplate, hanging upside down in the vacuum chamber to allow time of flight measurements on the atom cloud when the trapping fields are switched off. As can be seen in figure 9.14 the chipmount consists of a series of copper rods and stabilization clamps, attached to a vacuum flange to allow electrical connection to the outside. The copper structures used for MOT quadrupole field and intermediate magnetic trap generation are integrated into the Shapal Baseplate.

The atom chip used in the current experiment has been designed by Marco Wilzbach and fabricated by Sönke Groth. Hence the fabrication process is detailed in [102], while a detailed description of the chip and the vacuum chamber can be found in [30].

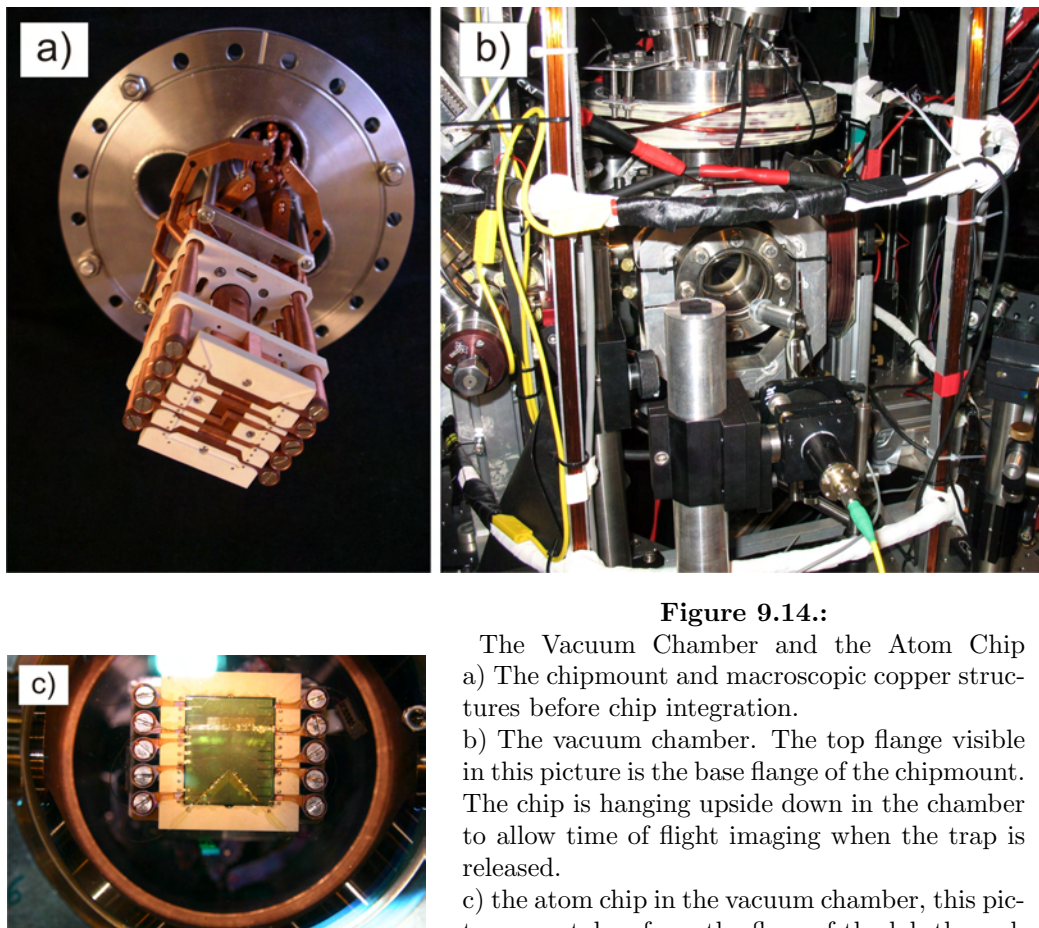


**Figure 9.14.:**

The Vacuum Chamber and the Atom Chip  
 a) The chipmount and macroscopic copper structures before chip integration.

b) The vacuum chamber. The top flange visible in this picture is the base flange of the chipmount. The chip is hanging upside down in the chamber to allow time of flight imaging when the trap is released.

c) the atom chip in the vacuum chamber, this picture was taken from the floor of the lab through the viewport used for ToF fluorescence imaging. Note the fibre holding structures on the chip.

### 9.4.1. Fibre Integration

The basic structure of the atom chip and the integrated detectors has been described in chapter 2. Here I will focus on the fibre integration on the chip.

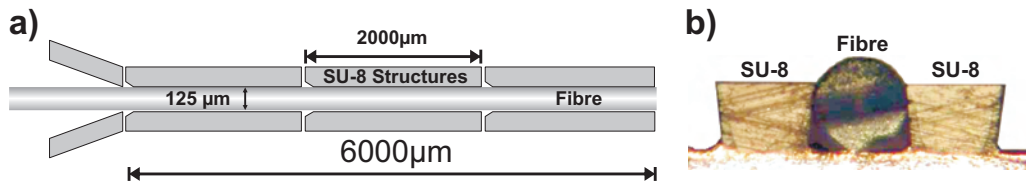


**Figure 9.15.:** SU-8 Holding Structure

- a) Schematic top view showing the three segments and the insertion funnel.
- b) Microscope image of a front view with inserted fibre.

For robust detection the excitation and detection fibres should be fully integrated into the atom chip. External mountings are poor alternatives since they might move relative to the chip structures and hence lead to non-reproducible results.

To achieve precise alignment and robust integration we employ lithographically defined superstructures fabricated directly on top of the chip structures to mount the fibres. The mounting structures are fabricated from SU-8, an epoxy based negative photo resist with high thermal, mechanical and chemical stability [103]. SU-8 is typically developed using UV-radiation in the range 365-436 nm, but can be used in x-ray-, e-beam and two-photon lithography as well. Once fully developed its glass transition temperature is approximately 200°C with a degradation threshold around 380°C. Both temperatures are not reached during operation of the atom chip.

In fabricating the fibre mounts a 7.5 % shrinkage of the SU-8 during development has to be taken into account, leading to a slight variability in the dimensions of the holding structures. It should be noted here that the variations in fibre diameters are large in comparison. Typically the diameter of a fibre used in the experiment is specified with a precision of only 1 μm to a cladding diameter of  $125 \pm 1$  μm.

With a single SU-8 layer a coating film thickness of up to 300 μm is possible, while multiple coatings allow creating structures as high as 3 mm.

The detection fibres are held in SU-8 trenches of 125 μm width, corresponding to the fibre diameter, with slightly undercut side walls of 90 μm height, as shown in figure 9.15. The side walls height is chosen to be larger than the fibre radius, which allows the undercut to effectively clamp the fibres to the chip surface, removing the necessity of additional glue fixation. The trenches are sectioned into three 2 mm long substructures to reduce mechanical stress during thermal expansion. The entry port is funnelled to simplify the insertion of the fibre.

### 9.4.2. Fibre Feedthrough

Unlike electrical connectors fibres cannot simply be welded into the vacuum flanges. To funnel the fibres out of the vacuum chamber we employ a method introduced by Abraham and Cornell [104]. Teflon cylinders with a central hole of 300  $\mu\text{m}$  diameter are inserted into a Swagelok compressible feedthrough<sup>11</sup>.

The hole allows leading the fibres out of the vacuum chamber while the remaining gap is closed by compressing the Teflon cylinder. This procedure has been demonstrated to be compatible with pressures below  $10^{-10}$  mbar.

## 9.5. External ToF Imaging

External absorption and fluorescence imaging is the standard method to observe ultra-cold atomic clouds in magnetic microtraps. Here an imaging probe beam is sent from the outside into the vacuum chamber at a small angle (typically  $8^\circ$ ) to the chip surface. One CCD Camera on the opposite side of the chamber detects the transmitted beam for absorption imaging. A second camera is mounted orthogonal to the plane of the chip, at  $90^\circ$  to the probe beam, to collect a fraction of the fluorescent light emitted by the atoms (see figure 9.16).

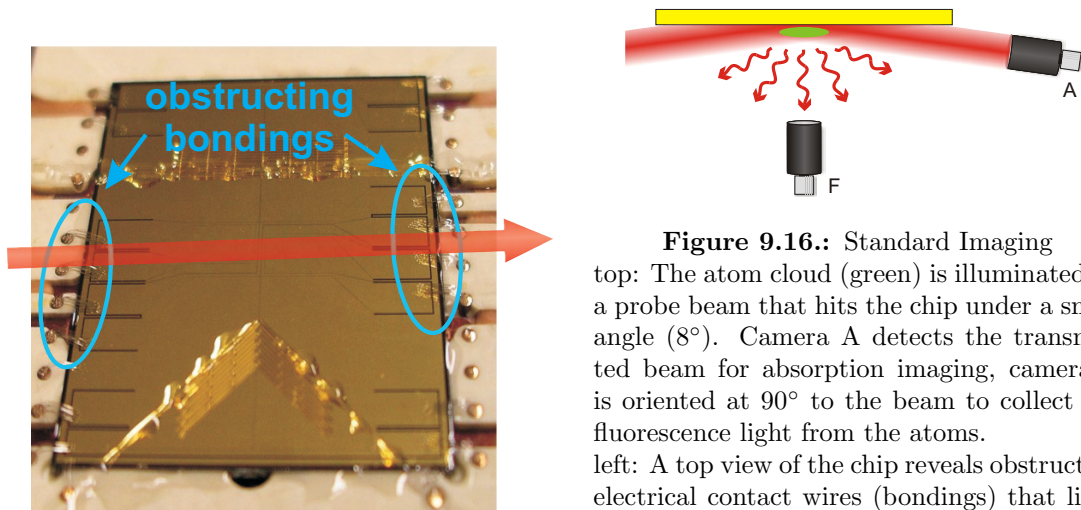


**Figure 9.16.:** Standard Imaging  
top: The atom cloud (green) is illuminated by a probe beam that hits the chip under a small angle ( $8^\circ$ ). Camera A detects the transmitted beam for absorption imaging, camera F is oriented at  $90^\circ$  to the beam to collect the fluorescence light from the atoms.  
left: A top view of the chip reveals obstructing electrical contact wires (bondings) that limit the field of view of the absorption imaging.

A peculiarity of our setup has been that the electrical connections to the chip (the bonding wires) partially obstruct the optical access to the centre region of the chip if seen from the side. Hence absorption imaging suffers from a limited field of view. A more detailed description of the imaging setup is given in [30]. To compensate for this obstruction the fluorescence imaging has been greatly improved upon during the rebuild of the experiment. Due to careful screening of stray light and ambient light

<sup>11</sup>Swagelok company, SS-2-TA-1, [www.swagelok.com](http://www.swagelok.com).

the fluorescence imaging performed supremely well, often outclassing the absorption imaging in terms of sensitivity and contrast.

Using time of flight measurements the atom number at the end of the Z-trapping phase, right before transfer into the 1D-guide, has been estimated to  $(2.0 \pm 0.2) \cdot 10^6$  atoms with fluorescence imaging<sup>12</sup>. Absorption Imaging measures only  $(1.3 \pm 0.2) \cdot 10^6$  atoms<sup>13</sup>. The lower result for absorption imaging is a systematic effect of the obstruction by the bonding wires.

Of the  $2 \cdot 10^6$  atoms in the Z approximately 40 % are transferred into the guide. The atomnumber in the guide could not be measured with time of flight techniques in our current setup. Here we rely on alternative methods.

## 9.6. Detection setup

The photon detection setup has been presented in chapter 2. Here I will add only a few technical details that have been omitted there to enhance the clarity of the presentation.

### 9.6.1. Fibres

The light is guided inside an optical fibre by total internal reflection (see [40], a good introduction is given in [41] as well).

#### Splice

Every connection between two fibres or coupling from fibre to free space and vice versa is connected with reflection losses. For the excitation light transmission losses in the fibre to fibre coupling are acceptable. Therefore a simple mechanical splice<sup>14</sup> could be used to connect the input fibre beam splitter (see section 9.3) to the tapered excitation fibre leading into the vacuum chamber.

For the signal collected by the detection fibre no such losses can be tolerated. Thus the MM detection fibre coming from the vacuum chamber has been fusion spliced to the MM fibre leading to the filter setup. The Ericsson FSU 995 PM fusion splicer employed features automatic alignment of the fibre ends and gives reliable measures for the splice loss.<sup>15</sup>

---

<sup>12</sup>Dataset 20071203Mon\_endofZ\_fluo

<sup>13</sup>Dataset 20071203Mon\_endofZ\_abs

<sup>14</sup>Newport F-SK-SA, available from [www.newport.com](http://www.newport.com).

<sup>15</sup>The fusion splicer has been borrowed to us on short notice by the good people of the ultrafast laser group at the Institut für Photonik, TU Wien.

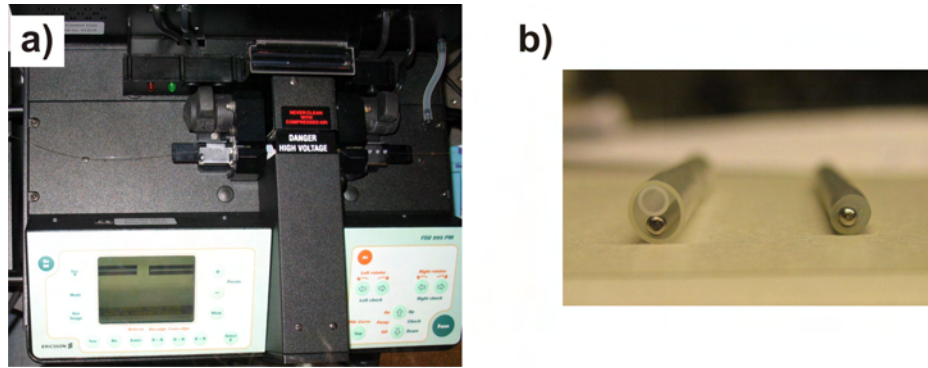


**Figure 9.17.:** Fusion Splicing the Detection Fibre

- a) The detection fibre has been spliced using an Ericsson FSU 995 PM fusion splicer.  
 b) Even a good splice can be considered as predetermined breaking point if bending stress is introduced. Therefore the newly made connection is protected by a metal rod stabilizer after splicing. On the left side you see the protective tube before the fibre is inserted. After splicing the plastic tube is heat-shrunk to fix the fibre to the supporting metal rod.

Our splice was estimated to exhibit a loss of 0.01 dB, corresponding to a 0.23 % reduction in transmission. Thus the coupling efficiency table for the Hanbury Brown-Twiss type setup presented in chapter 2 is actually given in full by the following table.

losses in photon detection (HBT setup)		
<i>loss channel</i>	<i>efficiency (transmission)</i>	<i>comment</i>
collection efficiency of the MM fibre	$\eta_{\text{coll}} = 0.019$	geometrical effect limited by NA
Fresnel loss MM	0.960	reflection at collection
Splice loss	0.998	0.01 dB attenuation
filter gap	$\eta_{\text{gap}} = 0.840$	including filter transmission
SPCM detection efficiency	$\eta_{\text{SPCM}} = 0.564$	
total photon detection efficiency	$\eta_{\text{ph}} = 0.00862$	

Needless to say that the final result is not changed significantly by the splice loss and  $\eta_{\text{ph}} > 0.86\%$  remains a good estimate.

It should be noted here that the assumption of 4 % reflection loss at the fibre facets is valid only for a flat  $0^\circ$  polish of the fibre facets as employed in our self-connectorized fibres. It is often overlooked that commercial fibres usually come with a PC polish, where PC stands for physical contact polished facets. A physical contact polish creates a slightly convex surface, allowing opposing fibre to touch slightly for optimal coupling efficiency. Here the 4 % reflection rule of thumb does not hold.

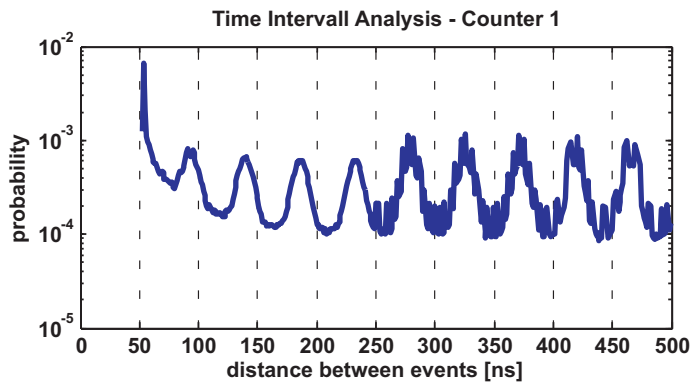


**Figure 9.18.:**

The time interval distribution of a strong signal, coupled with a 5 m long FC/PC MM fibre into the SPCM, exhibits oscillations due to reflections within the fibre.

The lack of signal between 0 ns and 52 ns is due to the dead time of the SPCM. The slope between 52 ns and 200 ns is caused by afterpulsing.

## Backreflections

Figure 9.18 demonstrates very nicely why flat surfaces should be avoided in correlation measurements. Here a strongly attenuated laser was coupled into a multi mode fibre with PC polished facets and send to the SPCM. The time interval distribution shows a clear oscillation with a period of 45 to 50 ns. Apparently a distance of  $t = 45 \cdots 50$  ns between detections is very likely. Using the refractive index  $n = 1.496$  of the fibre the distance  $s$  that the light travels during time  $t$  can be calculated.

$$s = \frac{c}{n} \cdot t = 9.02 \cdots 10.02 \text{ m}$$

The fibre has a length of 5 m. It appears therefore that these oscillations are caused by light travelling back and forth in the fibre due to reflections on the fibre facets.

These disturbances can be avoided using fibres that have at least one angle polished (APC) side.<sup>16</sup>

### 9.6.2. Counter Card Specifications

A P7888 Multiscaler PCI card<sup>17</sup> has been used to timestamp and record the photon counts generated by the single photon counting modules.

The P7888 card can record counts on two stop channels with 1 ns resolution or four stop channels with 2 ns resolution. Using wrap around mode continuous data acquisition for up to 65 s without dead time is possible.

Our characterization measurements show good synchronization between the channels for count rates below 10 kcps. At higher count rates time jitter of maximally 1 ns occurs with low probability. Hence the maximum synchronization error is on the level of the time resolution (1 ns), with channel 2 always receiving the later timestamp if a synchronisation error occurs.

<sup>16</sup>In contrast to PC polishing here the polishing plane is tilted by  $8^\circ$  with respect to the light propagation axis, strongly reducing backreflections.

<sup>17</sup>Available from FAST Comtec [www.fastcomtec.com](http://www.fastcomtec.com).

The maximum count rate is limited by the PCI bus speed and was specified to be 18 Mcps in sum over all channels. Our characterisation measurements yield a much lower threshold if two channels are supplied with synchronized signals. A rectangular test signal applied to both channels led to significant data loss. At count rates beyond 10 Mcps in sum over all channels all or most data of channel two is lost. Partial data loss occurs even well below 1 Mcps.<sup>18</sup>

The card has been thoroughly tested to faithfully record count rates below 10 kcps. Most of our measurements are performed at count rates between 1 and 10 kcps.

An investigation at the California Institute of Technology has shown, that the P7888 exhibits a 20 ns dead time after receiving a start signal [72].

This dead time has no influence on our measurements, since we start the measurements 50 ms prior to the arrival of the first atoms and background count rates are extremely low.

---

<sup>18</sup>The card is mounted as only PCI card on a fast mainboard. Neither optimizing DMA transfer rates, nor discussions with the FAST Comtec technical support could elevate the problem.



# 10. Magnetic Traps

Atom chips have become a standard tool in our experimental work. I will give here a brief summary of the basic idea of magnetic trapping, focussing on the one dimensional atom guide in a so called sideguide configuration. For further information on magnetic traps please refer to the comprehensive reviews available [13–15, 34, 36, 38, 39, 105].

## 10.1. Atoms in a Magnetic Field

An atom with magnetic moment  $\mu = g_F m_F \mu_B$  feels in a magnetic field of strength  $B$  the potential  $V$ .

$$V = -g_F m_F \mu_B B$$

Here  $g_F$  is the hyperfine Landé factor,  $m_F$  the magnetic quantum number, and  $\mu_B$  the Bohr magneton.

If the changes in magnetic field orientation are much slower than the precession of the atom magnetic moment, given by the Larmor frequency

$$\omega_L = \mu_B \frac{B}{\hbar}$$

then the magnetic moment will follow the direction of the magnetic field (adiabatic approximation).

This fundamental interaction between atoms and magnetic fields allows us to construct magnetic traps and guides for the atoms, enabling us to transport and localize the atoms at will.

In our experiments weak field seeking states, i.e. states with positive  $m_F$ , have been employed. These are trapped in regions with minimal field. Since high field seeking states reach energetically lower levels spinflips (change of  $m_F$ ) have to be avoided. Spinflips occur unrestricted at vanishing magnetic field, since there no quantization axis for the magnetic substates exists. It follows that, even though we trap the atoms in field minima, zero field regions should be avoided. This is usually achieved by adding a constant offset field orthogonal to the trapping fields, as we will see later.

## 10.2. The Sideguide

The magnetic field  $B_W$  generated by a current  $I$  flowing through a straight wire decays inversely proportional with the distance  $r$  to the wire.

$$B_W(r) = \frac{\mu_0 I}{2\pi r}$$

Figure 10.1 demonstrates the effect of superimposing a homogeneous Bias field  $B_b$ , oriented orthogonal to the wire. At a certain distance  $r_0$  to the wire the bias field will compensate the wire field, creating a potential minimum.

$$r_0 = \frac{\mu_0 I}{2\pi B_b} \quad (10.1)$$

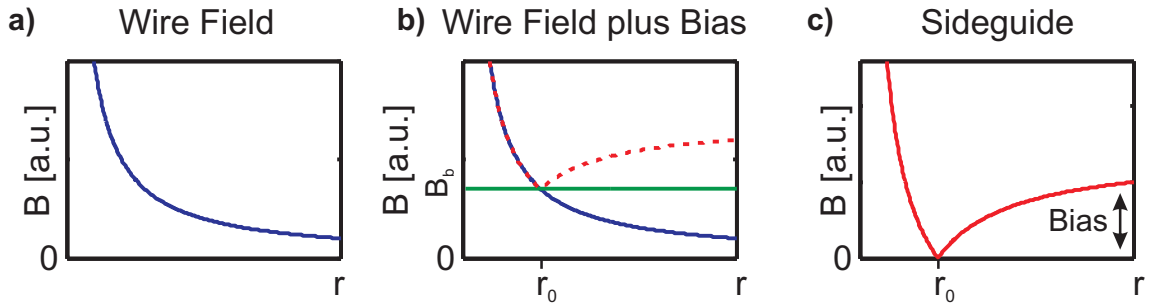


**Figure 10.1.:** Magnetic Field of a Wire Guide

- a) The magnetic field generated by a current flowing through a straight wire decays inversely proportional to the distance from the wire.
- b) Adding a constant bias field  $B_b$  orthogonal to the wire compensates the wire field at a distance  $r_0$ . The resulting absolute value of the field shown in c) is indicated by the dotted red line to illustrate the effect of the bias field. By shifting the magnetic field zero through subtraction of the bias field the field values of magnitude smaller than the bias field are effectively 'mirrored' on the new zero line if only the absolute value of the field is considered.

The field at  $r_0$  is exactly zero, allowing spinflips to occur. To avoid this an additional, constant bias field  $B_{\text{Ioffe}}$  is added along the guide direction (i.e. orthogonal to  $B_b$ ). This field is usually labelled as *Ioffe* field with a typical value of 1 G.

Figure 10.2 illustrates the direction of the magnetic fields relative to the current carrying wire. The resulting potential is a quadrupole-like 1D guide as shown in figure 10.3. The atoms are confined to a region around  $r_0$  above the guide wire, but can freely propagate along the guide.

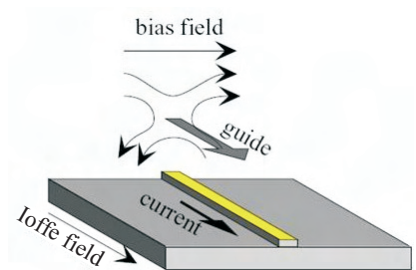


**Figure 10.2.:** The Wire Guide, image courtesy of Björn Hessmo

The effect of the Ioffe-field  $B_{\text{Ioffe}}$  on the potential shape is indicated in figure 10.3 by a red line. The zero field value at the potential minimum is lifted to a finite value.

Additionally the potential around the minimum can now be described in a harmonic approximation.

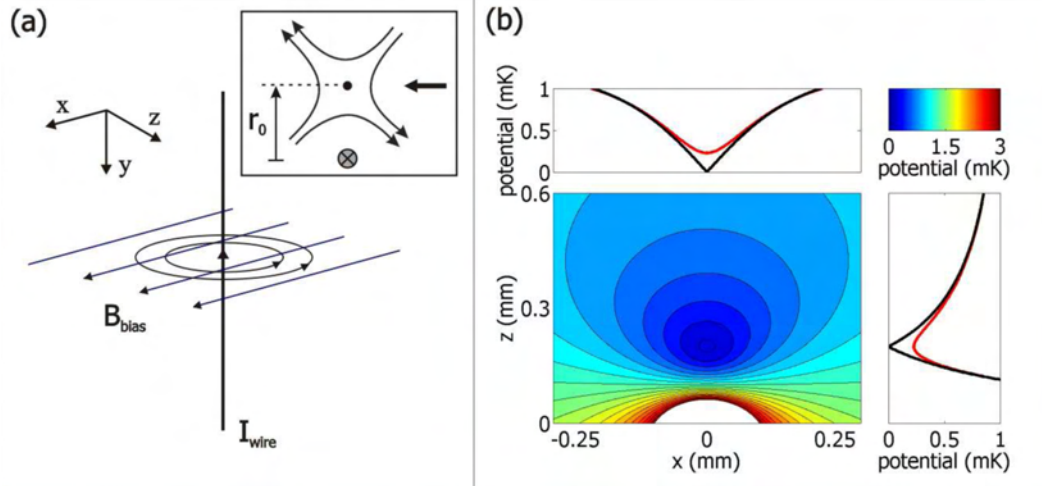


**Figure 10.3.:** The Wire Guide Potential

a) Schematic picture of the sideguide configuration. The magnetic field of a current carrying wire is superimposed with a homogeneous bias field. These two fields cancel at a distance  $r_0$  from the wire and form a quadrupole like field configuration close to the trap minimum (inset). Atoms can be guided along the wire in a one-dimensional quadrupole guide.

b) The magnetic potential in a plane perpendicular to the wire is shown. The calculation assumes an infinitely thin and long wire carrying a current of  $I = 2\text{A}$  and a bias field of  $B_b = 20\text{G}$ . The equipotential surfaces are equally spaced by  $B_b/10$ . The two one-dimensional plots (black curves) show cuts through the minimum of the magnetic trap. If a homogeneous Ioffe field of  $4\text{G}$  in the direction of the wire is added the zero at the minimum is lifted to a finite value leading to a harmonic field configuration (red curves).

Graph and descriptive text from [34].

**Harmonic Approximation** The energy  $E$  of a particle with mass  $m$  in an harmonic oscillator potential is given by the oscillation frequency  $\omega_t$  and the distance from the minimum  $r$ .

$$E = \frac{1}{2} m \omega_t^2 r^2$$

Hence, with the energy  $E = \mu \cdot B$  of a magnetic dipole moment  $\mu$  in a magnetic field  $B$ , a transversal trap frequency

$$\omega_t = \sqrt{\frac{\mu}{m_{\text{Rb}} B_{\text{Ioffe}}}} \frac{B_b}{r_0}$$

can be defined in the harmonic approximation

$$B = \frac{1}{2} \frac{d^2 B}{dr^2} r^2 = \frac{E}{\mu}$$

$$B = \frac{B_b^2}{2 B_{\text{Ioffe}} r_o^2}$$

**Gravitation** Since atom chips are typically mounted upside down, with the trap generated below the chip surface to allow ToF imaging, the trap has to hold the atoms against the pull of gravity.

An atom in a magnetic field with gradient  $\Delta B$  experiences a force  $F_B$ .

$$F_B = -\mu_B g_F m_F \Delta B$$

In order to compensate the pull of gravity the minimal trapping field gradient is given by the following relation.

$$\begin{aligned} F &= -m_{\text{Rb}} g = -\mu_B g_F m_F \Delta B \\ \Rightarrow \quad \Delta B_{\text{min}} &= \frac{m_{\text{Rb}} g}{-\mu_B g_F m_F} \end{aligned}$$

which results for the  $|F = 2, m_F = 2\rangle$  state of  $^{87}\text{Rb}$  to 15.3 G/cm [105].

**Trap Depth** Similarly, to hold atoms with temperature  $T$ , the minimum of the potential has to be at least  $E = k_B T$  deep.

$$\begin{aligned} E &= k_B T = \mu_B g_F m_F B \\ \Rightarrow \quad B_{\text{min}} &= \frac{k_B T}{\mu_B g_F m_F} \end{aligned}$$

The field  $B$  to consider here is  $B = B_b - B_{\text{offe}}$  as can be understood from comparing figures 10.1 and 10.3. Typically trap depths are given in mK, defining the maximum temperature an atomic ensemble can have before spilling out of the trap.

$$T = \frac{\mu_B g_F m_F B}{k_B}$$

### 10.3. Scanning the Guide

The relation between wire current  $I$  and the distance  $r_0$  of the trap minimum to the chip expressed in equation 10.1 allows us to probe the guide at different heights with our integrated fibre detector. Since the detection region is fixed at  $62.5 \pm 2.5 \mu\text{m}$  above the chip surface, shifting the guide potential minimum relative to the chip surface results in an examination of different slices through the guide (see figure 10.4).

Figure 10.5 shows the result of such a scan of the guide. Here the guide potential minimum was shifted in  $3.3 \mu\text{m}$  steps over the full extend of the guide. For a full analysis of similar measurements see [30].

---

<sup>1</sup>Dataset 20071203\_Guidescans\F3\, 5 measurements per guide height, stepped in  $3.3 \mu\text{m}$  increments.

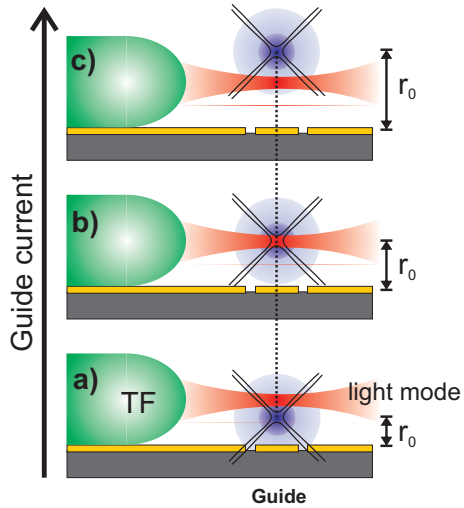


**Figure 10.4.:** Scanning the Guide Current  
 The guide potential (blue, with indicated quadrupole field lines) is shown for three different wire currents. The position of the guide potential minimum  $r_0$  shifts according to equation 10.1 while the tapered fibre (TF) and the excitation mode field (red) remain at a fixed position. Graph from [30].

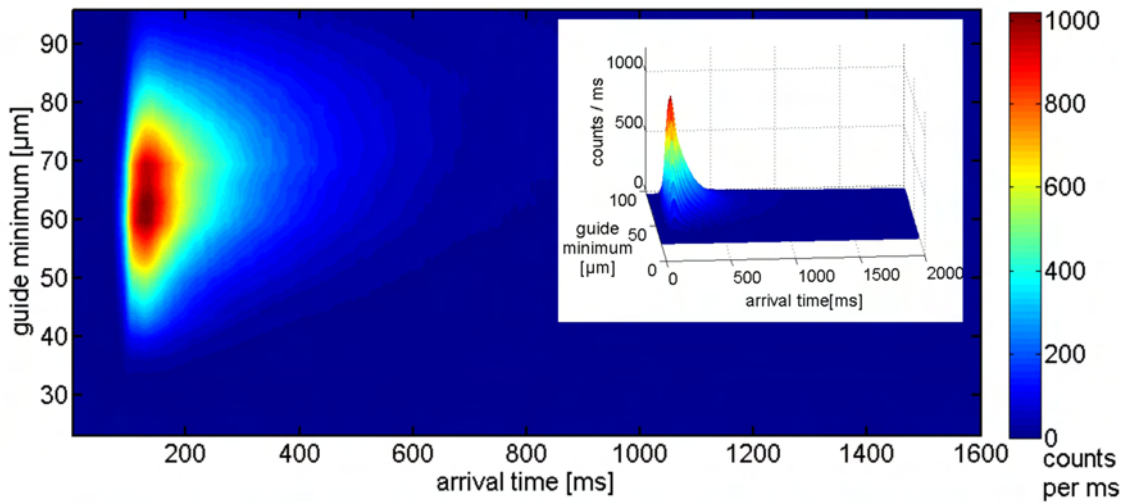


**Figure 10.5.:** A Guidescan over the Full Extend of the Guide

The contour plot shows the result of a scan where the guide minimum was shifted in  $3.3 \mu\text{m}$  steps.<sup>1</sup> For clarity of presentation only arrival times up to 1600 ms are displayed. The inset shows a 3D representation of the data over the full measurement time.



# 11. Tapered Amplifier

We have designed and constructed a supremely stable tapered amplifier laser system delivering an output power of up to 1.2 W at 780 nm and 2 A supply current. More than 500 mW can be fibre coupled into a single mode polarization maintaining fibre to be used as a MOT cooler beam. The tapered amplifier system design, characterization and technical details will be discussed in the following, while selected technical drawings can be found in appendix F.

For alternative designs by other groups see e.g. [106, 107] and of course the commercially available systems by the major scientific laser system suppliers.

To the best of our knowledge, though, the setup presented here has achieved a long term stability that is currently unmatched. The output power of the fibre coupled beam has remained stable under experimental conditions for more than a month without need for any re-adjustments.

## 11.1. Standard Laser Diode Systems

While diode lasers experience widespread use they are limited in the total output power achievable. At 780 nm we are in the fortunate situation of being able to draw low-cost diodes from a pool of well-developed commercial CD-ROM and CD-burner diodes.<sup>1</sup> Still, available standard single mode diodes reach up to 100 mW free running and typically 30 mW in an ECDL setup (see section 9.3).<sup>2</sup>

Even though high power single mode versions are available (at significantly higher price) that deliver up to 120 mW stabilized output in ECDL setups their performance is often less than satisfactory. Our experience has shown that not only beam quality and mode-hop-free scanning width is significantly reduced in comparison with standard diodes, but the lifetime of the diodes is drastically reduced as well. While small scanning width can be tolerated the reduced beam quality leads to less efficient fibre coupling, partially offsetting the gain in output power.



**Figure 11.1.:**  
Laser Diode [108]

<sup>1</sup>CD-ROMs operate at 785 nm, but the temperature dependence of the gain profile allows operating the diodes very efficiently at 780 nm.

<sup>2</sup>All quoted powers are at continuous wave (CW) operation.

High powers can be reached in TiSa laser systems as well, albeit the high price of these systems is often inhibitive. Alternatively, output powers of 50 to 100 mW are reached in master-slave setups, where one ECDL system is used to seed a second diode, operating without external cavity. Typically this approach has been followed so far in the experiments of our group to produce the MOT cooler beams.

The maximum output power in master-slave systems is still limited by the maximum power density a diode can sustain before internal heating leads to melting and recrystallization of the semiconductor material, a phenomenon referred to as catastrophic optical damage (COD). The output facet of a laser diode operating at 780 nm is typically approximately 1  $\mu\text{m}$  high and 3  $\mu\text{m}$  wide, leading to the characteristic elliptic beam shape. At these dimensions COD limits the theoretically attainable output powers to a few hundred mW, while diodes with useful lifetimes typically reach no more than 150 mW.

## 11.2. Tapered Amplifier Basics

In order to reach higher powers without destroying the diode the gain volume has to be increased. The height of the laser-active region is determined by the material properties, but the width is variable [95]. Unfortunately broad laser diodes will not emit a single mode beam, but usually operate on several spatial modes at once.

A solution to this problem has been found in using tapered amplification structures as depicted in figure 11.2. Here a single mode entry channel is used with front facet dimensions similar to a single mode laser diode. Inside the diode the gain region is tapered up to a much larger width, allowing an increase in power while keeping the power density constant and well below the COD threshold.

If a reflective region is integrated between the single mode channel and the start of the taper then these diodes can be used as high power single mode diodes in their own right. But usually much better results are achieved if the tapered diode is used only as a tapered amplifier (TA) for a single mode seed field.

To be used as tapered amplifiers the diodes are anti-reflex coated on both facets to prevent lasing emission without seeding. This of course makes the tapered amplifier diode extremely sensitive to reflections. Any light reflected backwards into the diode from the broad side will be amplified while passing upwards the taper, increasing the

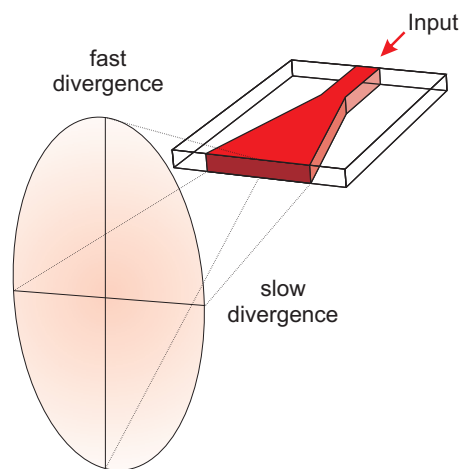


**Figure 11.2.:** Tapered Amplifier



power density and most likely destroying the diode. Hence backreflections should be avoided at all costs.

The output facet is typically 200  $\mu\text{m}$  wide and only 1  $\mu\text{m}$  high. This leads to very different divergences in horizontal and vertical direction that cannot be compensated for using a single lens. The fast divergence on the vertical axis has to be corrected for using a high NA lens directly after the TA. The remaining slow divergence can be corrected for by employing a cylindrical lens at a larger distance.

The broad amplification region leads to a broad gain profile in frequency space as well. Typically frequencies up to  $\pm 20$  nm around the design wavelength can be amplified.

Using tapered amplifier diodes output powers of several Watt can be reached. Even though beam profiles after amplification are quite ugly (see section 11.6 for examples) fibre coupling into a single mode fibre of 50 to 60 % of the total power is possible.

## 11.3. Tapered Amplifier Specifications

One of the major sources of instabilities in the old setup has been the extreme sensitivity of the MOT to power and position of the cooler beam. To remove this problem we designed and constructed a tapered amplifier system that delivered 500 mW of pure single mode fibre coupled laser light for the cooler beam of the MOT. This corresponds to a more than tenfold increase in cooler power combined with a dramatic increase in beam quality and thus trap homogeneity. The high power enables us to expand the cooler beam to a diameter of two inch, leading to a massive, saturated MOT.

We use an Eagleyard Photonics 1 W tapered amplifier diode<sup>3</sup> driven by a commercial Thorlabs Laserdriver<sup>4</sup> for our system.

The tapered amplifier diode is designed for operation at 780 nm and specified to sustain supply currents up to 3 A with a specified output of 1000 mW at 2.5 A and 25° C (see table 11.1). However, as will be seen in section 11.6, specifications from Eagleyard have to be understood as guaranteed minimal values and are typically exceeded by far.

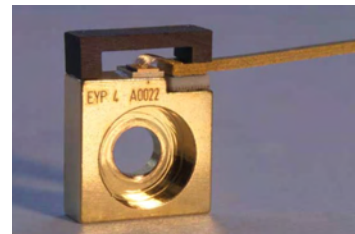


**Figure 11.3.:**

An Eagleyard Tapered Amplifier Diode, image from Eagleyard Photonics [www.eagleyard.com](http://www.eagleyard.com)

<sup>3</sup>Eagleyard Photonics, EYP-TPA-0780-01000-3006-CMT03-000, [www.eagleyard.com](http://www.eagleyard.com).

<sup>4</sup>Thorlabs LDC 8040, used in a PRO 8000-4 driver rack, [www.thorlabs.com](http://www.thorlabs.com).

Tapered Amplifier Characteristics at 25° C

Parameter	min	typ	max
forward current			3 A
reverse voltage			0 V
centre wavelength	770 nm	780 nm	785 nm
gain profile width (FWHM)	10 nm	20 nm	
output power at 2.5 A		1000 mW	
amplification at 2.5 A		20	
saturation power		50 mW	
input aperture width		3 $\mu$ m	
output aperture width		190 $\mu$ m	

**Table 11.1.:** Eagleyard EYP-TPA-0780-01000 Tapered Amplifier Diode Specifications as given by Eagleyard Photonics [www.eagleyard.com](http://www.eagleyard.com)

## 11.4. Setup

The key point in designing reliable tapered amplifier systems is stability. The seeding beam from a master laser has to be coupled into the single mode entry channel of the TA with an alignment precision exceeding 0.5  $\mu$ m.

To achieve long term stability of the alignment an extremely pointing stable master laser has to be used in combination with stable optic mounts and short beam paths. To this end we have constructed an inherently pointing stable master laser using a transmission grating variant of the Littman-configuration as detailed in section 11.5.

### Overview

The main design dogma of shortest possible beam paths and stable mountings was obeyed throughout the complete setup as illustrated in figure 11.4.

The collimated seed beam from the master laser is send via two mirrors to an incoupling lens, focussing the seed beam into the entry channel of the TA. On the way a small fraction of the master beam is picked off for spectroscopy and master stabilization. The amplified output beam is collimated by a combination of an achromatic lens with short focal length and a cylindrical lens. After passing through an optical isolator to suppress backreflections the amplified beam is coupled into a polarization maintaining single mode fibre, using two mirrors and a fibre collimator with adjustable collimation.

The baseplate for the prototype presented here has a dimension of 305 times 405 mm, roughly corresponding to an A3 sheet of paper. With the experience gained from this prototype I expect a decrease in base area of at least 30 % to be possible for future versions.

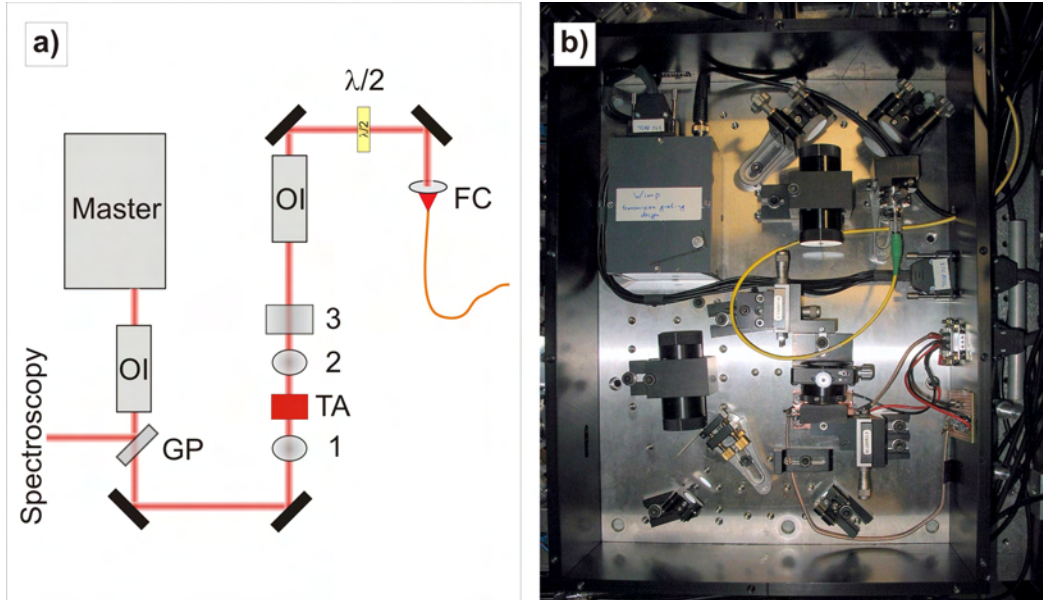
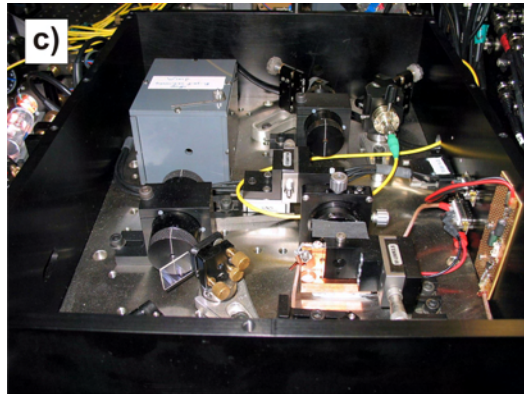


**Figure 11.4.:**

Tapered Amplifier Beam Path  
 a) Schematic view. An optical isolator (OI) protects the master laser from back-reflections and TA emission. A small part of the master beam is sampled by a glass plate (GP) and used for spectroscopy and stabilisation. Seeding of the tapered amplifier (TA) is achieved via the incoupling lens (1). An achromatic lens (2) and a cylindrical lens (3) collimate the amplified beam before it is sent through an optical Isolator (OI) and coupled into a polarization maintaining fibre at (FC). The half-wave plate is required to align the beam polarization to the fibre axis.

b) Top view of the setup.

c) Front view of the setup. (in b) and c) the half-wave plate was not yet integrated.)



### Master Beam Path

The beam from the master is sent through a 60 dB optical isolator<sup>5</sup> to avoid influencing the master operation by reflections or backwards directed emission of the TA. Despite the facets of the TA being anti-reflection coated it will still show weak emission in *both* direction.

Even though an unwanted feature the backward emission can be put to good use when coupling the master beam into the TA entry channel. Collimating the backward emission with the incoupling achromatic lens, and overlapping the master beam with the collimated backward emission gives a good starting point for the master incoupling. At this point seeding should already occur and only fine-adjustment is needed to optimize the TA output.

from frequency master

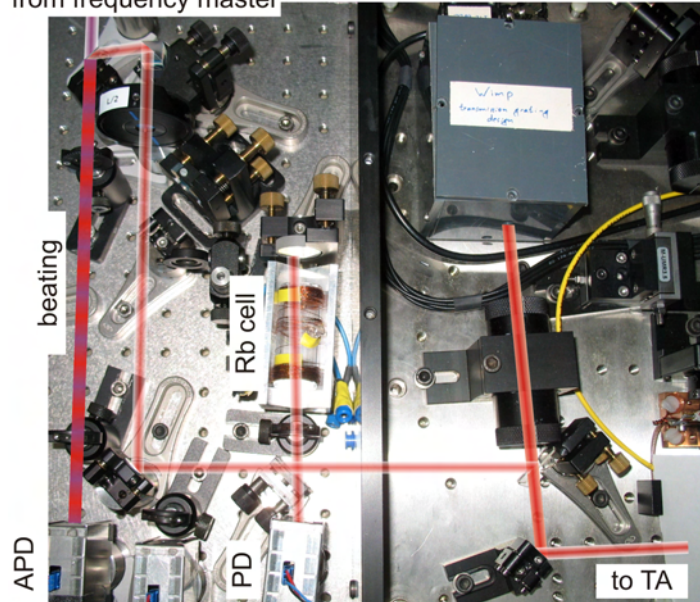


**Figure 11.5.:**

Master Spectroscopy and Lock  
A fraction of the TA master beam is sampled for spectroscopy and locking. The spectroscopy consists mainly of a Rb gas cell and a photodiode. The FO lock is established via measuring the beating frequency between TA master and frequency master (see section 9.3) in an APD.

A fraction of the master beam is directed to a standard Doppler free saturation spectroscopy setup and the laser lock (see figure 11.5). For active laser locking the master is superimposed to a beam from the frequency reference master. The beating of the two lasers is measured with an APD photodiode and used in an frequency offset lock (see e.g. [93, 99]). The frequency offset lock allows stabilizing the master laser (and thus the TA) on an arbitrary detuning to the  $F = 2 \rightarrow F' = 3$  transition. In addition the locking electronics developed together with the electronics workshop of the Physikalisches Institut, Universität Heidelberg, enable us to externally control and shift the lock point during the experimental cycle.

Controlling the cooler laser frequency by a frequency offset lock is superior to the standard method of double-pass AOM shifts, not only because of the complexity and

<sup>5</sup>Isowave/Döhner I-80-U4, 60 dB optical Isolator.

loss involved in a double-pass AOM setup, but as well due to independence of power and frequency in the frequency offset lock.

Since the entry facet of the TA matches the master diode output facet an optimal coupling is established if identical lenses are used for collimation of the master and incoupling into the TA.<sup>6</sup> To this end we employ a Thorlabs achromat with 6.16 mm focal length as incoupling lens<sup>7</sup>, mounted on a lockable Newport mini translation stage<sup>8</sup> for focus adjustment.

All diode lasers emit highly polarized light [94, 95]. Correspondingly the TA can only amplify seed light that is aligned to its preferred polarization axis. In our setup the polarization axes of master and tapered amplifier are automatically aligned, since both diodes are mounted with their junction orthogonal to the baseplate plane.

### Tapered Amplifier Mounting

**Mechanical Mounting** The tapered amplifier diode itself is mounted in a T-shaped copper block. The design of the TA mount is challenging insofar as it should have excellent mechanical stability while allowing the collimation lenses to be placed at minimal distance to the TA. Additionally good thermal conductivity is required as well to guarantee optimal thermal stabilization of the TA.

We have chosen copper as a material for the mount due to its high thermal conductivity and favourable machining properties. Thermal expansion coefficients are less important due to the small dimensions involved.

For temperature control a NTC temperature probe<sup>9</sup> is integrated in the copper mount and a peltier element<sup>10</sup> sandwiched between the mount and the baseplate. Temperature stabilization is achieved by controlling the peltier element current with a commercial temperature controller<sup>11</sup>. Thus the baseplate is used as a thermal reservoir for cooling the TA. The copper mount is fixed with plastic screws to the baseplate for thermal isolation.

A thin indium foil<sup>12</sup> squeezed between the TA diode and the copper block is used to guarantee good thermal contact between the TA and the thermal base. The soft indium fills any surface roughness induced gaps if gentle pressure is applied. Indium has

---

<sup>6</sup>Note that this explicitly means beam shaping optics, such as anamorphic prism pairs usually employed to correct the ellipticity of diode laser beams, are of little use in TA master setups. It means as well that fibre coupled master beams, as employed in pure amplifier stages without built in master, will have a suboptimal incoupling and hence higher saturation power. Fortunately due to the low saturation power of current TA diodes (see section 11.6) this is of little concern to the experimentalist.

<sup>7</sup>Thorlabs, C170TM-B, NA= 0.3,  $f = 6.16$  mm, [www.thorlabs.com](http://www.thorlabs.com).

<sup>8</sup>Newport, M-UMR3.5 with BM11.5 micrometer screw and CL3-5 locking screw, [www.newport.com](http://www.newport.com).

<sup>9</sup>10 k $\Omega$  negative temperature coefficient resistor, RS-components, RS388-0168, [www.rs-components.com](http://www.rs-components.com).

<sup>10</sup>28.7 W peltier element, RS-components, RS197-0348, [www.rs-components.com](http://www.rs-components.com).

<sup>11</sup>Thorlabs TED 8040, used in a PRO 8000-4 driver rack, [www.thorlabs.com](http://www.thorlabs.com).

<sup>12</sup>Purchased from Goodfellow, [www.goodfellow.com](http://www.goodfellow.com).

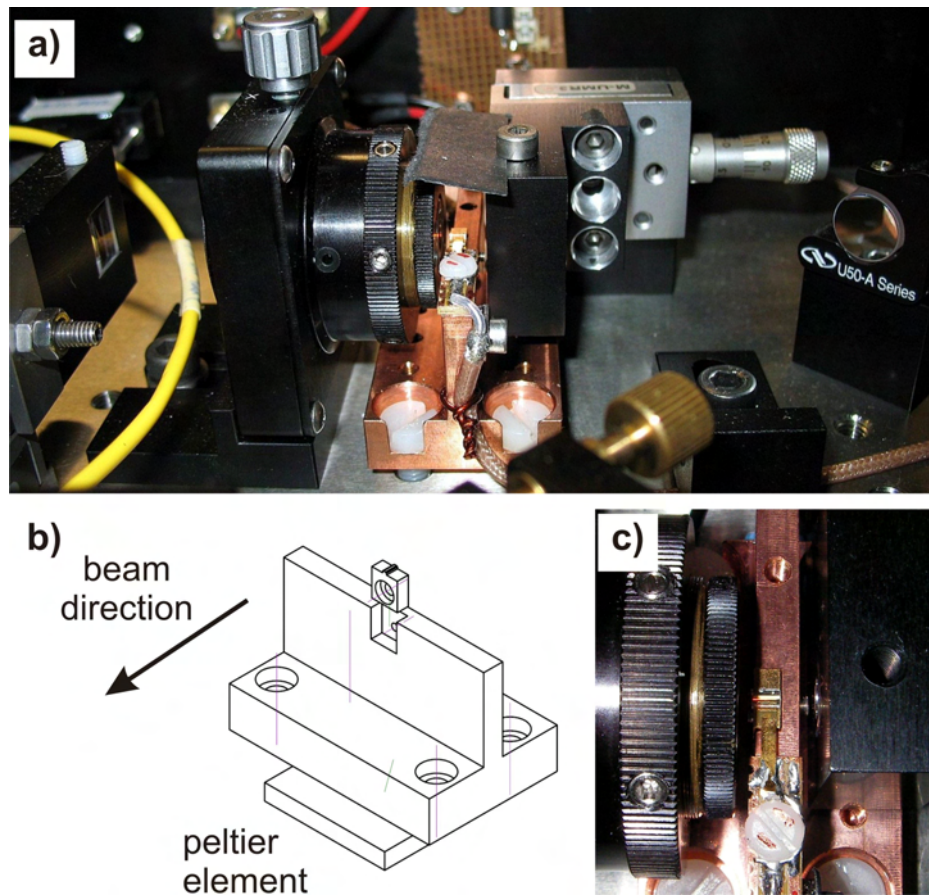


**Figure 11.6.:** Tapered Amplifier Mount

- a) side view
- b) schematic view, showing the peltier element
- c) top view

to be used here instead of commonly used thermal conductive paste (used e.g. for heat transfer in computer CPUs) because the fumes outgassed by the thermal conductive paste would settle on the TA facets, compromising the TA performance.

**Electrical Connection** The electrical connection of the TA to the laser driver are realized via a mounting wire (see figure 11.3), supplying a connector to the negative terminal of the TA, and the TA mount, connected to the positive terminal.

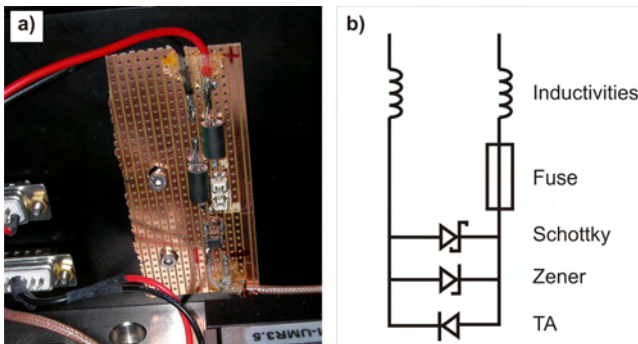


**Figure 11.7.:**  
Tapered Amplifier Safety Circuit  
a) Photo of the actual implementation.  
b) Safety circuit, consisting of two inductivities to filter high frequency noise, a 3 A fuse as protection against overcurrent, a Zener diode against overvoltage, a Schottky diode against reverse voltage and of course the TA itself.

Since tapered amplifier diodes are known to be extremely sensitive to supply voltage spikes an additional safety circuit is built into the setup. Voltage spikes need to be avoided at all costs. Even if the tapered amplifier survives a spark without immediate visible effect, the lifetime of the device will be reduced.

As shown in figure 11.7 the safety circuit consists of two high bandwidth chokes to filter high frequency noise, a 3 A fuse, a Schottky diode<sup>13</sup> to prevent reverse voltages and a series of three Zener diodes<sup>14</sup> as protection against overvoltages.

### Tapered Amplifier Output Collimation

As illustrated in figure 11.2 the extreme rectangular shape of the output facet with width 190  $\mu\text{m}$  and height 1  $\mu\text{m}$  leads to very different divergences in horizontal and vertical direction. The fast vertical divergence is corrected directly after the TA by a high NA achromatic lens<sup>15</sup>. The remaining horizontal divergence is collimated by a cylindrical lens<sup>16</sup> of 40 mm focal width. Note though, that due to the effect of the achromat, the distance between TA and cylindrical lens is much longer than the focal length. In the current setup it is positioned approximately 60 mm from the TA.

Careful positioning of the achromatic lens perpendicular to the beam direction is important to achieve an optimal beam shape. Since precise collimation is needed as well, we have employed a lockable XYZ-stage<sup>17</sup> to mount the achromatic lens.

<sup>13</sup>HP2-800-110, 4ns reaction time, remaining voltage drop 700 mV

<sup>14</sup>CD C401, breakdown voltage 3 to 5 V

<sup>15</sup>Thorlabs, C330TM-B, NA= 0.6,  $f = 3.1$  mm, [www.thorlabs.com](http://www.thorlabs.com).

<sup>16</sup>Thorlabs, LJ1402L1-B,  $f = 40$  mm, [www.thorlabs.com](http://www.thorlabs.com).

<sup>17</sup>Newport, LP-05A-XYZ, [www.newport.com](http://www.newport.com).

The XYZ-stage limits both the minimal beam height over the table and the minimal distance between achromat and TA.

Due to the long focal width of the cylindrical lens the collimation is quite insensitive to exact positioning of the lens and satisfactory results can be achieved by positioning the lens manually using a fixed mount. We have, nonetheless, chosen to use another lockable Newport mini translation stage<sup>18</sup> to mount the cylindrical lens, giving us an additional degree of freedom to optimize the fibre coupling.

### Optical Isolator

Any backreflection of light into the TA would result in catastrophic optical damage of the TA due to increasing power density in the amplification region if the taper is traversed backwards. To avoid this a 60 dB optical isolator<sup>19</sup> is integrated into the setup as close as possible to the TA, i.e. after the collimation optics.

Since the apertures of optical isolators are often the limiting elements for the beam size care has to be taken in selecting the collimation optics to avoid clipping of the beam at the optical isolator.

### Fibre Coupling

After passing the optical isolator the beam is directed via two stable mirrors and a half-wave plate to an SuK Fibre Coupler<sup>20</sup> to be coupled into a polarization maintaining single mode fibre<sup>21</sup>.

The amplified beam is used in the experiment as the MOT cooler beam, hence the polarization of the beam needs to be controlled. To this end a polarization maintaining single mode fibre had to be used, which in turn required a half-wave plate to align the beam polarization with the axis of the polarization maintaining fibre.

The overall coupling efficiency into the fibre was measured to be 48 % of up to 1.2 W incident on the fibre coupler, which is a reasonable value for a tapered amplifier. Voigt et al. have reported coupling efficiencies of a self-built tapered amplifier setup between 46 and 59 % at 200 mW, depending on the diode used [106]. While Nyman and coworkers have reached up to 60 % coupling efficiency at 400 mW [107]. In comparing these values one has to keep in mind that the beam profile of a tapered amplifier beam is far from being ideal, thus coupling efficiencies beyond 60 % are not expected. It should be noted as well that the beam profile is less distorted at low powers, thus higher coupling efficiencies can be reached for low power operation. We have measured coupling efficiencies far exceeding 50 % at 300 mW operation.

<sup>18</sup>Newport, M-UMR3.5 with BM11.5 micrometer screw and CL3-5 locking screw, [www.newport.com](http://www.newport.com).

<sup>19</sup>Isowave/Döhner I-80-U4, 60 dB optical Isolator.

<sup>20</sup>Schäfter+Kirchhoff 60FC-4-A8-07,  $f = 8$  mm, NA= 0.3, [www.sukhamburg.de](http://www.sukhamburg.de).

<sup>21</sup>Thorlabs HB750 bow-tie type polarization maintaining single mode fibre, [www.thorlabs.com](http://www.thorlabs.com)



Coupling efficiencies can be increased by employing more complex beam shaping optics. Good results have been achieved using first larger lenses for collimation followed by a telescope to size down the beam. The drawbacks here are that additional surfaces before the optical isolator have to be introduced, increasing the chance for backreflections and, of course, the increase in beam path and connected decrease in stability.

### Beam Height

To reduce vibrations in the opto-mechanical mounts the beam level should be kept as low as possible over the baseplate. In the current setup the beam height over the baseplate was limited by the XYZ-stage for amplified beam collimation to 35 mm.

### Baseplate

To guarantee pointing stability of the beam paths the whole tapered amplifier setup was built on a separate baseplate, fabricated from stainless steel.

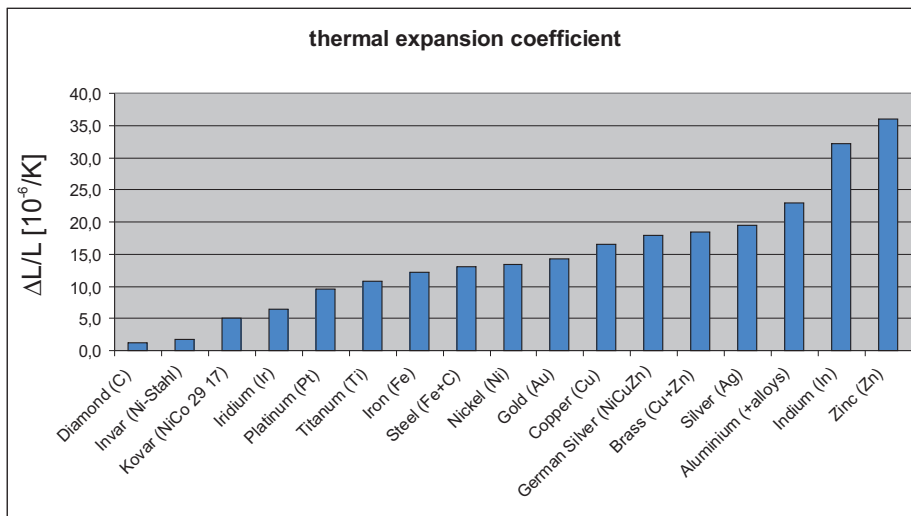


**Figure 11.8.:** Thermal Expansion for Different Materials

Given is the relative length change  $\Delta L/L$  at  $1^\circ \text{C}$  temperature change in the range  $20^\circ - 25^\circ \text{C}$ .

Steel was chosen for its low thermal expansion. Those materials shown in figure 11.8 that exhibit even less thermal expansion were rejected as baseplate materials either for financial reasons or because machining would have been unreasonably difficult.<sup>22</sup>

The baseplate serves as thermal reservoir for the temperature stabilization of master and tapered amplifier as well. Since limited transportability with minimal need for readjustments of the setup was desired the baseplate dimensions were chosen according to cautious estimations of bending and thermal stability. Height for this prototype

<sup>22</sup>Iron has been rejected due to its tendency to corrode.

was correspondingly chosen to be 30 mm, leading to a weight of approximately 25 kg (handles are included in the design to ensure portability).

The excellent performance of this device leads us to believe that future designs can well reduce the baseplate thickness without a compromise in stability. Even more so since the initially included option of water cooling the base (see below) can be omitted from future models.

To reduce stray light all mountings have been black anodised.

Surrounding walls of the device have been constructed of aluminium with conducting connections to act as an RF-shield. The tapered amplifier should always be operated with closed casing, both to keep air movement out and stray light in.

### Options

Since the tapered amplifier system presented here has been our first prototype it was kept intentionally very flexible in terms of placement of optics and additional options. Future designs can easily omit numerous threads in the baseplate and reduce the dimensions even further.

Notable options included in this prototype were free space outcoupling of the beam instead of fibre-coupled output and water cooling of the baseplate.

For free space outcoupling simple the first mirror after the optical isolator has to be removed and the beam will leave the TA system through an aperture in the sidewall.

Water cooling (or even nitrogen cooling) is often recommended to be used in tapered amplifier systems to increase thermal stability. We found it to be unnecessary if the thermal reservoir for peltier cooling is big enough.

### Care has to be taken

As a summary of the above discussion the following crucial points can be identified that have to be considered in the design of a tapered amplifier system.

Care has to be taken to,

- use a pointing stable seed beam (master)
- guarantee overall alignment stability
- avoid backreflections of light into the TA
- avoid voltage spikes (even more so than with standard diodes)
- not to use heat conductive paste in the vicinity of the tapered amplifier diode
- ensure polarization matching of the input beam to the TA
- protect your eyes. Even a diffuse reflection of an 1 W beam is strong enough to damage your eyes.

## 11.5. Transmission Grating Master

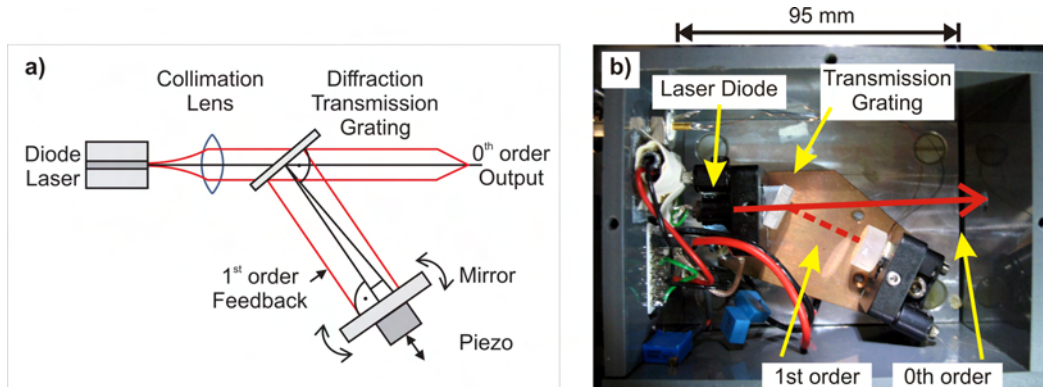


**Figure 11.9.:** Transmission Grating Cooler Master

Pseudo-Littman ECDL configuration employing a commercial transmission grating. Schematic view (a) and photo (b) of the setup. The major part of the beam passes unhindered through the grating and can be used as a pointing stable beam in the experiment. The first diffraction order is directed to a mirror, similar to a Littman configuration. Rotation of the mirror allows coarse wavelength selection while a piezo behind the mirror is used for fine frequency scans. Schematic view adapted from [42].

Most of our external cavity diode laser (ECDL) systems are built in Littrow-configuration (see section 9.3). Unfortunately the Littrow-configuration is not pointing stable and hence unsuited to be used as a tapered amplifier master. Since the master laser has to be coupled reliably and stable into the single mode entry channel of the tapered amplifier we decided to construct a pointing stable laser source based on a Littman-configuration.

The laser light is generated by a Rohm 785 nm diode<sup>23</sup> operated at 780 nm and driven by a commercial laser driver and temperature controller<sup>24</sup>.

Instead of a reflection grating, as employed in a standard Littman-setup, we use a commercial transmission grating<sup>25</sup> to generate the feedback. As illustrated in figure 11.9 the major part of the beam passes through the grating and can be used as a pointing stable beam in the experiment. The first diffraction order is directed to a mirror and there retro-reflected to supply feedback to the diode after an additional diffraction on the grating. Rotation of the mirror allows coarse wavelength selection while a piezo behind the mirror is used for fine frequency scans. Technical details can be found in [42], while the technical drawing can be found in appendix F.

In contrast to previous implementations of transmission grating stabilized ECDL laser systems [109–111] that have employed reflective or holometric transmission gratings we use a commercially available, purely diffractive transmission grating.

<sup>23</sup>Rohm, RLD78PZW2.

<sup>24</sup>Thorlabs ITC 8022DS15 in a PRO 8000-4 rack, [www.thorlabs.com](http://www.thorlabs.com).

<sup>25</sup>Thorlabs GT13-06V, 600 grooves/mm, [www.thorlabs.com](http://www.thorlabs.com).

Drawbacks of the transmission grating laser design are the high losses connected to both the inherent loss channel in a Littman design and higher order diffractions and multiple reflections in the transmission grating. The latter make the initial feedback alignment significantly harder than in our standard Littrow setups.

Overall the transmission grating design achieves smaller modehop-free tuning ranges and less output power than comparable Littrow configurations. Modehop-free scanning range<sup>26</sup> of 2.7 GHz and an output power, measured at the TA position, of 9 mW at 75.5 mA supply current. Laser threshold was measured to be at 27 mA.<sup>27</sup>

The reduced output power compared to Littrow-configurations is of no concern here, due to the low saturation level of the TA (see section 11.6).

While no replacement for the standard Littrow-configuration, the new transmission grating design is extremely useful in applications requiring pointing stable beams.

---

<sup>26</sup>The modehop-free scanning range given is achieved in a piezo scan at constant current. Much higher values can be reached if a current feed-forward is used in combination with the piezo scan, but I find constant current values to be better indicators of the quality of the feedback.

<sup>27</sup>Depending on the diode lasing thresholds as low as 23 mA can be achieved with Rohm RLD78PZW2 diodes in a Littrow configuration.

## 11.6. Performance

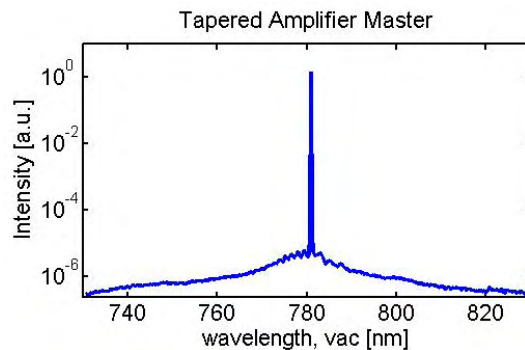
A thorough characterization of the tapered amplifier system allows operating it at the optimal point.

### 11.6.1. Gain Width

A plot of the free-running diode emission versus wavelength can be very instructive to find the optimal temperature at which a laser diode should be operated.

The spectrum of a typically laser diode is several nanometer broad, enabling amplification of light at a range of different wavelengths. To achieve maximum output power, optimal stability and largest mode-hop free scanning range the diode should be operated at its natural frequency, i.e. at the peak of its free-running output spectrum.

Optical spectrum analysers are therefore invaluable tools in setting up ECDL diode laser systems. With the capability to measure the output characteristic of a diode its temperature dependence can be exploited to shift the emission peak to the desired frequency.



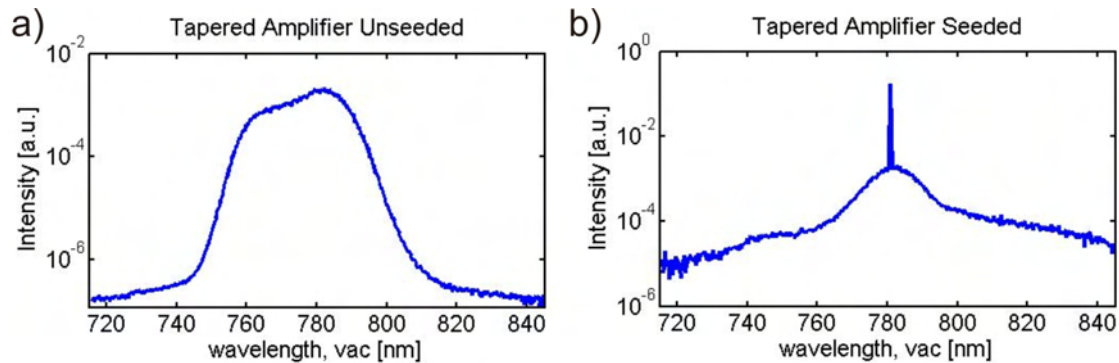
**Figure 11.10.:**  
Transmission Grating Master Spectrum

Figure 11.10 shows the output spectrum of the transmission grating master laser measured with an Anritsu MS9710C optical spectrum analyser.<sup>28</sup> The strong central emission at 780.2 nm, forced by the external cavity, can be observed on top of a broad background of amplified spontaneous emission (ASE). Note that the peak of the background spectrum is located at 780 nm, indicating optimal adjustment of the laser.

ASE can be problematic in optical dipole traps, contributing significantly to the heating rate. For the measurements presented here ASE is not an issue.

The gain width of the tapered amplifier diode was specified to be typically around 20 nm. Figure 11.11a) shows the spectrum of the unseeded tapered amplifier, demonstrating a 3dB gain width of 17.1 nm centred around 780 nm. If the master is seeding the tapered amplifier predominantly the seed wavelength is amplified as can be seen from fig.11.11b). The intensity scales of the two plots are not comparable since, obviously, at seeded operation the beam had to be massively attenuated. Both measurements are performed on the fibre coupled signal. Therefore the measured gain

<sup>28</sup>Measurement resolution was chosen to be 0.05 nm for the 130 nm scan presented here.



**Figure 11.11.:** Tapered Amplifier Spectrum

- a) At unseeded operation the whole gain width of 17.1 nm (3dB) can be seen emitting almost homogeneously.
- b) At seeded operation the seed wavelength is dominantly amplified. Note that the amplitude of the lasing peak is strongly suppressed in this graph due to limited resolution.

bandwidth has to be interpreted as a lower limit, since the fibre acts as a spectral filter.

Note that ASE is a much bigger problem in tapered amplified beams than in standard diodes due to the higher gain width. It has been shown that ASE in tapered amplifiers can be suppressed by operating at the edge of the gain profile and by highly saturated operation [106].

### 11.6.2. Beam Profile

The beam profile of a tapered amplifier is usually far from a nice gaussian mode. Figure 11.12 shows measurements of our beam profile after the optical isolator for different currents. An Airy pattern generated by diffraction on a 1  $\mu\text{m}$  times 190  $\mu\text{m}$  rectangular aperture is shown as a rough guide for comparison.

The profile exhibits a clear central spot carrying the bulk of the intensity. A series of diffraction spots can be seen extending to the left, as expected from the Airy pattern. The right half of the diffraction spots is missing, most likely caused by clipping of the beam on the optical isolator aperture. It should be noted here that the camera used to take these pictures was rotated relative to the optical table, so that the diffraction pattern actually marks the horizontal direction.

The beam profile is relatively stable for currents between 1 A and 2 A, but, as can be seen from figure 11.12, at low currents the profile changes significantly. Experience has shown that any significant change in current or temperature requires a re-optimization of the fibre coupling.

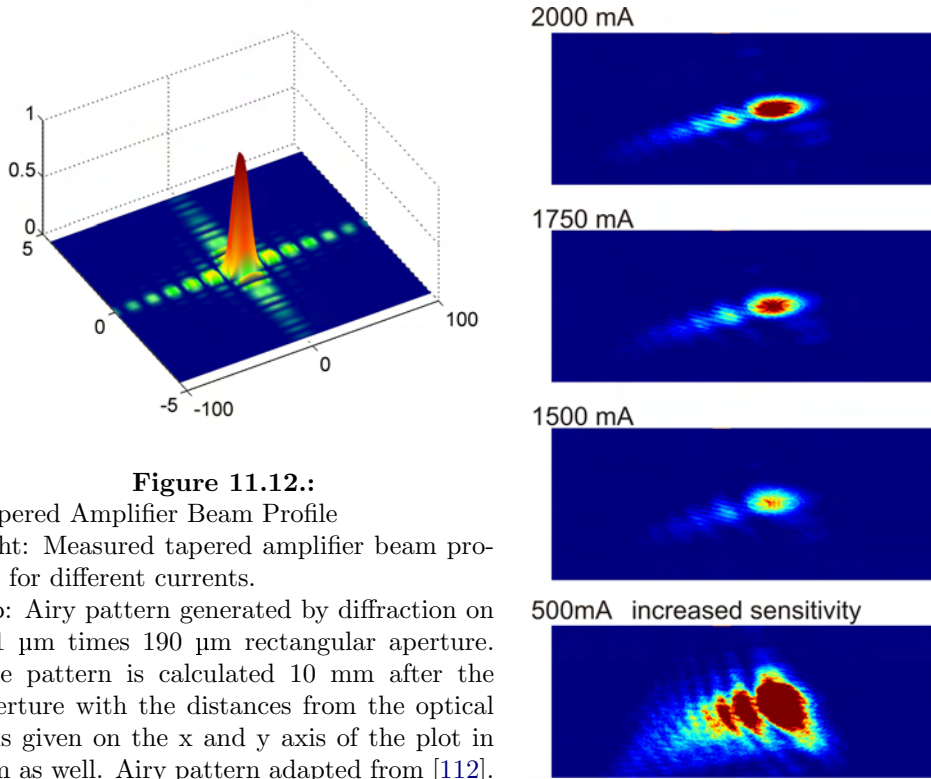


**Figure 11.12.:**  
Tapered Amplifier Beam Profile  
right: Measured tapered amplifier beam profile for different currents.  
top: Airy pattern generated by diffraction on a 1 μm times 190 μm rectangular aperture. The pattern is calculated 10 mm after the aperture with the distances from the optical axis given on the x and y axis of the plot in mm as well. Airy pattern adapted from [112].

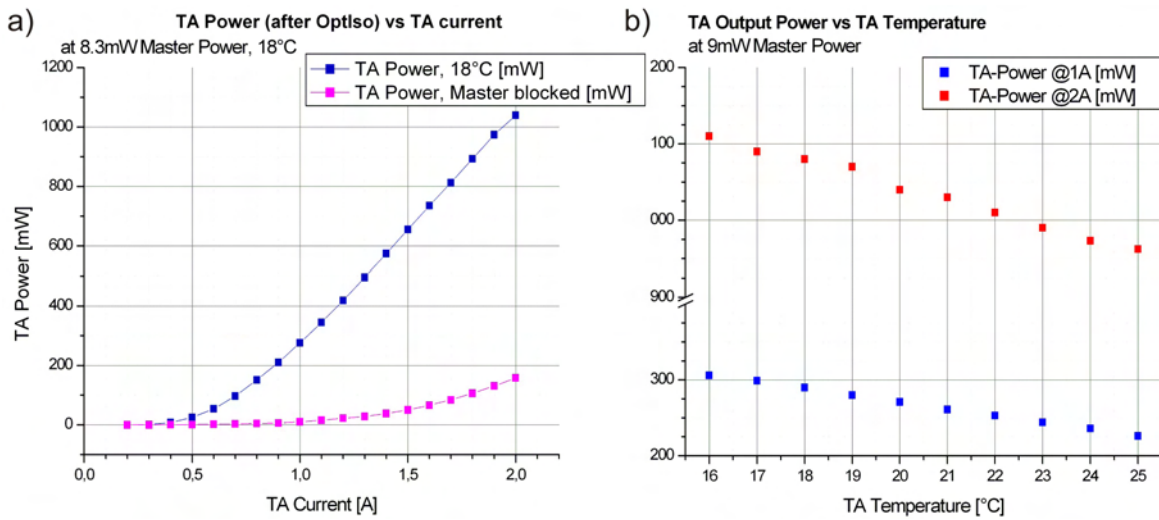


**Figure 11.13.:** Tapered Amplifier Parameter Response  
a) Tapered amplifier power as function of the current. The pink line shows the tapered amplifier output power for unseeded operation, while the blue line shows the output for a master power of 8.3 mW. The tapered amplifier has been operated at 18° C for this measurement.  
b) Tapered amplifier power as function of the temperature for two different currents.

### 11.6.3. Characterisation

Figure 11.13 shows the tapered amplifier output power in seeded and unseeded operation as function of the current. For seeded operation a linear relation between the tapered amplifier current and the amplification can be observed.

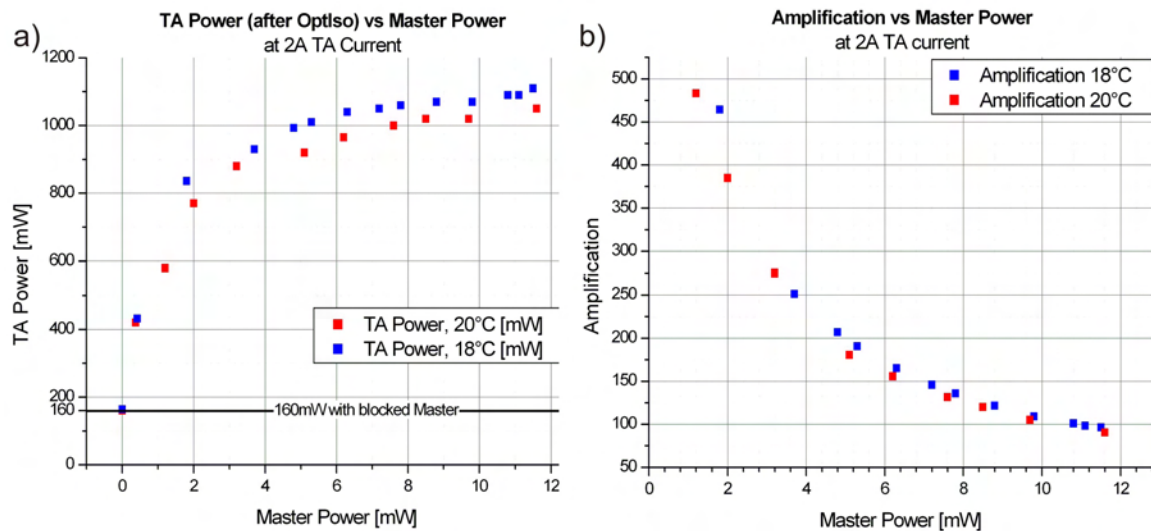


**Figure 11.14.:** Tapered Amplifier Amplification

- a) Tapered amplifier output power as function of input power for two different temperatures. The horizontal line shows the unseeded tapered amplifier output level.  
 b) Amplification as function of input power.

Figure 11.14 illustrates the saturation behaviour of the tapered amplifier for two different temperatures. Already at input powers larger than 6.5 mW the TA appears to be saturated, with only minimal increases in output power if the input power is further increased.<sup>29</sup>

Note as well that the amplification increases for lower TA temperature. A plot of the amplification in figure 11.14b) allows extracting the gain in the limit of high saturation to approximately 90.

<sup>29</sup>As the output power still slowly increases with input power the definition of saturation power is somewhat arbitrary, but has been chosen to correspond to the  $1 - 1/e$  point.



### 11.6.4. Specifications and Reality

The characterisation of the used tapered amplifier diode has demonstrated that the specifications given by Eagleyard Photonics (see table 11.1) have to be understood as industry level specifications, and are indeed always exceeded. In fact we have been assured that technologically these diodes can deliver up to 4 W, albeit at a lifetime reduction roughly proportional to the relative increase in current needed [113].

The following table lists the core parameter specifications and our measurement results.

Tapered Amplifier Specifications and Measurements

Parameter	Specification	Measurement
output power	1000 mW at 25° C and 2.5 A	> 1100 at 20° C and 2.0 A
amplification	20 at 25° C and 2.5 A	≈ 90 at 20° C and 2.0 A
saturation power	50 mW	6.5 mW

Here the saturation power has been defined as the  $1 - 1/e$  power beyond which only marginal increases in output power are reached.

We would have liked to examine variability of the measured parameters with different diodes of the same model. Unfortunately the opportunity for these measurements has not yet arisen, since at the time of writing this thesis the first tapered amplifier diode built into our prototype has been running flawless for now more than two years.

## 11.7. Cost Estimate

At the Physikalisches Institut of the Universität Heidelberg we have been in the fortunate situation to have access to both an excellent mechanical and an excellent electronics workshop. This combination has made it possible to construct a custom, ultra-stable tapered amplifier system at about 50 % of the cost of an available commercial system.

It should be well understood that the following cost estimate cannot compare competing prices, since only the financial impact on the groups funds has been considered. Work-time of electronics and mechanical workshop, as well as my own time spent designing, assembling, adjusting and calibrating the system have been completely neglected.

With this in mind the following table gives an overview of the *costs* of our system that has to be compared to the *price* of approximately 40.000 Euro paid for a commercial system bought by a neighbouring experiment that delivers slightly less power at inferior stability.<sup>30</sup>

Position	Cost [Euro]
Tapered Amplifier	1992.20
Laserdriver	6714.60
Optical Isolators	4048.40
Laser Stabilization Electronics	2382.05
Master Laser	320.46
Opto-mechanics	2039.10
Optics	452.99
Fibre-coupler	215.00
Spectroscopy	357.52
<b>Overall System Cost</b>	<b>18523.32</b>

Here the costs have been based on the actual amount paid, including discounts, for items bought externally. For items fabricated in the electronics workshop, such as the laser lock electronics, only material costs are listed. For items constructed and machined in the mechanical workshop only consumed tools and costs for anodising are considered. Material costs do not apply as such, since our parts were small enough to be constructed from left-over pieces from previous projects. The exception is the stainless steel baseplate for which 368.30 Euro material costs and 150 Euro in used tools are included in the opto-mechanics.

<sup>30</sup>The commercial system actually does not include lock electronics.

## 11.8. Improvements

Based on the experience made with the prototype tapered amplifier system constructed in the course of this thesis I offer the following suggestions for future versions.

Apart from a reduction of baseplate thickness the overall dimensions of the system can be reduced even further, since the final position of the optical elements is now known. Especially the beam path from master to TA and TA to optical isolator can be shortened.

### 11.8.1. Lens Mounts

The mounting of the incoupling lens has been adequate, but the outcoupling lens mounting should be improved. The XYZ stage used shows strong hysteresis on all degrees of freedom and a coupling between the degrees of freedom, making alignment more a gamble than a predictable process. Unfortunately two alternative XYZ stages from competing suppliers have been tested and show similar behaviour to the employed stage. It seems therefore that XYZ stages are unsuitable as lens mounts on the required level of precision.

Experience has shown that X and Y positioning (orthogonal to the optical axis) are less critical than expected. Even though precise positioning on the optical axis does enhance the quality of the beam profile this influence is of less significance to optimal behaviour of the TA than Z positioning (focussing). Hence I suggest to align the lens carefully to the optical axis during initial construction, but then fix its X and Y position, mounting it only on a Newport mini translation stage for Z movement (collimation).

Dispensing of the XYZ stage has the added benefit of a possible reduction of the beam height over the baseplate, increasing stability. Additionally a custom mount may allow reducing the distance between outcoupling lens and TA output facing, thus smaller focal length lenses can be used, reducing the beam diameter which leads to less clipping of the beam on the optical isolator.

The cylindrical lens does not necessarily need a translation stage for collimation. Good results can be achieved by manual positioning, the translation stage should only be used if the fibre incoupling efficiency is critical.

In choosing lenses and designing mounts one should be well aware that simulations of lens systems and placements based on specified divergences are only of limited use. It is my experience that the divergence of the TA output beam, as well as the beam shape, changes significantly with TA current. Whether this is connected to a possible thermal expansion or an intrinsic effect of the TA could not be established.

### 11.8.2. Options

As discussed above the TA can well do without water cooling, making that option obsolete.

For high efficiency fibre incoupling an additional telescope for beam shaping before the optical isolator might be considered. In doing so one should be well aware of the connected drawbacks (additional reflective surfaces, added complexity, longer beam paths).

## 11.9. Safety

It cannot be stated often enough that a 1 W laser system has to be treated with respect. At this power even a diffuse reflection can damage your eyes. Specular reflexes from any object in the beam path, *will* create irreparable damage.

Laser goggles should be worn at all times when the tapered amplifier is not enclosed, since the diode emits considerable amounts of light in all directions if operated at 2 A. Do remember that the visible part of a 780 nm beam is only a small fraction of the total power. Your blinking reflex does not work for infra-red radiation.

Figure 11.15 shows the effect of the collimated (*not* focussed) beam on a piece of paper unwisely used as a beam block.



Figure 11.15.: Laser Safety First

**Part III.**  
**Conclusion**



## 12. Summary

In the course of this thesis an extremely stable ultra-cold atom experiment was constructed to perform single atom detection on an atom chip with an integrated fluorescence detector.

**Technical Developments** The achieved high stability allowed performing continuous measurement runs for more than 72 h without human intervention, corresponding to several thousand single measurements. Of key importance to this has been a laser system with high long-term stability and the development and construction of a tapered amplifier laser system.

The tapered amplifier system delivers more than 1 W of output power or more than 500 mW of fibre coupled pure single mode power in a polarization maintaining fibre. The system has outperformed commercial tapered amplifier systems of neighbouring experiments both in terms of total power and long term stability.

The fluorescence detector itself is composed of a tapered single mode excitation fibre and a multi mode detection fibre, both passively aligned and mounted in a lithographically defined SU-8 structure on an atom chip.

The use of a tapered excitation fibre creates a highly selective excitation region from which fluorescence light is collected via the multi-mode detection fibre. This design allows an efficient suppression of background noise to a level of 311 cps, corresponding to a mean distance of 3.2 ms between background counts, as well as highly localized probing of the atomic ensemble.

**Single Atom Detection** It has been demonstrated that the integrated, fibre based fluorescence detector is capable of detecting single atoms with up to 66 % efficiency, despite a finite photon detection efficiency of only 0.9 %. The mean signal per atom has been measured to 1.08 counts per atom from a total of 119 photons emitted. The  $1/e$  interaction time of the atoms with the detector has been estimated to 12  $\mu$ s.

The above results have been conclusively confirmed by three independent methods of analysis.

The background rate of the current detector was measured to 311 cps, leading to a false detection probability of up to 8.9 %. It has been shown as well that the false detection probability can be reduced to 0.1 % while maintaining a 50 % single atom detection efficiency by limiting the detection time to 20  $\mu$ s, corresponding to 50 kHz

bandwidth. A signal to noise ratio of 100 can be reached at detection times smaller than 175  $\mu\text{s}$ , with a single atom detection efficiency up to 65 %.

**Statistical Distribution of the Atoms** The arrival times of the atoms at the detector have been measured to follow a Poissonian distribution, allowing to conclude that we observe a thermal ensemble of atoms distributed over several modes of the guide. Both a shot to shot variance analysis presented in chapter 6 and the time interval analysis of chapter 7 allow identifying the statistical distributions of the atoms from fluorescence measurements.

While the variance analysis requires a high number of measurements at identical parameters time interval analysis allows extracting information already from a single measurement. Therefore, time interval analysis of fluorescence emissions promises to become an important diagnostic tool in ultra-cold atom studies, giving a live feedback of the influence of experimental parameters on the statistical distribution of the atoms. Possible applications include watching transitions from thermal distributions to Bose-Einstein condensed states. Even differentiating between Bose-Einstein condensed atoms and 1D condensates like Tonks-Girardeau gases seems possible. Here the fluorescence detector presents an in-situ measurement alternative to the commonly used time of flight observation methods, where only expanded clouds outside of the traps can be examined.

**Non-classical Correlations** Using two single photon detectors in a Hanbury Brown and Twiss type configuration fluorescence signals from atoms passing the detector were recorded with 1 ns temporal resolution. It has been demonstrated that detector artefacts can be successfully removed from the measured signal.

With this setup quantized photon emission from single atoms could be observed. This is a direct observation of photon anti-bunching with  $g^{(2)}(0) = 0.0005 \pm 0.0010$  from single neutral atoms. It should be stressed that these observations were performed on atoms passing the detector, confined only in the transversal direction, but not localized in the detection region.

The measured anti-correlation indicates a mean photon number in the detection fibre of  $n = 1.0005 \pm 0.0010$  photons, which indicates that the detector can be used as a high quality source of single photons.

Rabi oscillations of the correlation function have been observed and proven to be in excellent agreement with the theoretical expectations.

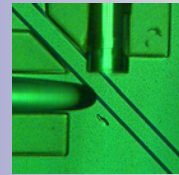
In an unprecedented measurement it was demonstrated that the measured value of  $g^{(2)}$  for vanishing lag is proportional to atom density over three orders of magnitude in density.

**Detector Performance Overview** The relevant operational parameters of the integrated fluorescence detector are summarized in figure 12.1.



# Fluorescence Detector

## Data Sheet



### Technical Parameters

Distance from Z trap	5.5mm
Excitation Fibre Focal Length	$40\mu\text{m} \pm 1\mu\text{m}$
Excitation Fibre Focus Waist	$5\mu\text{m} \pm 1\mu\text{m}$
Focus Height over Chip	$62.5\mu\text{m}$
Saturation Power	325pW
Stray Light Suppression	$10^{-8}$ (30cps/nW)

Background Level 311cps

Detection Fibre Core Diameter	$62.5\mu\text{m} \pm 3\mu\text{m}$
Detection Fibre NA	$0.275 \pm 0.015$
Photon Collection Efficiency	1.9%
Total Photon Detection Efficiency	0.909%

### Single Atom Detection Efficiency

Detection Time	300 $\mu\text{s}$	45 $\mu\text{s}$	20 $\mu\text{s}$
Single Atom Detection Efficiency	66%	60%	50%
False Positive Detection Probability	8.9%	1.4%	0.6%

### Signal Strength

Counts per Atoms	1.08	0.92	0.72
Photons per Atom	119	101	79

Interaction Time (1/e)  $12\mu\text{s} \pm 1\mu\text{s}$

Figure 12.1.: Datasheet of the Integrated Fluorescence Detector



# 13. Improvements

From the experience made with the current prototype integrated fluorescence detector we draw several suggestions for improvements of future detector version.

For improvements of the tapered amplifier laser system please refer to chapter 11.

The performance of the detector hinges essentially on two points. The first being the efficiency to detect fluorescent photons emitted from the atoms in the detection region. The detection efficiency can be improved by an increase in the collection efficiency and reduced losses in photon transmission. The second important factor influencing the performance is the level of background suppression that can be attained. Even though already very good background suppression has been reached in the present device, some room for improvement still exists.

In presenting the suggested improvements I will distinguish between measures that can be implemented in the current setup and those that require fabricating a new atom chip.

## 13.1. Improvements of the Current Detector

The following improvements can and should be immediately implemented in the current setup, requiring mainly financial efforts.

### 13.1.1. Background Reduction

The background count rate of currently 311 cps is dominated by the dark count rate of the SPCM. The setup can be upgraded to a total background of less than 91 cps simply by replacing the SPCM with a more costly module of the same series, reducing the SPCM dark count contribution from 245 cps to less than 25 cps.<sup>1</sup>

If additionally thermal emission from hot Rubidium dispensers can be avoided, e.g. by LIAD methods [76–79], the total background count rate of the detector will be reduced to less than 55 cps.

While the background reduction does not influence the atom detection efficiency it does reduce the probability for false positive detections. With an atom detection threshold of 1 count per bin single atoms can be detected with an efficiency of 66 % with a false

---

<sup>1</sup>PerkinElmer SPCM-AQR-16

positive detection probability of  $p_{\text{false1}} = 8.9\%$ . Reducing the background to 55 cps correspondingly reduces the false positive detection probability to  $p_{\text{false1}} = 1.6\%$  (see chapter 6).

At a background of 55 cps signal to noise ration 100 would be exceeded at a detection bin size of 175  $\mu\text{s}$ , while a detection bin size of 20  $\mu\text{s}$  yields false positive detections with only  $p_{\text{false1}} = 0.1\%$  at still 50 % single atom detection efficiency.

### 13.1.2. Removal of Distortions

The quality of the correlation analysis would benefit from replacing the metal shielded MM fibres delivering the signal from the filter gap to the SPCMs by longer fibres.

At the current length of 5 m secondary emission effects distort the measured correlations at time lags of  $60 \pm 5 \mu\text{s}$  (see chapter 4). This unfortunately overlaps with the timescale of non-classical correlations. I recommend employing fibre lengths of more than 15 m, to shift the secondary emission distortions into less interesting regions, hence removing the necessity for a correction of the measured correlation functions.

To further examine the photon anti-bunching over a large range of atom densities data loss in the counter card has to be eliminated.

## 13.2. Improvements of Future Detectors

Obviously the improvements discussed in the last section should be implemented in future designs as well. Additionally a redesign of the atom chip and fibre holding structures open possibilities for further enhancements.

There are basically two options to increase the signal from the atoms: increasing the interaction time or increasing the photon collection efficiency.

### 13.2.1. Increasing the Collection Efficiency

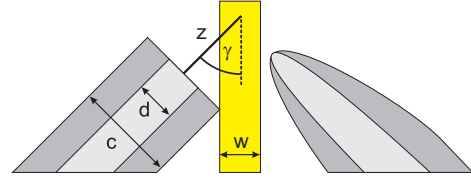
The photon collection efficiency of the detector can be increased by replacing the MM detection fibre with a fibre of higher collection efficiency. An additional factor two can be gained by using not one, but two detection fibres, e.g. facing one another on opposite sides of the guide.

#### Single Detection Fibre

It should be well understood that a higher numerical aperture does *not* necessarily result in higher collection efficiencies. The discussion in appendix B demonstrates that at a fixed distance from the interaction region a high NA can only be used to

full extend if the fibre core is correspondingly large. To exploit the high numerical aperture of a fibre with small core the fibre would have to be placed at very small distance to the interaction region.

**Minimal Distance** For the current application of detecting neutral atoms in a magnetic guide the minimal distance  $z$  between detection fibre and interaction region is determined by the width of the magnetic guide and the angle  $\gamma$  between the guide direction and the detection fibre.



If the detection fibre is brought closer part of the guide will be shadowed by the fibre, obstructing possible experiments situated further along the guide.<sup>2</sup> For a rough estimation of the guide width I will use the width  $w$  of the guide wire. Together with the fibre core diameter  $d$  and the cladding diameter  $c$  we can express the minimal distance  $z$  by the following simple expression.

**Figure 13.1.:** Minimal Distance of the detection fibre to the interaction region.

$$z = \frac{w}{2 \cdot \sin \gamma} + \frac{c}{2 \cdot \tan \gamma} \quad (13.1)$$

Hence for the employed detection fibre of  $c = 125 \mu\text{m}$  cladding diameter at  $45^\circ$  to the guide a minimal distance of  $z = 98 \mu\text{m}$  is found.

Of course the minimal distance can be decreased by increasing  $\gamma$ , even though I recommend evaluating every deviation from the  $45^\circ$  geometry carefully. At the present geometry minimal scattering of stray excitation light into the detection fibre is guaranteed by the  $90^\circ$  alignment of excitation and detection fibre. Larger angles will most likely increase the excitation light background.

Alternatively the distance can be slightly reduced by polishing the fibre facet to a dome shaped profile. The effort in polishing will likely pay off only for fibres with high cladding diameters.

**Maximum useful NA** From the minimal distance  $z$ , given by equation 13.1, and the optimal distance for a given NA and core diameter  $d$  given by equation B.3 of appendix B we can calculate the maximum useful  $\text{NA}_{\text{max}}$  by solving equation B.3 for NA.

$$\text{NA}_{\text{max}} = \frac{d}{2z \sqrt{1 + \left(\frac{d}{2z}\right)^2}} \quad (13.2)$$

Hence, for a fibre with core diameter of  $62.5 \mu\text{m}$  and cladding diameter  $125 \mu\text{m}$  positioned under  $45^\circ$  the maximum useful numerical aperture is  $\text{NA}_{\text{max}} = 0.3042$ , which is only slightly higher than the employed  $\text{NA} = 0.275$ .

<sup>2</sup>Even though fluorescence detection is destructive shadowing should be avoided to have the flexibility of either using the detector or other experiments on the guide.

**Single Atom Detection Efficiency** With equation B.2 from appendix B describing the photon collection efficiency  $\eta_{\text{coll}}$  at the optimal distance

$$\eta_{\text{coll}} = \frac{1 - \sqrt{1 - \text{NA}^2}}{2}$$

we can calculate the single atom detection efficiency  $\eta_{\text{at},1}$  as function of the fibre parameters.

It was estimated in chapter 6, that an atom emits approximately  $n = 119$  photons during the full interaction time. For 20  $\mu\text{s}$  detection time still  $\alpha = 0.72$  counts per atom could be measured, corresponding to  $n = 79$  photons per atom emitted.

From chapter 2 we know the total losses to be composed of the finite filter transmission of  $t_f = 0.995899$ , three Fresnel losses at the fibre facets with transmission  $t_r = 0.96$  each and the SPCM photon detection efficiency of  $\eta_{\text{SPCM}} = 0.564$ . Hence we can write the the single atom detection efficiency  $\eta_{\text{at},1}$  as follows, assuming as in chapter 6 a detection threshold of 1 count.

$$\eta_{\text{at},1} = 1 - e^{-n \eta_{\text{coll}} t_r^3 t_f \eta_{\text{SPCM}}} \quad (13.3)$$

For the maximum useful NA of  $\text{NA}_{\text{max}} = 0.3042$ , for  $c = 125 \mu\text{m}$ ,  $d = 62.5 \mu\text{m}$  and  $\gamma = 45^\circ$ , the photon collection efficiency is  $\eta_{\text{coll}} = 2.4 \%$  instead of 1.9 % as for the fibre employed in our experiments.

This leads to an increase in the maximal single atom detection efficiency from 66 % in the device presented here to 75 %.

Figure 13.2 shows the the single atom detection efficiency as function of the numerical aperture. If a fibre with  $\text{NA} = 0.6$  can be used to full extend a single atom detection efficiency of  $\eta_{\text{at},1} = 99.73 \%$  can be reached

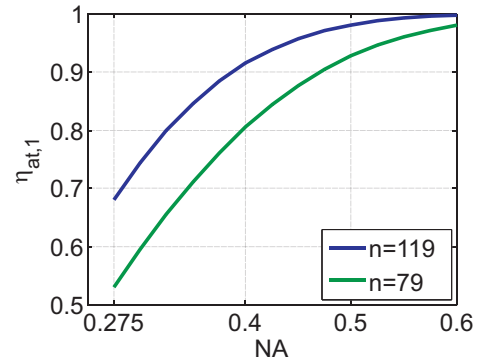


**Figure 13.2.:** Single Atom Detection Efficiency as Function of NA for full signal (119 photons per atom) and 20  $\mu\text{s}$  detection time (79 photons per atom)

**Stray Light** An increase in photon collection efficiency will lead to higher background count rates from stray probe light as well. For a rough estimate we assume the number of collected photons due to stray light to be proportional to the photon collection efficiency. Note that this is not necessarily true, since the photon collection efficiency is calculated for photons emitted in the detection region, while stray probe photons are more likely to be emitted from the tapered fibre tip or scattered from the chip surface.

Nonetheless, a pessimistic estimate of the number  $n_s$  of stray light photons collected can be gained by

$$n_s = 30 \cdot \frac{\eta_{\text{coll}}}{1.9 \%}$$

**Available Fibres** Unfortunately high numerical aperture fibres are not easily fabricated. Most high NA fibres commercially available have rather high cladding to core diameter ratios, making them unsuitable for our application.

Of the medium NA range commercially available fibres a Thorlabs fibre<sup>3</sup> with NA=0.48 should be considered for future fibre detectors. With a core diameter of 200  $\mu\text{m}$  and 230  $\mu\text{m}$  cladding diameter a minimal distance of 150  $\mu\text{m}$  under 45° can be reached, fully compatible with the optimal distance of 183  $\mu\text{m}$  to exploit the full NA. With this fibre a photon collection efficiency of  $\eta_{\text{coll}} = 6.1 \%$  can be reached, corresponding to a single atom detection efficiency of 97.3 %.

An interesting alternative are fibres manufactured by CeramOptec, featuring NA=0.53 and cladding to core diameter ratio of only 1.1.<sup>4</sup> Employing such a fibre single atoms could be detected with 98.9 % efficiency.

The following table gives an overview of the projected sensitivity increase for the fibres discussed. Here  $\eta_{\text{coll}}$  denotes the photon collection efficiency,  $\eta_{\text{ph}}$  the total photon detection efficiency and  $\eta_{\text{at},1}$  the single atom detection efficiency with a detection threshold of 1 count.<sup>5</sup>

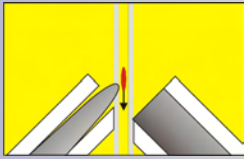
	current fibre GIF-625	Thorlabs BLF48-200	CeramOptec Optran WFGGe
NA	0.275	0.48	0.53
$\eta_{\text{coll}}$	1.9 %	6.1 %	7.6 %
$\eta_{\text{ph}}$	0.91 %	3.05 %	3.78 %
$\eta_{\text{at},1}$	66.0 %	97.3 %	98.9 %

**Projected Performance** Figure 13.3 gives an overview of the projected parameters of an improved single detection fibre detector.

<sup>3</sup>Thorlabs, BLF48-200, NA=0.48, cladding diameter 230  $\mu\text{m}$ , core diameter 200  $\mu\text{m}$ , available from [www.thorlabs.com](http://www.thorlabs.com).

<sup>4</sup>CeramOptec, Optran WFGGe, [www.ceramoptec.de](http://www.ceramoptec.de).

<sup>5</sup>All values given here assume the full 119 photons per atom to be collected to reach the maximum detection efficiency. As has been discussed in chapter 6 some applications might favour shorter photon collection times, resulting in a reduced single atom detection efficiency, but higher SNR.

Improved Fluorescence Detector Single Optran WFGe Detection Fibre Projected Data Sheet				
<b>Technical Parameters</b>				
Distance from Z trap	5.5mm			
Excitation Fibre Focal Length	40 $\mu\text{m} \pm 1\mu\text{m}$			
Excitation Fibre Focus Waist	5 $\mu\text{m} \pm 1\mu\text{m}$			
Focus Height over Chip	62.5 $\mu\text{m}$			
Saturation Power	325pW			
Stray Light Suppression	10 <sup>-8</sup> (120cps/nW)			
Background Level	<145cps			
Detection Fibre Core Diameter	200 $\mu\text{m}$			
Detection Fibre NA	0.53			
Photon Collection Efficiency	7.6%			
Total Photon Detection Efficiency	3.78%			
<b>Single Atom Detection Efficiency</b>				
Detection Time	300 $\mu\text{s}$	45 $\mu\text{s}$	20 $\mu\text{s}$	
Single Atom Detection Efficiency	98.9%	97.8%	95%	
False Positive Detection Probability	<4.3%	<0.7%	<0.3%	
<b>Signal Strength</b>				
Counts per Atoms	4.50	3.83	3.00	
Photons per Atom	119	101	79	

**Figure 13.3.:** Projected Datasheet of the Improved Integrated Fluorescence Detector  
Here a single Optran WFGe detection fibre was assumed. The background level is based on the assumption that a low noise SPCM is employed, the dispenser contribution removed and that stray light from the excitation fibre scales proportional to the photon collection efficiency. Note that the stray light background and hence the false detection probabilities are likely much smaller in reality.



**SU-8** The fibres recommended above have a larger cladding diameter (e.g. 230  $\mu\text{m}$  for the Thorlabs BLF48-200) than the currently used 125  $\mu\text{m}$ . Fabricating fibre holding structures for these fibres requires an increase in SU-8 layer thickness. While a thickness of 300  $\mu\text{m}$  is in itself not a problem to fabricate with SU-8, here we have to keep in mind that the cladding diameter of the tapered excitation fibre is still 125  $\mu\text{m}$ .

We propose to use a common layer thickness of 300  $\mu\text{m}$ , but different trench width for the holding structures of the excitation and detection fibre, to be able to effectively clamp both fibre types to the chip surface.

### Two Detection Fibres

If even higher detection efficiencies are required the photon collection efficiency can easily be doubled by employing two detection fibres instead of just one. The geometrical alignment suggests as an optimal approach using two identical fibres facing one another as depicted in figure 13.4.

Care has to be taken here to avoid obstructing the central region of the atom chip, used for initial magnetic trapping and cooling of the atoms. In this region optical access from the side for time of flight absorption and fluorescence imaging is desired. Therefore one of the two fibres will have to be bend carefully to avoid obstruction of the imaging beams.

The minimum recommended bending radius before losses occur is 300 times the cladding radius. For a 230  $\mu\text{m}$  diameter fibre this corresponds to a minimum bending radius of 34.5 mm.

Additionally care has to be taken that none of the two detection fibres points in the direction of possible background sources (such as the dispensers).

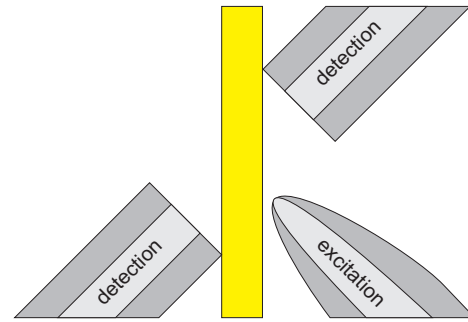


**Figure 13.4.:** Fluorescence Detector Employing Two Detection Fibres

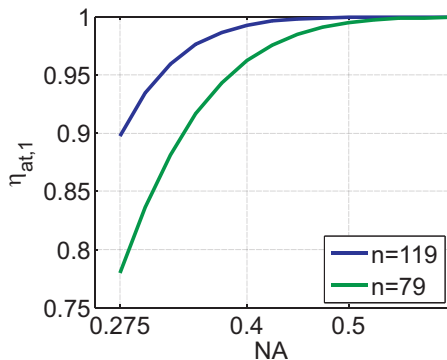


**Figure 13.5.:** Single Atom Detection Efficiency as Function of NA for Two Detection Fibres for full signal (119 photons per atom) and 20  $\mu\text{s}$  detection time (79 photons per atom)

**Single Atom Detection Efficiencies** If two detection fibres are employed, single atoms can be detected with certainty even for moderate values of the numerical aperture.

Figure 13.5 demonstrates that even for NA=0.4 a single atom detection efficiency of  $\eta_{\text{at},1} = 99.3 \%$  is reached. A reduction of the detection time to 20  $\mu\text{s}$  still results in a single atom detection efficiency of  $\eta_{\text{at},1} = 96.2 \%$  for NA=0.4.

The following table gives an overview of the projected sensitivity for the fibres discussed above in the case of 119 photons per atom.

**Projected Sensitivity for different Fibres-types  
2 Fibre Detector**

	<b>current fibre GIF-625</b>	<b>Thorlabs BLF48-200</b>	<b>CeramOptec Optran WFGe</b>
NA	0.275	0.48	0.53
$\eta_{\text{coll}}$	3.9 %	12.3 %	15.2 %
$\eta_{\text{ph}}$	1.9 %	6.1 %	7.6 %
$\eta_{\text{at},1}$	89.8 %	99.9 %	99.99 %

Figure 13.6 gives an overview of the expected performance of an integrated detector employing two Optran WFGe detection fibres.

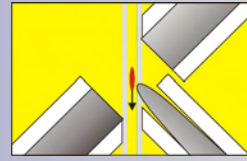
### Other Geometries

Non-planar arrangements of the excitation and detection fibres are imaginable as well. For example the atomic ensemble could, with the excitation fibre vertical to the chip surface, be illuminated from above or from below through a hole in the atom chip.

# Improved Fluorescence Detector

## Two Optran WFGe Detection Fibres

### Projected Data Sheet



#### Technical Parameters

Distance from Z trap	5.5mm
Excitation Fibre Focal Length	$40\mu\text{m} \pm 1\mu\text{m}$
Excitation Fibre Focus Waist	$5\mu\text{m} \pm 1\mu\text{m}$
Focus Height over Chip	$62.5\mu\text{m}$
Saturation Power	325pW
Stray Light Suppression	$10^{-8}$ - $10^{-7}$ (240cps/nW)
Background Level	<265cps
Detection Fibre Core Diameter	2 * $200\mu\text{m}$
Detection Fibre NA	2 * 0.53
Photon Collection Efficiency	15.2%
Total Photon Detection Efficiency	7.55%

#### Single Atom Detection Efficiency

Detection Time	300 $\mu\text{s}$	45 $\mu\text{s}$	20 $\mu\text{s}$
Single Atom Detection Efficiency	99.99%	99.94%	99.75%
False Positive Detection Probability	<7.6%	<1.2%	<0.5%

#### Signal Strength

Counts per Atoms	8.97	7.64	5.98
Photons per Atom	119	101	79

Interaction Time (1/e)	$12\mu\text{s} \pm 1\mu\text{s}$
------------------------	----------------------------------

**Figure 13.6.:** Projected Datasheet of the Improved Integrated Fluorescence Detector  
 Here two facing Optran WFGe detection fibres were assumed. The background level is based on the assumption that a low noise SPCM is employed, the dispenser contribution removed and that stray light from the excitation fibre scales proportional to the photon collection efficiency. Note that the stray light background and hence the false detection probabilities are likely much smaller.

### 13.2.2. Increasing the Interaction Time

If the interaction time of the atoms with the probe light can be increased, a higher total number of photons is emitted and hence the signal increases. In order to keep the atoms for a longer time in the interaction region additional trapping forces are necessary.

**Magnetic Trapping** A redesign of the atom chip should therefore include additional wires structures in the detection region to generate a magnetic trap in front of the excitation fibre. As illustrated in figure 13.7 this can be achieved for example, by the addition of slightly overlapping U structures. Ultimately the atom chip will be realized in a multi layer structure, allowing flexible trapping geometries [114]. See chapter 10 for a list of basic magnetic trapping literature.

Depending on the application it might even be desirable to transport the atoms into the detection region in a controlled way, e.g. employing magnetic conveyor belts [15, 39].

**Optical Trapping** Trapping the atoms in an optical dipole trap in the interaction region is, so to say, a built-in feature of the fibre detector. If some kind of trap in the detection region exists the tapered excitation fibre can be exploited to create an optical dipole trap, as well as deliver resonant excitation light.

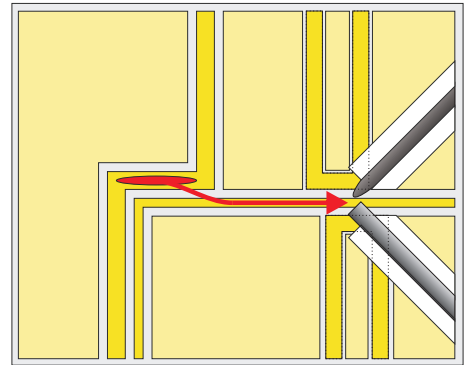


**Figure 13.7.:** Atom Chip with Magnetic Trap in the Detection Region

*"I have not failed, I've just found 10,000 ways that won't work."*

Thomas Alva Edison

# 14. Outlook

As has been discussed before already the current prototype detector promises to become an invaluable diagnostics tool in ultracold atom experiments. We expect to be able to distinguish the atom statistics of thermal ensembles, BECs and 1D condensates.

The detector presented here is conceptionally much simpler than comparable integrated detectors employing cavity assisted detection [10, 11, 18] and can be produced using only standard commercially available lithographic techniques. Neither cavity nor trapping of the atoms [20] is necessary to reach single atom sensitivity.

With the improvements suggested in chapter 13 implemented, the counting resolution (see chapter 3) will be high enough to perform atom counting. Resolving the exact atom number for low atomic densities is within reach, as discussed in [30, 84].

In fact, possible applications of the detector are not limited to ultracold atom physics. Its fibre based design and inherent background suppression offer interesting applications in a divers range of sciences.

Life sciences, for example, is faced with the very similar problem of detecting single molecules. Here the fluorescence detector should perform equally well as for single atom detection. Integration of the detector into micro-fluidic channels seems very feasible, creating an experimental situation quite similar to the detection of atoms in a 1D magnetic guide.

The capability of the device to perform state selective detection allows for identification of different particle species.

Even though for the current application integration of the detector was desired it might be rewarding for future applications to follow the opposite approach and construct a mobile fibre detector in a similar geometry. Consisting of a tapered excitation fibre and an aligned multi-mode detection fibre, mounted on a moveable head, a fibre detector could be used for selective detection at arbitrary positions, instead of a fixed position, as presented here. The fibre based design makes such a detector extremely suitable for applications involving a movable detection head.

A moving head single particle fluorescence detector can be applied to the localization of single molecules on surfaces as well as in scaleable quantum computing systems.



**Part IV.**  
**Appendices**





# A. The $^{87}\text{Rb}$ D2 Transition

Daniel A. Steck of the Los Alamos National Laboratory has composed an extremely useful reference of the  $^{87}\text{Rb}$  D line data [44], which I will summarize in the first section of this appendix, giving a brief overview of the physical and optical properties of  $^{87}\text{Rb}$ , as far as they are relevant to the experiments presented here.

Doing that I will concentrate only on the D2 transition, a spectroscopy of which is presented in the second section. For a spectroscopy of the D1 transition refer to my diploma thesis [48], where the level structure of the D1 transition was used to slow and store a pulse of light in rubidium vapour.

Atomic Number	$Z$	37
Total Nucleons	$Z + N$	87
Relative Natural Abundance	$\eta(^{87}\text{Rb})$	27.83(2)%
Nuclear Lifetime	$\tau_n$	$4.88 \cdot 10^{10}$ yr
Atomic Mass	$m$	86.909180520(15) u $1.44316060(11) \cdot 10^{-25}$ kg
Density at 25°C	$\rho_m$	1.53 g/cm <sup>3</sup>
Melting Point	$T_M$	39.31° C
Boiling Point	$T_B$	688° C
Specific Heat Capacity	$c_p$	0.363 J/g·K
Molar Heat Capacity	$C_p$	31.060 J/g·K
Vapour Pressure at 25°C	$P_v$	$3.0 \cdot 10^{-7}$ Torr
Nuclear Spin	$I$	3/2
Ionization Limit	$E_I$	33690.8048(2) cm <sup>-1</sup> 4.1771270(2) eV

**Table A.1.:**  $^{87}\text{Rb}$  Physical Properties, from [44]

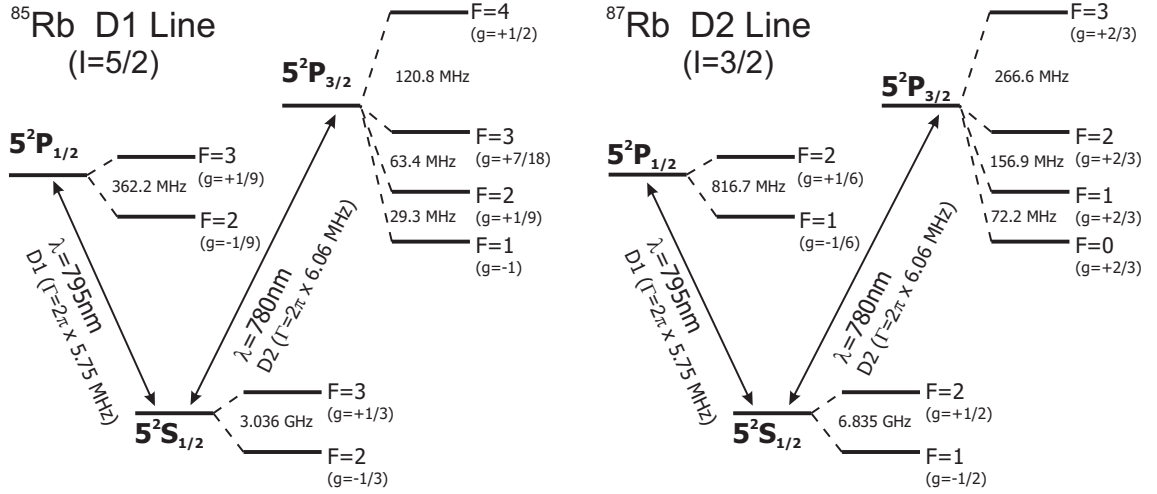


**Figure A.1.:** Hyperfine Structure of the Main Rubidium Isotopes

The frequency differences of the hyperfine level are given, as well as the central transition wavelengths, natural line widths and Landé- $g_F$ -factors for  $^{85}\text{Rb}$  (left, from [115]) and  $^{87}\text{Rb}$  (right, from [44]).

The physical properties of  $^{87}\text{Rb}$  are listed in table A.1. Rubidium occurs naturally in a mixture of  $^{85}\text{Rb}$  and  $^{87}\text{Rb}$ , with a natural abundance of the stable isotope  $^{85}\text{Rb}$  of more than 72 %.  $^{87}\text{Rb}$  decays with a nuclear lifetime of  $4.88 \cdot 10^{10}$  years to  $\beta^- + ^{87}\text{Sr}$  and can thus be considered stable for the duration of a typical PhD thesis.

## A.1. Energy Levels and Transitions

Coupling between the orbital angular momentum  $L$  and the spin angular momentum  $S$  removes the degeneracy of the  $5P_{1/2}$  and the  $5P_{3/2}$  levels, resulting in a fine-structure splitting of the  $5S \rightarrow 5P$  transition into two lines, approximately 15 nm apart. These are the D1 (at 795 nm) and the D2 (at 780 nm) lines (see figure A.1).

Further coupling between the resulting angular momentum  $J$  and the total nuclear angular momentum  $I=3/2$  to a total atomic angular momentum  $F$  leads to hyperfine splitting, removing the degeneracy between the  $5^2S_{1/2} \quad F=2$  and the  $5^2S_{1/2} \quad F=1$  states, splitting them apart by 6.8 GHz.

The transition strengths of from the excited state  $F' = 1$  have been given in figure 6.2.

Each hyperfine-level contains  $2F+1$  magnetic sublevels, corresponding to the different possibilities to align the vector of the total angular momentum  $F$  to the quantization axis that is given by the direction of the B-field. If the energy-shift induced by the B-field is small compared to the hyperfine splitting, then  $F$  is a good quantum number

and the level splitting can be written as (choosing B to be pointing in z-direction):

$$\Delta E_{|F m_F\rangle} = \mu_B g_F m_F B_z \quad (\text{A.1})$$

Where  $\mu_B$  is the Bohr-magneton,  $g_F$  the Landé-factor and  $m_F$  the magnetic quantum number of the shifted substate.

The magnetic traps used in the experiments presented here trap the weak field seeking  $m_F = 2$  and  $m_F = 1$  substates of the  $5^2S_{1/2}$   $F = 2$  ground state [36].

Frequency	$\omega_0$	$2\pi \cdot 384.230\,484\,468\,5(62)$ THz
Wavelength (Vacuum)	$\lambda_{\text{vac}}$	780.241 209 686(13) nm
Wavelength (Air)	$\lambda_{\text{air}}$	780.032 00 nm
Lifetime	$\tau = \frac{1}{\Gamma}$	26.24(4) ns
Decay Rate	$\Gamma$	$38.11(6) \cdot 10^6 \text{ s}^{-1}$
Natural Line Width (FWHM)		$2\pi \cdot 6.065(9)$ MHz
Recoil Velocity	$v_r$	5.8845 mm/s

**Table A.2.:**  $^{87}\text{Rb}$  D2 ( $5^2S_{1/2} \rightarrow 5^2P_{3/2}$ ) Transition Optical Properties, from [44]

## A.2. Spectroscopy

Figure A.2 shows a Doppler-free saturation spectroscopy of the whole Rubidium D2 transition recorded scanning the master laser with additional current feed forward. For both isotopes two Doppler valleys can be identified, corresponding to the two ground states. The separate transitions to the excited states are resolved as Lamb-dips in the Doppler valleys by Doppler-free saturation spectroscopy.

The isotopes can be easily distinguished by the relative depth of the Doppler valleys. Since the natural abundance of  $^{85}\text{Rb}$  to  $^{87}\text{Rb}$  is roughly 2 to 1, the  $^{85}\text{Rb}$  Doppler valleys are correspondingly approximately twice as deep as the  $^{87}\text{Rb}$  Doppler valleys.

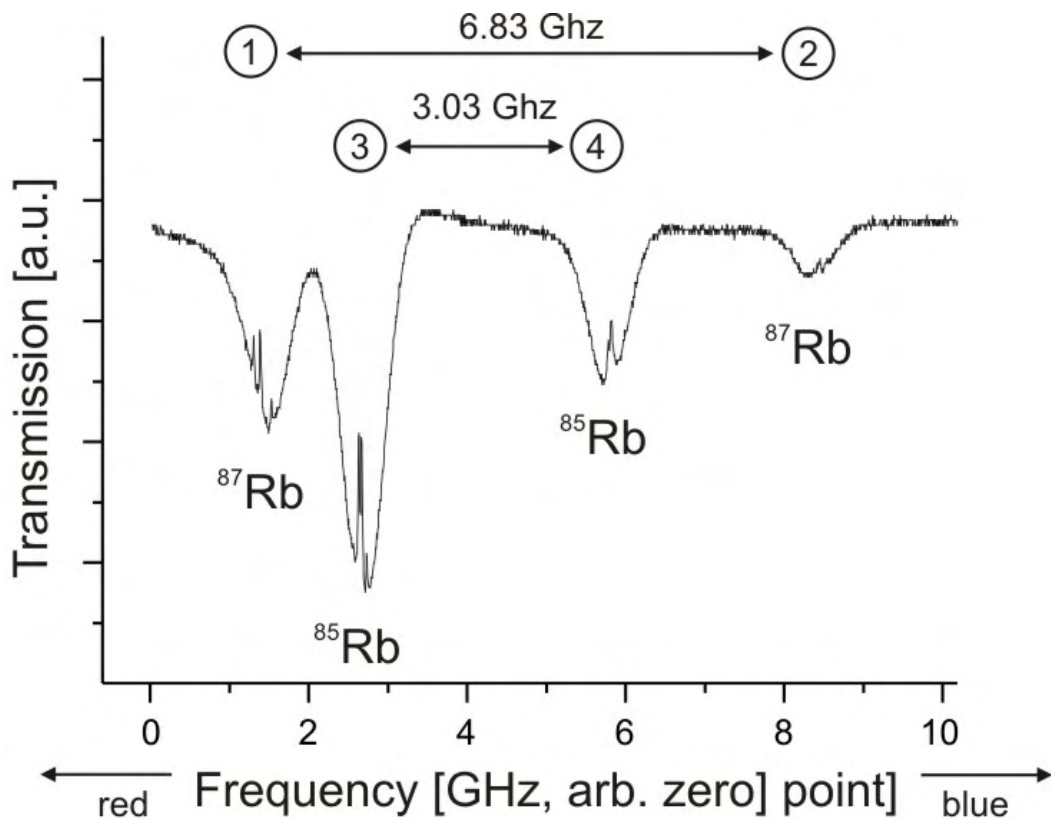


**Figure A.2.:** The Rubidium D2 Line

A modehop free Doppler-free saturation spectroscopy scan over the full Rubidium D2 Line performed with the master laser, using current feed-forward. Each Doppler valley contains all transitions originating from one ground state. The transitions themselves are resolved as Lamb-dips in the Doppler valleys.

$$(1) \quad ^{87}\text{Rb} \quad F = 2 \rightarrow F'$$

$$(2) \quad ^{87}\text{Rb} \quad F = 1 \rightarrow F'$$

$$(3) \quad ^{85}\text{Rb} \quad F = 3 \rightarrow F'$$

$$(4) \quad ^{85}\text{Rb} \quad F = 2 \rightarrow F'$$

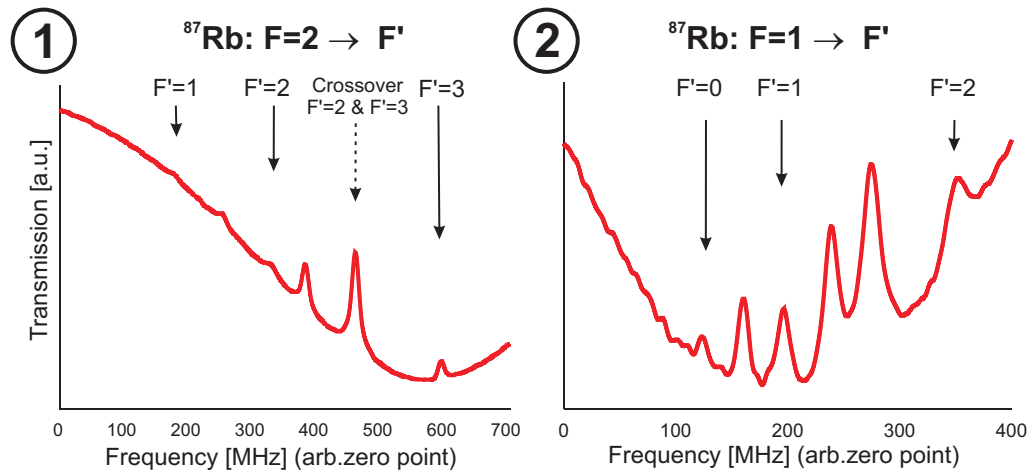


**Figure A.3.:** Details of the  $^{87}\text{Rb}$  D2 line spectroscopy. The transitions and selected cross-over peaks are labelled by the excited states of the transition.

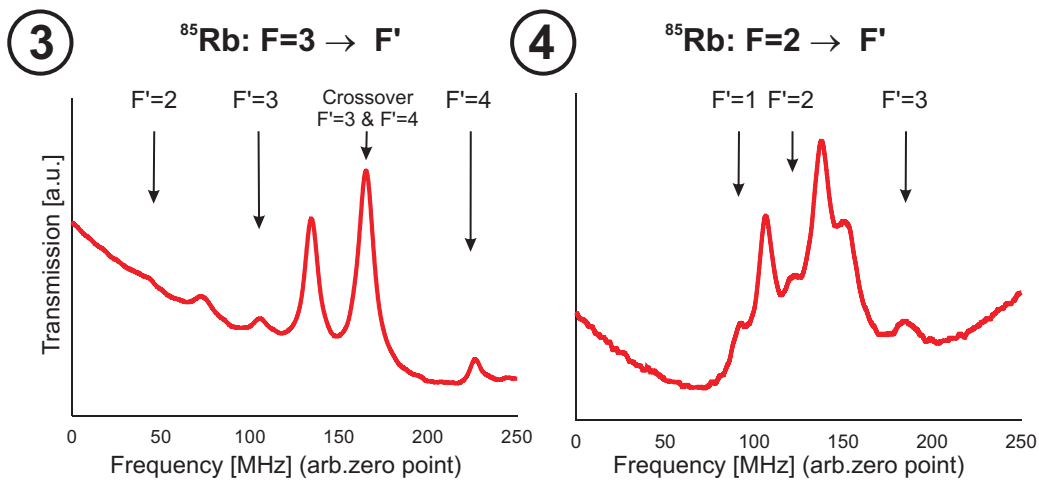


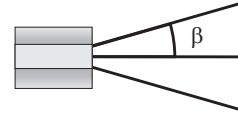
**Figure A.4.:** Details of the  $^{85}\text{Rb}$  D2 line spectroscopy. The transitions and selected cross-over peaks are labelled by the excited states of the transition.



## B. Numerical Aperture

The numerical aperture of a fibre is defined as sinus of the half-angle  $\beta$  of the cone of light emitted by the fibre.

$$\text{NA} = \sin \beta$$

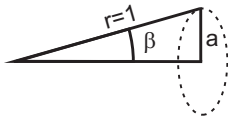


Since light is guided inside a fibre by total internal reflection the angle  $\beta$  is as well the maximum acceptance angle for light entering the fibre. Hence the fibre collects a cone of light with half-angle  $\beta$ .

We will now try to estimate the ratio of collected light from the emission of a point like source.

Let the source emit isotropically in  $4\pi r^2$ . We use polar coordinates  $r, \phi$  and  $\theta$  with the source at the origin. The light gathered by the fibre then corresponds to a small piece of the surface of the illuminated sphere given by  $\phi = [-\beta, \beta]$  and  $\theta = [0, 2\pi]$ .

**Approximation** In first order this is a plane circle with radius  $a$ .



$$\text{NA} = \sin \beta = \frac{a}{1}$$

$$\text{Surface } \pi a^2 = \pi \text{NA}^2$$

The collection efficiency  $\eta_{\text{coll}}$  is in this approximation simply given by

$$\eta_{\text{coll}} = \frac{\pi \text{NA}^2}{4\pi}$$

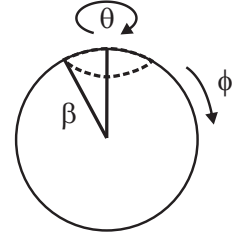
$$\eta_{\text{coll}} = \frac{\text{NA}^2}{4} \tag{B.1}$$

**Exact Calculation** To calculate  $\eta_{\text{coll}}$  exactly we have to integrate over the sphere to get the area  $A$  corresponding to the acceptance cone of the fibre.

$$A = \int_{\phi=0}^{\beta} \sin \phi \, d\phi \int_{\theta=0}^{2\pi} d\theta$$

$$A = 2\pi (1 - \sqrt{1 - \sin^2 \beta})$$

$$A = 2\pi (1 - \cos \beta)$$



For small  $\beta$  this can again be approximated to  $A = \pi \text{NA}^2$ .

The collection efficiency from the exact calculation is given by

$$\eta_{\text{coll,opt}} = \frac{1 - \cos \beta}{2} = \frac{1 - \sqrt{1 - \text{NA}^2}}{2} \quad (\text{B.2})$$

For a numerical aperture of  $\text{NA} = 0.275$  the approximation from equation B.1 yields  $\eta_{\text{coll}} = 1.89\%$  while the exact calculation yields  $\eta_{\text{coll}} = 1.93\%$ .

## B.1. Fibre Core Diameter

When trying to increase the collection efficiency one should keep in mind that the numerical aperture is not the only parameter influencing how much light is collected. As illustrated in figure B.1 the fibre core has to be large enough to collect the full acceptance cone.

A fibre with huge NA but tiny core has only limited use, since it would have to be placed at very short distance  $z$  to the source to make use of the full NA. The opposite is true as well. A fibre with huge core can only be used to full effect if the NA is correspondingly large.

**Optimal Distance** The optimal distance  $z_{\text{opt}}$  is reached when the fibre core diameter  $d$  equals the diameter of the acceptance cone for given  $\text{NA} = \sin \beta$ .

This is fulfilled when

$$\tan \beta = \frac{d/2}{z_{\text{opt}}}$$

With  $\beta = \arcsin \text{NA}$  and

$$\tan \arcsin \text{NA} = \frac{\text{NA}}{\sqrt{1 - \text{NA}^2}}$$

the above relation can be solved to yield  $z_{\text{opt}}$ .

$$z_{\text{opt}} = \frac{d}{2} \frac{\sqrt{1 - \text{NA}^2}}{\text{NA}} \quad (\text{B.3})$$



The following table lists optimal distances for three important values of NA, assuming a fibre core diameter of 62.5  $\mu\text{m}$ .

Optimal Distances	
NA = 0.275	$\rightarrow z_{\text{opt}} = 109.3 \mu\text{m}$
NA = 0.5	$\rightarrow z_{\text{opt}} = 54.1 \mu\text{m}$
NA = 0.6	$\rightarrow z_{\text{opt}} = 41.7 \mu\text{m}$

At the optimal distance the maximum possible fraction of light  $\eta_{\text{coll,opt}}$  for a given NA, given by equation B.2, is collected.

**Too Close** At distances  $z < z_{\text{opt}}$  the core cannot be fully used, since the beams from the source reach the edge of the core at angles larger than the critical angle given by NA. It follows that the fraction of light collected stays limited by  $\eta_{\text{coll,opt}}$  even for arbitrarily short distances.

Hence reducing the distance to the source beyond  $z_{\text{opt}}$  or using a larger core diameter does not pay off for a given NA.

**Too Far Away** In the opposite case of  $z > z_{\text{opt}}$  we collect all light hitting the core, but do not use the full NA. The beams from the source reach the edge of the core at angles smaller than the critical angle. Here NA does not play a role any more and the collection efficiency is only limited by the apparent size of the core as seen from the source.

The core is seen under an half-angle

$$\xi = \arctan \frac{d/2}{z}$$

The fraction  $\eta_{\text{coll}}(z)$  of light collected can be calculated using the same approach as calculating the optimal collection efficiency. Only here  $\xi$  is used as integration boundary instead of  $\beta$ . The collection efficiency for overly large NA or distances becomes then

$$\eta_{\text{coll,opt}}(z) = \frac{1}{2} \left( 1 - \frac{1}{\sqrt{1 + \left(\frac{d}{2z}\right)^2}} \right) \tag{B.4}$$

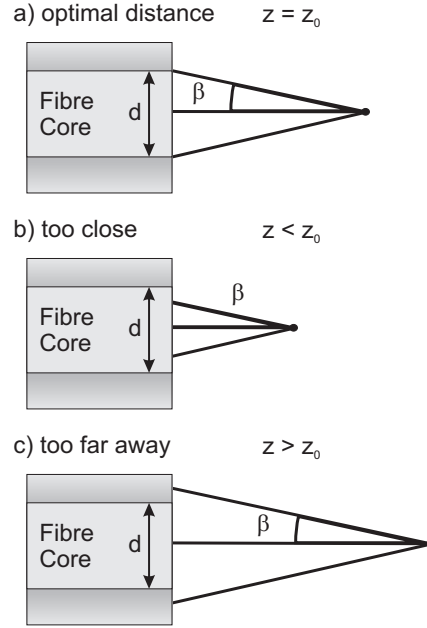


**Figure B.1.:** Influence of Distance on the Collection Efficiency  
 a) The fibre is at the optimal distance to the source. The acceptance cone diameter at the fibre facets equals the fibre core diameter.  
 b) The fibre is too close. A part of the core area cannot be used.  
 c) The fibre is too far away, the NA can not be used to full extend.



## C. Poisson Distribution

The Poisson Distribution was introduced by Simeon Denis Poisson in 1837 to describe the probability of criminal and civil verdicts. Here it will be used to describe the photon count distribution generated by illuminating a detector with a light source of constant intensity.

A measurement of a constant source over a time  $T$  will lead to  $n_{\text{cts}}$  being generated with a random distribution of arrival times. If the time axis is separated into a large number of bins of equal width  $t_b$ , the probability to record a count in a certain bin is given by the mean rate  $\lambda = n_{\text{cts}}/(T/t_b)$ , provided the bin size is small enough to guarantee  $\lambda < 1$ . The probability to measure  $k$  counts in a bin is then given by the Poisson distribution.

$$p_\lambda(k) = \frac{\lambda^k}{k!} e^{-\lambda} \quad (\text{C.1})$$

The characteristic feature of the Poisson distribution is that its variance equals its mean value.

$$\text{Var}(k) = \langle k \rangle = \lambda$$

In the following the Poisson distribution will be derived from the Binomial distribution, motivating its use for photon detection and giving limits of its applicability.

### C.1. Derivation from the Binomial Distribution

The generation of counts in timebins can be considered a classical binomial process. For each bin the only possible outcomes of a measurement are either there is a count (with probability  $p$ ) or there is no count (with probability  $1 - p$ ).

Assuming the probability  $p$  to be constant, meaning that the outcome of a previous measurement does not influence the current bin, we can write the probability to find  $k$  counts in  $n$  bins using the binomial distribution.

$$p(k) = \binom{n}{k} p^k (1 - p)^{n-k} \quad \text{with} \quad \binom{n}{k} = \frac{n!}{k!(n-k)!}$$

### Transition to the Poisson Distribution

For a very large number of trials ( $n \rightarrow \infty$ ) and small probability ( $p \rightarrow 0$ ) with constant  $n \cdot p = \lambda$  the binomial distribution can be approximated by the Poisson distribution [40, 116].

$$\begin{aligned}
 p(k) &= \binom{n}{k} p^k (1-p)^{n-k} \\
 &= \frac{n!}{k!(n-k)!} \left(\frac{\lambda}{n}\right)^k \left(1 - \frac{\lambda}{n}\right)^{n-k} \\
 &= \frac{n \cdot (n-1) \cdot (n-2) \cdot \dots \cdot (n-(k-1))}{n^k} \frac{\lambda^k}{k!} \left(1 - \frac{\lambda}{n}\right)^{n-k} \\
 &= \left(1 - \frac{1}{n}\right) \cdot \left(1 - \frac{2}{n}\right) \cdot \dots \cdot \left(1 - \frac{k-1}{n}\right) \cdot \left(1 - \frac{\lambda}{n}\right)^{-k} \cdot \left(1 - \frac{\lambda}{n}\right)^n \cdot \frac{\lambda^k}{k!} \\
 \lim_{n \rightarrow \infty} p(k) &= \frac{\lambda^k}{k!} \lim_{n \rightarrow \infty} \left(1 - \frac{\lambda}{n}\right)^n \\
 \lim_{n \rightarrow \infty} p(k) &= \frac{\lambda^k}{k!} e^{-\lambda}
 \end{aligned}$$

The Poisson distribution can in turn be approximated by the Gauss distribution for  $\lambda > 30$ .

## C.2. Mean and Variance

### Mean

The mean value  $\langle k \rangle$  is given by the expectation value of the Poisson distribution.

$$\begin{aligned}
 \langle k \rangle &= \sum_{k=0}^{\infty} k \cdot p_{\lambda}(k) = \sum_{k=0}^{\infty} k \frac{\lambda^k}{k!} e^{-\lambda} = \lambda e^{-\lambda} \underbrace{\sum_{k=0}^{\infty} \frac{\lambda^k}{k!}}_{e^{\lambda}} \\
 \langle k \rangle &= \lambda
 \end{aligned}$$

### Variance

Similarly the variance can be calculated by use of  $\text{Var}(k) = \langle k^2 \rangle - \langle k \rangle^2$ .

$$\text{Var}(k) = \sum_{k=0}^{\infty} (k^2 \frac{\lambda^k}{k!} e^{-\lambda}) - \lambda^2 = \sum_{k=0}^{\infty} (k(k-1) + k) \frac{\lambda^k}{k!} e^{-\lambda} - \lambda^2 = \lambda^2 + \lambda - \lambda^2$$

$$\text{Var}(k) = \lambda = \langle k \rangle$$

### Variance / Mean

The characteristic feature of a Poisson distribution is

$$\frac{\text{Var}(k)}{\langle k \rangle} = 1$$

due to  $\text{Var}(k) = \lambda = \langle k \rangle$ .

## C.3. Time Intervals

If the recorded counts are Poisson distributed, then the time intervals between successive events follow an exponential distribution. This can be seen by realizing that for a distance of  $d$  bins between two events to occur each of the intermediate bins has to have had zero counts with a probability of  $p_\lambda(0) = e^{-\lambda}$ . Thus the probability to have separation time of  $d$  bins between two events is given by

$$p_{\text{dist}}(d) = e^{-\lambda d} \tag{C.2}$$

## C.4. Applicability

The Poisson distribution describes the photon number in a single mode of a monochromatic coherent light field, e.g. an ideal Laser well above threshold. It can be an excellent approximation for the photon statistics of a more general class of emitters as well, including multi mode thermal light [40]. While the photon number in a single mode thermal light field follows a Bose-Einstein distribution, photons in a multi mode field can often be considered to be independent of one another. Indeed the background signal in the fluorescence detector generated by collection of light from thermal sources such as the vacuum gauge or the dispensers via the multi mode fibre has been proven to follow Poissonian statistics.

Generally speaking light sources can be assumed to have a Poisson photon number distribution unless photon anti-bunching occurs [64] or explicitly single modes of a thermal source are considered.

### Requirements

In summary the Poisson distribution describes the photon count distribution of a photon stream measurement given that the following conditions are fulfilled.

- The photon rate (source intensity) has to be constant.
- The probability to register a count should be small and constant.
- A large number of bins is considered.
- The events have to be independent, i.e.:
  - No photon anti-bunching occurs on the timescales considered.
  - Multi mode collection is used for thermal sources.

## D. Analysis Programs

The software used to analyse the data recorded by the FAST ComTec P7888 counter card has been programmed in the course of this thesis using the MATLAB<sup>1</sup> technical computing language.

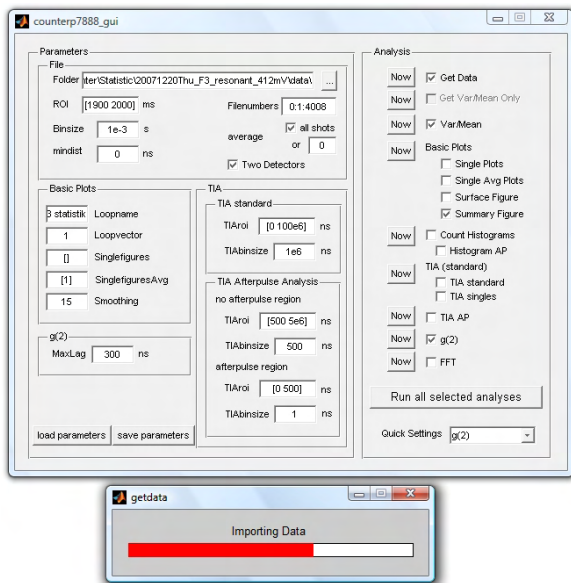


**Figure D.1.:** Graphical User

Interface of the MATLAB Analysis Program. The left hand side of the graphical user interface allows setting frequently accessed analysis parameters used in multiple subroutines. While on the right hand side the different analyses to be performed can be conveniently selected and run individually or consecutively.

For storage space efficient documentation and reproducibility of performed analyses all settings can be saved. At each save both a human readable and an internal save file are generated.

Since different, independent analyses need to be performed that all need a common set of mutual basic functions (e.g. data retrieval and basic data manipulation) the analysis software was designed modular and function oriented. This ensures easy replacement of subroutines should alternative calculations be implemented or simply the desire for a different presentation of the results arise.

The P7888 counter card stores the acquired data as timestamps of events. Hence for variance analysis the event files are used to reconstruct a bin representation of the data, with empty bins for those times where no timestamp was recorded. Time interval and correlation analysis directly process the event files without the intermediate reconstruction.

To facilitate access to the analysis parameters a graphical user interface (GUI), depicted in figure D.1, has been devised, where all relevant analysis or plotting parameters can be set in one common mask. Additionally the GUI allows executing of the

<sup>1</sup>MATLAB technical computing language from The MathWorks, [www.mathworks.com](http://www.mathworks.com).

different analyses directly from the main mask either individually or in a user defined combination.

To guarantee consistent documentation and reproducibility of the performed analyses all settings can be exported, both in human readable and in program internal format. This ensures as well that previous analysis can be performed with updated versions, where certain subroutines have been replaced, since the GUI mask and the associated parameters serve as an defined interface.<sup>2</sup>

The GUI and all settings can be remotely accessed from MATLAB scripts, to allow complex analyses involving several measurements located in different folders or loops of analysis parameters.

In total the analysis software consists of 32 scripts and 36 functions, fully commented for a total of 3667 lines of code plus 1220 lines in the main GUI-function.<sup>3</sup> Hence, even though the analysis software should be reprinted here for documentation purposes I abstain from this for practical reasons.

The software follows in all calculations the procedures outlined in chapters 4, 6, 7 and 8.

---

<sup>2</sup>Internal initialisation routines ensure that parameters settings saved with old GUI versions can still be used. Default values are used for such parameters that were not yet existing in old versions.

<sup>3</sup>The numbers are only quoted to justify that the code is not reprinted here. I strongly urge my successors to keep using the software and built upon the code. It was designed highly modular to be easily adaptable for future applications.



# E. How to built an ECDL Laser

Since, fortunately, ECDL lasers are quite durable devices most students do not have day to day contact with the intestines of their lasers. It is my experience that students introduced into the fine art of laser building therefore tend to have difficulties accessing their passive knowledge when finally the time comes to retune or revive a laser in need.

Therefore I wrote this guide as a reminder to those who have forgotten certain steps of the construction process. It should not be understood as a substitute for a professional instruction. For basics please also refer to [94, 97].

## E.1. Ingredients

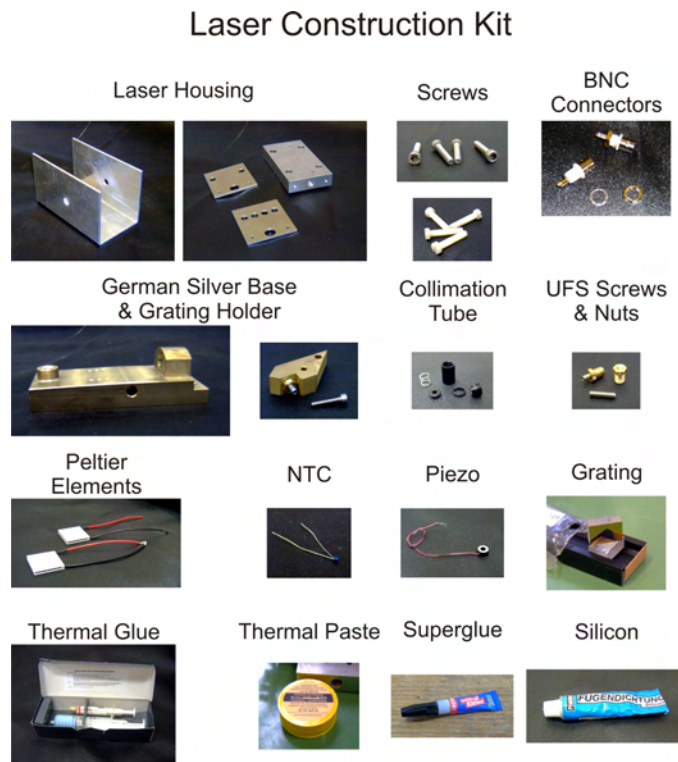


Figure E.1.: Laser Construction Kit

To build an ECDL laser you need the following items (Figure E.1 shows an exemplary laser building kit) :

- 1 laser housing
- 4 M6 screws to fix the housing to the table  
(if you prefer to electrically and mechanically isolate your laser from the optical table use a rubber foil between the housing and the optical table and plastic screws)
- 5-6 insulated BNC connectors
- 1 german silver (Neusilber) base
- 4 M4 plastic screws to fix the german silver base to the housing
- 1 german silver (Neusilber) grating holder
- 1 M4 screw to fasten the grating holder
- 2 UFS (ultra-fine) screws and nuts
- 1 collimation tube with lens
- 1 NTC (negative temperature coefficient resistor)
- 1 Holographic Grating
- 1 Piezo
- 2 Peltier elements (for modified short bases one suffices)
- two-component thermal glue
- thermally conductive paste
- superglue
- cables
- optional: silicon sealant

And, somewhat obviously, a laser diode.

## E.2. Building the Laser

Selected steps of the following list are depicted in figure E.3.

1. insert BNC connectors into the housing side walls
  - check orientation of base plate (countersink for M6 screws should be on top)
  - Note that most people prefer not attaching the side walls to the base plate until actually soldering the cables to the BNC connectors, thus having more freedom of movement until then
2. insert height-controlling UFS screw into german silver base
3. insert frequency-controlling UFS screw into german silver grating holder
4. insert collimation tube (without lens) into german silver base
  - check for correct orientation (in case of the Thorlabs collimation tubes the groove marks the lens-side)
  - glue the collimation tube using the two-component thermal glue
    - there are different approaches of how to do this
      - \* either apply some small drops of mixed glue on the collimation tube, insert it into the base while twisting it, to ensure a homogeneous, thin layer of the adhesive and good thermal contact
      - \* or put a drop of glue on some paper and roll the collimation tube through it to get a homogeneous layer of adhesive before inserting it into the base
    - either way take care not to spill adhesive on the threads
    - remove surplus glue
    - check the data-sheet of the glue used to learn how fast it will cure
  - glue the NTC into the tiny hole above collimation tube. The NTC needs to be in good thermal contact (i.e. as close as possible) to the collimation tube, again using the two-component thermal glue  
Exert care not to create a short-circuit between the NTC connectors and/or the german silver base. The thermal glue itself is a good insulator, keeping the legs of the NTC apart, but a suggested procedure is to apply a drop of silicon sealant on top of the *cured* thermal glue as an additional insulator, since the silicon's flexibility protects the feeble NTC legs from breaking at the contact point.
5. prepare cables for the laser diode
6. solder cables to the laser diode

- *Note:* in case of the Optima 5.6mm collimation tube first insert the diode into the collimation tube *then* solder the cables to the laser diode, since here the pins are accessible after screwing the laser diode in
  - observe color convention (laser diode: red, photodiode: green, ground: black)
  - *note: do NOT touch the diode without being grounded*
7. insert diode into collimation tube, junction has to be vertical
  8. insert lens into collimation tube
  9. insert M6 screws into base
  10. attach the Peltier elements to the base
    - use a *very thin* layer of thermally conductive paste
    - *note: this stuff is called paste because it is NOT a glue, thus it will not get hard. And you are supposed to use thermal paste and not thermal glue here to enable you (or someone else) to recycle the Peltier elements when the laser has fallen victim to the cruelties of lab-life and the diode goes where happy dead diodes go to.*
    - make sure that the orientation of the Peltier elements is identical
  11. fix the german silver base to the housing base, using the M4 plastic screws
  12. solder the cables to the BNC connectors
    - laser diode cables
    - Peltier elements
    - NTC (measure the resistance to check whether the NTC is alive and the connectors are OK. At central european room temperature the resistance should be around  $10 \pm 2 \text{ k}\Omega$ .)
  13. glue the piezo on the back of the grating
    - use very little glue
    - Be careful to place the piezo exactly in the centre of the grating.
  14. 1st run, seek position for grating holder
    - to connect the laser to the laser driver check whether the diode is AG or CG (see figure E.2) and consult the Laser Driver Manual. CG means cathode (is) ground, therefore in CG configuration the laser diode cathode is connected to ground. Diodes are usually drawn such that they point in the direction of technical current (plus to minus). And laser diodes are of course operated in conducting direction.
    - be careful with your eyes, it is strongly advised that you and everybody else in the lab wears laser safety goggles during these and the following steps

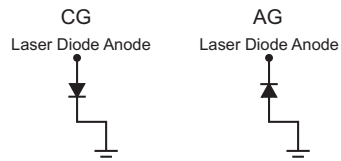


**Figure E.2.:**  
circuit diagram for AG  
and CG diodes

- account for piezo and grating thickness
  - you may use a printed circuit board as spacer between base and grating holder to get the grating holder to the right height
15. glue grating and piezo on grating holder
  16. screw grating holder on base
  17. solder the piezo cables to the BNC-connectors
  18. rough collimation
  19. adjust grating angle
    - reflect the first diffraction order back into diode
    - *note: use an offset piezo voltage of about 200V*
  20. observe zeroth diffraction order
    - turn the laser current right below the threshold
    - tune the feedback into the 'flash', using the height-screw
    - feedback fine-tuning (using a photodiode and modulating the injection current around the threshold)
  21. fine collimation
  22. recheck feedback
  23. adjust temperature stabilization
    - check the polarity of the Peltier elements (meaning, if you have a thermal runaway after turning on the temperature stabilization, then you need to change the polarity of the Peltier elements)
  24. adjust laser frequency, using a wavemeter
  25. recheck feedback

## Snapshots During Production

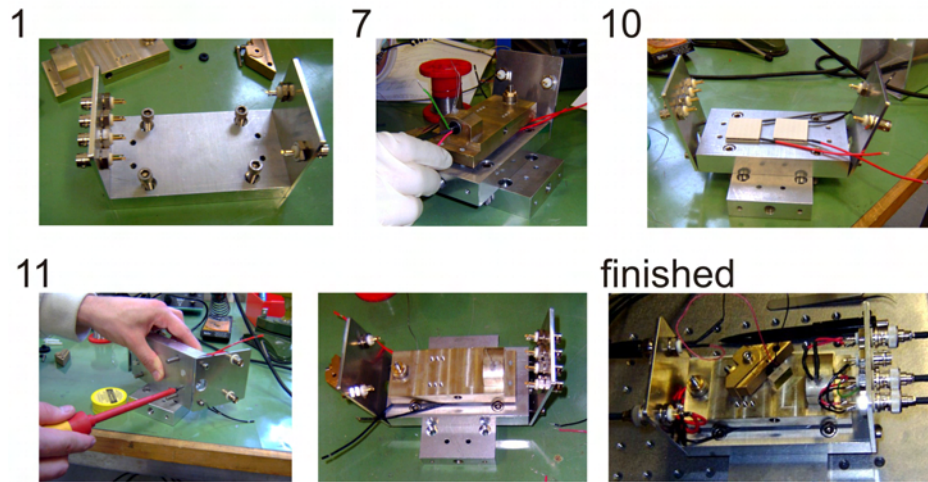


**Figure E.3.:** Selected Steps in the Laser Construction

A few rather randomly selected steps in the laser construction. The numbers refer to the steps listed in the main text. Note though that in step 7 depicted here the german silver base is already fixed to the baseplate when inserting the diode. I advise to fix the diode orientation before attaching the german silver base to the baseplate.

### E.3. Suppliers

- **laser housing, german silver base, german silver grating holder**  
your friendly mechanical workshop  
remember that you still need to supply the german silver
- **ultra-fine screws and nuts**  
Thorlabs  
[www.thorlabs.com](http://www.thorlabs.com)
  - F19SS075 (screw) 3/16" 100 TPI by 3/4"
  - N100L5 (nut) 3/16" 100 TPI with 5/16" 32 TPI thread
- **collimation tube with lens**  
Optima  
[www.optima-optics.com](http://www.optima-optics.com)  
LDM 3700 Kit (for 9mm diameter diodes)  
LDM 3756 Kit (for 5.6mm diameter diodes)  
(formerly we used Thorlabs collimation tubes LT110P-B to LT240P-B)
- **NTC**  
RS-components  
[www.rs-components.de](http://www.rs-components.de)  
Datasheet at [www.hy-line.de](http://www.hy-line.de)  
RS388-0168 , 10k $\Omega$   $\pm$  0, 2°C

- **Piezo**

Piezomechanik Dr. Pickelmann  
www.piezomechanik.com  
HPSt 500/10-5/L=5mm

- **Peltier elements**

Melcor, supplied by RS-components  
www.rs-components.de  
RS 197-0348, 28.7 W, 30x30x3.8 mm

- **insulated BNC connectors**

Farnell  
www.farnell.com  
583-522  
or, alternatively, RS-components  
www.rs-components.de  
RS 405-045

- **Thermal Glue (Thermal Bonding System)**

*careful ! toxic !*

Electrolube TBS203, supplied by RS-components  
www.rs-components.de  
RS 155-8320

*alternatively a silver and epoxy based compound, commonly used for CPUs*

Arctic silver, supplied by Conrad Elektronik  
www.conrad.de  
150367-12

- **Thermally conductive paste (thermal compound)**

*careful ! possibly toxic !*

Fischer Elektronik or alternatively RS-components  
www.rs-components.de  
RS 113-0455

*alternatively a silver based compound, commonly used for CPUs*

Arctic Silver, Conrad Elektronik  
www.conrad.de  
150352-12

- **Holographic Grating**

1800 lines per mm, gold on BK7-substrate, size 15mm\*10mm  
Zeiss Jena  
www.zeiss.de  
263232 9051 325

## E.4. Variants

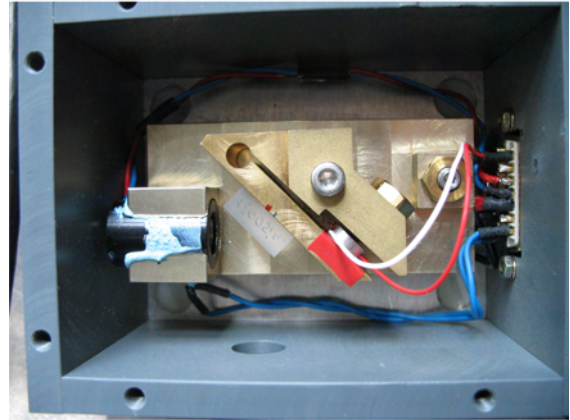
Of course many variants of the original ECDL design [97] exist. Figure E.4 shows two of the by now quite numerous variants that I have tested. One of the aims in both designs was to reduce the overall size of the setup to increase the stability. Additionally both setups require only one Peltier element for stabilization.

The design shown on the top uses a german silver base, similar to the standard base, but minimized in size. Actually the size shown here is at the practical limit. At this short resonator length careful feedback adjustment is necessary to avoid multi mode operation.

Usually the piezo is mounted behind the grating, thus in a piezo scan the grating is moved forward and backwards, changing the length of the cavity, but not the reflected wavelength for feedback. Ideally the grating should be rotated as well, giving maximum feedback always to the wavelength corresponding to the current cavity length. If the grating is situated under  $45^\circ$  to the beam at a distance  $L$  from the diode the optimal pivot point is at a distance  $h = L/\sqrt{2}$  from the grating centre [117]. In this design a rotation of the grating was achieved by inserting the piezo in the gap of the grating holder instead of behind the grating. Here a Noliac piezo was used instead of the normally employed Pickelmann piezos, due to its ruggedness and smaller thickness. Note as well that here instead of multiple BNC connectors one Sub-D connector was used.

The main aim of the lower design was simplification of the setup. Apart from reducing the size a simple aluminium base was employed. The standard bases and grating holders employed need to be fabricated by skilled mechanics, if only because a wire eroding machine is required to accurately machine the slits. This design however can be fabricated with little skill and a milling machine, which is proven by the fact that I machined the mount myself. The slits and fine thread screws needed for grating adjustment are replaced by a commercial, but stable, mirror mount.<sup>1</sup>

Short and Narrow Base  
Grating Rotates



Simplified Aluminium Mount  
Mirror Mount Grating Holder

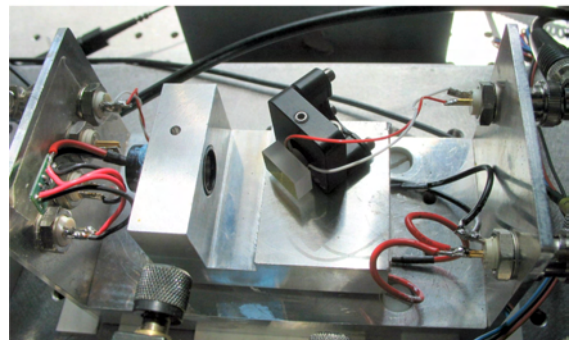


**Figure E.4.:**  
Two Examples of Variants of the ECDL Design

<sup>1</sup>Newport, U50-P, [www.newport.com](http://www.newport.com).



## E.5. NTC

The NTC resistance vs temperature characteristic is given in figure E.5.

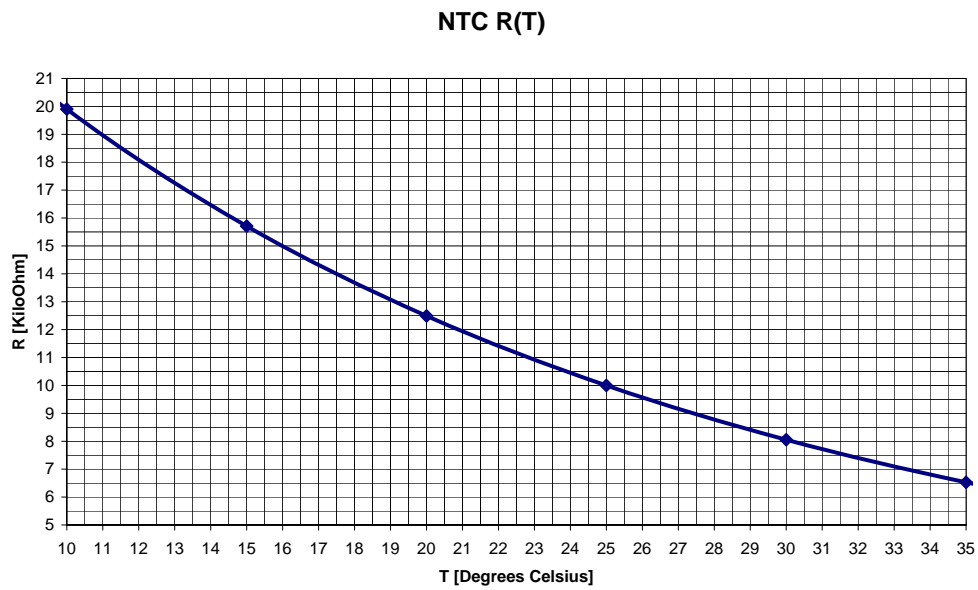


**Figure E.5.:** NTC Resistance vs Temperature, data from [www.hy-line.de](http://www.hy-line.de)

## E.6. Technical Drawings

The commonly used technical drawings are reproduced in figures E.6 to E.10 for completeness. They are originally part of Alex Kasper's work.

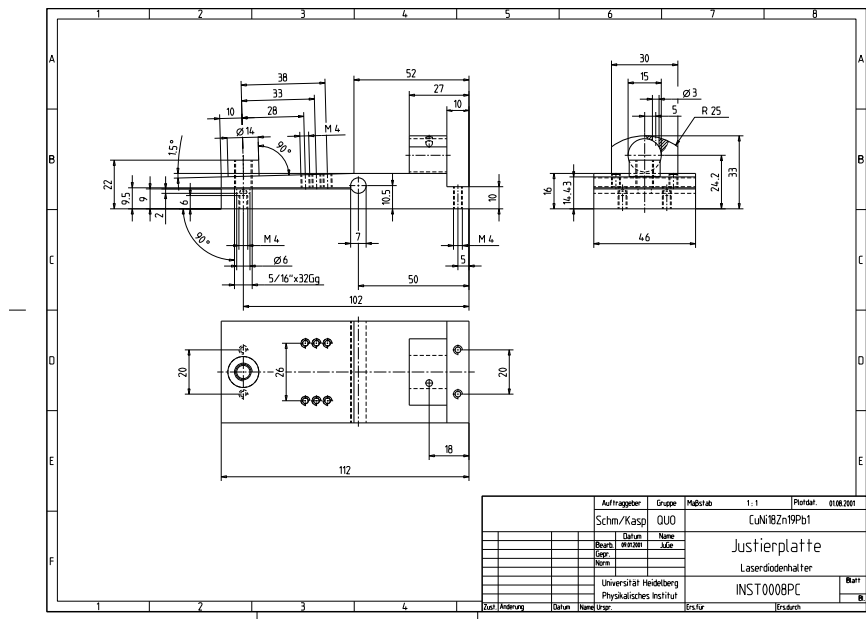


Figure E.6.: German Silver Baseplate



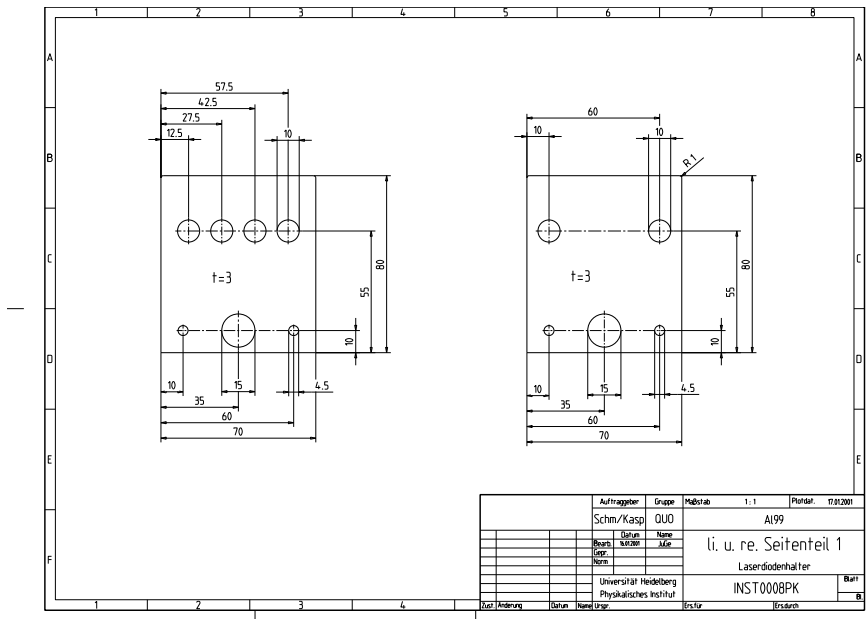


Figure E.9.: Side Walls

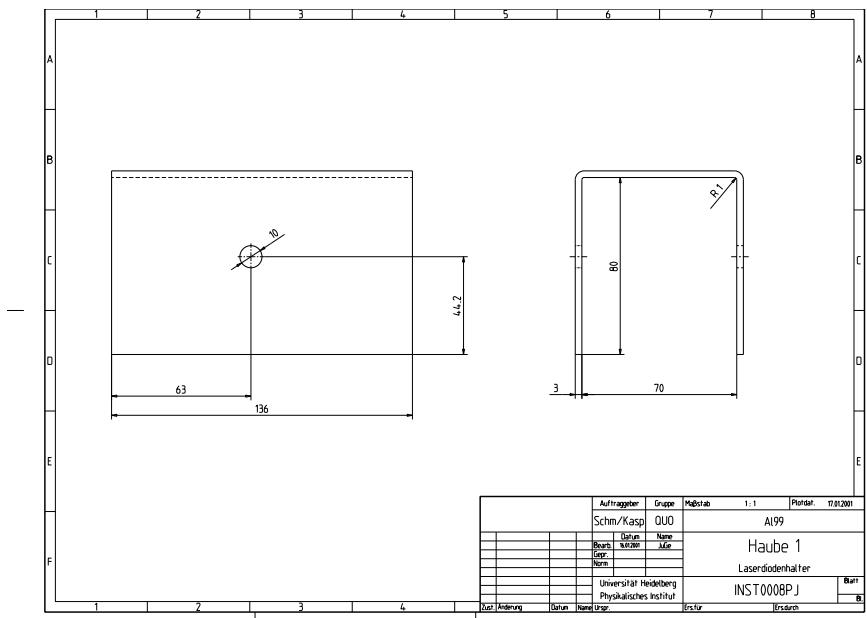


Figure E.10.: Lid

# F. Tapered Amplifier Technical Drawings

This chapter includes a small selection of the technical drawings generated in the course of this thesis to construct the mechanical parts of the tapered amplifier system. All together 26 different designs for a total of 51 items have been produced. The full set of technical drawings is of course available upon request and was only omitted here to save space.

All drawings have been created using Alibre Design<sup>1</sup>.

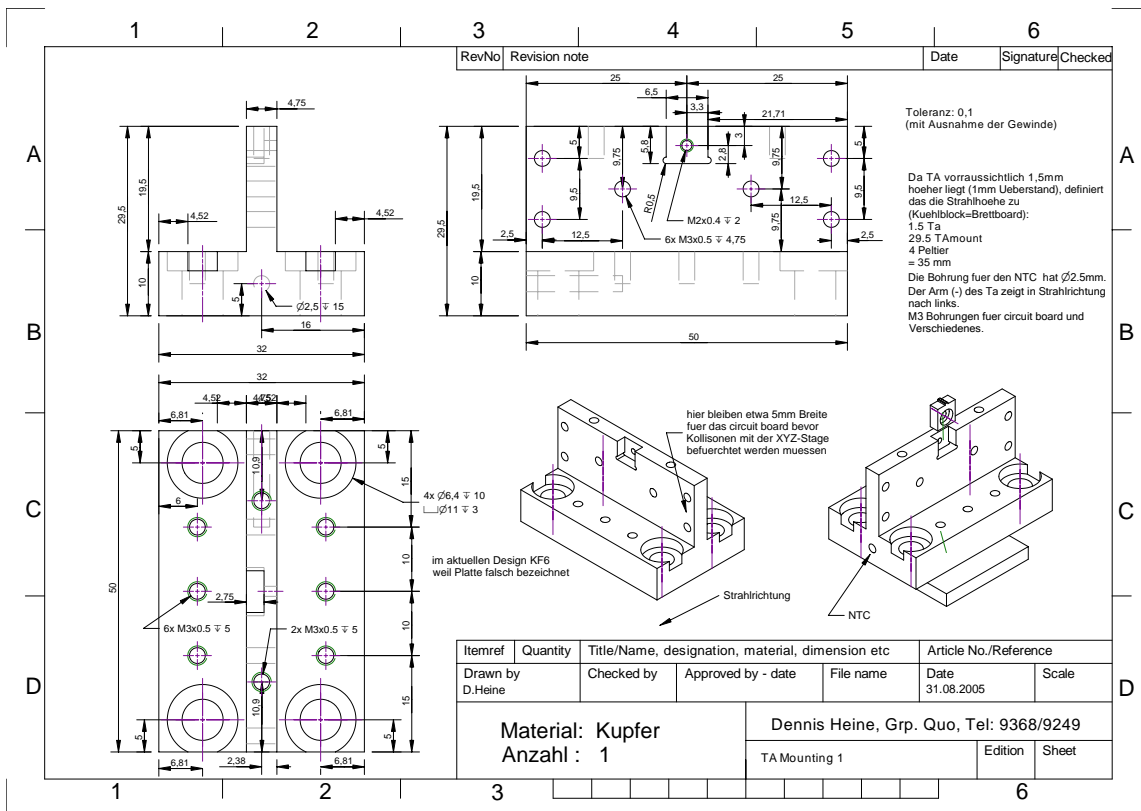


Figure F.1.: Tapered Amplifier Mount

<sup>1</sup>A CAD software from Alibre Inc, a free version is available at [www.alibre.com](http://www.alibre.com).

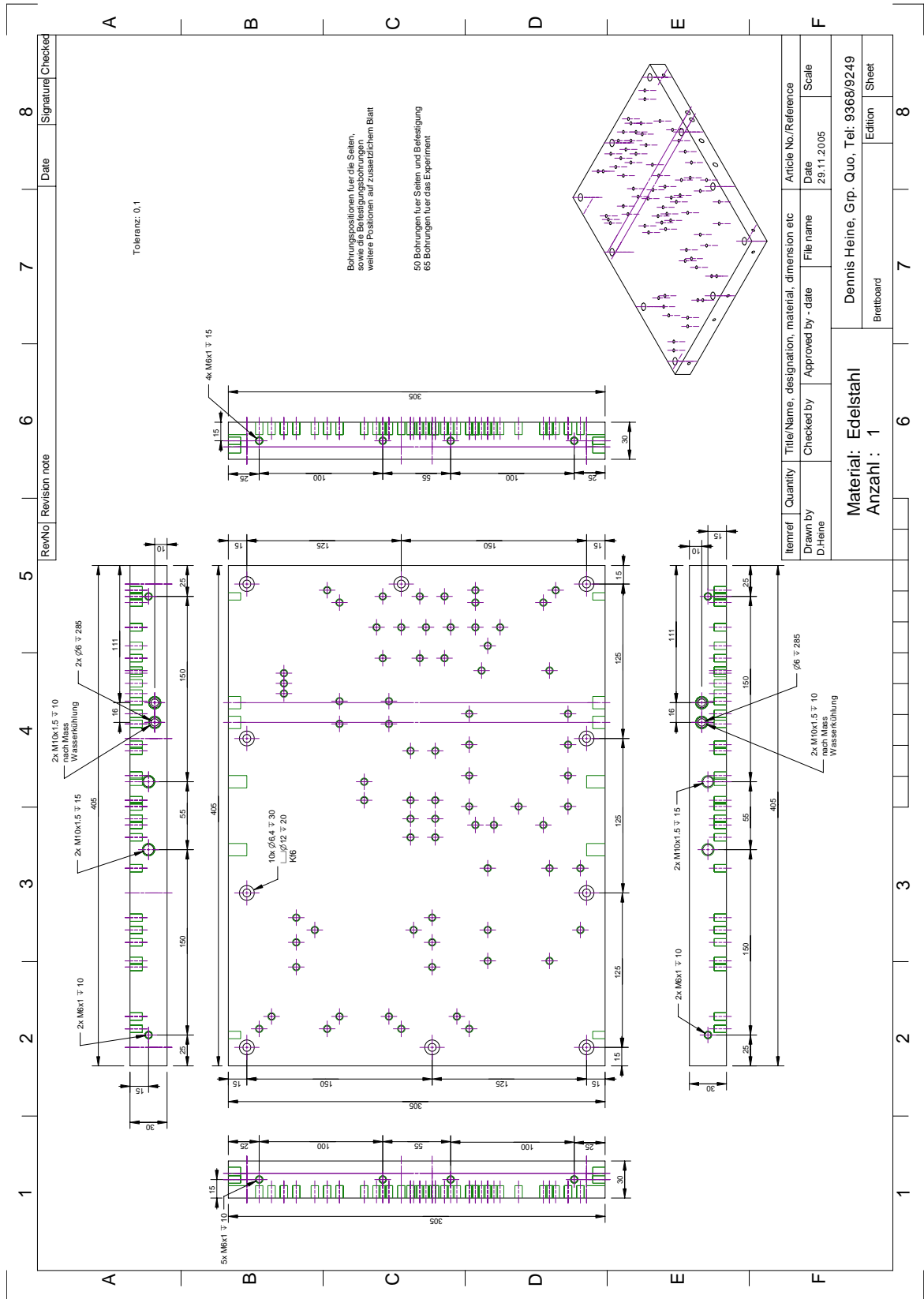


Figure F.2.: Tapered Amplifier Baseplate

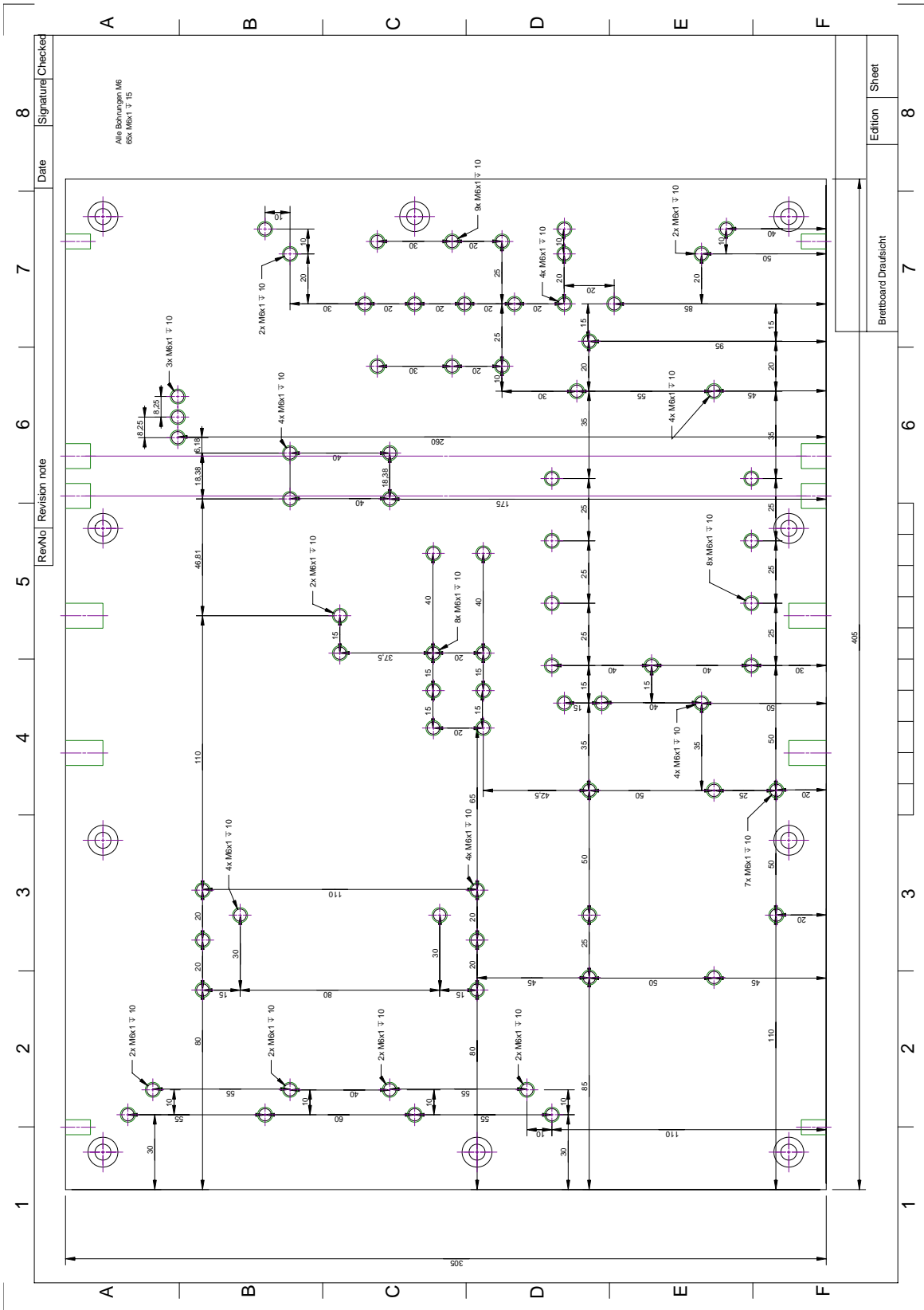


Figure F.3.: Tapered Amplifier Baseplate Threads

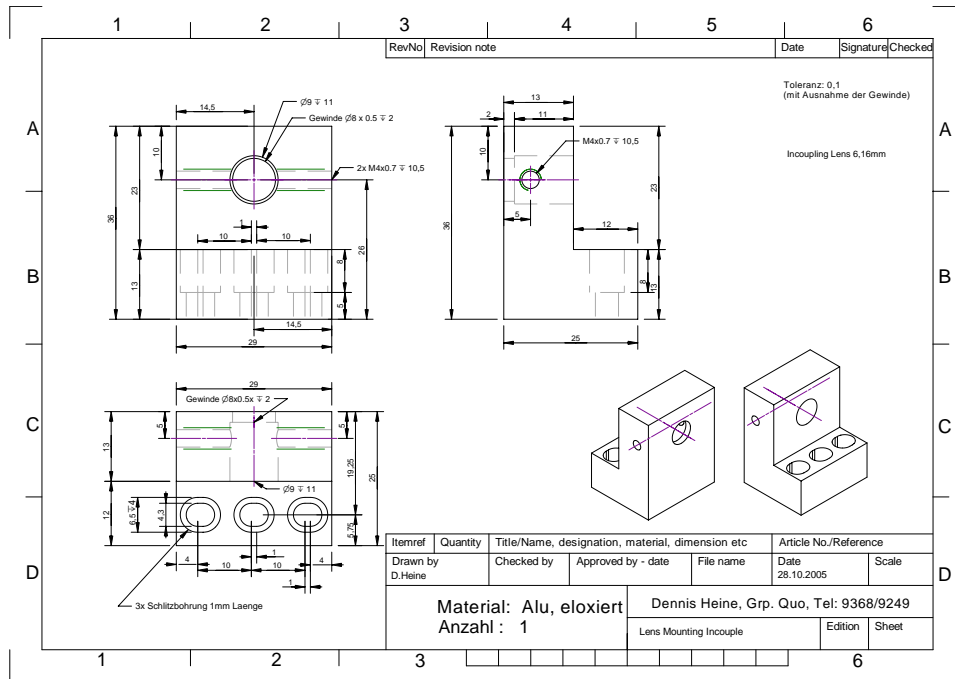


Figure F.4.: Incoupling Lens Mount

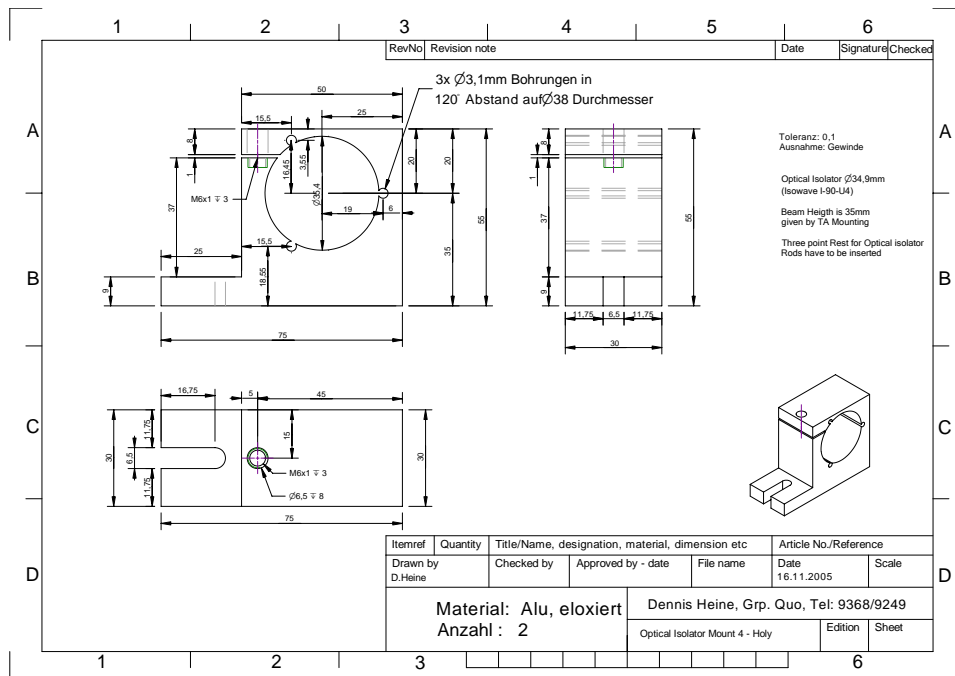


Figure F.5.: Optical Isolator Mount



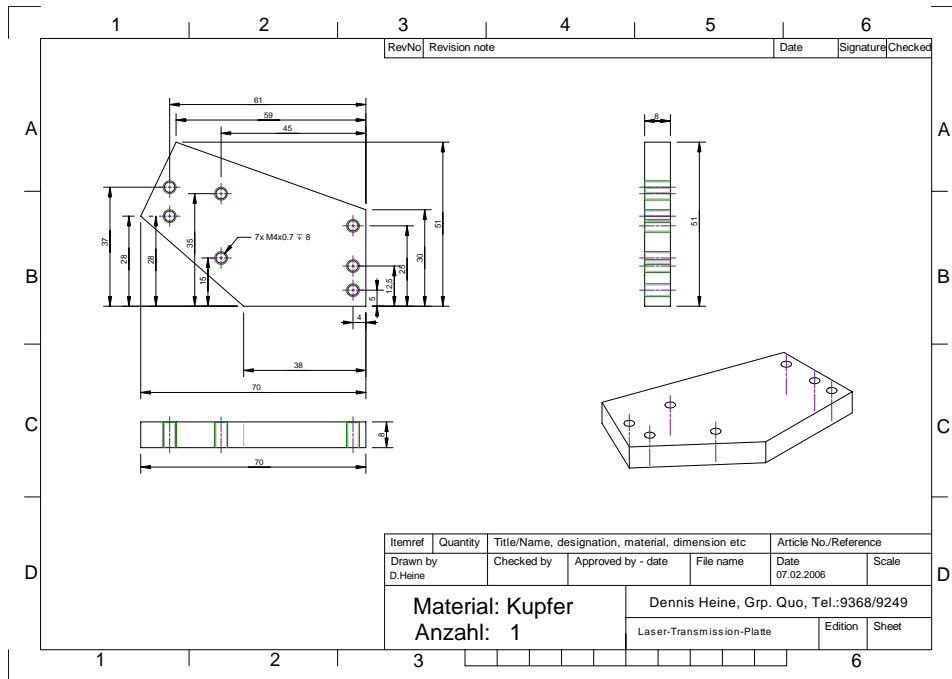


Figure F.6.: Transmission Grating Laser Base

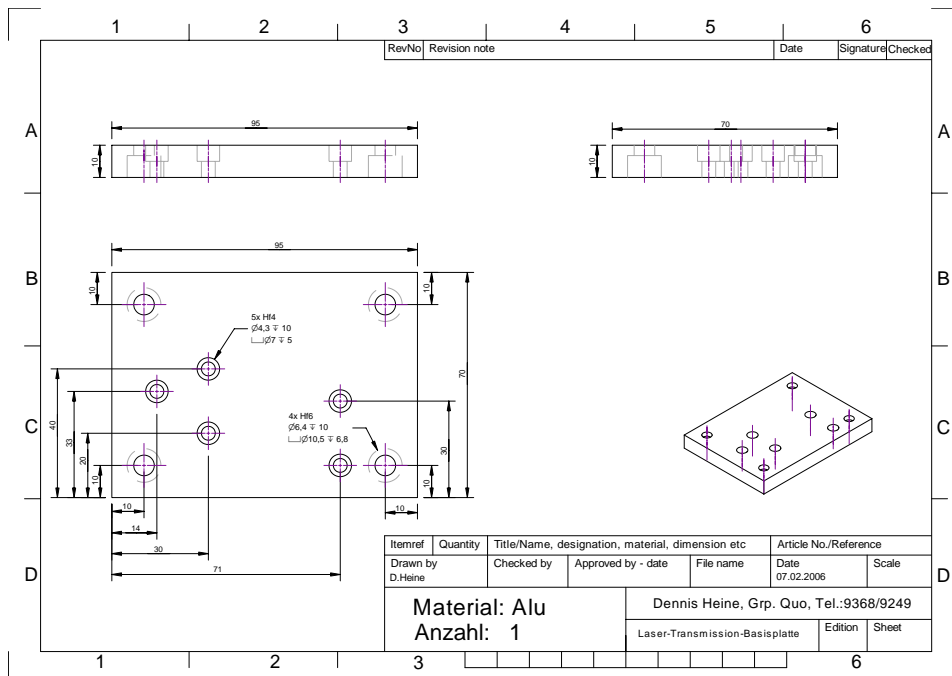


Figure F.7.: Transmission Grating Laser Baseplate

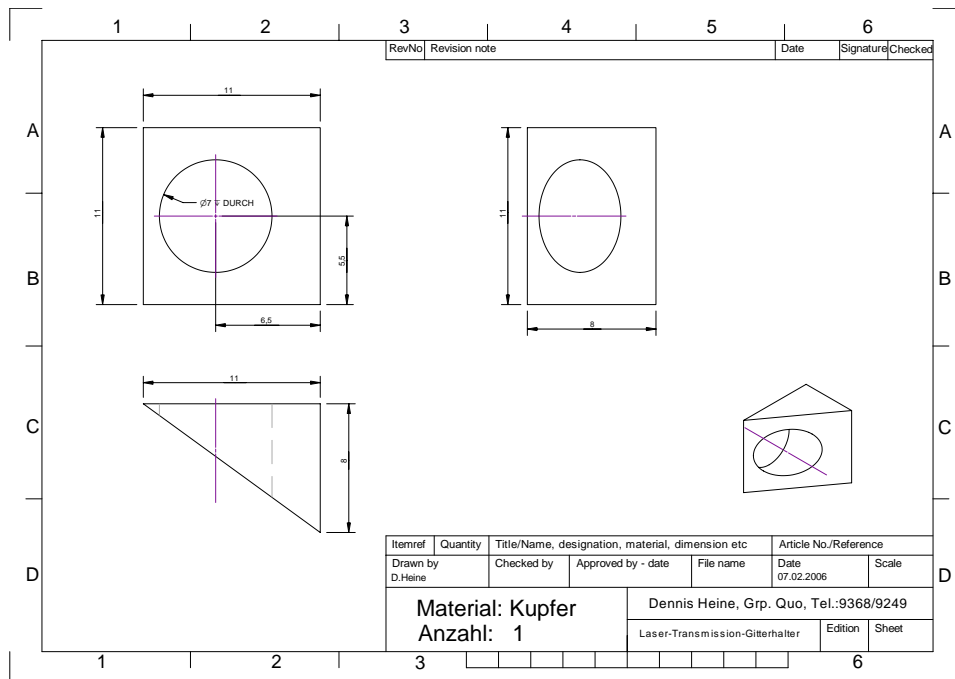


Figure F.8.: Transmission Grating Laser Grating Holder

# Bibliography

- [1] G. S. Hurst, M. H. Nayfeh, and J. P. Young.  
A demonstration of one-atom detection.  
*Applied Physics Letters*, 30(5):229–231, 1977
- [2] F. Diedrich and H. Walther.  
Nonclassical radiation of a single stored ion.  
*Phys. Rev. Lett.*, 58(3):203–206, 1987
- [3] J. I. Cirac and P. Zoller.  
Quantum Computations with Cold Trapped Ions.  
*Phys. Rev. Lett.*, 74(20):4091–4094, 1995
- [4] M. Weber, J. Volz, K. Saucke, C. Kurtsiefer, and H. Weinfurter.  
Analysis of a single-atom dipole trap.  
*Physical Review A (Atomic, Molecular, and Optical Physics)*, 73(4):043406, 2006
- [5] P. Münstermann, T. Fischer, P. Maunz, P. W. H. Pinkse, and G. Rempe.  
Dynamics of Single-Atom Motion Observed in a High-Finesse Cavity.  
*Phys. Rev. Lett.*, 82(19):3791–3794, 1999
- [6] A. Öttl, S. Ritter, M. Köhl, and T. Esslinger.  
Correlations and Counting Statistics of an Atom Laser.  
*Physical Review Letters*, 95(9):090404, 2005
- [7] C. J. Hood, T. W. Lynn, A. C. Doherty, A. S. Parkins, and H. J. Kimble.  
The Atom-Cavity Microscope: Single Atoms Bound in Orbit by Single Photons.  
*Science*, 287(5457):1447–1453, 2000
- [8] H. Mabuchi, Q. A. Turchette, M. S. Chapman, and H. J. Kimble.  
Real-time detection of individual atoms falling through a high-finesse optical cavity.  
*Opt. Lett.*, 21(17):1393, 1996
- [9] A. Haase, B. Hessmo, and J. Schmiedmayer.  
Detecting magnetically guided atoms with an optical cavity.  
*Opt. Lett.*, 31(2):268–270, 2006
- [10] I. Teper, Y.-J. Lin, and V. Vuletić.  
Resonator-Aided Single-Atom Detection on a Microfabricated Chip.  
*Physical Review Letters*, 97(2):023002, 2006

- 
- [11] Y. Colombe, T. Steinmetz, G. Dubois, F. Linke, D. Hunger, et al.  
Strong atom-field coupling for Bose-Einstein condensates in an optical cavity on a chip.  
*Nature*, 450(7167):272–276, 2007.  
ISSN 0028-0836
- [12] M. Trupke, J. Goldwin, B. Darquié, G. Dutier, S. Eriksson, et al.  
Atom Detection and Photon Production in a Scalable, Open, Optical Microcavity.  
*Physical Review Letters*, 99(6):063601, 2007
- [13] R. Folman, P. Krüger, and J. Schmiedmayer.  
Microscopic Atom Optics: From Wires to an Atom Chip.  
*Advances in Atomic, Molecular, and Optical Physics*, 48:263–356, 2002
- [14] J. Fortágh and C. Zimmermann.  
Magnetic microtraps for ultracold atoms.  
*Reviews of Modern Physics*, 79(1):235, 2007
- [15] J. Reichel.  
Microchip Traps and Bose-Einstein Condensation.  
*Applied Physics B*, 75:469–487, 2002
- [16] P. Horak, B. G. Klappauf, A. Haase, R. Folman, J. Schmiedmayer, et al.  
Possibility of single-atom detection on a chip.  
*Phys. Rev. A*, 67(4):043806, 2003
- [17] M. Wilzbach, A. Haase, M. Schwarz, D. Heine, K. Wicker, et al.  
Detecting neutral atoms on an atom chip.  
*Fortschr. Phys.*, 54(8 – 10):746–764, 2006
- [18] S. Eriksson, M. Trupke, H. Powell, D. Sahagun, C. Sinclair, et al.  
Integrated optical components on atom chips.  
*The European Physical Journal D*, 35(1):135–139, 2005
- [19] T. Purdy and D. Stamper-Kurn.  
Integrating cavity quantum electrodynamics and ultracold-atom chips with on-chip dielectric mirrors and temperature stabilization.  
*Applied Physics B*, 90(3-4):401–405, 2008
- [20] A. Takamizawa, T. Steinmetz, R. Delhuille, T. W. Hänsch, and J. Reichel.  
Miniature fluorescence detector for single atom observation on a microchip.  
*Opt. Express*, 14(23):10976–10983, 2006
- [21] Y. Ishii and T. Yanagida.  
Molecule Detection in Life Science.  
*Single Molecules*, 1(1):5–16, 2000

- [22] S. C. Kitson, P. Jonsson, J. G. Rarity, and P. R. Tapster.  
Intensity fluctuation spectroscopy of small numbers of dye molecules in a micro-cavity.  
*Phys. Rev. A*, 58(1):620–627, 1998
- [23] D. P. DiVincenzo.  
The Physical Implementation of Quantum Computation.  
*Fortschr. Phys.*, 48(9-11):771–783, 2000
- [24] C. Monroe.  
Quantum information processing with atoms and photons.  
*Nature*, 416(6877):238–246, 2002
- [25] E. Rieffel and W. Polak.  
An introduction to quantum computing for non-physicists.  
*ACM Comput. Surv.*, 32(3):300–335, 2000
- [26] H.-J. Briegel and P. Zoller.  
Quantencomputer.  
*Physikalische Blätter*, 55(9):37, 1999
- [27] ARDA.  
A Quantum Information Science and Technology Roadmap Part 1: Quantum Computation, 2004.  
[qist.lanl.gov](http://qist.lanl.gov)
- [28] N. Gisin, G. Ribordy, W. Tittel, and H. Zbinden.  
Quantum cryptography.  
*Rev. Mod. Phys.*, 74(1):145–195, 2002
- [29] ARDA.  
A Quantum Information Science and Technology Roadmap Part 2: Quantum Cryptography, 2004.  
[qist.lanl.gov](http://qist.lanl.gov)
- [30] M. Wilzbach.  
Single atom detection on an atom chip with integrated optics.  
Ph.D. thesis, Universität Heidelberg, Germany, 2007
- [31] W. D. Phillips.  
Nobel Lecture: Laser cooling and trapping of neutral atoms.  
*Rev. Mod. Phys.*, 70(3):721–741, 1998
- [32] S. Stenholm.  
The semiclassical theory of laser cooling.  
*Rev. Mod. Phys.*, 58(3):699–739, 1986

- [33] C. Wieman, G. Flowers, and S. Gilbert.  
Inexpensive laser cooling and trapping experiment for undergraduate laboratories.  
*American Journal of Physics*, 63(4):317–330, 1995
- [34] S. Wildermuth.  
One-dimensional Bose-Einstein condensates in micro-traps.  
Ph.D. thesis, Universität Heidelberg, Germany, 2005
- [35] W. Ketterle, D. S. Durfee, and D. M. Stamper-Kurn.  
Making, probing and understanding Bose-Einstein condensates.  
ArXiv, 1999.  
<http://arxiv.org/abs/cond-mat/9904034v2>
- [36] S. Schneider.  
Bose-Einstein Kondensation in einer magnetischen Z-Falle.  
Ph.D. thesis, Universität Heidelberg, Germany, 2003
- [37] S. Wildermuth, P. Krüger, C. Becker, M. Brajdic, S. Haupt, et al.  
Optimized magneto-optical trap for experiments with ultracold atoms near surfaces.  
*Phys. Rev. A*, 69(3):030901, 2004
- [38] T. Schumm.  
Bose-Einstein condensates in magnetic double well potentials.  
Ph.D. thesis, Universität Heidelberg, Germany, 2006
- [39] W. Hänsel.  
Magnetische Mikrofallen für Rubidiumatome.  
Ph.D. thesis, Ludwig-Maximilians-Universität München, Germany, 2000
- [40] B. E. Saleh and M. C. Teich.  
Fundamentals of Photonics.  
Wiley-Interscience, 2nd ed., 2007
- [41] M. Schwarz.  
Aufbau eines Glasfaserresonators zur Detektion einzelner Atome auf einem Atomchip.  
Master's thesis, Universität Heidelberg, Germany, 2004
- [42] K. Wicker.  
Micro Cavities for Cavity QED.  
Master's thesis, Universität Heidelberg, Germany, 2006
- [43] Semrock.  
LL01-780 Datasheet, 2007.  
[www.semrock.com](http://www.semrock.com)

- [44] D. A. Steck.  
Rubidium 87 D Line Data, 2002.  
<http://george.ph.utexas.edu/~dsteck/alkalidata>
- [45] K. Bergmann, H. Theuer, and B. W. Shore.  
Coherent population transfer among quantum states of atoms and molecules.  
*Rev. Mod. Phys.*, 70(3):1003–1025, 1998
- [46] D. Meschede.  
Optik, Licht und Laser.  
Teubner, 1999
- [47] R. P. Feynman, R. B. Leighton, and M. Sands.  
The Feynman Lectures on Physics, vol. 1.  
Addison-Wesley, 1977
- [48] D. Heine.  
Trapping Light with Dark States.  
Master's thesis, Ruprecht-Karls-Universität Heidelberg, Germany, 2003
- [49] S. J. van Enk and H. J. Kimble.  
Single atom in free space as a quantum aperture.  
*Phys. Rev. A*, 61(5):051802, 2000
- [50] S. J. van Enk and H. J. Kimble.  
Strongly focused light beams interacting with single atoms in free space.  
*Phys. Rev. A*, 63(2):023809, 2001
- [51] S. J. van Enk.  
Atoms, dipole waves, and strongly focused light beams.  
*Phys. Rev. A*, 69(4):043813, 2004
- [52] R. Grimm and M. Weidemüller.  
Optical Dipole Traps for neutral atoms.  
*Advances in Atomic, Molecular and Optical Physics*, 42:95–170, 2000
- [53] D. Frese, B. Ueberholz, S. Kuhr, W. Alt, D. Schrader, et al.  
Single Atoms in an Optical Dipole Trap: Towards a Deterministic Source of Cold Atoms.  
*Phys. Rev. Lett.*, 85(18):3777–3780, 2000
- [54] C. E. Wieman, D. E. Pritchard, and D. J. Wineland.  
Atom cooling, trapping, and quantum manipulation.  
*Rev. Mod. Phys.*, 71(2):S253–S262, 1999
- [55] D. Leibfried, R. Blatt, C. Monroe, and D. Wineland.  
Quantum dynamics of single trapped ions.  
*Rev. Mod. Phys.*, 75(1):281–324, 2003

- [56] J. J. Hope and J. D. Close.  
Limit to Minimally Destructive Optical Detection of Atoms.  
*Phys. Rev. Lett.*, 93(18):180402, 2004
- [57] J. J. Hope and J. D. Close.  
General limit to nondestructive optical detection of atoms.  
*Physical Review A (Atomic, Molecular, and Optical Physics)*, 71(4):043822, 2005
- [58] J. E. Lye, J. J. Hope, and J. D. Close.  
Rapid real-time detection of cold atoms with minimal destruction.  
*Phys. Rev. A*, 69(2):023601, 2004
- [59] T. Bondo, M. Hennrich, T. Legero, G. Rempe, and A. Kuhn.  
Time-resolved and state-selective detection of single freely falling atoms.  
*Optics Communications*, 264(2):271, 2006
- [60] G. Wrigge, I. Gerhardt, J. Hwang, G. Zumofen, and V. Sandoghdar.  
Efficient coupling of photons to a single molecule and the observation of its resonance fluorescence.  
*Nature Physics*, 4:60–66, 2008
- [61] S. Cova, M. Ghioni, A. Lacaita, C. Samori, and F. Zappa.  
Avalanche photodiodes and quenching circuits for single-photon detection.  
*Appl. Opt.*, 35(12):1956, 1996
- [62] R. G. W. Brown, K. D. Ridley, and J. G. Rarity.  
Characterization of silicon avalanche photodiodes for photon correlation measurements. 1: Passive quenching.  
*Appl. Opt.*, 25(22):4122, 1986
- [63] D. Dravins, D. Faria, and B. Nilsson.  
Avalanche Diodes as Photon-Counting Detectors in Astronomical Photometry.  
*SPIE proceedings*, 4008:298–307, 2000
- [64] A. Spinelli, L. M. Davis, and H. Dautet.  
Actively quenched single-photon avalanche diode for high repetition rate time-gated photon counting.  
*Review of Scientific Instruments*, 67(1):55–61, 1996
- [65] R. G. W. Brown, R. Jones, J. G. Rarity, and K. D. Ridley.  
Characterization of silicon avalanche photodiodes for photon correlation measurements. 2: Active quenching.  
*Appl. Opt.*, 26(12):2383, 1987
- [66] PerkinElmer Optoelectronics.  
SPCM-AQR, Single Photon Counting Module, 2006.  
Datasheet, <http://www.optoelectronics.perkinelmer.com>



- [67] G. Bedard.  
Dead-time corrections to the statistical distribution of photoelectrons.  
*Proceedings of the Physical Society*, 90(1):131–141, 1967
- [68] M. Höbel and J. Ricka.  
Dead-time and afterpulsing correction in multiphoton timing with nonideal detectors.  
*Review of Scientific Instruments*, 65(7):2326–2336, 1994
- [69] L. Hillesheim and J. Müller.  
The photon counting histogram in fluorescence fluctuation spectroscopy with non-ideal photodetectors.  
*Biophysical Journal*, 85:1948–1958, 2003
- [70] M. Ware, A. Migdall, J. Bienfang, and S. Polyakov.  
Calibrating photon-counting detectors to high accuracy: background and dead-time issues.  
*Journal of Modern Optics*, 54(2):361–372, 2007
- [71] PerkinElmer.  
FAQ, 2007.  
<http://optoelectronics.perkinelmer.com/FAQs/>
- [72] J. McKeever.  
Trapped Atoms in Cavity QED for Quantum Optics and Quantum Information.  
Ph.D. thesis, California Institute of Technology, 2004
- [73] L. Campbell.  
Afterpulse measurement and correction.  
*Review of Scientific Instruments*, 63(12):5794–5798, 1992
- [74] M. Zhao, L. Jin, B. Chen, Y. Ding, H. Ma, et al.  
Afterpulsing and Its Correction in Fluorescence Correlation Spectroscopy Experiments.  
*Appl. Opt.*, 42(19):4031–4036, 2003
- [75] C. Kurtsiefer, P. Zarda, S. Mayer, and H. Weinfurter.  
The breakdown flash of silicon avalanche photodiodes - back door for eavesdropper attacks?  
*Journal of Modern Optics*, 48(13):2039–2047, 2001
- [76] B. P. Anderson and M. A. Kasevich.  
Loading a vapor-cell magneto-optic trap using light-induced atom desorption.  
*Phys. Rev. A*, 63(2):023404, 2001
- [77] S. Du, M. B. Squires, Y. Imai, L. Czaia, R. A. Saravanan, et al.  
Atom-chip Bose-Einstein condensation in a portable vacuum cell.  
*Phys. Rev. A*, 70(5):053606, 2004

- [78] C. Klempt, T. van Zoest, T. Henninger, O. Topic, E. Rasel, et al.  
Ultraviolet light-induced atom desorption for large rubidium and potassium magneto-optical traps.  
*Physical Review A (Atomic, Molecular, and Optical Physics)*, 73(1):013410, 2006
- [79] E. Mariotti, M. Meucci, P. Bicchi, C. Marinelli, and L. Moi.  
An efficient photo-atom source.  
*Optics Communications*, 134:121–126, 1997
- [80] L. Mandel and E. Wolf.  
Coherence Properties of Optical Fields.  
*Rev. Mod. Phys.*, 37(2):231–287, 1965
- [81] G. Arfken and H.-J. Weber.  
Mathematical Methods for Physicists.  
Elsevier, 2005
- [82] D. Durfee and W. Ketterle.  
Experimental studies of Bose-Einstein condensation.  
*Opt. Express*, 2(8):299–313, 1998
- [83] P. Öhberg and L. Santos.  
Dynamical Transition from a Quasi-One-Dimensional Bose-Einstein Condensate to a Tonks-Girardeau Gas.  
*Phys. Rev. Lett.*, 89(24):240402, 2002
- [84] T. Raub.  
An integrated fluorescence detector.  
Master's thesis, Universität Heidelberg, Germany, 2008
- [85] R. Loudon.  
The Quantum Theory of Light.  
Oxford Science, 3rd ed., 2000
- [86] M. Orrit.  
Photon Statistics in Single Molecule Experiments.  
*Single Molecules*, 3(5-6):255–265, 2002
- [87] A. Boca.  
Experiments in Cavity QED: Exploring the Interaction of Quantized Light with a Single Trapped Atom.  
Ph.D. thesis, California Institute of Technology, 2005
- [88] S. Chopra and L. Mandel.  
An Electronic Correlator for Photoelectric Correlation Measurements.  
*Review of Scientific Instruments*, 43(10):1489–1491, 1972

- [89] H. J. Kimble, M. Dagenais, and L. Mandel.  
Multiatom and transit-time effects on photon-correlation measurements in resonance fluorescence.  
*Phys. Rev. A*, 18(1):201–207, 1978
- [90] H. J. Kimble, M. Dagenais, and L. Mandel.  
Photon Antibunching in Resonance Fluorescence.  
*Phys. Rev. Lett.*, 39(11):691–695, 1977
- [91] M. Dagenais and L. Mandel.  
Investigation of two-time correlations in photon emissions from a single atom.  
*Phys. Rev. A*, 18(5):2217–2228, 1978
- [92] B. Darquie, M. P. A. Jones, J. Dingjan, J. Beugnon, S. Bergamini, et al.  
Controlled Single-Photon Emission from a Single Trapped Two-Level Atom.  
*Science*, 309(5733):454–456, 2005
- [93] M. Wilzbach.  
Aufbau eines Experiments zur miniaturisierten und integrierten Detektion neutraler Atome.  
Master’s thesis, Universität Heidelberg, Germany, 2002
- [94] C. E. Wieman and L. Hollberg.  
Using diode lasers for atomic physics.  
*Review of Scientific Instruments*, 62(1):1–20, 1991
- [95] D. Meschede.  
Optik, Licht und Laser.  
Teubner, Stuttgart, 1999
- [96] M. G. Littman and H. J. Metcalf.  
Spectrally narrow pulsed dye laser without beam expander (ET).  
*Appl. Opt.*, 17(14):2224, 1978
- [97] L. Ricci, M. Weidemüller, T. Esslinger, A. Hemmerich, C. Zimmermann, et al.  
A compact grating-stabilized diode laser system for atomic physics.  
*Optics Communications*, 117(5-6):541–549, 1995
- [98] C. J. Hawthorn, K. P. Weber, and R. E. Scholten.  
Littrow configuration tunable external cavity diode laser with fixed direction output beam.  
*Review of Scientific Instruments*, 72(12):4477–4479, 2001
- [99] M. Rückel.  
Frequenzstabilisierung eines Diodenlasers.  
Master’s thesis, Universität Heidelberg, Germany, 2002

- [100] K. Singer, S. Jochim, M. Mudrich, A. Mosk, and M. Weidemüller.  
Low-cost mechanical shutter for light beams.  
*Review of Scientific Instruments*, 73(12):4402–4404, 2002
- [101] L. P. Maguire, S. Szilagy, and R. E. Scholten.  
High performance laser shutter using a hard disk drive voice-coil actuator.  
*Review of Scientific Instruments*, 75(9):3077–3079, 2004
- [102] S. Groth.  
Development, Fabrication and Characterisation of Atom Chips.  
Ph.D. thesis, Universität Heidelberg, Germany, 2006
- [103] A. del Campo and C. Greiner.  
SU-8: a photoresist for high-aspect-ratio and 3D submicron lithography.  
*Journal of Micromechanics and Microengineering*, 17:R81–R95, 2007
- [104] E. R. Abraham and E. A. Cornell.  
Teflon Feedthrough for Coupling Optical Fibers Into Ultrahigh Vacuum Systems.  
*Appl. Opt.*, 37(10):1762–1763, 1998
- [105] P. Hommelhoff.  
Bose-Einstein-Kondensate in Mikrochip-Fallen.  
Ph.D. thesis, Universität München, Germany, 2002
- [106] D. Voigt, E. Schilder, R. Spreeuw, and H. van Linden van den Heuvell.  
Characterization of a high-power tapered semiconductor amplifier system.  
*Applied Physics B: Lasers and Optics*, 72(3):279–284, 2001
- [107] R. A. Nyman, G. Varoquaux, B. Villier, D. Sacchet, F. Moron, et al.  
Tapered-amplified antireflection-coated laser diodes for potassium and rubidium atomic-physics experiments.  
*Review of Scientific Instruments*, 77(3):033105, 2006
- [108] Wikipedia.  
Laser Diode, 2004.  
[Online; accessed 17-April-2008] PD image, originally courtesy of NASA,  
[http://en.wikipedia.org/w/index.php?title=Laser\\_diode&oldid=205661684](http://en.wikipedia.org/w/index.php?title=Laser_diode&oldid=205661684)
- [109] G. Ewald, K.-M. Knaak, S. Götte, K. Wendt, and H.-J. Kluge.  
Development of narrow-linewidth diode lasers by use of volume holographic transmission gratings.  
*Applied Physics B: Lasers & Optics*, 80(4/5):p483 – 487, 20050401
- [110] M. Vainio, M. Merimaa, and E. Ikonen.  
Iodine spectrometer based on a 633 nm transmission-grating diode laser.  
*Measurement Science and Technology*, 16:1305–1311, 2005

- [111] M. Merimaa, H. Talvitie, P. Laakkonen, M. Kuittinen, I. Tittoonen, et al. Compact external-cavity diode laser with a novel transmission geometry. *Optics Communications*, 174(1-4):175–180, 2000
- [112] R. Barth. Digital In-Line X-Ray Holographic Microscopy with Synchrotron Radiation. Ph.D. thesis, Univeristät Heidelberg, Germany, 2008
- [113] Eagleyard, 2007. Private communication
- [114] M. Trinker, S. Groth, S. Haslinger, S. Manz, T. Betz, et al. Multi-layer atom chips for versatile atom micro manipulation, 2008. <http://arxiv.org/abs/0801.3351>
- [115] E. Arimondo, M. Inguscio, and P. Violino. Experimental determinations of the hyperfine structure in the alkali atoms. *Rev. Mod. Phys.*, 49(1):31–75, 1977
- [116] M. H. DeGroot and M. J. Schercish. Probability and Statistics. Addison-Wesley, 2002
- [117] M. Kemman. Laserinduzierte und spontane Molekülbildung in einer magneto-optischen Atomfalle. Master’s thesis, Universität Freiburg, Germany, 2001

*”Originality is the fine art of remembering what you hear but forgetting where you heard it.”*

Laurence J. Peter



# Thank You

To the following people I am indebted, due to their instrumental contributions to the realization of this thesis.

**My Supervisors** Prof. Jörg Schmiedmayer, fountain of surprising insights, and Dr. Björn Hessmo, who values his notebook higher than his face.

**Prof. Cremer** , who was so kind to accept the thankless job of a second referee. I felt pangs of guilt towards him with every page that this thesis grew...

**The Electronics Workshop** of the Physikalisches Institut, Universität Heidelberg for all their ingenious developments. Most specifically Mr. Rusnyak, who, personally, is the very reason why my lasers obey me.

**The Mechanical Workshop** of the Physikalisches Institut, Universität Heidelberg headed by Mr. Stahl. Your skills are unmatched and it was a pleasure working with you and learning from you. Thank you for making our work possible.

**The Ultrafast Laser Group** , from the Institut für Photonik, TU Wien, most specifically Prof. Andrius Baltuska and Dr. Dmitry Sidorov for borrowing the fusion splicer at short notice.

**Alexander Kasper** , the man who taught me to built those nifty little lasers.

**Marco Wilzbach** , lab mate baffling all description. I hope you like what I made of your baby. If you ask me I'd say we built a beautiful little machine. Oh, and I still have those pictures, -so behave.

**Thorsten Schumm** for being a beacon of hope.

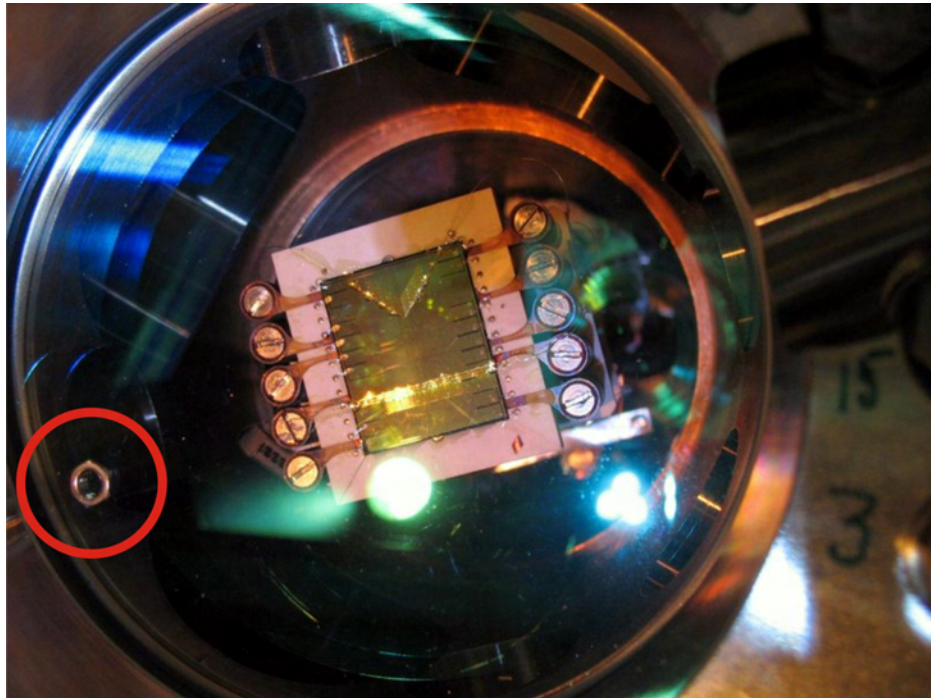
Of course many more colleagues and friends have been invaluable sources of support and friendship, without some I could not have persevered. Even though you may not be listed here by name, partly because I hope you already know my feelings, and partly because mere printed words would not suffice, please know that I value each and every one of you greatly.

*"..study was never a one-way thing. A man might spend his life peering at the private life of elementary particles and then find he either knew who he was or where he was, but not both."*

T.Pratchett, Hogfather

## ..and finally

I thank german engineering and the inventors of redundancy for keeping the sky from falling on my head.



*"If it works, it works very well."*

J.S.